Spring 2021

Structural Origin Of Thermal, Mechanical Properties And Morphological Behaviors Of Semiconducting Polymers

Song Zhang

Structural Origin Of Thermal, Mechanical Properties And Morphological Behaviors Of Semiconducting Polymers

by

Song Zhang

ADissertation
Submitted to the Graduate School,
the College of Arts and Sciences
and the School of Polymer Science and Engineering
at The University of Southern Mississippi
in Partial Fulfillment of the Requirements
for the Degree of Doctor of Philosophy

Approved by:

Dr. Xiaodan Gu, Committee Chair
Dr. Sarah E. Morgan
Dr. Jason D. Azoulay
Dr. Sergei Nazarenko
Dr. Derek Patton

May 2021

Published by the Graduate School

ABSTRACT

The past decades have witnessed a surging exploration of semiconducting polymers for the application of wearable and flexible organic electronic devices. Despite the increased amounts of molecular engineered polymers and their much-improved electrical performances, a systematic study of the structure-thermal/mechanical property-morphology relationship of semiconducting polymers is still less investigated.

To understand the thin-film mechanical properties, a pseudo-free standing tensile tester was self-built and utilized to obtain their real-time stress-strain behaviors through uniaxial stretching on top of the water surface. It also enables the first quantitative measurement of fracture energy on ultrathin polymeric films. Through multiple mechanical testing methods (i.e., strain-rate dependent tensile tests, stress-relaxation, hysteresis tests, etc.), we found surprising viscoelastic behaviors from recently emerged donor–acceptor (D–A) type diketopyrropyrrole (DPP)-based semiconducting polymers, despite their rigid polymer backbones. Such observation was later directly correlated with their sub-room temperature glass transition temperature (T_g).

Thus, it is vital to explore the structural origin of the low-T_g nature in D–A polymers and the T_g prediction guidelines. Both backbone- and side-chain engineered DPP-based polymers were synthesized to investigate their thermal and mechanical performances. A modified dynamic mechanical analysis (DMA) and alternating current (AC)-chip calorimetry were utilized to measure the bulk and thin-film T_g, respectively. Our findings suggested the low-T_g results from the high weight fraction of flexible side-chains (typically > 50%). Furthermore, we developed a predictive mass-per-flexible bond model that establishes a linear relationship between chain flexibility and polymer T_g.

Moreover, a detailed morphological analysis was performed on tensile-aligned DPP-based polymer thin films through experimental measurements and molecular modeling. Two primary strain-induced alignment mechanisms were addressed: highly oriented crystalline domains coupled with crystallographic slippage, and substantial chain slippage in the amorphous domain.

To boost the mechanical and electrical performance of organic electronic devices, a semiconducting polymer composite was engineered by incorporating a low-T_g butyl rubber elastomer as the matrix. A mechanically and electrically self-healable composite system was obtained through careful control over the multi-scale phase separation behaviors. Such a method is proved to be broadly applicable to both n-type and p-type D–A polymers.

ACKNOWLEDGMENTS

First and foremost, I would like to express my deepest gratitude to my Ph.D. advisor, Prof. Xiaodan Gu, for bringing me into this research field, guiding me through every aspect of the Ph.D. training from experimental design, scientific writing to conference presentations, and continually supporting me in the past five years. His passion, vision, and creativity have always impressed and inspired me. I am tremendously fortunate to be one of the first students in the Gu lab, all the challenges and failures here have forged me into an independent researcher today.

I want to thank Prof. Jason D. Azoulay, Prof. Derek Patton, Prof. Sarah E. Morgan, and Prof. Sergei Nazarenko for serving as my dissertation committee member, providing me instrumental access, collaboration opportunities, and vital suggestions throughout my research towards this dissertation. Special thanks to Prof. Morgan for allowing me to join the Polymer Science and Engineering program of the University of Southern Mississippi. I must thank all the faculty members, staff, my 2016 PSE classmates and friends who make my time at Hattiesburg memorable.

I am grateful to have all past and present members from the Gu Research Group, your friendship, assistance, and mental support make my graduate life much easier. It is a pleasant experience to be one of the founding members with Daniel Weller and Dakota Ehlenburg. I enjoyed Luke Galuska's daddy jokes, honored Zhiqiang Cao's enthusiasm about academia, Guorong Ma's curiosity at everything, and amazed at Nathaniel Prine's perseverance. For all my fellow mentees, Ben Appleby, Catherine Teh, Sujata Dhakal, Zac Ahmad, Juan Correa Ruiz, and Yunfei Wang, thank you for being forbearing, and you have made me a better person.

All my projects and publications are impossible without my fantastic collaborators from over ten institutions in multiple countries. I especially would like to thank Prof. Simon Rondeau-Gagné's group from the University of Windsor for their long-term collaborations on the synthesis of customizable polymer systems, Prof. Yu-Cheng Chiu's group from the National Taiwan University of Science and Technology for the fabricating and testing of electronic devices, as well as Prof. Wenjie Xia's group from North Dakota State University and Prof. Lihua Jin's group from University of California, Los Angeles for simulation studies.

I also want to acknowledge Advanced Light Source (ALS) at Lawrence Berkeley National Lab (LBNL), Stanford Synchrotron Radiation Lightsource (SSRL) at Stanford Linear Accelerator Center (SLAC) National Accelerator Laboratory, Center for Nanophase Materials Sciences (CNMS) and Spallation Neutron Source (SNS) at Oak Ridge National Laboratory (ORNL), and National Synchrotron Light Source II (NSLS-II) at Brookhaven National Laboratory (BNL) that allow me to get access to advanced instruments. I sincerely appreciate the helpful discussions from Dr. Cheng Wang, Dr. Eric Schaible, Dr. Alison Pawlicki, Dr. Nikolay Borodinov, Dr. Changwoo Do, and Dr. Guillaume Freychet.

Finally, I am beyond grateful to have my family members being the anchor of my life. My parents Hongtao Zhang and Juan Li, my fiancée Yihan Liu, my grandparents, Peichu Zhang, Yanfang Li, Dahua Li, and Wenying Yuan, your trust in me are always driving me to be a better version of myself.

DEDICATION

To my loving parents, Hongtao Zhang and Juan Li

TABLE OF CONTENTS

LIST OF TABLES

LIST OF ILLUSTRATIONS

LIST OF SCHEMES

LIST OF ABBREVIATIONS

AA	All-Atomistic
AC	Alternating Current
ALS	Advanced Light Source
ASTM	American Society for Testing and Materials
BDS	Broadband Dielectric Spectroscopy
BHJ	Bulk Heterojunction
BR	Butyl Rubber
CG-MD	Coarse-Grained Molecular Dynamics
CP	Conjugated polymer
CVD	Chemical Evaporation Deposition
D–A	Donor–acceptor
DCB	Double-Cantilever Beam
DI	Deionized
DIC	Digital Image Correlation
DMA	Dynamic Mechanical Analysis
DPP	Diketopyrrolopyrrole
DSC	Differential Scanning Calorimetry
FOW	Film-On-Water
GCIS	Gas Cluster Ion Source
GET	Generalized Entropy Theory
GIWAXS	Grazing-incidence wide-angle X-ray scattering

GPC	Gel-permeation Chromatography
IDTBT	Indacenodithiophene-co-benzothiadiazole
IID	Isoindigo
IR	Infrared
LAMMPS	Large-scale Atomic/Molecular Massively Parallel Simulator
LMIS	Liquid Metal Ion Source
MAF	Mobile Amorphous Fraction
MEMS	Microelectromechanical Systems
MOF	Metal-Organic Frameworks
MSD	Mean-Squared Displacement
NEXAFS	Near-edge X-ray Absorption Fine Structure Spectroscopy
OFET	Organic field-effect transistors
OLED	Organic light-emitting diode
OM	Optical Microscope
OPV	Organic photovoltaics
ORNL	Oak Ridge National Laboratory
OTS	Octadecyltrichlorosilane
P3DDT	Poly(3-dodecylthiophene)
P3HT	Poly(3-hexylthiophene)
p-AQM	para-Azaquinodimethane
PBC	Periodic Boundary Conditions

PBTTT	*P*oly(2,5-bis(3-alkylthiophen-2-yl)thieno(3,2-b)thiophene)
PCE	Power Conversion Efficiency
PDMS	Polydimethylsiloxane
PDPPTVT	Poly(2,5-bis(2-decyltetradecyl)-3,6-di(thiophen-2-yl)diketopyrrolo[3,4-c]pyrrole-1,4-dione-alt-thienovinylthiophene
PMMA	Poly(methyl methacrylate)
PNDI(2HD)T	Poly{[N,N'-bis(2-hexylldecyl)naphthalene-1,4,5,8-bis(dicarboximide)-2,6-diyl]-alt-2,5-thiophene}
PS	Polystyrene
PSS	Poly(sodium 4-styrene sulfonate)
RAF	Rigid Amorphous Fraction
rDoC	relative Degree of Crystallinity
RSoXS	Resonant soft X-ray scattering
SANS	Small-angle Neutron scattering
SAXS	Small-angle X-ray scattering
SDZ	Shear Deformation Zone
SEBS	Polystyrene-block-poly(ethylene-co-butylene)-block-polystyrene
SNS	Spallation Neutron Source
SSRL	Stanford Synchrotron Radiation Lightsource

STM	Scanning Tunneling Microscopy
TEM	Transmission Electron Microscopy
TGA	Thermogravimetric Analysis
THF	Tetrahydrofuran
UV-vis	Ultraviolet-visible
UV-vis	Ultraviolet-visible
VASE	Variable Angle Spectroscopic Ellipsometry

CHAPTER I - BACKGROUND

1.1 Overview

Polymer-based semiconductors have received significant attention for their applications in electronics and optoelectronics (i.e., organic light-emitting diodes (OLEDs), organic field-effect transistors (OFETs), organic photovoltaics (OPVs)).[1,2,11,12,3–10] These semiconducting polymers or conjugated polymers (CPs) are comprised of rigid polymer backbones with alternating single- and double-bond providing overlapped electron clouds, and long, flexible side-chains contributing to solution solubility. Thus, compared with traditional rigid inorganic semiconductors like Si and Ge, CPs exhibit many benefits like intrinsic mechanical flexibility, large-scale solution processability, and structural tunability, which enable their applications in flexible and wearable technologies.[13–27]

The past decades have witnessed the development of semiconducting polymers from pentacene, polyfluorene, polythiophene, to recently emerged donor–acceptor (D–A) type polymers. Meanwhile, their thin-film device performances have been drastically improved with a high charge carrier mobility (> 12 $cm^2V^{-1}s^{-1}$) approaching crystalline silicon.[13–15] The electrical performance of semiconducting polymers can be greatly affected by a variety of factors: molecular structure, molecular weight, thin-film morphology, film thickness, device geometry, etc. While previous efforts have mainly focused on the structure-morphology-electrical property relationship of CPs, it is still conceptually challenging to design organic semiconductors with desired thermal and mechanical performance.

Thus, this dissertation will focus on understanding the structure-thermal/mechanical property-morphology relationship of semiconducting polymers. The discussion is divided into the following six chapters, followed by envisioned future directions.

Chapter II: We built a pseudo-free-standing tensile tester to study the mechanical performance of ultra-thin films for a range of polymers. The viscoelastic behavior of semiconducting polymer thin films was explored with detailed analysis, and the thin-film mechanical-thermal property relationship was established.

Chapter III: We performed the first quantitative fracture energy measurement on free-standing ultra-thin films. A ductile-to-brittle transition was observed as both film thickness and molecular weight decreased. Such behavior was also verified through finite element analysis.

Chapter IV: We studied the effect of backbone thiophene on the thermal and mechanical properties of semiconducting polymers. A Flory-Fox equation was successfully applied to describe the observed glass transition behavior in a variety of backbone-engineered semiconducting polymers.

Chapter V: We investigated the effect of side-chain length on the thermal and mechanical properties of DPP-based semiconducting polymers with various backbone structures. A predictive empirical model was developed to describe the linear relationship between the backbone T_g and chain flexibility.

Chapter VI: We probed the chain alignment mechanism of DPP-based polymer thin films through multimodal morphological analysis and molecular simulations. The

behavior of amorphous and crystalline regions, as well as the role of backbone and side-chain in the crystalline region upon chain alignment were deconvoluted.

Chapter VII: Through the physical blending of semiconducting polymers with low-T_g and tacky butyl rubber elastomer, we achieved a tear-resistant and self-healable polymer composite without degrading its electrical performance.

1.2 Thermal analysis for semiconducting polymers

1.2.1 Background

The thermal property of semiconducting polymers had been neglected for a long time in the field due to the limitations of traditional thermal analysis methods for bulk samples, including differential scanning calorimetry (DSC), thermogravimetric analysis (TGA), dynamic mechanical analysis (DMA), and shear rheology. While a normal DSC can successfully measure the melting behavior of CPs, it can hardly detect the backbone T_g.[16,17] Both the high backbone stiffness and the semicrystalline nature of the polymer result in limited heat capacity change during the glass transition.[16] Meanwhile, it is difficult to maximize the amorphous content in CPs due to the ultrafast crystallization rate and their similar melting temperature (T_m) and degradation temperature (T_d). In the meantime, both DMA and shear rheology tests are not widely applicable due to the poor synthetic scalability and limited availability of polymers per batch (< 100 mg). To address this issue, substrate-supported DMA measurements were developed, where the sample was prepared by drop casting ~ 5 mg samples onto glass fiber meshes or Kapton films. Similarly, a specially designed sample mold that only takes ~ 15 mg of the polymer was introduced for rheological measurements.[18–22]

The thin-film T_g for CPs (< 100 nm) is also difficult to obtain experimentally. While their limited volume leads to weaker thermal signals, the potential film-substrate interaction can also affect the measured result. Some commonly reported techniques that can measure thin-film T_g include ellipsometry, fast scanning DSC, and AC-chip calorimetry (temperature-modulated differential fast scanning calorimetry).[19,23–26] Since ellipsometry uses a laser to measure the thermal expansion of thin films, the absorption spectrum of CPs needs to be carefully addressed. Compared with normal DSC, fast scanning DSC provides an ultrafast heating and cooling rate that can suppress the crystallization of CP thin films and detect the weak glass transition signal. On a different note, alternating current (AC)-chip calorimetry can effectively measure the thin-film T_g due to its high sensitivity, broad temperature range, as well as wide modulation of the frequency range. This dissertation will focus on the utilization of glass fiber-assisted DMA measurement and AC-chip calorimetry to measure the T_g of the bulk sample and thin-film, respectively.

1.2.2 Experimental methods for T_g measurement

A typical DMA measurement is shown in **Figure 1.1(a-b)**, where the sample is prepared through drop-casting polymer solutions on top of the glass fiber mesh. The glass fiber was cut into rectangular strips, where the fiber has a 45° angle with the stretching direction. For each measurement, only ~5 mg of sample is required to fully cover the glass fiber and fill the voids. Next, the sample was transferred to the DMA chamber and gripped tightly on two ends. A fixed frequency of 1 Hz was applied under strain-controlled mode with a heating rate of 3 °C min^{-1}. The T_g can be obtained from the peak location in either the loss modulus curve or Tan δ curve, corresponding to different

modes of motions along the polymer chain. In this dissertation, the Tan curve will be used to identify the peak location, while the loss modulus curve serves as a reference. The alkyl side-chain typically has a T_g below 0 °C, while the backbone T_g is much higher and can be significantly influenced by the side-chain content, as discussed later in Chapter III and IV.

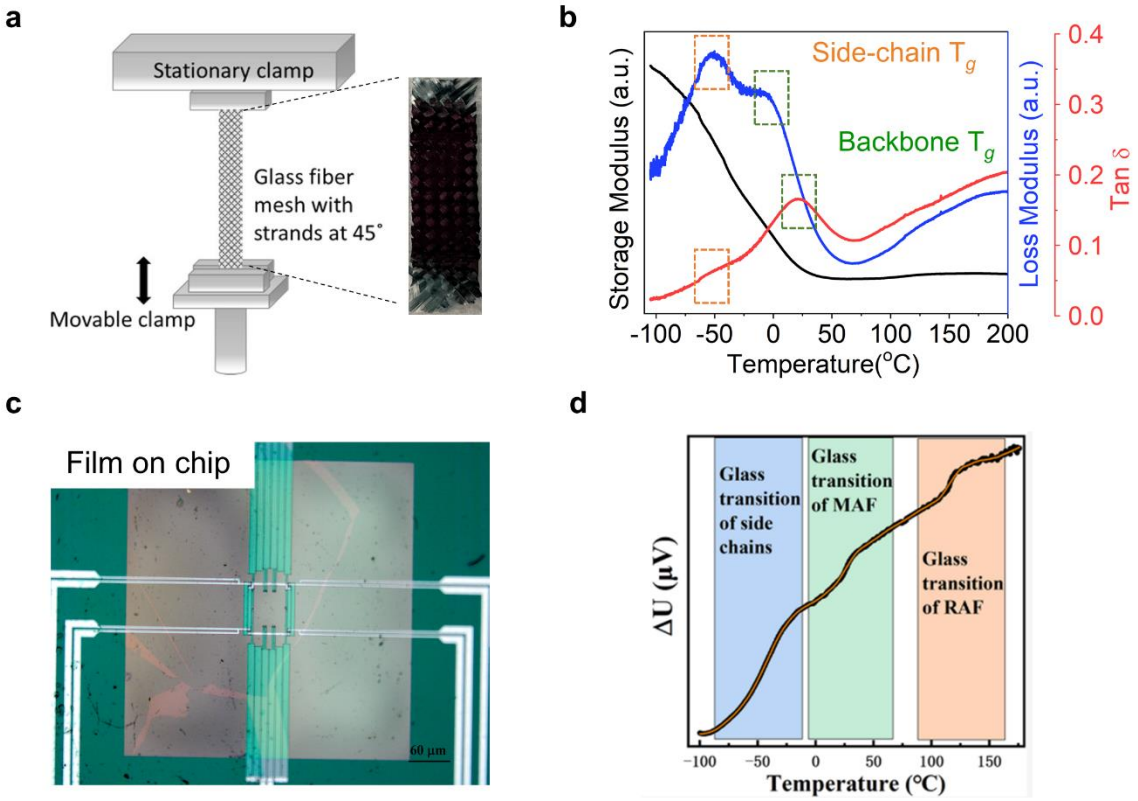

Figure 1.1 *Thermal analysis methods for conjugated polymers. (a) Schematic of a clamped DMA sample prepared by coating polymer solutions on the glass fiber mesh.*[27] *(b) DMA scan for a DPP-based polymer showing the storage modulus, loss modulus, and tan δ curves. The glass transition is shown in dotted squares. (c) Optical microscope image of a thin film sitting on top of the measuring chip.*[18] *(d) Representative AC-chip calorimetry heating scan of a DPP-based polymer showing three transition steps.*[25]

In addition to the measurement of bulk T_g, AC-chip calorimetry will also be applied to detect the glass transition from CP thin-films. As shown in **Figure 1.1(c-d)**, a thin film is transferred onto a sensor with a heated area of 100 μm * 100 μm. Similar to a

normal DSC measurement, a heat-cool-heat scan is performed to remove the thermal history, with a second heating scan rate of 1 °C/min under a frequency of 10 Hz. The amplitude of the complex differential voltage is shown as a function of temperature, where the step change can be directly correlated with the heat capacity change.[26] Due to the high sensitivity of AC-chip calorimetry, multiple transitions can be detected, including the rigid amorphous fraction (RAF) and mobile amorphous fraction (MAF).[25]

1.3 Film-on-water tensile tests for ultra-thin films

(Adapted from "Zhang S, Gu, X. Thin-film tensile test on the water surface. Under Preparation, 2021.")

1.3.1 Background

Decades of technological development has witnessed an expanding market of thin films in the field of microelectromechanical systems (MEMS), electro and optical coatings, semiconducting materials, and photovoltaic solar cells, etc.[28–32] These novel miniaturized materials with a micro-size or nano-size scale have shown superior performances, while an in-depth understanding of their mechanical properties is still lacking. For real-life applications with a high demand for materials' mechanical integrity and stability, it is essential to understand thin-film mechanics through mechanical tests, which will provide the most fundamental material-property relationships and guidelines for material selection and product development of thin films.[19,33–35]

Among various mechanical testing methods (tensile, bending, shearing, compression, torsion, etc.), a uniaxial tensile test is the most straightforward method by applying uniform stress and strain fields to the material. A typical tensile tester for bulk materials (i.e., Instron) is comprised of an extensometer and a load cell, while a free-

standing sample is held by tensile grips. However, materials in their thin-film state can only take a limited amount of load, despite being more bendable than their bulk state (i.e., metal, silicon, and graphene).[36–39] Thus, the proper handling, gripping, and loading of thin films without introducing defects are incredibly vital. To address these problems, substrates are frequently used to support thin films. An underlying solid substrate layer is commonly applied to create a double-layer composite, followed by tensile testing.[40–45] However, the extra substrate layer can be problematic in terms of two phenomena. For films much thinner than the substrate, a successful extraction of thin-film mechanical property is complicated; the interaction between film and substrate could affect thin-film mechanics.[46–48] While free-standing tensile tests on thin films can eliminate the substrate effect, the procedures to release thin-films from the substrate without damaging the film or creating cracks/wrinkles are still challenging.[49–52] To balance the need for the absence of substrate effect and less damage during transferring, a novel film-on-water technique is introduced.[18,53–55] Compared with other liquids like organic solvents (i.e., ethanol, toluene) and ionic liquids as the support layer, water is more environmental-friendly, more compatible with various materials, and importantly, water has high surface tension and low viscosity.[53,56] Thus, the water surface provides a near-frictionless sliding environment without film-substrate adherence like a solid substrate.

1.3.2 Experimental methods of FOW test

The fabrication of a thin-film tensile specimen for the FOW test involves two steps: Deposition of thin films on the substrate and transferring them onto the water surface. The choice of thin film-substrate combination is highly dependent on the material of interest. The deposition method of thin films can be roughly classified into

two categories: Physical deposition through evaporation or sputtering; Chemical deposition through sol-gel techniques, chemical bath deposition, spray pyrolysis technique, plating, or chemical evaporation deposition (CVD).[57] A high-quality thin-film specimen with limited defects like voids are desired to avoid low crack-onset strain (or fracture strain) and toughness. Different from the relatively thick material specimen with a standard geometry based on the American Society for Testing and Materials (ASTM) standard, up to now, no standard geometry for thin-film specimen has been reported. The reported sample geometry varies with the material choice and the preference of the research group. In most cases, a dog-bone like geometry is preferred to avoid the potential rupture from the sample-grip contact position. Past works have shown that direct laser patterning of a dog-bone geometry on the thin-film (**Figure 1.2(a)**),[58–60] deposition of thin-film through a reversed dog-bone shaped mask (**Figure 1.2(b)**),[53] and plasma etching of the thin-film with a protective dog-bone mask (**Figure 1.2(c)**) are several practical alternatives.[18,55,61]

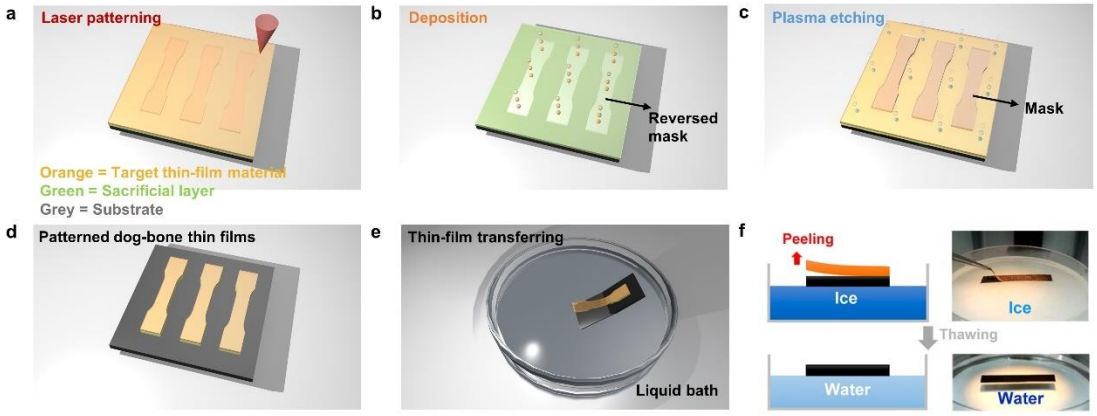

Figure 1.2 *Methods to transfer thin-film on water. (a) Laser patterning of dog-bone shaped thin-film. (b) Deposition of thin-film through a reversed dog-bone shaped mask. (c) Plasma etching of thin-film with a dog-bone shaped mask on the top. (d) Patterned dog-bone shape thin films on the substrate. (e) Thin-film floated on the liquid surface through dissolving the sacrificial layer. (f) Ice-assisted thin-film separation method. A*

fuel-cell electrode (black) coated on a decal transfer substrate (orange) is frozen on the water surface, followed by peeling off the decal substrate. Upon ice thawing, the electrode is fully floated on the water surface.[62]

Followed by thin-film deposition, the substrate needs to be removed to realize a pseudo-free-standing thin film (**Figure 1.2(d,e)**). For polymer samples, a water-soluble polymer layer like poly(acrylic acid) (PAA)[54] and poly(sodium 4-styrene sulfonate) (PSS)[18] are commonly coated underneath the target polymer film to form a double-layer thin-film composite. Upon dipping in water, the sacrificial layer will be dissolved; thus, the thin film sample can be floated. Except for using a water-soluble polymer, any material that can be removed by a corresponding dissolving solvent can be used as the sacrificial layer. A gold thin film supported by a copper layer has been demonstrated to float on a copper etchant solution, followed by transferring to a water bath.[53] Similarly, multilayer graphene being CVD deposited on a nickel (Ni)-deposited silicon wafer can be released by weakening the Ni-SiO_2 interface and Ni etching.[63] Another novel transfer technique is shown in **Figure 1.2(f)** successfully floated a thin fuel-cell electrode on the water surface by taking advantage of the water phase transformation phenomenon. A polyimide substrate (decal)-coated fuel-cell electrode is first floated on the water surface. Upon water frozen into ice, a strong binding force will form between the electrode and ice due to the existence of Nafion ionomer in the electrode. Next, the decal substrate can be peeled off by a tweezer, and the electrode is fully floated on the water surface after the ice thaws.[62]

1.3.3 Stress-strain measurements for FOW test

Except for a high-quality thin-film sample, a successful tensile experiment is also highly dependent on the measurement accuracy of the force exerted on the sample (F)

and the displacement that the sample experiences (Δl). Based on the sample geometry, both engineering stress-strain curve and true stress-strain curve can be built through the following equations:

$$\sigma_E = \frac{F}{A_0} \tag{1.1}$$

$$\varepsilon_E = \frac{\Delta l}{l_0} \tag{1.2}$$

$$\sigma_T = \sigma_E * (1 + \varepsilon_E) \tag{1.3}$$

$$\varepsilon_T = \ln(1 + \varepsilon_E) \tag{1.4}$$

where σ_E, ε_E, σ_T, and ε_T represent engineering stress and strain, as well as true stress and strain, respectively. A_0 is the cross-section area and l_0 stands for the original sample length. For a thin-film sample with limited A_0 and l_0, the force and strain rate can be as low as a few millinewtons and several micrometers per second, respectively. Thus, high resolution and precision are required for the tensile tester.

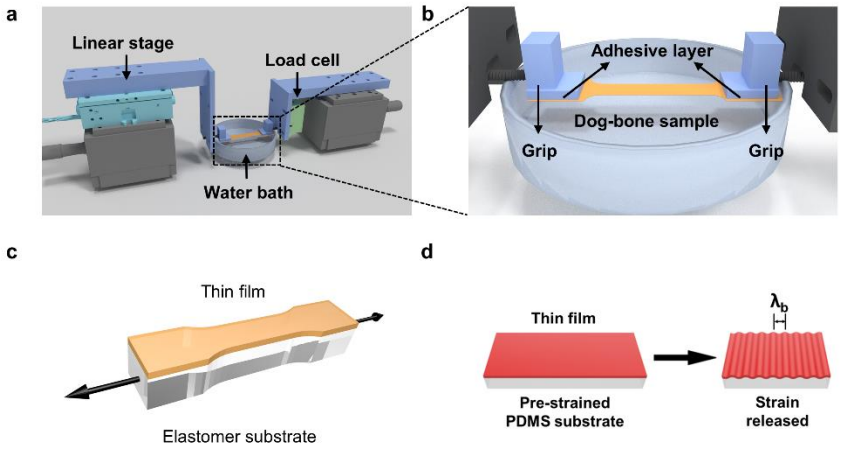

Figure 1.3 *(a) 3D schematic of the pseudo-free standing tensile tester. (b) Zoom-in scheme of thin-film gripped by a PDMS sheet. (c) Schematic of a thin-film on an elastomer substrate under uniaxial stretching. (d) Schematic of the buckling metrology method.*[64]

The measurement of force and displacement can be achieved in multiple ways. As shown in **Figure 1.3(a)**, a pseudo-free-standing tensile tester operates by attaching two ends of the thin-film to a high-resolution load cell and a linear stage, separately, with two grips in between. A thin polydimethylsiloxane (PDMS) sheet is usually coated on the bottom of the grip to provide strong adhesion force with the sample and avoid potential slippage or delamination (**Figure 1.3(b)**). Here, a tight grip with an adequately aligned bottom surface, as well as a soft contact of PDMS with the sample, are necessary to ensure a reliable force measurement. The proper co-alignment of grips and the thin-film sample is also essential for a validated uniaxial measurement. The sample displacement can be calculated by subtracting the linear stage movement with the PDMS deformation and the load cell compliance along the strain direction. A digital image correlation (DIC) technique is also useful to track the strain through pre-deposited particles on the thin-film sample surface.[65]

1.3.4 Comparison with Film-on-elastomer method

Along the in-plane loading direction, the substrate deforms to the same degree as the thin-film sample. Thus, a compliant substrate (i.e., PDMS) is frequently applied to avoid obscuring the thin-film response. Generally, two categories of thin-film elastic modulus measurements have been reported: modeling of a double-layer composite and buckling metrology (**Figure 1.3(c)**). The first category is based on the known substrate modulus and a bilayer model to extract the thin-film modulus from the bilayer composite.[41,43] The second method, on the other hand, is a wrinkling-based technique, where a soft and elastic substrate is first stretched to a few percent, followed by transferring thin-film samples to the substrate surface and releasing the substrate (**Figure**

1.3(d)).[42,66] Due to the compressive energy, periodic wrinkling patterns will form on the thin-film. The elastic modulus of thin-film can be calculated by the following equation:

$$\frac{E_f}{(1-v_f^2)} = \frac{3E_s}{(1-v_s^2)} \times (\frac{\lambda_b}{2\pi h})^3 \quad (1.5)$$

where E_f, E_s, v_f, v_s represent for the elastic modulus and Poisson's ratio of film and substrate, respectively, λ_b is the wavelength, and h is film thickness. However, there are several requirements to validate this equation: (a) the compressive strain is small enough ($\ll$10%) and within the sample's elastic strain limit, (b) $\frac{E_f}{E_s} \gg 1$, (c) The substrate is much thicker than the film, (d) the buckling amplitude is much smaller than the wavelength. Therefore, as an indirect method, an accurate modulus measurement should consider the softness of the elastic substrate, the applied strain-rate (releasing rate), and the linear elastic limit for the thin film.[64,67]

For the measurement of fracture strain, a simple pulling test of the double-layer composite is typically used to observe the onset of crack formation in thin films.[40,45] Thus, strong adhesion between film-substrate is vital to avoid potential delamination. It is to be noted that the compliant substrate layer absorbs most strain energy. Thus, the thin-film crack-onset strain is frequently overestimated. It can also be challenging for OM to detect microcracks in ultra-thin films (< 50 nm) with high transparency. The fracture behavior of thin-films has also been quantitatively investigated under the support of the substrate.[68] Except for a traditional four-point bending technique mentioned before, a scratch testing method has also been introduced to characterize the thin-film cohesive and adhesive behaviors.[69] By observing crack density or the aspect ratio change of a microvoid in thin films, the ductility of thin films can be quantified.[68] Hence, easy

quantitative measurement of thin-film fracture energy remains difficult for the in-plane loading on a solid substrate.

Except for the intrinsic difference in testing procedures, the potential substrate effect on thin-film properties is frequently neglected. Past works have demonstrated the interaction between substrate and thin-film can either increase or reduce the thin-film T_g, thus influence the mechanical properties.[70,71] Overall, the in-plane loading of the film-on-solid substrate method is accessible to all researchers, the thin-film sample is easy to handle, and the experiment is straightforward to perform. However, it is an indirect method and limited in testing soft materials with a similar modulus to the substrate, or thin films that cannot bind well with the substrate. Also, much attention needs to be paid to control the strain rate. In comparison, the FOW test requires a more complicated and expensive setup while it provides a more direct measurement of thin-film modulus, failure, and fracture behavior. When compared with solid substrates, water plays a similar but less strong stabilization effect on thin films.

1.4 Morphological characterizations for semiconducting polymer thin films

1.4.1 Background

Thin-film morphology is one of the most crucial parameters in controlling both thermomechanical and electrical properties. It is also susceptible to many internal and external factors, including molecular weight, dispersity, chemical structure, processing condition, post-treatment condition, etc. Meanwhile, the favorable morphology is highly dependent on the type of device and the critical performance parameters. For example, a bulk heterojunction (BHJ) morphology with interpenetrated donor and acceptor polymers that phase separated into ~ 20 nm domains is preferrable for the efficiency of OPVs.[72–74]

For OFETs and thermoelectric devices, aligned polymer backbones and improved molecular packing typically enable efficient charge transport and a high power factor, respectively.[75,76,85,77–84] This dissertation will focus on investigating thin-film morphologies towards the application of OFET devices.

Due to the heterogeneous rigid backbone/soft side-chain combination and strong π- π interactions between polymer backbones, semiconducting polymers usually show complicated morphological characteristics like crystalline domains, amorphous chains, and local aggregations. While most CPs are semicrystalline polymers, in the early investigations, a general rule to improve the charge carrier mobility of CPs is through the engineering of highly crystalline polymers, i.e., poly(2,5-bis(3-alkylthiophen-2-yl)thieno(3,2-b)thiophene) (PBTTT), due to the efficient charge transport along polymer backbones.[4] Until recently, a surprisingly high charge mobility (> 1 $cm^2V^{-1}s^{-1}$) is demonstrated in a near-amorphous indacenodithiophene-co-benzothiadiazole (IDTBT) polymer, which introduces a new concept of engineering 'disorder-free' CPs.[8,86] Physical alignment of polymer backbones has been proven to be a universal way to improve the electrical performance of different types of CP thin films, i.e., shear alignment, tensile alignment, etc.[32,75–82,87]

1.4.2 Experimental methods for thin-film morphology characterization

To differentiate different domains in the thin-film, multimodal characterization methods including scattering, spectroscopy, and microscopy techniques are required. The scattering technique focuses on the orderly packed geometries, like polymer crystallites. The most applied technique in the literature is grazing-incidence wide-angle X-ray scattering (GIWAXS), which allows for a large scattering volume from thin films

through a reflection mode. It provides molecular packing characteristics inside of polymer crystallites with three main packing directions (side-chain packing, backbone packing, and π-π stacking) along two directions of interests (in-plane and out-of-plane direction). It is also feasible to compare the relative degree of crystallinity (rDoC) of different CP thin films through a quantitative pole figure analysis based on the lamellar peak.

The spectroscopy technique, however, does not specifically differentiate the crystalline and amorphous regions. Techniques like ultraviolet-visible (UV-vis) spectroscopy, infrared spectroscopy, and fluorescence spectroscopy probe local molecular level bond vibration modes based on the specific light-bond interactions. UV-vis spectroscopy is widely applied to determine the molecular aggregation behavior in CP thin films. An HJ-aggregate model can be used to describe the favorable molecular interaction based on the intensity of two vibronic peaks (0-1 and 0-0) from the absorption spectrum. While a J-type aggregate represents intra-chain interactions, an H-type aggregate corresponds to inter-chain interactions. Thus, it is feasible to compare the effect of molecular characteristics and processing conditions on the type and fraction of aggregates.

Microscopy techniques like an optical microscope (OM) and atomic force microscopy (AFM) provide visual observations of thin-film surface morphology. In contrast, other advanced techniques like (scanning) transmission electron microscopy ((S)TEM) and scanning tunneling microscopy (STM) can even produce atomic-level imaging.[88–90] This dissertation will cover most of the techniques mentioned above, like

GIWAXS, UV-vis, and AFM, as well as other state-or-the-art methods like soft/tender X-ray scattering and near-edge X-ray absorption fine structure spectroscopy (NEXAFS).

CHAPTER II – ULTRA-THIN FILM TENSILE TESTS ON THE WATER SURFACE

(Adapted from "Zhang, S.; Ocheje, M. U.; Luo, S.; Ehlenberg, D.; Appleby, B.; Weller, D.; Zhou, D.; Rondeau-Gagné, S.; Gu, X. Probing the Viscoelastic Property of Pseudo Free-Standing Conjugated Polymeric Thin Films. Macromol. Rapid Commun. 2018, 39 (14), 1800092.")

2.1 Introduction

Flexible electronics have gained significant attention due to their wide range of applications in flexible, wearable and implantable devices with the potential of being solution processed at low cost.[1–3] The heart of organic electronic devices is the active layer consisting of a thin film of conjugated polymer, which plays a pivotal role in the functions of devices and dictates overall device performance. The charge transport property of organic thin film transistors has witnessed steady growth through the past decades, and surpassed amorphous silicon thanks to concerted works in chemistry, physics and device engineering. In addition to enhanced electrical properties, flexibility or stretchability is being implemented into organic electronic devices through various design concepts.[19,44,68,91–97] Several recent reviews highlighted the impressive progress for making highly conductive yet mechanically robust conjugated polymers.[2],[98–101] Despite those successes, fundamental understanding of the structure-mechanical property relationship for free-standing semiconducting polymers has dramatically lagged behind, with only few reports recently pioneered by Kim.[53,102–104]

Compared to readily available commodity plastics, mechanical measurements on free-standing semiconducting films are challenging, mainly due to limited material availability. Traditional mechanical tensile testers (e.g., Instron Inc.) typically require

large amounts of polymer (hundreds of mg per test), which is not easily obtainable for many conjugated polymers. A few exceptions are poly(3-alkyl thiophene) (P3AT) based polymers, synthesized through chain growth polymerization, as oppose to the polycondensation polymerization typical for D-A polymers.[5,105–107] Furthermore, measurements taken from bulk samples might deviate from that of films thinner than 100 nm due to the influence of air-polymer interface and polymer-substrate interactions.[108]

Great progress has been made to measure mechanical properties of supported polymeric thin films. In the past decade, thin film buckling methodology by Stafford *et al*.[42,109–111] has been widely adopted by the polymer community to indirectly measure the elastic modulus of buckled polymer films and more recently conjugated films.[44,68,91,92,112] In this method, a polymeric film is first transferred to a pre-stretched (< 2% strain) elastic substrate (i.e. poly(dimethylsiloxane) (PDMS)). Upon releasing the stress, the polymeric film undergoes periodic buckling due to energetic competition between film bending and substrate deformation. The periodicity of the buckled film can be correlated to the elastic modulus of the film and the underlying substrate. Additionally, yield strain of a supported film can also be measured by laser light diffraction of the film after cyclic straining and relaxing until it plastically deforms.[95,113] Lastly, crack onset strain is obtained by monitoring the formation of cracks while continuously stretching the film on elastomer with the aid of an optical microscope.[96] Lipomi group has extensively used the above mentioned techniques to quantify the mechanical property of conjugated polymeric thin films.[2,17,117–123,44,68,91,92,94,114–116] Interested readers should refer to recent review papers on this topic.[91,98]

With the help of buckling metrology, researchers have forged forward to create impressive stretchable devices while discovering trends in structure property relationships. Roth *et al*. reported mechanical properties on a library of D-A polymers, finding that polymers with large fused rings on the backbone tend to be more brittle, while longer branching side chains tend to increase the stretchability.[123] This observation is in accordance with other reports from Lu *et al*.[124] and Wu *et al*.[125] It is also reported that introducing the flexible linker unit[105,126,127], hydrogen bonding unit[97], or conjugation breaker[128–130] to the backbone can soften the polymer, making the polymer more deformable. Other methods such as physical blending with elastomer,[19,121,131–133] cross-linking[134] and addition of additievs[60] show great potential for improving mechanical properties. In one impressive example, Jie *et al*. reported that by using nanoscale confined polymer fibers through blending D-A polymers and polystyrene-block-poly(ethylene-co-butylene)-block-polystyrene (SEBS), stretchable device could have charge mobility as high as $1 cm^2 V^{-1} s^{-1}$ under 100% strain.[19]

As most mechanical tests thus far have been performed on supported films, direct measurements of stress-strain response in free standing semiconducting polymer thin films, especially the D-A polymers with high electrical performance, is lacking. Only recently has a thin film tensile test methodology emerged. Pioneered by Kim and coworkers, “pseudo-free standing tensile test” provides a direct way to measure the stress-strain response of sub-100 nm thin films, mimicking a traditional bulk material tensile test.[53,102–104] This method is advantageous since it produces a full stress-strain curve and eliminates the substrate effect that might obfuscate mechanical properties in buckling metrology.[44] In this paper, we successfully utilized the pseudo-free standing

tensile test method to systematically study the thickness-dependent mechanical property of two representative semiconducting polymers: P3HT and DPP-TVT (**Figure 2.1** for chemical structure). We find that despite their vast difference in charge carrier mobility and thin film morphology, both films showed viscoelastic response due to sub room temperature T_g. We further quantify the viscoelastic property of the thin films through strain rate-dependent mechanical behavior, hysteresis for cyclic strain and stress relaxation for the first time on conjugated polymer thin films.

2.2 Experimental

2.2.1 Materials

PDMS (Sylgard 184, Dow Corning), PS (Polymer Source, number-averaged molecular weight M_n = 173 kg/mol, polydispersity index (PDI) = 1.06), P3HT (Sigma-Aldrich, M_n = 19,600 Da, Dispersity = 2.74, regio-regularity ≥ 98%) were purchased and used as received. DPP-TVT (M_n = 46,900 Da, Dispersity = 2.1) was synthesized as previous reports.[97] The molecular weight for conjugated polymer was measured by high-temperature GPC (Agilent Tech, PL-GPC 220).

2.2.2 Ultra-thin dog-bone shaped sample preparation

The samples were prepared through following steps. First, PS dissolved in toluene, P3HT and DPP-TVT dissolved in chlorobenzene at various concentrations (1 mg/ml to 20 mg/ml) were spun-cast on Si substrate covered with water soluble poly (sodium 4-styrenesulfonate) (PSS) layer (~ 30 nm) to form a bilayer composite film structure with a semiconducting film of 20 to 110 nm thick. The thickness of the film was measured using an interferometer (Filmetrics Inc. UVX). Then, the polymer films were etched into the dog-bone shape through an oxygen plasma etcher (Diener electronics Inc.)

with a dog-bone shaped polymer etch mask (See **Figure A.2** for the mask design). After patterning the semiconducting film to a dog-bone shape (See **Figure A.3** for patterning process), the bilayer film was slowly dipped into a deionized water bath to release and float the dog-bone semiconducting film by dissolving the underlying water-soluble PSS layer.

2.2.3 Thin film mechanical test

After the dog-bone shaped films were floated, two aluminum tensile grips coated with a thin layer of PDMS (~ 0.5 mm) were carefully lowered to contact the polymeric film (**Figure 2.1(a) and Figure A.1**). The polymeric film was bonded tightly to PDMS pads through Van der Waals forces, as shown in **Figure 2.1(c)**. The tensile test was performed by applying various strains to the film through a motorized linear stage equipped with a digital encoder (Micromix Inc.), while monitoring the force exerted on the film with a high-resolution load cell (KYOWA Inc.). A CCD camera (THOR LABS) was used to aid the sample alignment, visualization of the stretching process, and performing digital image correction (See **Figure A.1** for the set-up). Stress-strain curves were obtained from force-displacement curves, stress equaling force divided by the cross-sectional area of the thin film. Strain was obtained by monitoring the displacement in sample length over the original length of the film, 10mm.

2.2.4 Alternating current (ac) chip calorimeter test

The glass transition temperature of the polymeric thin film was measured by an AC chip calorimeter. Thin film samples were floated off from a Si substrate and then transferred to the sensor XI392 (Xensor integrations, NL), containing a large smooth heated area (100 μm × 100 μm). The experiments were performed at a frequency of 10

Hz and a heating/cooling rate of 1 °C/min. Each sample was scanned three times under a protecting nitrogen atmosphere. The amplitude of the complex differential voltage as a function of measuring temperature was obtained. The dynamic glass transition temperature was determined as the half-step temperature of the amplitude as previous reported.[26]

2.2.5 Grazing incidence wide angle X-ray scattering (GIWAXS)

GIWAXS of polymeric thin films on silicon substrate were performed on a laboratory beamline system (Xenocs Inc. -Xeuss 2.0) with an X-ray wavelength of 1.54 Å and sample to detector distance of 17.1 cm. An incidence angle of 0.2° was used. Samples were kept under vacuum to minimize air scattering. Diffraction images were recorded on a Pilatus 1M detector (Dectris Inc.) with an exposure time of 1 hour and processed using the Nika software package, in combination with WAXSTools.[135]

2.2.6 Atomic force microscopy

AFM images were acquired on Bruker Dimension Icon in tapping mode.

2.3 Results and discussion

2.3.1 Stress-strain response for pseudo-free standing semiconducting polymeric thin film

We first tested the mechanical properties of three polymeric films. **Figure 2.2** shows the stress strain curves for PS, P3HT and DPP-TVT respectively, with film thickness ranging from 20 nm to 110 nm. Each mechanical measurement was tested five times and was very reproducible as shown in **Figure A.4(a)**. We started by testing well-studied PS to confirm that the set-up is accurate and reproducible. The stress-strain curves in **Figure 2.2(a)** clearly identify the elastic region, yield process and plastic

deformation region, which agrees well with previous reports.[55,136,137] The film is elastically deformed until yields at ~ 2.5 ± 0.5% strain. After yield, PS begins to follow a cold-draw process evident from the nearly constant stress with the increase of strain. A shear deformation zone (SDZ), which is the local thinning in an area of the film, was evident from different optical reflections oriented perpendicularly to the strain direction (**Figure 2.1c**) and the AFM image (**Figure A.5**).[55],[138–140]

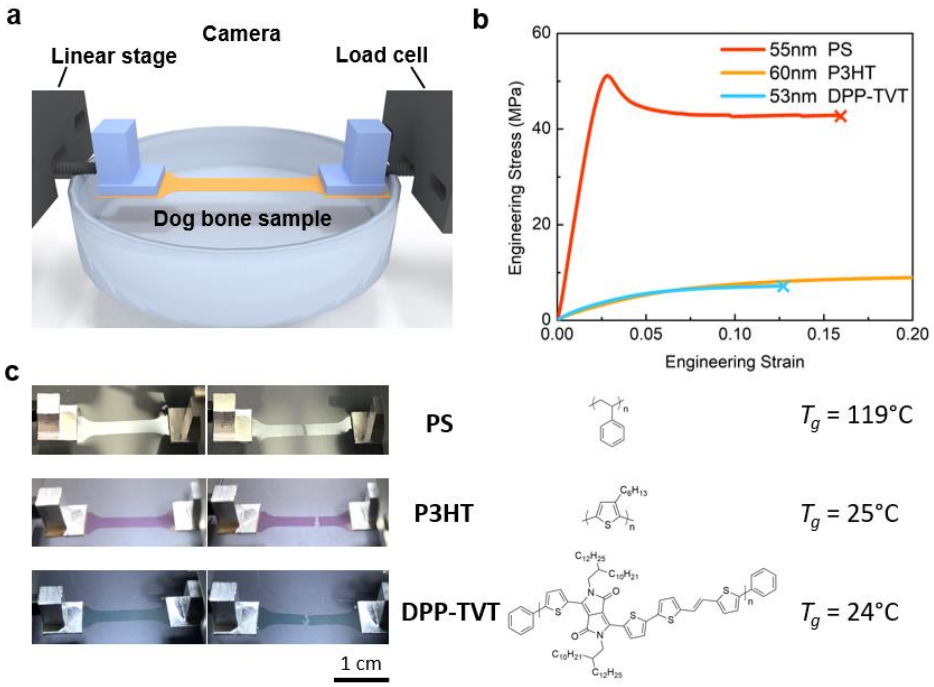

Figure 2.1 *Pseudo free-standing thin film tensile tester for measuring mechanical property of conjugated polymers. (a) Schematic illustration of tensile tester set-up for floated ultrathin film. A pre-patterned dog-bone shaped film floating on the surface of water was attached by two aluminum grips coated with silicone rubber. (b) an example of the stress-strain curves for different polymers. (c) Photographs of thin films floating on the surface of water before and after stretching. The samples are PS, P3HT, and DPP-TVT respectively from top to the bottom. Chemical structures and T_g data measured by ac-chip calorimetry are shown next to the photo.*

The elastic modulus, yield stress and strain were extracted from the stress-strain curves. The elastic modulus of PS film is calculated based on the slope of the stress-strain curve measured by fitting the first 1% of strain, which was determined to be ~ 2.4 GPa

for films with thicknesses above 50 nm. This value is in agreement with previously reported value by Hasegawa *et al*. on pseudo free-standing PS film,[55] but slightly lower than the value reported by buckling metrology, which is around ~ 4 GPa.[109] Thermal annealing of films at 120 °C had negligible influence on elastic modulus (**Figure A.4(b)**). A similar mismatch in elastic moduli between the two techniques was observed for P3HT films.[44,103] The differences result from different loading modes (tensile vs compression) and substrate effects (free-standing vs film on elastomer). **Figure 2.2(d)** clearly shows a reduction of elastic modulus for PS film as the thickness dropped below 23 nm. Additionally, yield strain and yield stress for PS also dropped with decreased film thickness **(Figure A.4(c))**. As expected, both yield stress and yield strain followed a linear trend as the thickness increased, since thicker films have a longer elastic region and a tendency to be stretched longer by forming more shear deformation zones. Using PS thin films as a model system, we have shown that the thin film tensile set-up is highly accurate and reproducible.

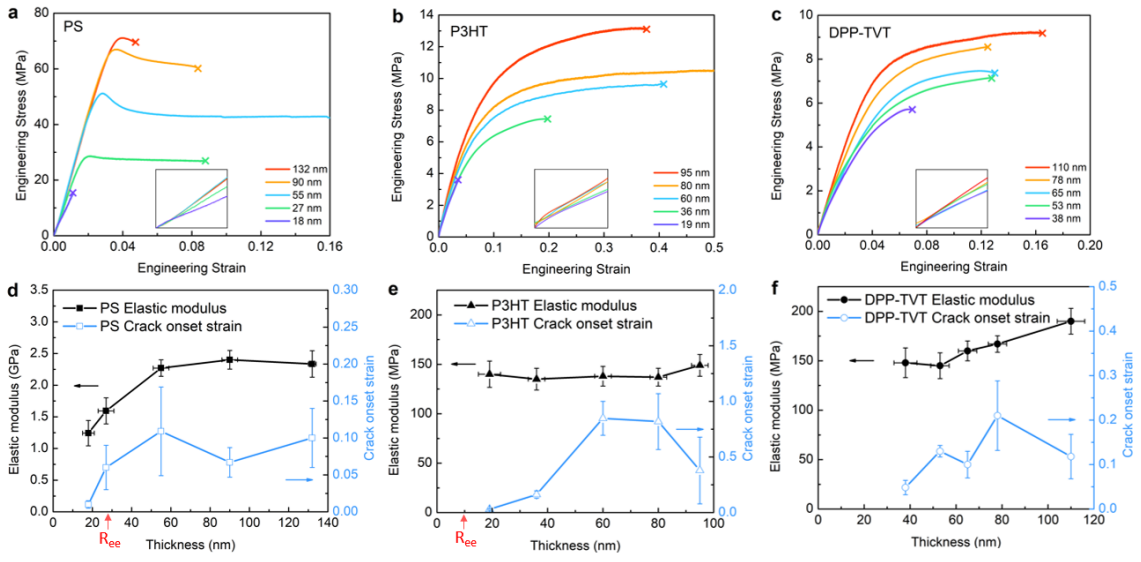

Figure 2.2 *Film thickness dependence of mechanical property for (a) PS, (b) P3HT, and (c) DPP-TVT thin film using pseudo-free standing tensile test. The stress-strain curves were plotted for various film thickness. Zoom in figures for strain up to 1% were inserted. Thickness-dependent elastic modulus and crack onset strain of (d) PS, (e) P3HT, and (f) DPP-TVT were plotted. Error bars denote standard deviations for five independent measurements on the same polymer. The samples were tested at strain rates of* $5*10^{-4}$ s^{-1}, $2*10^{-4}$ s^{-1} *and* $2*10^{-4}$ s^{-1}, *respectively.*

Thin film mechanical properties of P3HT and DPP-TVT were tested following PS validation. Stress-strain curves of P3HT with different film thickness are shown in **Figure 2.2(b)**, which are very different compared to PS films. The curve shows an initial linear slope up to ~ 5% strain, which slowly transitions into a plateau. Such stress-strain curves are commonly observed in viscoelastic polymers. Viscoelastic behavior in P3HT can be rationalized due to its low glass transition temperature (T_g). P3HT of similar molecular weight was measured to be 25 °C using AC chip calorimetry (**Figure A.9**), similar to others reports by a variety of characterization techniques, including differential scanning calorimetry,[17] simulation,[141] and rheometry.[142] The boundary between the elastic region and plastic deformation region is hard to determine solely based on the stress-strain curve and thus we will discuss later in the hysteresis experiment. The elastic modulus of P3HT is 135 ± 15 MPa, and interestingly there is no dependence between the elastic modulus and film thickness above 19 nm. This elastic modulus agrees reasonably well with previous report by Kim *et al*., despite the observed high crack onset strain.[103] Please note that the elastic modulus for viscoelastic polymer is strain rate dependent, and the P3HT samples were performed at a strain rate of $2*10^{-4}$ s^{-1}. Remarkably, the pseudo free-standing P3HT film can be plastically deformed up to 100% strain before it failed. Lastly, the DPP-TVT polymeric thin films were tested and shown in **Figure 2.2(c)**. D-A polymers have long been regarded as brittle due to large fused phenol rings and rigid

backbones.[123–125] Interestingly, DPP-TVT showed similar viscoelastic behavior as with P3HT (**Figure 2.2(c)**). Again, the high stretchability of DPP-TVT was attributed to its T_g near room temperature. Consequently, the polymer chains were not kinetically frozen at room temperature and plastically deformed upon stretching. The elastic modulus of DPP-TVT was determined to be 165 ± 35 MPa, and similarly no strong correlation between the film thickness and elastic modulus down to 38 nm was observed.

Another very important observation is that the crack onset strain for all three samples drops significantly with reducing film thickness, shown in **Figure 2.2(d-f)**. This phenomenon also causes difficulty attaining stress-strain curves of ultra-thin film with thickness less than 15 nm. These films simply break apart during the floating process or a gentle vibration of the water bath shattered the film (**Figure A.6**). Thus, we were unable to perform tests on thin films that are less than 15 nm. The sudden reduction in the crack onset strain happens when film thickness is reduced to a length similar to the end-to-end distance (R_{ee} or coil size) of the polymer chain. The decreasing crack onset strain in ultra-thin films is attributed to the decreasing inter-chain entanglements for thin films. Consequently, polymer chains are more likely to be broken apart upon further stretching. Our observation, at first glance, may seem contradictory with other studies using film supported on elastomer method, which reported that ultra-thin films have improved stretchability when the thickness is reduced.[92,143] This difference comes from the substrate effect. In bulking metrology, polymeric films were bonded to the elastomer and the strain was delocalized across the entire polymeric film. Loss of chain entanglements allows the chains to be more easily deformed. Another possible reason is that it is challenging to observe the formation of micro cracks in ultra-thin films using optical

method due to limited resolution and reduced optical contrast for thin films. AFM is a potential alternative to better determine micro cracking.[93,124] In pseudo-free standing tensile test, however, the stress is localized on the pre-existing defects, and water plays no effect on delocalization of the stress for polymer films. We also attribute the decrease of stretchability in thicker films to higher probability of defects in the spin coated films, from which cracks can initiate and propagate, so that the fracture in thicker films appears earlier than that of films with intermediate thickness (e.g., 95 nm thick P3HT films statistically have lower crack onset strain than 60nm thick P3HT films).

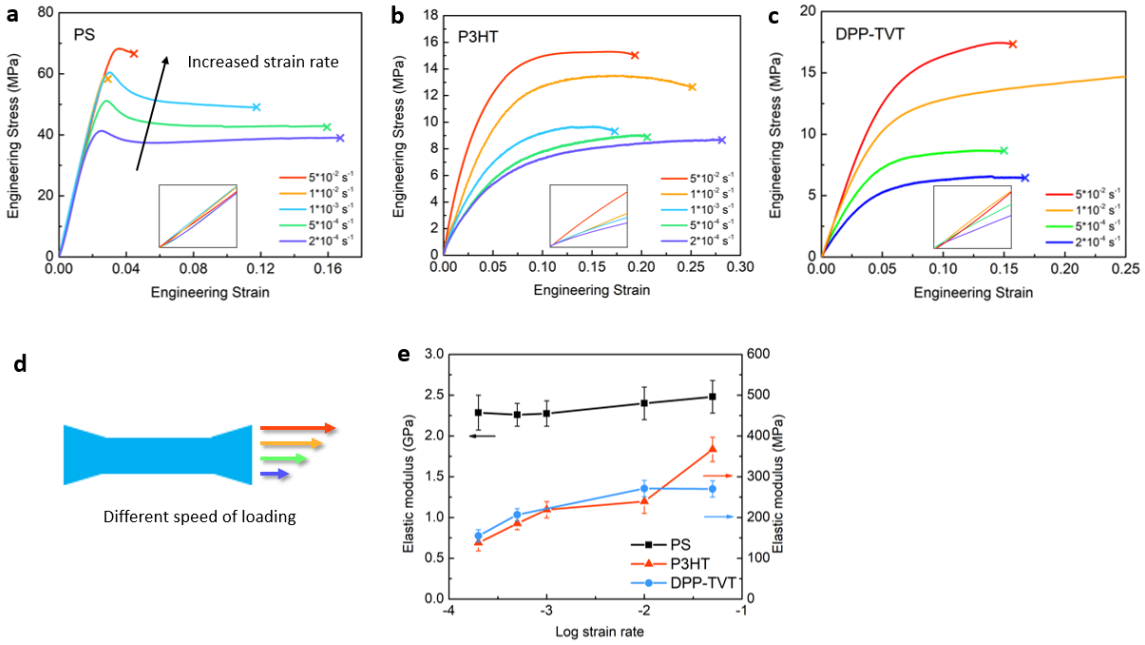

Figure 2.3 *Strain rate dependence of stress-strain relationship for viscoelastic conjugated polymers. (a) 50 nm thick polystyrene film (b) 60 nm thick P3HT film (c) 100 nm thick DPP-TVT film respectively. The strain rate was varied from 0.0002 to 0.05 s^{-1}. (d) Scheme of polymer film under different strain rate (e) Elastic modulus-strain rate relationship for three polymers.*

2.3.2 Strain rate dependent mechanical property

For viscoelastic polymers, their mechanical responses are dependent on strain rate. **Figure 2.3** presents the strain rate dependent mechanical response for three different

polymers: PS, P3HT and DPP-TVT respectively. The elastic modulus for PS shows weak dependence on strain rate, which is commonly seen for polymers deformed below glass transition temperature.[144,145] The polymer chains are "frozen" at room temperature, and are less sensitive to deformation rate. At high strain rate, the specific degrees of freedom of polymer chains becomes restricted, which increases the resistance to overall material deformation, and observed as the increased yield stress.[146] In comparison, both P3HT and DPP-TVT showed an increase of elastic modulus with strain rate from 135 MPa to 360 MPa and 145 MPa to 250 MPa, respectively. Viscoelastic polymers can be modeled as a combination of elastic springs and viscous damping dashpots. At high strain rate, more stress is required to overcome the viscous flow in the dashpot, resulting in a higher apparent elastic modulus.[147–149]

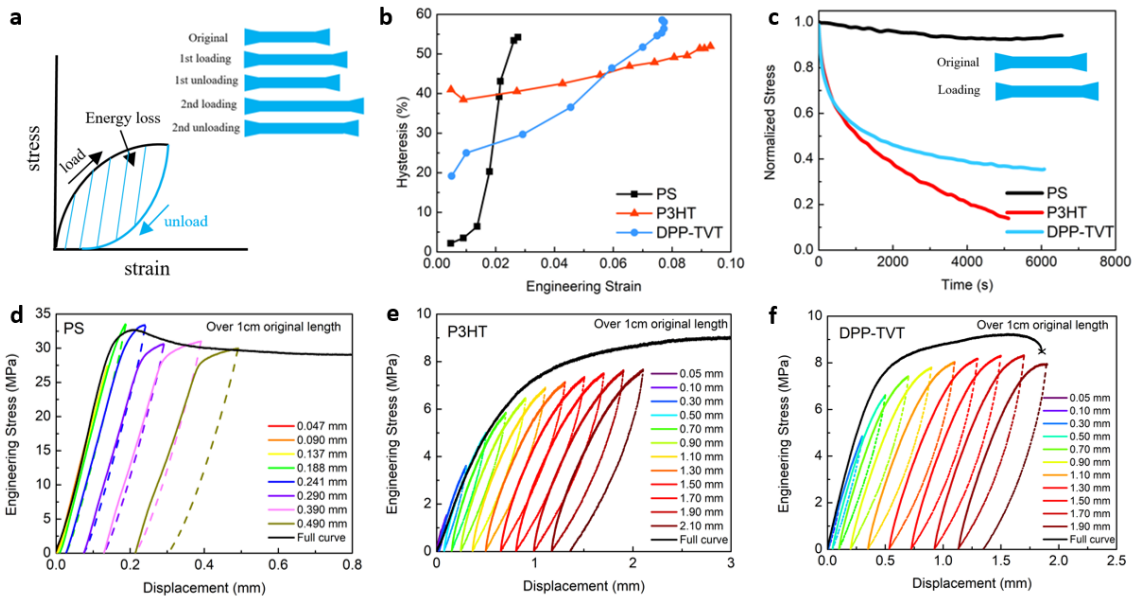

Figure 2.4 *(a) Schematic illustration of hysteresis plot for typical viscoelastic polymer. (b-d) Stress-strain curves of (b) PS, (c) P3HT and (d) DPP-TVT under cyclic loading. (e) Hysteresis calculated from stress-strain curves. (f) Stress relaxation plot.*

2.3.3 Hysteresis effect for viscoelastic polymer during cyclic mechanical deformation

The cyclic loading-unloading-reloading process further provide the understanding of the sample's viscoelastic property. The samples were tested as following: the film was first stretched to a small strain, then the stress was released at the same strain rate until fully relaxed, afterwards the film undergoes additional load-unload cycle with a slightly larger strain (**Figure 2.4(a)**). The stress vs displacement curve during repeated stretch was plotted in **Figure 2.4(d-f)**. For PS thin film, the loading and unloading curves showed elastic behavior and overlapped with each other at small strain (i.e., <1.4% or 0.14mm). As cyclic strain surpassed 1.8%, permanent plastic deformation through yielding (**Figure 2.2(a)**) was seen and significantly higher hysteresis (up to 54%) was observed as shown in **Figure 2.4(b)**. Both P3HT and DPP-TVT showed vastly different mechanical responses. A characteristic non-overlapped load-unload curve was seen, suggesting that both samples demonstrated a combined elastic and viscoelastic behavior under the applied stress. The unloading curve showed a fast drop of the stress, indicating recovery of the elastic fraction of the strain, then followed by the viscoelastic recovery of the strain. Permanent plastic deformation was seen at very low strain (~ 0.5% for P3HT and ~ 1% for DPP-TVT). The reloading/re-unloading stress-strain curves showed close resemblance to the initial loading/unloading curve and were independent of cycle numbers.[150,151]

Figure 2.4(b) plots the percent of hysteresis, also known as the energy loss, versus strain during the cycle. The hysteresis was calculated by the ratio of the energy lost (the area between the loading and unloading curve) divided by the energy excreted on the film (the area below the loading curve) (**Figure 2.4(a)**). Polystyrene showed a negligible amount of hysteresis (< 5%) within ~ 1% strain, followed by a rapid growth

when the film is cycled above ~ 1.5% strain. The large hysteresis comes from the energy being consumed during the yielding and plastic deformation of the glassy PS. P3HT and DPP-TVT showed > 40% and > 20% hysteresis respectively at just 1% strain due to viscoelastic nature of both polymers. More interestingly, the hysteresis of P3HT and DPP-TVT showed different behaviors at different degrees of strain. As strain increased, the time for the polymer to relax increased which contributed to more energy loss, which explains almost a linear relationship between hysteresis and strain. The fraction of lost energy due to plastic deformation increased much faster in DPP-TVT than that of P3HT, which is very likely to be correlated to the chain entanglement due to differences in chain length and backbone rigidity. Compared to P3HT, DPP-TVT has more sterically hindered backbones and longer side chains, which provide more sites for energy loss upon stretching of DPP-TVT. The potential sources of loss energy include plastic slip in crystalline domains, friction between crystalline domains, and interaction between amorphous and crystalline domains, etc.[152]

2.3.4 Stress relaxation for viscoelastic polymer film

Stress relaxation tests for all three samples were performed to further examine the differences between the viscoelastic property of P3HT and DPP-TVT. As a reference material, PS film was strained to 0.8% (slightly below the yield point) and stress was monitored continuously. Similar procedure was performed on P3HT and DPP-TVT thin films, which were strained to 20% and 15% respectively. The stress was normalized by the peak stress after stretching. As shown in **Figure 2.4(c),** PS maintained nearly a constant force over the tested time period of 1.5 hours. A slight drop in the stress is likely due to the relaxation of PDMS pad used to hold the PS film. In comparison, P3HT and

DPP-TVT showed a fast initial drop in normalized stress, then slowly dropped until reaching a plateau. DPP-TVT relaxed slightly different than P3HT. Both P3HT and DPP-TVT were modeled by a series of two Maxwell model (**Figure A.8**). Future in-depth rheology work is under way to elucidate the difference between P3HT and DPP-TVT.

2.3.5 Morphological characterization

Films morphology was characterized by AFM and GIWAXS before and after tensile deformation. AFM was used to characterize the surface morphology of P3HT and DPP-TVT thin films upon stretching. As shown in **Figure 2.5(a-c)**, P3HT formed fibril structure after deposition with random orientation. With increased strain, the polymer maintained the fibril structure and still the fibrils showed no favored orientation, even along the stretching direction, this can be attributed to deformation occurring in the non-crystalline region. DPP-TVT films did not form fibril structures (**Figure 2.5(d-f)**). There is limited morphology change before and after stretching for DPP-TVT from the AFM images. To better understand the effect of strain on the crystalline domain, GIWAXS was performed on P3HT and DPP-TVT with 0%, 10% and 20% strain (**Figure 2.6**). The X-ray beam was oriented parallel to the strain direction. By observing the diffraction pattern of lamellar region and π-stacking region, the change of crystallinity, and polymer chain orientation can be inferred. P3HT without strain showed semicrystalline structure, with strong (h00) lamellar stacking peaks in the out-of-plane direction, and the π- π stacking peak (010) in the in-plane direction. Before strain, P3HT has a preferred edge-on orientation with respect to the substrate. Upon stretching, there were two distinct effects. First, the (100) lamellar peak showed diffraction signal in the in-plane direction. Additionally, the edge-on packing peak was displaced by face-on peak. At 20% strain,

almost no edge-on stacking is presented. For DPP-TVT, no obvious orientation change in the crystal packing was observed. However, the lamellar peak was observed became smaller and broader with the increase of strain, which indicated stress process is coupled with a decrease in crystallinity (See **Table A.1** for the table of peak positions).

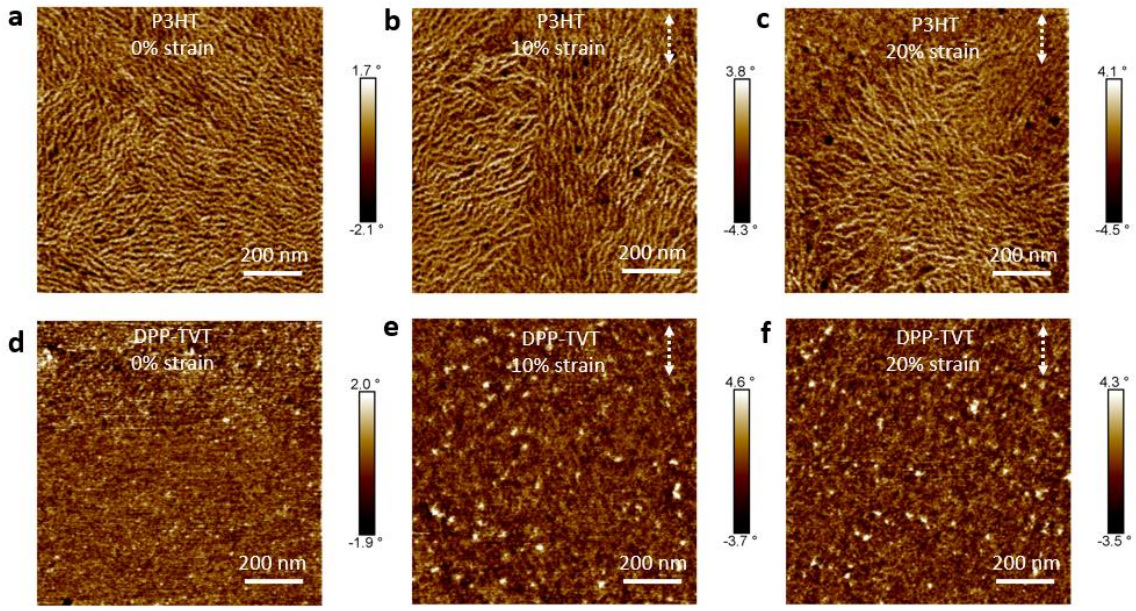

Figure 2.5 *Surface morphology of the strained films. AFM phase images of P3HT (a) without strain (b) under 10% strain (c) under 20% strain and DPP-TVT (d) without strain (e) under 10% strain (f) under 20% strain using tapping mode. The strain direction is shown as the white arrow.*

2.3.6 Thickness dependent property

Many bulk polymer properties dramatically change when under strong confinement, like when thickness is reduced to tens of nanometers. The T_g of polystyrene films decreases with its thickness, and the reason for that has been attributed to the existence of "free surface", an ultra-thin layer of film (a few nanometers) contacted with air. The chain mobility of free surface can be orders of magnitude faster than that of bulk.[108,153–155] The observed thickness dependent glass transition temperature strongly

linked to the chain confinement effect through the comparison between film thickness and end-to-end distance (R_{ee}) of polymer chains.[136,137]

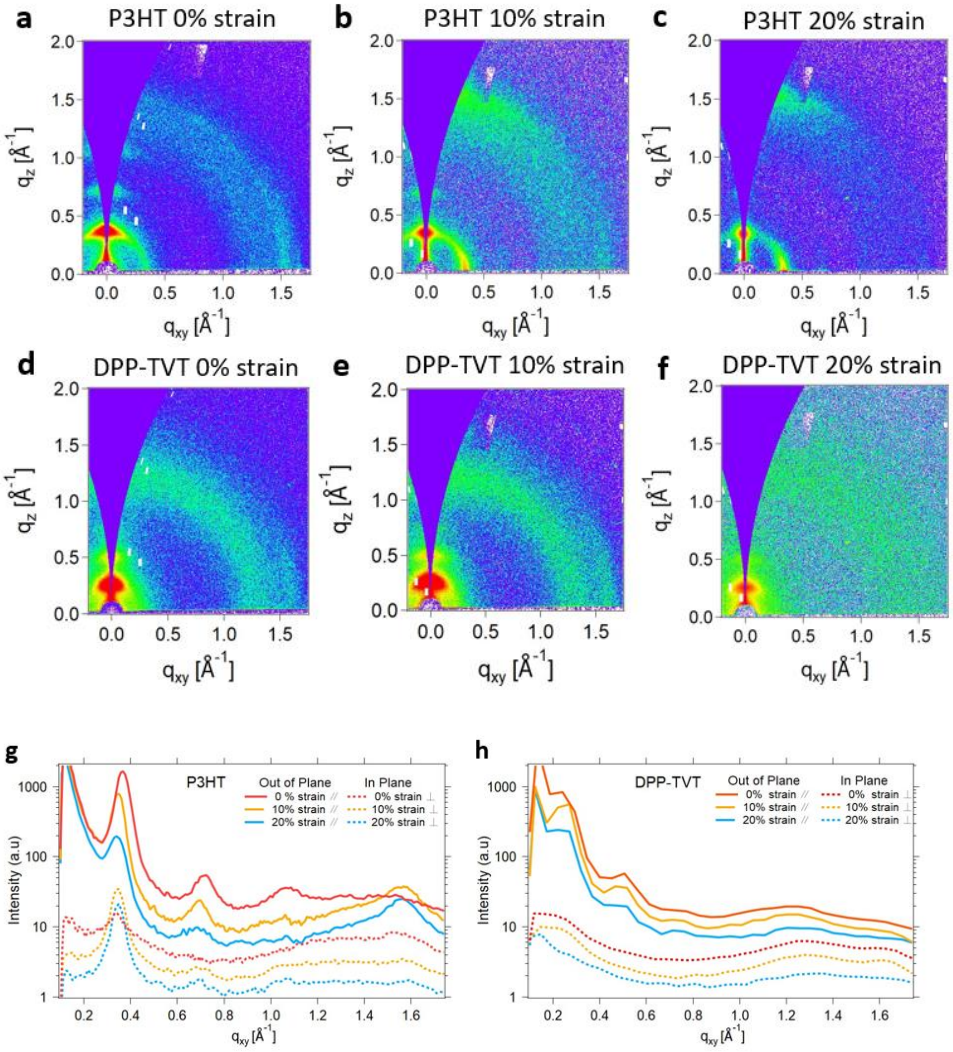

Figure 2.6 Crystalline structure change after stretching. GIWAXS 2D images for of P3HT (a) without strain (b) under 10% strain (c) under 20% strain and DPP-TVT (d) without strain (e) under 10% strain (f) under 20% strain. 1D line-cut for (g) P3HT and (h) DPP-TVT from in-plane and out-of-plane directions are shown for reference, data was offset for clarity.

Similar thickness dependent phenomena have been observed for the elastic modulus of PS films measured by both buckling metrology and pseudo-free standing tensile test. Stafford *et al.* observed a decrease in elastic modulus for PS (M_n= 103

kg/mol and M_n=1,636 kg/mol) films below 40 nm using buckling metrology method.[109] Similar conclusions for thickness dependent mechanical property of PS thin films were drawn by Liu *et al.* and Hasegawa *et al.* with pseudo-free standing tensile test method.[54,55] As Si *et al.* described, the proportion of self-chain entanglement increases with decreasing film thickness, and the elastic modulus will be lower.[138] This phenomenon was not observed for conjugated polymers above 40nm. To rationalize the observed thickness dependent elastic modulus, we estimated the end-to-end distance for a given polymer by Equation 2.1, and compared to the film thickness tested:

$$R_{ee}^2 = C_\infty * n * l^2 \quad (2.1)$$

R_{ee} is the end-to-end distance of the polymer chain C_∞ is the characteristic ratio of polymer chain, which is proportional to the chain rigidity. n represents for the number of repeating units, and l is the length of one repeating unit. The R_{ee} for PS with M_n = 173 kg/mol was estimated to be around 28nm.[55] For P3HT, the characteristic ratio ranges from 3.49 to 12.1 were reported from literature,[156,157] consequently the R_{ee} was determined to be between 8 nm and 14.8 nm, which explains the independence of elastic modulus on thickness above 20 nm. DPP-TVT polymer films are only tested for thicker films above 40nm, the elastic modulus showed an increase above 53nm, which do not attribute to the free surface effect, but the experimental error in thickness measurement using interferometry. The end-to-end distance for DPP-TVT could not be obtained here, without further information of characteristic ratio, which requires additional characterization using solution-based X-ray or neutron scattering to model the chain conformation.

There is still debate on the dependence of crack onset strain on film thickness, some suggested an increased crack onset strain is linked with decreasing thickness using bulking metrology method,[67,143] while others presented conflicting results using pseudo-free standing tensile method.[54] For conjugated polymer films, the nano-confinement effect is mostly studied by buckling metrology.[19,68,93,158] O'Connor and coworkers found no thickness dependence for some polythiophene polymers down to 50 nm.[96] Balar et al. reported a few polymers with thickness-dependent elastic modulus and attributed the cause to the morphology differences associated with different casting conditions to obtain the desired film thickness.[93]

2.3.7 Correlation between electronic and mechanical properties

One of the challenges for designing flexible organic electronics is to engineer semiconducting polymers with both good electrical and mechanical properties. Strong evidence exists linking the mechanical and electrical properties of polythiophenes.[96,121] An increase in the electronic property correlated with stiffening and embrittlement of the polymeric film. This observation was rationalized through the idea that a rigid and coplanar backbone increase the conjugation length by promoting delocalized electronic clouds. This observation does not apply to the DPP-TVT polymer studied here. Charge carrier mobility of the DPP-TVT has been previously reported ~ 1.5 $cm^2 V^{-1} s^{-1}$,[159] two orders of magnitude higher than P3HT (~0.01 $cm^2 V^{-1} s^{-1}$), and yet their mechanical properties are very similar. The correlation between mechanical property and electronic property warrants more investigations in future works.

2.3.8 Origin of the low-glass transition temperature

The origin of T_g for conjugated polymers is complicated, due to the effects from various parameters like molecular weight, chain rigidity, side pendent groups and π-π stacking.[160] However, it has been reported that T_g of conjugated polymers is available from broadband dielectric spectroscopy (BDS),[161] dynamic mechanical analysis (DMA),[162] DSC,[163] rheometry,[100,142] UV-vis[94] and variable-temperature ellipsometry.[164] As for now, systematic study on glass transition temperature on D-A polymer is not yet fully performed. One of the challenges is that there is little thermal signal using traditional DSC equipment, where most lab relies on. Typically, a specialized AC chip calorimeter is needed to accurately measure T_g (See **Figure A.9** for test results).[19] Recent reports on using temperature dependent UV-Vis by Lipomi group[94] and linear viscoelastic rotational rheometry by Gomez and Colby group are alternative ways to probe T_g. More in-depth relationship between the polymer structure and glass transition temperature is unclear and warrant more work in this direction.

2.4 Conclusions

In this work, we use the pseudo-free standing tensile test to measure the intrinsic mechanical properties of two representative conjugated polymers, P3HT and a DPP-based polymer. The mechanical properties of these two polymers are identical in terms of elastic modulus both around 140 ± 20 MPa and can be stretch at up to 20% strain without break. Both films showed typical viscoelastic properties, including enhanced modulus (up to 350 MPa for P3HT) with increased strain rate, stress relaxation down to 25% for P3HT and 45% for DPP-TVT in one hour, and strong hysteresis under cycling loading and unloading. Viscoelastic behavior is prevalent due to a sub room temperature T_g. Interestingly, the electrical property between the polymers differs by up to two orders of

magnitude! This interesting finding clearly indicates that mechanical and electrical properties are not inherently correlated, which opens a new direction for polymer chemists to design D-A polymers with both high charge transport and desirable mechanical properties.

CHAPTER III - DIRECT PROBING THE FRACTURE BEHAVIOR OF ULTRATHIN POLYMERIC FILMS

(From "Zhang, S.; Koizumi, M.; Cao, Z.; Qian, Z.; Jin, L.; Gu, X. Direct probing the fracture behavior of ultrathin polymeric films. Under Review. 2021.")

3.1 Introduction

Recent technology development has brought wide applications of ultrathin polymer films (< 100 nm) into our daily life, such as optical coatings, filtration membranes and semiconducting devices.[32,165–169] Characterizing ultrathin films' mechanical properties is critical in such applications, but extremely challenging because of their delicacy nature. Traditionally, an underlying solid substrate is required to support thin films in mechanical tests[42,109]. However, this is unfavorable because unknown film-substrate interactions might obscure the intrinsic properties of thin films[137,154,170–172]. Recent reports on pseudo-free-standing tensile tests address this limitation through testing ultrathin films on the top surface of water, and their mechanical properties, like elastic modulus and crack-onset strain, have been successfully measured[18,53,54,58,173,174].

Nevertheless, measuring fracture energy, an intrinsic material property that quantifies the capability of a material to resist propagation of a pre-existing crack, is missing in the literature despite its decisive role in determining the failure behavior of bulk polymer samples[175,176]. Previous works like microprojectile impact test have been applied to obtain the energy absorption of ultrathin films under high-strain rate deformation[177], four-point bending test and double-cantilever beam test (DCB) are shown to measure the adhesive/cohesive fracture energy for multi-layer thin film systems or binary systems[178–180]. However, the influence of thermal energy dissipation and the

substrate effect can obscure the final quantitative comparison, respectively. The direct characterization of fracture energy of ultrathin films can provide the most fundamental material-property relationships and guidelines for material selection and product development.

Here, we present the first direct measurement of fracture energy of ultrathin glassy polymer films down to a thickness of 26 nm through a pseudo-free-standing tensile tester with the Begley-Landes method and pure shear method. Combining experiments and finite element simulations, we determine the stress distribution near a crack tip and the critical condition for crack propagation. The crack tip stress fields are characterized by wrinkling patterns perpendicular to the strain direction near the crack and propagating downstream as the crack extends. In a model material system, polystyrene (PS) ultrathin films, the fracture energy is shown to undergo a significant reduction, showing a ductile-to-brittle transition, when the molecular weight is decreased below a critical value, which is attributed to the loss of inter-chain entanglement in short polymer chains[181–183]. Similarly, due to the loss of inter-chain entanglement under nanoscale confinement, the fracture energy of PS also reduces as the film thickness approaches the end-to-end distance (R_{ee}) of the polymer chains[136,137]. To highlight the broad applicability of this methodology, the fracture energy of several conjugated polymers with low glass transition temperatures (T_g) is tested. Our technique provides a general platform for fracture energy measurement of ultrathin film materials, including polymers, metals, and emerging 2D materials, which are vital for energy and health care applications.

3.2 Experimental

3.2.1 Materials

All polymers (polystyrene (PS), Poly{[N,N'-bis(2-hexylldecyl)naphthalene-1,4,5,8-bis(dicarboximide)-2,6-diyl]-alt-2,5-thiophene} (PNDI(2HD)T) and poly(3-hexylthiophene) (P3HT)) and solvents (toluene, chlorobenzene) were purchased from commercial sources and used as received. The number-average molecular weight (M_n) and the dispersity (PDI) of PS were evaluated by a gel-permeation chromatography (GPC) system consisting of a Waters Alliance 2695 separations module, an online multiangle laser light scattering (MALLS) detector fitted with a gallium arsenide laser (power: 20 mW) operating at 658 nm (miniDAWN TREOS, Wyatt Technology Inc.), an interferometric refractometer (Optilab rEX, Wyatt Technology Inc.) operating at 35 °C and 685 nm, and two PLgel (Polymer Laboratories Inc.), and mixed E columns (pore size range 50–103 Å, 3 μm bead size). Freshly distilled tetrahydrofuran (THF) served as the mobile phase and was delivered at a flow rate of 1.0 ml min^{-1}. The M_n and PDI of PNDI(2HD)T and P3HT were measured by high temperature (HT)-GPC using trichlorobenzene as the eluent at 160 °C, polystyrene for calibration, viscometer, and light scattering as the detectors. Poly(sodium 4-styrene sulfonate) (PSS) was purchased from Sigma-Aldrich and used as received. Polydimethylsiloxane (PDMS) was purchased from Corning and used as received. PDMS stab was prepared by mixing the base and curing agent at a ratio of 10:1.

3.2.2 Fabrication of bilayer thin films

PSS was dissolved in deionized (DI) water at a concentration of 3 mg/ml. Polystyrene was dissolved in toluene with a concentration ranging from 5 mg/ml to 20 mg/ml. PNDI(2HD)T and P3HT were dissolved in chlorobenzene at a concentration of

10 mg/ml. The PSS solution was first spin-coated on top of a 6 * 6 cm silicon wafer at the speed of 4000 rpm for 1 min to form a 30 nm thick layer film. Next, the target polymer solution was spin-coated on top of the PSS layer at a speed of 2000 rpm for 2 mins to form a composite film; the film thickness was later measured by AFM.

3.2.3 Thin film fracture energy test with Begley-Landes method

The polymer films were etched by an ultra-fast laser cutter to pattern into dog-bone shape on a silicon wafer, followed by patterning five different sizes of notches (0 mm, 0.2 mm, 0.4 mm, 0.6 mm, 0.8 mm) (**Figure B.1**). Three samples of each notch size were prepared. Thin-film tensile tests were performed by a home-made pseudo-free-standing tensile tester. Details about the tensile stage setup can be referred to our previous publication.[18] The force-displacement curve for an unnotched sample was first recorded during the tensile test at a strain rate of 5×10^{-4} s^{-1}, followed by converting it to a nominal stress-strain curve. The elastic modulus was obtained from the slope of the stress-strain curve using the first 0.5% strain. All samples with various notch sizes were separately tested and monitored with a high-resolution camera. The force-displacement curves were recorded until the onset of crack propagation. The total work is done to the sample, i.e., the area underneath each curve was calculated and plotted versus the initial notch length under a fixed displacement, where the fracture energy was derived from the slope.

3.2.4 Thin-film fracture energy test with the pure shear method

The polymer film is laser-etched into I-shape with a 2 mm * 16 mm rectangular gauge, and two 2 mm * 20 mm rectangular pads. For a notched sample, an 8 mm long notch was introduced to its center along the width direction. The tensile test for all

samples is performed at a strain rate of 5×10^{-3} s^{-1}. The critical displacement for stable crack propagation is identified from the force-displacement curve of notched samples.

3.2.5 Shear rheometry test

The linear viscoelastic response of 173 kg/mol PS was obtained from small amplitude oscillatory shear measurements performed on an ARES-LS rheometer (TA Instruments) using 8-mm aluminum disposal parallel plates. A PS sample was prepared to form a disk shape by compression molding under vacuum at 150 °C. The sample was loaded between the parallel plates and heated to 170 °C within a nitrogen-purged oven. Frequency sweep measurements were carried out over a temperature range of 170 °C to 120 °C with -10 °C increment, and the applied strain was in the linear range. The frequency range for the dynamic measurements was 100 to 0.1 rad/s.

3.2.6 Differential scanning calorimetry (DSC)

DSC measurement was performed on Mettler-Toledo DSC 3+ equipped with FRS6+ sensor under dry nitrogen gas purge with a flow rate of 50 ml/min. To remove the thermal history, a heat-cool-heat cycle with a heating/cooling rate of 10 °C/min was utilized over a temperature range of 160 °C to 50 °C. The data analysis was performed on the reheating scan.

3.2.7 Dynamic mechanical analysis (DMA)

A TA Q800 DMA was used to perform DMA measurements by a modified DMA method. Polymer solutions (5 mg mL^{-1}) were made and then drop-casted on top of a glass fiber mesh to prepare the samples. The temperature corresponding to the peak of tan δ was determined as the backbone T_g. In strain-controlled mode, temperature ramp experiments were performed at a temperature range of −110 to 150 °C and a heating rate

of 3 °C min^{-1} with a fixed frequency of 1 Hz. The strain imposed was in the linear regime.

3.2.8 Finite element simulations

We simulated deformation and crack propagation in polymer thin films subjected to an external load under a plane stress condition using ABAQUS/Explicit finite element analysis. While the 51 kg/mol PS films are modeled as a linearly elastic material, the 173 kg/mol PS films are modeled as an elasto-plastic material using a J_2 flow theory and isotropic hardening with the Gent hardening law shown in Equation 3.1. The elastic modulus for both PS is E = 3.01 GPa obtained by fitting the linear regime of the experimental stress-strain curve (**Figure 3.4(a)** and **Figure B.3(c)**), and the Poisson's ratio υ = 0.34. For 173 kg/mol, the yield stress is σ_Y = 84 MPa, G_p = 15 MPa, $J_m = 200$. These values are selected based on fitting with experimental data and literature.[184,185] All films are modeled using the plane-stress 4-node linear elements with reduced integration (CPS4R), while a cohesive layer with the 4-node two-dimensional cohesive elements (COH2D) is inserted ahead of the crack tips in notched films to allow crack propagation (**Figure B.3 (a)**).

In order to model the fracture behavior of the 51 kg/mol and 173 kg/mol PS, we selected a bilinear cohesive zone model governed by the maximum cohesive stress σ_c, maximum separation distance between the crack planes, and the intrinsic fracture energy Γ_0 (**Figure B.3(b)**). The damage initiation of the cohesive elements follows the maximum cohesive stress criterion

$$max\left\{\frac{\langle t_n \rangle}{\sigma_c}, \frac{\langle t_s \rangle}{\sigma_c}\right\} = 1 \tag{3.6}$$

where *t* represents the traction on the crack surface, and the subscripts n and s denote the normal and tangential directions, respectively. The cohesive elements enter their softening phase where the cohesive stress starts to linearly decrease when Equation 3.6 is satisfied. Complete separation between the crack planes is achieved when the cohesive stress becomes zero. The maximum cohesive stress for the bilinear traction separation law was set as $\sigma_c = 300$ MPa and the area under the traction separation law is the intrinsic fracture energy $\Gamma_0 = 100\ J/m^2$. To ensure that the cohesive elements do not suffer from interpenetration between crack surfaces, we arbitrarily made the elastic stiffness of the cohesive elements as high as possible but small enough to prevent spurious oscillations of the tractions in a cohesive element.[186] Therefore, we chose the initial slope of the bilinear traction separation law to be $E_{ts} = 78750$ GPa. To correctly capture the stress distribution inside the cohesive zone for accurate prediction of crack propagation, we refined our cohesive mesh until convergence was met. As a result, the length of each cohesive element is less than a tenth of the bridging zone size defined as $E\Gamma_0/{\sigma_c}^2$, i.e., 16 cohesive elements are modeled within the bridging zone. To obtain the force displacement curves of the notched samples, displacement in the vertical direction is applied to the top edge of the film at a strain rate of 1%/s to ensure quasi-static crack analysis, while the other edge is only free to move in the horizontal direction. To obtain the R-curves, displacement boundary conditions given in Equation 3.5 is applied on the entire circumference of the circular K-field zone. The amplitude of the prescribed displacement fields in the both the x and the y directions is incrementally increased at strain rate of 1%/s. For the pure shear simulations, the entire bottom edge is firmly clamped whereas the entire top edge can only displace in the vertical direction at the

same strain rate of 1%/s, and the side edges of the pure shear specimens are free surfaces. Since the stable time increment in explicit simulations depends on the velocity of the elastic wave traveling through the smallest elements, we used mass scaling up to 6 orders of magnitude to artificially reduce the elastic wave speed, thereby increasing the time increment for the simulations to finish in a reasonable time limit. Excessive mass scaling can result in inaccurate results due to inertia interfering with the quasi-static crack analysis. However, we confirmed that our mass scaling does not influence the results by verifying it with linear elastic crack analysis.

3.3 Results and discussion

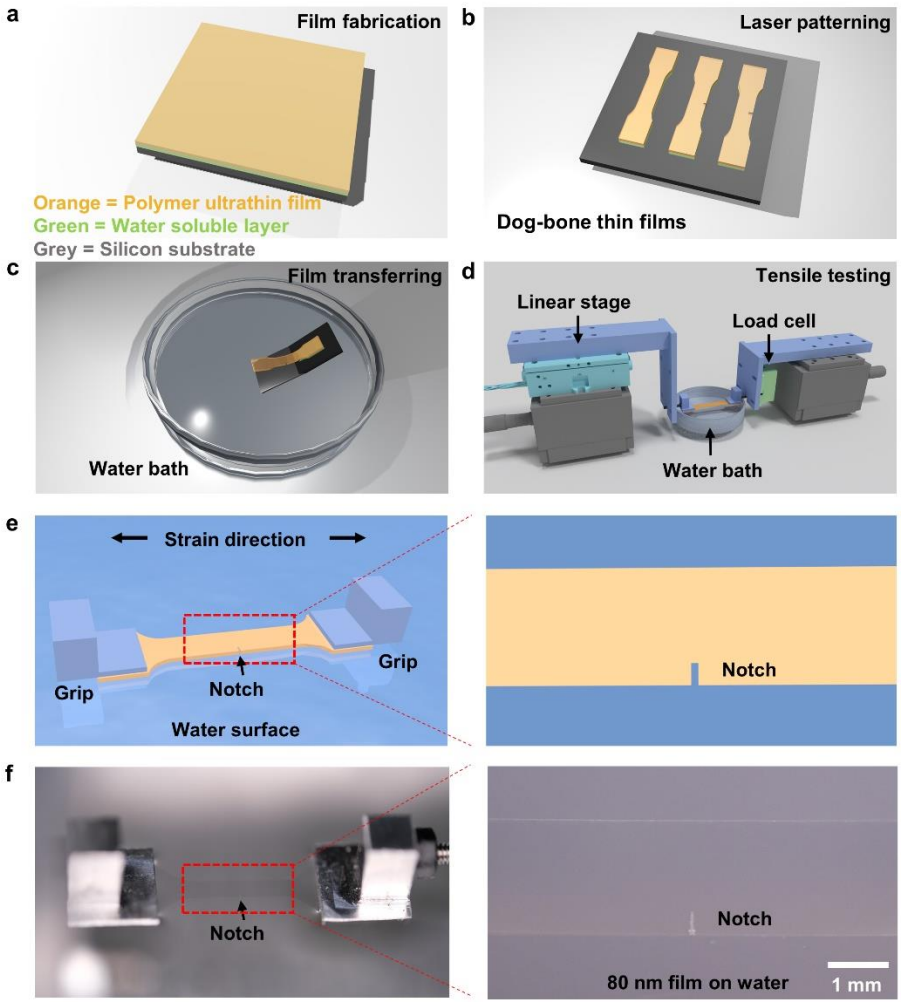

Figure 3.1 *Demonstration of the thin-film fracture energy test based on an 80 nm thick polystyrene film with a molecular weight of 173 kg/mol. (a-e) 3D schematics showing the procedures of fabricating and conducting the fracture test to the thin film. (a) A double-layer thin film composed of a water-soluble layer and a polystyrene layer cast on a silicon wafer. (b) Laser patterning of dog-bone shaped films with varied notch lengths. (c) Ultrathin films floating on the water surface by releasing the water-soluble layer. (d) Tensile testing of thin-film mechanics through a pseudo-free standing tensile tester. (e) Uniaxial tensile testing of a notched ultrathin film on the water surface with grips on both ends. (f) Optical images showing an 80 nm polystyrene ultrathin film with a notch size of 0.4 mm floating on water. The gauge length and width are 8 mm and 2 mm, respectively.*

In this work, we introduce a new technique to directly measure the fracture energy of ultrathin films (e.g., < 100 nm) supported on the water surface. We used a classic glassy polymer PS, with a number-averaged molecular weight of 173 kg/mol, as a model system to demonstrate the capability of this methodology (**Figure 3.1**). A water-soluble layer poly(styrenesulfonate) (PSS) was spun coated on the top of a silicon wafer, followed by coating a layer of 80 nm PS ultrathin film to form a bilayer composite (**Figure 3.1(a)**). Next, the film was laser-patterned into a dog-bone shape with a gauge width of 2 mm and length of 8 mm, where a single-edge notch with a length *c* of 0 mm, 0.2 mm, 0.4 mm, 0.6 mm, and 0.8 mm was also introduced through laser etching (**Figure 3.1(b)**, **Figure B.1**). Upon dipping in water, the PSS layer dissolved, and the PS layer was released on the water surface (**Figure 3.1(c)**). Later, the PS ultrathin film was transferred and mounted to two aluminum grips, one connected to a linear stage and the other attached to a load cell (**Figure 3.1(d)**); a similar transfer method was also described in detail in our previous publications[18,59,61,187]. Both schematics and optical microscope images of a notched film floating on the water surface are shown in **Figure 3.1(e)** and **Figure 3.1(f)**, respectively.

During the stretching process, the film first experiences elastic deformation at a small external displacement; correspondingly, the film surface stays flat when the notch is widened along the strain direction. Next, periodical wrinkling patterns perpendicular to the strain direction are observed around the notch due to the gradual increase of the compressive stress in the vicinity of the notch tip (**Figure 3.2(a, b)**)[188]. **Figure 3.2(c)** shows optical images of notched PS ultrathin films with a thickness of 80 nm with different notch lengths at different displacements. As the displacement increases, the wrinkling pattern slowly builds up near the notch tip and propagates outwards, indicating a larger region of the film undergoes high compressive stress. Wrinkles pack more densely in the area closer to the tip, indicating higher stress. For samples with a longer initial notch, the number of wrinkles at a given displacement is higher, owing to the reduced cross-section area and higher stress at the notch tip. When the stress around the tip reaches a critical value, the film begins yielding plastically. As the crack starts to propagate, plastic deformation dominates, indicated by the expanding white triangle regions near the tip, known as the shear deformation zone (SDZ) (**Figure 3.2(c)** and **Figure B.2(a)**). During the crack propagation, the original wrinkles disappear while new ones show up along with the propagation of the SDZ due to the redistribution of the stress field.

To demonstrate the evolution of the stress field in the film as the external displacement increases, we also conducted finite element simulations of PS films with a pre-crack of various lengths, same as the experiments subjected to external displacement loading under the plane stress condition using ABAQUS. The PS film is modeled as an elasto-plastic material using a J_2 flow theory and isotropic hardening. Previous literature

has shown that the post-yielding stress-strain relation of glassy thermoplastics shows strain hardening and follows the Gaussian chain statistics in accordance with rubber elasticity [185]. In this study, considering the stress concentration in the vicinity of a crack tip, we substitute the Gent model for the Gaussian equation to capture the strain stiffening effect under large deformation

$$\sigma = \sigma_Y + \left(\frac{J_m G_p}{J_m - \lambda^2 - 2/\lambda}\right)\left(\lambda^2 - \frac{1}{\lambda}\right) \quad (3.1)$$

where σ is the true von Mises stress, σ_Y is the yield stress, λ is the equivalent stretch defined as $\lambda = exp(\epsilon_p)$ with ϵ_p the true equivalent plastic strain, and G_p is the strain hardening modulus. The parameter J_m governs the strain stiffening effect, and when $\lambda^2 - 2/\lambda$ reaches J_m, stress σ approaches infinite. We determine the parameters σ_Y = 84 MPa from our measurement (**Figure 3.4(a)** and **Figure B.3(c)**), G_p = 15 MPa from the literature, J_m = 200, along with Young's modulus E = 3.01 GPa and Poisson's ratio υ = 0.34 for the linearly elastic regime (See Method Section).[184] A layer of cohesive elements modeled by a bilinear traction-separation law is inserted in front of the notch to allow propagation of the notch under the assumption of a pure mode I crack (See Method Section, **Figure B.15(a, b)**). Here we set the following parameters: the intrinsic fracture energy $\Gamma_0 = 100\, J/m^2$, maximum cohesive stress $\sigma_c = 300\, MPa$, and the interfacial stiffness of the cohesive elements $E_{ts} = 78750$ GPa (see the discussion about **Figure 3.4** and Method section for additional details).

As a result, stress concentrates at the crack tip, dominated by plasticity (**Figure 3.2(d)**, **Figure B.2(b)**). **Figure 3.2(d)** shows the distribution of the minimum principle stress, where the direction of a line represents the orientation of the principle stress. The

negative value of the minimum principle stress indicates wrinkling patterns should form along its orientation, perpendicular to the crack, similar to the experimental observation. As the external displacement increases, the compressive stress increases, and the wrinkling patterns expand. Since some films have catastrophically failed before the displacement 0.2 mm in our simulations, their stress distributions are shown at smaller displacements, i.e., 0.19 mm, 0.16 mm, and 0.14 mm for samples with a notch size of 0.4 mm, 0.6 mm and 0.8 mm, respectively. As the initial notch length increases, the wrinkling regions enlarge and align more in the crack direction. High tensile stress exists at the notch tip in the perpendicular direction, represented by the maximum principle logarithmic stress, implying the formation of the SDZ at similar locations to the experiments (**Figure 3.2(d)**).

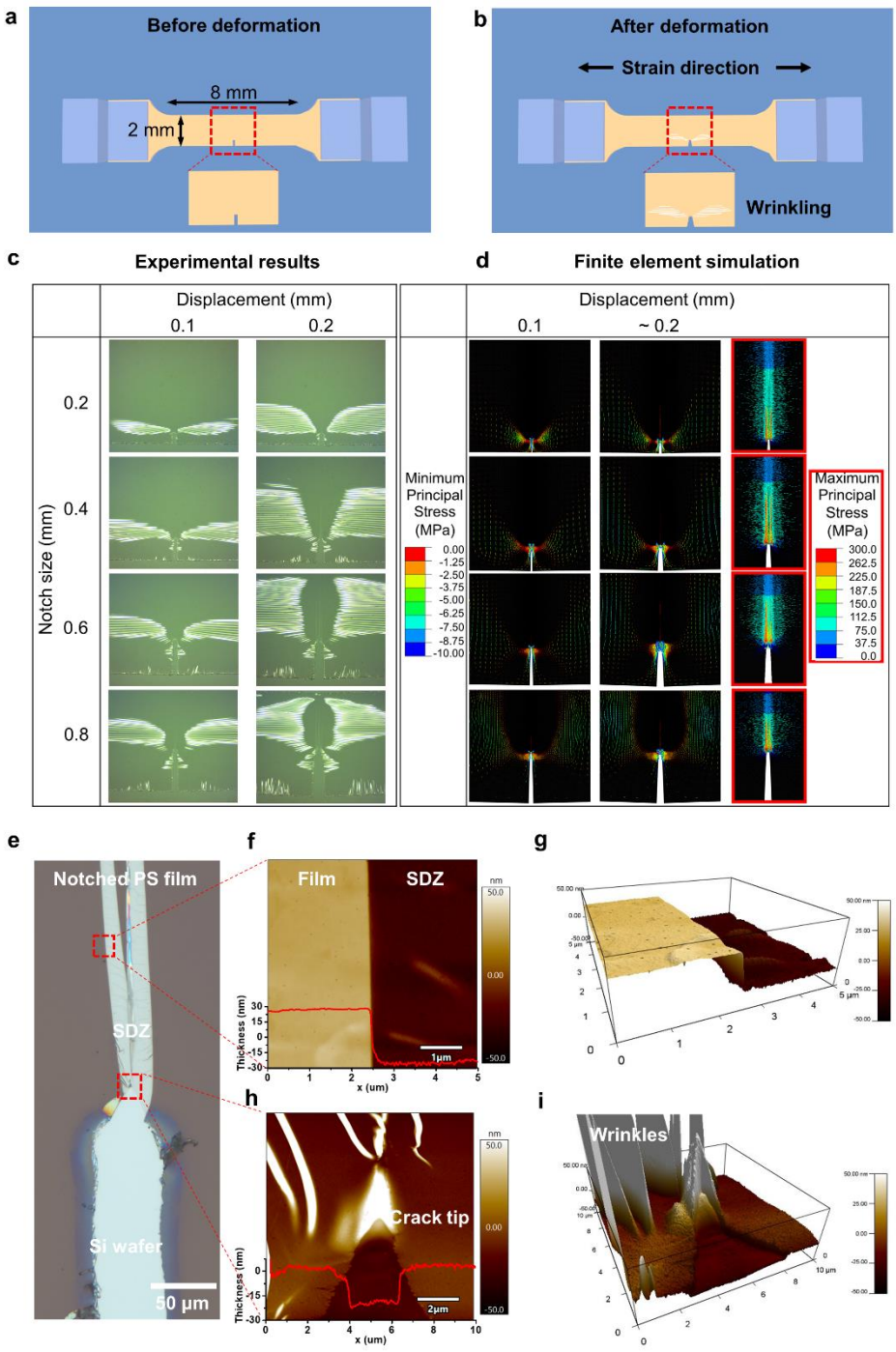

Figure 3.2 *Deformation process of notched polystyrene thin films. (a, b) 3D scheme showing a dog-bone sample with a notch (a) before and (b) after deformation. When the deformation is large enough, wrinkles show up near the notch. (c) Optical images of thin films with notches of various sizes being uniaxially deformed to different displacements. (d) Finite element simulation results of minimum principle stress distribution in notched*

polystyrene thin films of various notch sizes under different deformation. The orientation of the minimum principle logarithmic stress indicates the direction of the wrinkling patterns. Since some films have catastrophically failed at the displacement 0.2 mm, the strain distributions are shown at smaller displacements (0.2 mm, 0.19 mm, 0.16 mm, and 0.14 mm for samples with a notch size of 0.2 mm, 0.4 mm, 0.6 mm and 0.8 mm, respectively). Images with red frames represent the corresponding maximum principle logarithmic strain distributions, which show high tensile strain at the crack tip. (e) Optical image of the crack tip for a notched film sitting on a silicon wafer (0.4 mm notch size and 0.2 mm displacement). (f) AFM 2D and (g) 3D height images showing the boundary between a shear deformation zone (SDZ) and the rest of the film. 1D line cut is overlaid to show the film thickness along the sample. (h) AFM 2D and (i) 3D height images of the notch tip. 1D line cut is overlaid to show the film thickness along the sample.

To better visualize the deformation behavior around the notch, both optical microscope and atomic force microscope (AFM) were applied to investigate the thin-film morphology near the crack tip. The ultrathin PS film with a notch size of 0.4 mm was strained to 2.5% externally (0.2 mm displacement), then picked up from the water with a silicon substrate (**Figure 3.2(e-i)** and **Figure B.4**). It is observed that as the notch propagates, the nearby PS film undergoes substantial plastic deformation, which induces chain reorientation, chain pull-out, and chain scission. In particular, the chain pull-out behavior corresponds to the formation of SDZs at the notch tip, seen as the white band-like regions around the crack tip (**Figure 3.2(e)**). AFM height images of the SDZ indicate its thickness of 25 nm, which means a 70% reduction in its original thickness of 80 nm, suggesting a significant amount of plastic deformation in the SDZ (**Figure 3.2(f-i)**). Similar observations have also been reported elsewhere.[189] It is worth noting that when compared with bulk PS, no apparent crazes were observed here, which is different from previously reported “2D craze” morphology with pinholes in the plastic deformation zone for 137 kg/mol PS ultrathin films at a similar thickness [58,190,191].

To further measure the fracture energy of the ultrathin PS films, the dependence of force F on displacement D was recorded and plotted in **Figure 3.3(a)**. The unnotched sample curve is shown in black color, where only a portion of the full curve is shown for better comparison. The cross on the end of each curve represents the onset of crack propagation, as visualized through a high-resolution camera. The total work is done to the sample, $U(D)$, can be calculated from the area underneath the force-displacement curve for various notch sizes *c*, and later plotted as a function of *c* (**Figure B.3(b)**). The fracture energy was calculated based on the following equation[192,193]:

$$G_b = \frac{1}{t}\frac{dU}{dc}\Big|_D \tag{3.2}$$

where *t* is the film thickness, D represents the selected displacement that is close to the onset of crack propagation (i.e., D_1, D_2, D_3), As a result, the fracture energy of an 80 nm thick 173 kg/mol PS film was determined to be 995 J/m^2, which was within the range from 200 to 1700 J/m^2, as reported by various studies on bulk PS samples[175,194]. This wide range of values in the literature was ascribed to different sample preparation and processing methods, as well as morphology change during crack growth[191,195].

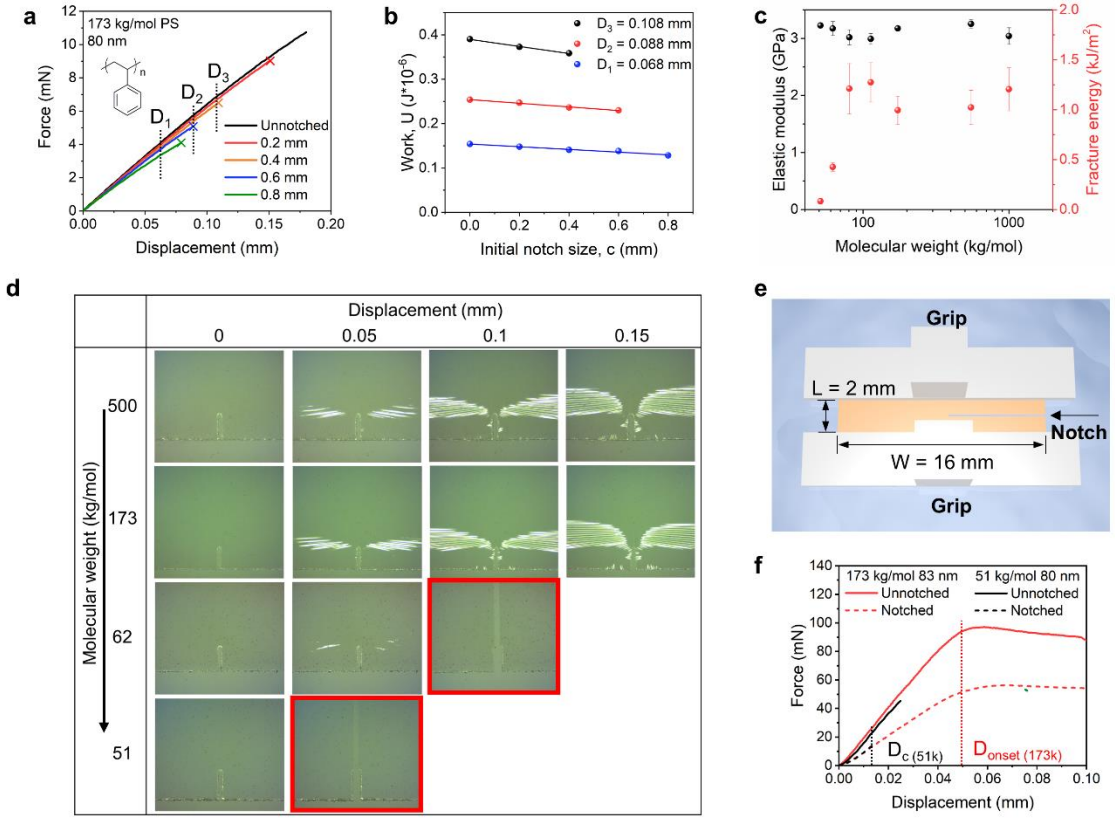

Figure 3.3 *Fracture energy measurements of PS ultrathin films through experimental methods. (a-d) Begley-Landes method. (a) Force-displacement curves for various notch lengths of 173 kg/mol PS thin films. The endpoints of the curves represent the beginning of crack propagation. (b) Total work done to samples, calculated using the area underneath of the force-displacement curves at given displacement values, are plotted as a function of the initial notch size. (c) Elastic modulus (black) and fracture energy (red) for 80 nm PS ultrathin films with different molecular weights. (d) Optical images of 80 nm PS film with 0.4 mm notch length and various molecular weights at different displacements. Images with red frames represent fractured films. (e, f) Pure shear test. (e) Schematics of the test setup with a rectangular notched sample attached to grips on two ends. (f) Force-displacement curves for unnotched and notched PS films with the molecular weight of 173 kg/mol and 51 kg/mol. D_c represents the critical displacement of 51 kg/mol PS, D_{onset} represents the onset of notch propagation for 173 kg/mol PS.*

Next, we examined the role of plastic deformation in resisting crack propagation by varying the molecular weight. Previous studies on bulk PS have shown a ductile-to-brittle transition with decreasing molecular weight, indicating molecular weight-dependent fracture energy[183,196]. A similar phenomenon has also been widely observed

in other polymers like poly(methyl methacrylate) (PMMA) and polyimide[182,197–199]. Micro-projectile impact tests performed on free-standing PS thin films show decreased impact energy as the chain entanglement decreases[177]. Here, we also tested PS ultrathin films with various molecular weights (51 kg/mol, 62 kg/mol, 81 kg/mol, 113 kg/mol, 500 kg/mol, 1000 kg/mol) at a similar film thickness of around 80 nm. (**Figure 3.3(c, d)**, and **Figure B.5-B.12**). Their corresponding elastic moduli and fracture energies are plotted in **Figure 3.3(c)** and summarized in **Table B.1**. While ductile behavior is found in 173 kg/mol PS films, 51 kg/mol PS films showed brittle failure. The elastic modulus shows no apparent dependence on the molecular weight since the lowest molecular weight tested here is well above the entanglement molecular weight of PS (M_e = 18 kg/mol) (**Figure B.13(a)**)[154,200]. Similarly, their bulk glass transition temperature T_g is independent of the molecular weight in the range studied here (**Figure B.13(b)**)[201]. In contrast, the fracture energy drops significantly at below 82 kg/mol, i.e., the fracture energy of 62 kg/mol and 51 kg/mol PS is 426 J/m^2 and 84 J/m^2, which are 68% and 90% lower than that of 173 kg/mol PS, respectively. The fracture energy of a PS film can be composed of the intrinsic fracture energy caused by chain scission and plastic energy dissipation caused by chain reorientation and chain pull-out[196]. Owing to the high entanglement density in high molecular weight PS, the amount of plastic energy dissipation is more pronounced than that of low molecular weight PS. The reduction in fracture energy also results in a transition from ductile-to-brittle failure behavior with a decreasing molecular weight in ultrathin PS films. As seen in the optical images, the notch tip for 173 kg/mol got wider and blunted under displacement, followed by crack propagation. Conversely, 51 kg/mol and 62 kg/mol PS display brittle failure instantly

after the limited stress accumulation (**Figure 3.3(d)** and **Figure B.7, B.8**). This observation demonstrates the vital role of inter-chain entanglement in enhancing the fracture energy of polymer ultrathin films.

When plastic energy dissipation has substantial contribution to the total fracture energy, the total fracture energy is supposed to rise as the crack extends until reaching a steady state value.[202] To confirm our observation of the brittle-to-ductile transition of PS ultrathin films with the molecular weight, we also conducted pure shear tests on both 51 and 173 kg/mol PS to obtain the steady-state fracture energies (**Figure 3.3(e, f)**, and **Figure B.14**). The bilayer ultrathin film was also laser-patterned into a rectangular shape with a thickness t of 80 nm, width W of 16 mm, and a length L of 2 mm, corresponding to a width-to-length ratio of 8 (**Figure 3.3(e)**). For each polymer, the force-displacement curves were measured for both an unnotched sample and a notched sample with a pre-crack half of the length of the sample. The measured steady-state fracture energy G_p can be obtained by[192,203]

$$G_p = \frac{U(D_c)}{Wt} \tag{3.3}$$

where $U(D_c)$ is elastic energy of the unnotched sample at the critical displacement D_c between the two grips when the stable notch turns into a running crack and can be calculated by the area underneath the force-displacement curve of the unnotched sample. For 51 kg/mol PS, the critical displacement can be easily identified due to its brittle fracture behavior, and the fracture energy was determined to be around 95 J/m^2, agreeing well with that measured from the Begley-Landes method, which indicates a negligible contribution of plastic dissipation to the total fracture energy. For 173 kg/mol PS, the fracture energy based on the measurement of the onset displacement for crack

propagation, D_{onset}, is 1744 J/m^2. Unfortunately, before reaching the stable crack propagation condition, the stress concentration in the gripping region triggers an additional crack, which makes it challenging to accurately measure the fracture energy of 173 kg/mol PS. However, even the underestimated steady-state fracture energy value is much higher than that from the Begley-Landes method, indicating the significant contribution of plastic deformation to the total fracture energy, which leads to the brittle-to-ductile transition.

Further fracture analysis of PS films was performed through the cohesive zone model in finite element simulations (see Method section for details). The intrinsic fracture energy for the cohesive elements for both the 51 kg/mol and 173 kg/mol PS films is prescribed as 100 J/m^2, which is equal to the averaged total fracture energy measured for the 51 kg/mol PS at different thicknesses, as shown later in Fig. 5C. Since the molecular weights of both are much higher than the entanglement molecular weight of 18 kg/mol, the intrinsic fracture energies are not expected to differ. In contrast to the 173 kg/mol PS, the 51 kg/mol PS is modeled as a linearly elastic material with the same modulus and Poisson's ratio as those of the 51 kg/mol PS. The simulated force-displacement curves of an 8 mm × 2 mm sample with a 0.6 mm notch (the same dimension as that in the experiment) for both 173 kg/mol and 51 kg/mol PS agree well with the experimental measurements (**Figure 3.4(a)**). The 173 kg/mol PS exhibits ductile fracture, indicated by the blunting of the crack tip with a large plastic zone size developed before the crack propagates, which results in a peak force as high as around 8 mN. The similar crack tip blunting was also observed in the experiment (**Figure B.2** and **Figure B.10**-**B.12**). In contrast, the 51 kg/mol PS exhibits brittle fracture, without plasticity as an

energy dissipation mechanism. As a result, the crack propagates immediately once the intrinsic fracture energy is achieved, resulting in a low peak force around 1.5 mN.

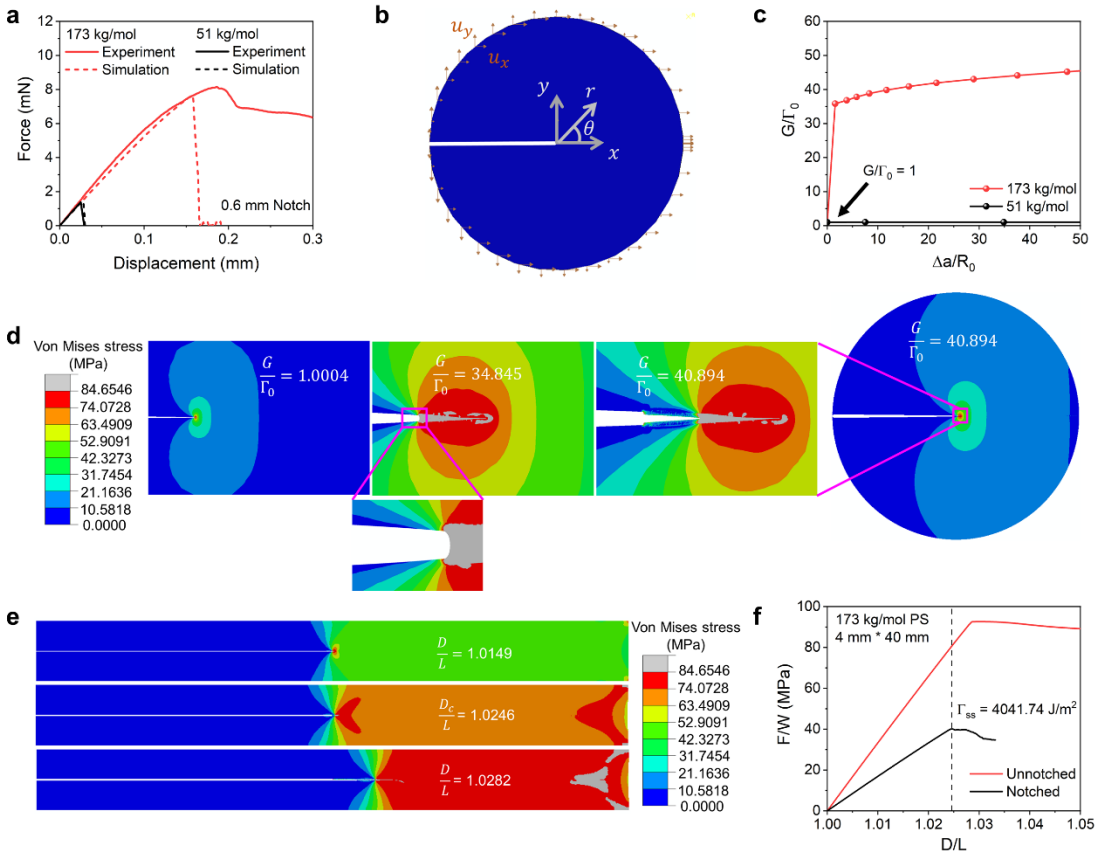

Figure 3.4 *Fracture energy measurements of PS ultrathin films through finite element analysis. (a) Comparison of force-displacement curves between experimental and simulation results for 173 kg/mol and 51 kg/mol PS with 0.6 mm notch. The material model used to simulate 173 kg/mol PS is the Gent model with an initial modulus of 15 MPa and a strain stiffening parameter J_m of 200. (b) Schematic of K-field zone with applied displacement field. (c) Evolution of plastic zone size. At gray region, σ_{yy} is greater than yield stress. (d) Crack growth resistance curves (R-curve) for 173 kg/mol and 51 kg/mol PS using a J_2 flow theory and isotropic hardening model satisfying Gent model with an initial modulus of 15 MPa and J_m of 200. (e) Evolution of plastic zone size and crack propagation in pure shear simulation model of 173 kg/mol PS. The height, width, and notch length are 0.4 cm, 4 cm and 2 cm, respectively. (f) Nominal stress stretch plots for the notched and unnotched 173 kg/mol PS pure shear simulation model with dimensions specified in (e).*

To determine the fracture resistance curve (R-curve) of the 173 kg/mol and 51 kg/mol PS, their mode I crack growth under the plane stress condition is simulated subject to the small-scale yielding condition[202]. We modeled a large K-field zone of radius 2 cm, where the x-axis aligns along the crack plane, and the origin is positioned at the initial crack tip (**Figure 3.4(b)**). We selected the radius of the K-field zone to be 2 cm to guarantee it is much larger than the initial plastic zone size estimated by $R_0 = E\Gamma_0/\pi{\sigma_Y}^2 = 0.00134$ cm, and the developing plastic zone size even after considerable crack propagation as the external loading increases. The displacement field, in accordance with linear elastic fracture mechanics, is prescribed on the outer circular boundary of the K-field zone.

$$\begin{aligned} u_x &= \frac{2K_I(1+\nu)}{E}\sqrt{\frac{r}{2\pi}}cos\left(\frac{\theta}{2}\right)\left[\frac{1-\nu}{1+\nu}+sin^2\left(\frac{\theta}{2}\right)\right], \\ u_y &= \frac{2K_I(1+\nu)}{E}\sqrt{\frac{r}{2\pi}}sin\left(\frac{\theta}{2}\right)\left[\frac{1-\nu}{1+\nu}+cos^2\left(\frac{\theta}{2}\right)\right], \end{aligned} \tag{3.4}$$

where r and θ are the radial and circumferential coordinates, and K_I is the stress intensity factor, governing the amplitude of the displacement. The energy release rate G is directly calculated using the following equation,

$$G = \frac{{K_I}^2}{E}. \tag{3.5}$$

The relation of G and the crack extension Δa is recorded as the R-curve.

As the applied displacement field increases, the plastic zone develops at the crack tip for the 173 kg/mol PS. When G reaches 100 J/m^2, the first cohesive element reaches the maximum separation distance δ_{max}, and the plastic zone size is 0.0134 mm, which is consistent with R_0 (**Figure 3.4(c)**). As G increases, the plastic zone size expands, and the crack tip blunts, consistent with the experimental observation (**Figure B.2** and **Figure**

B.10-B.12). The crack does not propagate until *G* reaches a much higher value 3600 J/m^2, i.e., $G/\Gamma_0 = 36$ (**Figure 3.4(d)**), which corresponds to the fracture energy experimentally measured by the Begley-Landes method. As *G* further enlarges, the crack extends downstream, and the material points in the plastic zone unload. Finally, the steady-state condition is reached where the stress field behind the advancing crack tip is invariant (**Figure 3.4(c, d)**). The steady-state fracture energy for the 173 kg/mol PS from the simulation is 4089 J/m^2, more than 40 times of its intrinsic fracture energy. Correspondingly, the plastic zone size is 40 times larger than the initial size, but still remains much smaller than the radius of the K-field zone. The significant increase of the total fracture energy compared to the intrinsic fracture energy originates from the plastic dissipation of the material when the plastic zone is unloaded as the crack propagates downstream. We also studied the effect of strain stiffening parameter J_m on the fracture behavior. As J_m increases, the fracture energy increases since the less stiffened polymer induces a larger plastic zone size (**Figure B.15(a)**). On the other hand, the maximum force that the notched sample discussed in **Figure 3.4(a)** can sustain before the notch catastrophically propagates decreases as J_m decreases (**Figure B.15(b)**). Therefore, we chose J_m = 200 to better fit the simulation results to the experimental measurements. In contrast, the R-curve for the 51 kg/mol PS is a horizontal line of value *G* = 100 J/m^2, indicating the steady-state fracture energy is exactly equal to the intrinsic fracture energy without plastic dissipation. Unlike the 173 kg/mol PS, the crack does not blunt for the 51 kg/mol PS, and the crack catastrophically propagates once *G* reaches the intrinsic fracture energy.

To further confirm the steady-state fracture energy obtained from the simulated R-curve by the K-field zone method, the pure shear test is simulated using the same cohesive zone elements with the same parameters. We chose the length and width of the simulated pure shear test sample to be 4 mm and 40 mm, respectively. Similar to the experiment, one notched and one unnotched sample are stretched quasi-statically along the length direction at a strain rate of 1%/s under the clamp boundary condition. In the notched sample, a pre-crack of 2 cm is introduced, and cohesive elements are implemented ahead of the crack tip. As the external displacement increases, the stress in the sample increases and the plastic zone develops at the crack tip (**Figure 3.4(e)**). Again, the crack tip blunts before the crack propagates. The external stress reaches the maximum at the critical stretch $D_c/L = 1.0246$, indicating the onset of unstable crack growth (**Figure 3.4(f)**). (L is the initial length of the pure shear sample at 0.4 cm, and D_c is the critical displacement when unstable crack growth occurs.) From the simulation of the unnotched sample, the normalized force-displacement relation is obtained (**Figure 3.4(f)**). Using Equation 3.3, we obtain the steady-state fracture energy of the 173 kg/mol PS as 4042 J/m^2, which agrees well with that from the R-curve based on the K-field zone method. Although the pure shear test can measure the steady-state fracture energy of samples undergoing large scale yielding, the sample dimension needs to be large enough so that the boundary effect does not interfere with the fracture behavior of the material. This is the reason why we selected the width and length of the sample to double that of the experiments. The pure shear simulation of the sample with the same dimension as the experiment measures a lower steady-state fracture energy 2874 J/m^2 (**Figure B.16**),

which can be another reason that the experiment may underestimate the steady-state fracture energy.

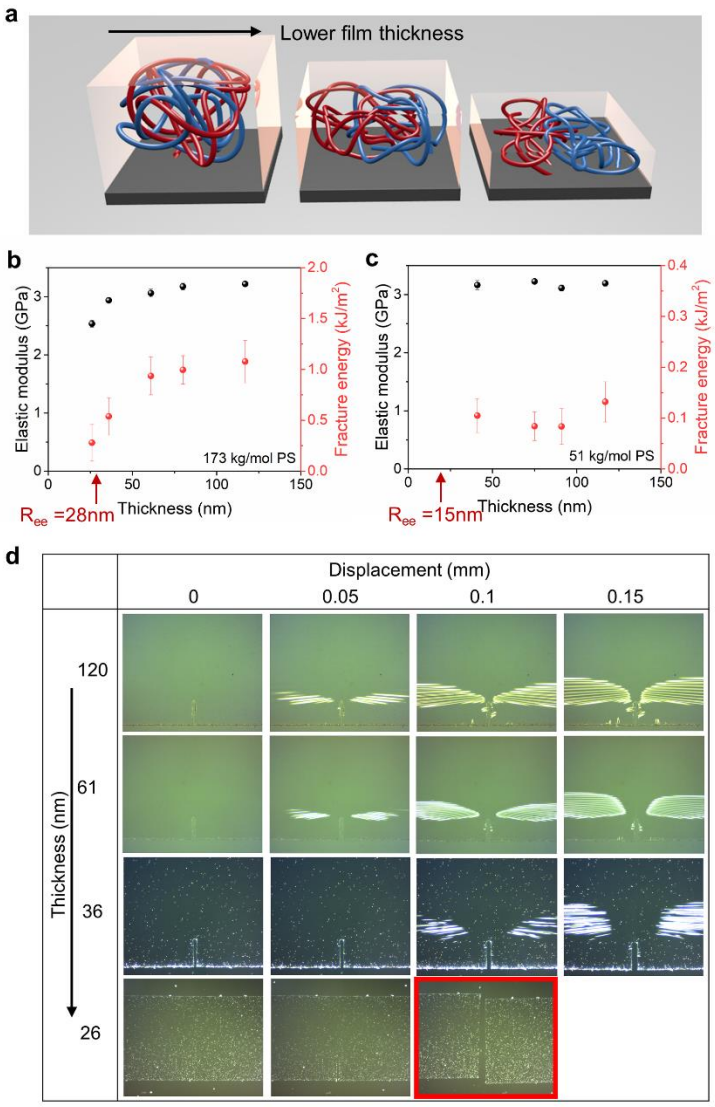

Figure 3.5 *Effect of film thickness on the fracture behavior of PS ultrathin films. (a) Schematic showing the confinement effect on the number of chain entanglements under the same molecular weight. As the thickness decreases, the number of inter-chain entanglements decreases, while intra-chain entanglements increase. (b, c) Elastic modulus (black) and fracture energy (red) versus thickness for (b) 173 kg/mol and (c) 51 kg/mol PS. (d) Optical images of 173 kg/mol PS film with 0.4 mm notch length and various film thicknesses at different displacements. Image with a red frame represents fractured films.*

Besides the effect of molecular weight, film thickness could also play a critical role on the fracture behavior of ultrathin films due to two mechanisms: polymer chains at the air-film interface have higher mobility than the bulk[136,137]; polymer films with a thickness below the end-to-end distance, R_{ee}, of the polymer chains could have less inter-chain entanglements and more intra-chain entanglements (**Figure 3.5(a)**)[189,204]. Previous works using the film-on-elastomer method have demonstrated the elastic modulus of ultrathin PS films is lower than those of the bulk, while the crack onset strain is higher for thinner film[109,143]. The micro-projectile impact test shows lower penetration energy for thinner films[177]. However, quantitative measurement for the ultrathin film fracture energy has not been reported in the literature. In this study, we measure the fracture energies of 173 kg/mol and 51 kg/mol PS representing ductile and brittle systems, respectively, of various thicknesses (**Figure 3.5(b, c)** and **Figure B.17-B.25**). For 173 kg/mol PS, as the film thickness goes down, the fracture energy drops from around 1000 J/m^2 at a thickness above 50 nm, to 538 J/m^2 at 36 nm, and 276 J/m^2 at 26 nm, corresponding to a 75% reduction. This trend agrees well with the elastic modulus reduction when the thickness drops below 50 nm, which is close to the R_{ee} of 28 nm[189]. However, due to the low R_{ee} of 15 nm, the 51 kg/mol PS shows near-constant fracture energy of around 100 J/m^2 for films with a thickness from 40 to 120 nm. A much thinner PS film was not tested due to the challenge in transferring a brittle notched sample onto water surface. Here, we observe the effect of confinement on facture behavior of ultrathin films. It is also noticed that a 26 nm 173 kg/mol PS film exhibits a fracture energy roughly three times that of a 120 nm 51 kg/mol PS film, which suggests the significant

role of polymer chain length in producing energy dissipation. For even thinner films, the wrinkles are less visible due to the weak light reflection from low wrinkle amplitude.

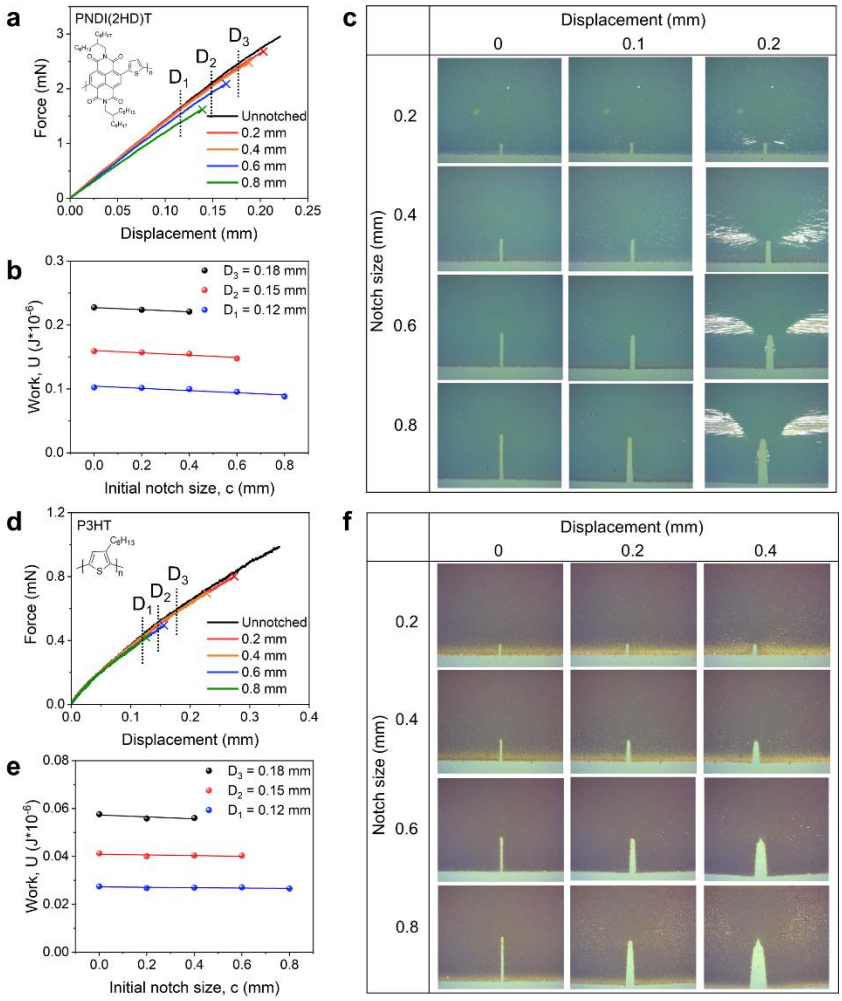

Figure 3.6 *Fracture energy measurements for low-T_g polymers PNDI(2HD)T (58 nm) and P3HT (51 nm). (a, d) Force-displacement curves for dog-bone samples with various notch sizes for (a) PNDI(2HD)T and (d) P3HT films with various notch sizes. (b, e) The work done as a function of notch size for the polymer thin films (b) PNDI(2HD)T and (e) P3HT. (c, f) Optical images of polymer ultrathin films with various notch sizes at different displacements for (c) PNDI(2HD)T and (f) P3HT.*

In addition to the model PS system, the same technique is employed to measure fracture energies of functional semicrystalline polymers that are widely used in thin-film electronic devices to gain insights into their fracture behavior. Here, two semiconducting

polymers are chosen, Poly{[N,N'-bis(2-hexyldecyl)naphthalene-1,4,5,8-bis(dicarboximide)-2,6-diyl]-alt-2,5-thiophene} (PNDI(2HD)T) and poly(3-hexylthiophene) (P3HT), which have received tremendous attention due to their potential in fabricating future flexible electronic devices. Previous researches mainly focused on their thermal and mechanical properties like T_g, elastic moduli, and crack-onset strains[27,102], but their fracture energies are still unknown. As a result, PNDI(2HD)T exhibits a high T_g of 115 ºC and a high elastic modulus of 890 MPa, while the fracture energy is determined to be 320 J/m^2 (**Figure 3.6(a-c)**, and **Figure B.26, B.27**). Upon deformation, a scattering of bright spots slowly builds up around the notch at an external displacement of 0.1 mm, followed by plastic failure without forming an SDZ. Correspondingly, less pronounced wrinkling patterns are observed than those of PS films (**Figure 3.6(b)**). These wrinkling patterns slowly disappear with time, even under a fixed displacement due to the viscoelastic nature of PNDI(2HD)T. On the other hand, P3HT with a T_g of 25 ºC and an elastic modulus of 315 MPa shows much lower fracture energy of 78 J/m^2 (**Figure 3.6(d-f)**, **Figure B.28**). Furthermore, no obvious wrinkles are observed on P3HT thin films except for some bright spots, indicating its highly mobile nature at room temperature (**Figure 3.6(e)**). The disparity between two polymer's fracture energy and wrinkling behavior likely results from the much softer polymer chains and the lower molecular weight of P3HT than PNDI(2HD)T. Our method presented here would represent the first direct measured fracture energies of semiconducting polymers.

3.4 Conclusions

In this work, we demonstrate a new technique to measure the fracture energies of ultrathin films in confined state. The proposed technique has been demonstrated in both amorphous and semicrystalline polymer systems. A ductile-to-brittle transition is observed in PS ultrathin films when either the molecular weight or film thickness decreases. From an experimental Begley-Landes method, the fracture energy shows a reduction from 1000 J/m^2 for 173 kg/mol PS to 100 J/m^2 for 51 kg/mol PS. Meanwhile, under the same molecular weight of 173 kg/mol, the fracture energy reduces for 75% from 61 nm to 26 nm. Direct visualization of the stress field distribution, quantitative measurement of the fracture energy, and predictive finite element fracture simulations of the R-curve provide us the understanding that plastic dissipation due to chain reorientation, pull-out, and scission accounts for the significant increase of the total fracture energy compared to the intrinsic fracture energy. Besides its promising applications in the polymeric thin films, this method can also be widely used in other fields and serve as a new platform to study fracture mechanics of inorganic or metallic thin films and emerging 2D-materials at the device-relevant thickness range.

CHAPTER IV – BACKBONE THIOPHENE EFFECT ON THE MECHANICAL AND THERMAL PROPERTIES OF DONOR–ACCEPTOR SEMICONDUCTING POLYMERS

(Adapted from "Zhang, S.; Ocheje, M. U.; Huang, L.; Galuska, L.; Cao, Z.; Luo, S.; Cheng, Y.; Ehlenberg, D.; Goodman, R. B.; Zhou, D.; Liu, Y.; Chiu, Y.; Azoulay, J. D.; Rondeau-Gagné, S.; Gu, X. The Critical Role of Electron-Donating Thiophene Groups on the Mechanical and Thermal Properties of Donor–Acceptor Semiconducting Polymers. Adv. Electron. Mater. 2019, 5 (5), 1800899.)

4.1 Introduction

Polymer-based semiconductors are receiving more and more attention due to their intrinsic mechanical flexibility, solution processability and chemical tunability, together with their applications in organic electronics like organic field effect transistors (OFET),[6,205–208] organic photovoltaics (OPV) and thermoelectrics.[209–214] Building upon the success of polythiophene polymers, recent efforts have been devoted to synthesizing new conjugated polymers such as low band-gap donor-acceptor (D-A) polymers to boost their charge carrier mobility for OFETs and power conversion efficiency (PCE) for OPVs.[12,115,215–219] Although great improvements have been achieved in devices' electronic and optical performance, there is an increasing need for improving their mechanical property, i.e., lower stiffness and higher stretchability,[121] laying a foundation for future applications in wearable, stretchable electronics,[91,98,99] and bioelectronics.[220,221]

Early studies on the mechanical property of conjugated polymers started from polythiophene polymers have shown that backbone engineering, side chain engineering,

copolymerization with deformable blocks and physical blending with elastomers can efficiently improve the stretchability and reduce the elastic modulus.[96,105,132,222] Similar methods were later applied to D-A polymers, a class of conjugated polymers with superior electrical performance relative to P3ATs.[99,223] Diketopyrrolopyrrole (DPP)-based conjugated polymers are one of heavily studied D-A semiconducting materials with a top performing charge mobility above 12 $cm^2 V^{-1} s^{-1}$,[13–15] which is as good as the polycrystalline silicon, allowing many practical applications in electronic devices. Encouraged by its promising electronic property, several methods have been explored to improve the mechanical property of DPP-based polymers and unravel the role of backbone and side chain structure in their intrinsic stretchability and charge mobility in order to achieve the best of two worlds.[13,15,19,98,120,125,129,224–226]

Backbone engineering of the DPP polymer comes from two strategies, either by tuning conjugated donor or acceptor groups or flexible non-conjugated linker groups.[123,128,130] Along this line, Roth *et al*. investigated a library of low band-gap polymers and qualitatively concluded that fused rings on the backbone would increase the elastic modulus and reduce the ductility, while branched side chains will have an opposite effect.[123] Similar conclusions were drawn by Lu *et al*., where DPP polymers with branched side chains were noticed to be less stiff and more stretchable than linear ones.[124,226] Savagatrup *et al*. showed that by introducing flexible groups like alkyl chains to the conjugated backbone, the crack onset strain increased from 4% without spacer to 12% with 70% ratio of spacer while retaining a decent charge mobility around 0.05 $cm^2 V^{-1} s^{-1}$.[128] Furthermore, carefully designed non-conjugated linkers can also improve the solution processability of DPP polymers, which can be dissolved in benign solvents.[227]

Apart from backbone engineering, functional side chains were also used to improve the mechanical performance. Wang's work showed that covalent crosslinking between side chains using oligo-siloxane can improve the elasticity and the ductility of the system, while maintaining the electrical performance even after 500 cycles at 20% strain.[134] Non-covalent crosslinking like hydrogen bonding was also shown to be useful by introducing self-healable electrical and mechanical properties to the polymer system.[97,228] Despite the versatility in improving the mechanical performance of D-A polymers, the dynamics of the conjugated polymer backbone, described by the glass transition temperature, upon using isolated or fused thiophene linkers in the polymer backbone is still not well explored. This hinders rational design of the conjugated polymers with target T_g as well as mechanical property.

Herein, we have systematically varied the main chain structure by inserting different donor moieties, including thiophene (T), bithiophene (T2), terthiophene (T3), thienothiophene (TT) and dithienothiophene (TTT) (**Figure 4.1(a)**) into the DPP polymer to study their impact on the thermomechanical property of conjugated polymer thin films. Our study revealed that all the thiophene building blocks act as anti-plasticizers and slow down the backbone dynamics, resulting in an increase in the elastic modulus for the thin polymeric film. Further morphological studies on DPP thin films using grazing incidence wide-angle X-ray scattering (GIWAXS), atomic force microscopy (AFM) and ultraviolet visible spectroscopy (UV-Vis) showed that there is no significant influence of aggregation state on the mechanical property while the degree of crystallinity would increase the elastic modulus slightly. Crystalline packing structure, degree of aggregation, and surface roughness do not directly correlate with the mechanical property

of DPP polymers. This study provided a new understanding of the effect of the thiophene unit insertion on the mechanical behaviors and chain dynamics of conjugated polymer thin films. Using the knowledge gained here, we finally designed and synthesized a new DPP polymer that has a record low backbone T_g and elastic modulus for the reported DPP family. This work will provide guidance to the future design of stretchable semiconducting polymers with the desired thermomechanical property.

4.2 Experimental

4.2.1 Materials and processing

Five DPP-based conjugated polymers with systematically controlled main chain structures were synthesized. The electron donating unit was varied by introducing different numbers of thiophene units or sizes of fused thiophene rings. Their chemical structures were shown in **Figure 4.1(a)**. The synthesis procedures of DPP-T,[229,230] DPP-T2,[231,232] DPP-T3,[224] DPP-TT[233,234] and DPP-TTT[235] have been reported elsewhere. The number molecular weight was measured by high temperature gel permeation chromatography (HT-GPC) using trichlorobenzene as the eluent at 160 °C, polystyrene for calibration, viscometer and light scattering as the detector. One additional purposely engineered DPP-based conjugated polymer with additional flexible alkyl chains on the thiophene unit (Scheme C.1) has been synthesized using a protocol detailed in Appendix C. Polymer thin films were fabricated by spin coating of conjugated polymer solutions in chlorobenzene (CB) on the silicon substrate with native oxide layer. Thermal annealing of the deposited polymer film was performed at 200 °C for 10 mins inside of a glove box and allowed to cool down to room temperature before additional testing.

4.2.2 Small angle neutron scattering

Small-angle neutron scattering (SANS) study was performed at the extended Q-range small-angle neutron scattering diffractometer (EQ-SANS BL-6) line at the Spallation Neutron Source (SNS) located at Oak Ridge National Laboratory (ORNL). Two wavelengths and their corresponding sample-to-detector distances were used to obtain a wide q range: 2.5 Å at 2.5 m, and 8 Å at 8 m. The solution was made by dissolving the polymer in deuterated chlorobenzene with a concentration of 5 mg/ml. Data reduction was performed in MantidPlot to obtain the polymer scattering data by subtracting the solution signal with solvent scattering signal. Later, the obtained polymer scattering data was fitted by using SasView.

4.2.3 Pseudo-free Standing Tensile Test

Thin film tensile tests were performed on the water surface through pseudo-free-standing tensile tester. Details about the tensile stage setup can be referred to our previous publication.[18] Briefly speaking, the polymer thin films (~ 90 nm) were patterned into dog-bone shape by oxygen plasma etching process and floated on top of water before being further unidirectionally pulled at a strain rate of $5*10^{-4}$ s^{-1} until the film fractures. At least six independent samples were measured for each conjugated polymer to provide statistically averaged mechanical property. The elastic modulus was obtained from the slope of the linear fit of the stress-strain curve using the first 0.5% strain (elastic region).

4.2.4 Alternating Current (AC) Chip Calorimetry

The AC chip calorimeter was used to obtain the T_g of the polymeric thin film.[26] The experiments were performed at a frequency of 10 Hz and a heating/cooling rate of 1

°C/min. The dynamic T_g was determined as the half-step temperature of the amplitude of the complex differential voltage.

4.2.5 Grazing Incidence Wide Angle X-ray Scattering (GIWAXS)

GIWAXS experiments were performed on beamline 11-3 at the Stanford Synchrotron Radiation Lightsource (SSRL). Data was collected under helium environment with an incident beam energy at 12.7 keV and an incidence angle of 0.12°. The sample to detector distance is about 300 mm. Diffraction data analysis was performed using Nika software package for Wavemetrics Igor, in combination with WAXStools.

4.2.6 Atomic Force Microscopy (AFM)

AFM images were acquired on Bruker Dimension Icon in tapping mode. The samples were casted on the flat silicon substrate as described above.

4.2.7 UV-Vis-NIR Absorption Spectroscopy

The solid-state UV-Vis-NIR spectra were recorded on Agilent Cary 5000 using polymer thin films deposited on glass slides.

4.3 Results and discussion

4.3.1 Thermomechanical property of DPP polymers

Five different DPP polymers were synthesized according to previous reports.[224,231–233,235] After the synthesis, the samples were purified and characterized by high temperature GPC in trichlorobenzene at 160 °C to gain insights into their molecular

weight and polydispersity. **Figure 4.1(a)** and **Table 4.1** summarized the structure and the material's property of the synthesized DPP polymers.

We first probed the mechanical property of ~ 90 nm pseudo-free standing thin films using custom-made thin film tensile tester as shown in **Figure 4.1(b)**. The details of the set-up were described in our previous publication.[18] This methodology eliminates the effect of the supporting elastomeric substrates compared to another popular thin film mechanical characterization technique named "buckling metrology",[42] thus providing the intrinsic mechanical property of the thin film. To provide a fair comparison between different DPP polymers, conjugated polymers with relatively high molecular weights were targeted and synthesized, followed by processing into thin films of similar thickness, and annealing under the same temperature and time. We carefully controlled the film thickness to be between 80 nm and 100 nm for all five samples by changing the solution concentration, in order to avoid the influence of film thickness effect, also known as the confinement effect, on the mechanical property of thin films, as reported in previous studies.[18,54,189] The molecular weight is another factor that has been observed to critically influence the mechanical property of a given polymer, which was carefully tuned to be in the similar range, as shown in **Table 4.1**. The effect of film processing, film morphology, and molecular weight on their mechanical property will be discussed in more detail in the following section.

Table 4.1 *Physical properties of DPP polymers*

Polymer	M_n (kg/mol) [a]	$Đ_w$ [b]	Side chain T_g (°C) [c]	Backbone T_g (°C) [d]	Backbone T_g (°C) [e]	Elastic modulus (MPa) [f]	Crack onset strain [f]
DPP-T	47	2.83	-54.29	-3.96	-11	173 ± 10	0.53 ± 0.20
DPP-T2	44	3.96	-51.89	11.95	17	281 ± 9	0.44 ± 0.09
DPP-T3	27	3.18	-47.93	18.98	19	319 ± 49	0.44 ± 0.10
DPP-TT	51	3.62	-52.99	2.76	3.5	400 ± 41	0.16 ± 0.03
DPP-TTT	26	3.69	-52.49	4.11	22	480 ± 40	0.03 ± 0.01

Note: [a] Number-average molecular weight measured by high temperature GPC using trichlorobenzene as eluent at 170 °C. [b] Weight dispersity. [c] Obtained from peak of the loss modulus by DMA. [d] Obtained from the peak of tan δ plot in DMA. [e] Obtained from AC-chip calorimetry on thin film sample. Note that different T_g is expected due to different probing methods between DMA and calorimetry techniques. [f] Obtained from pseudo-free standing tensile test.

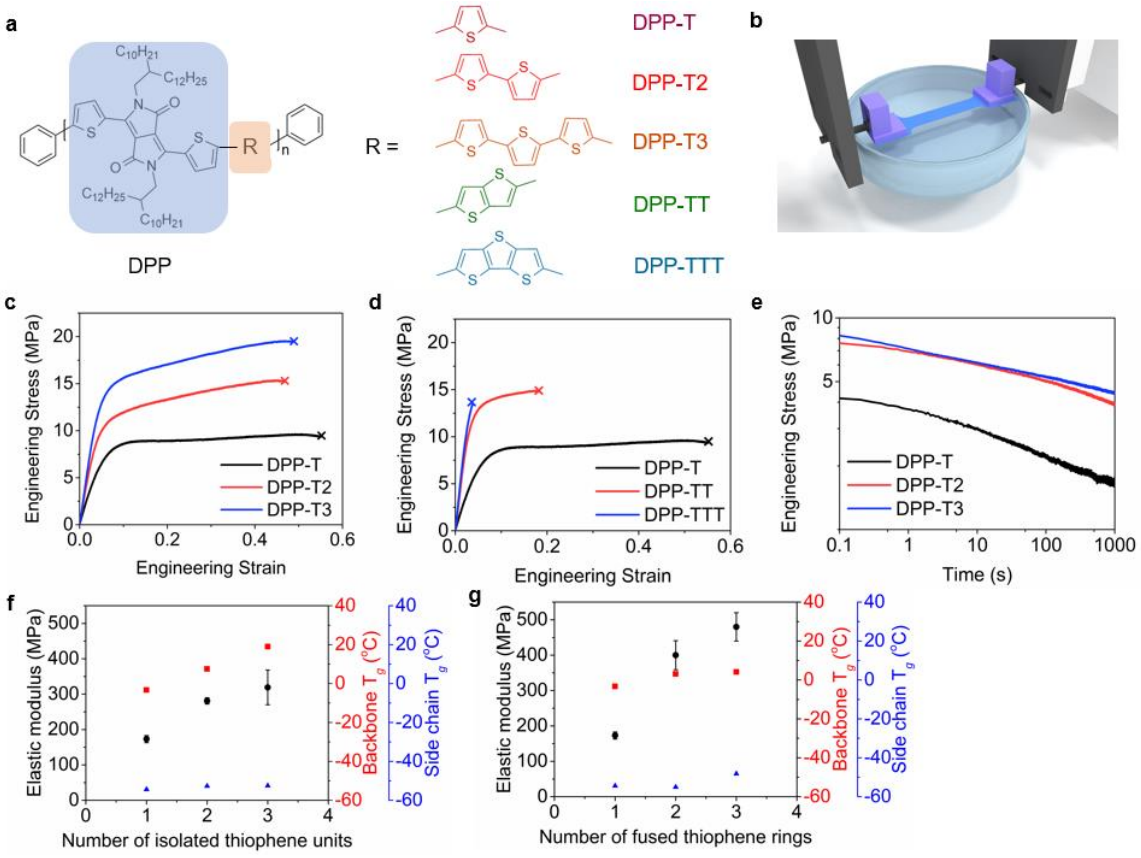

Figure 4.1 *Thin film mechanical property of various DPP polymers. (a) Chemical structures of DPP polymers with different number of isolated thiophene units and fused*

thiophene rings. (b) Scheme of pseudo-free standing tensile test set-up. Comparison of stress strain curves for as-cast DPP-based D-A polymer (M_n ~ 50 kg/mol) films around 90 nm thick. (c) Stress strain curves for thin DPP polymer films with different numbers of thiophene units, DPP-T, DPP-T2 and DPP-T3; and (d) different sizes of fused thiophene rings, DPP-T, DPP-TT and DPP-TTT. (e) Stress-relaxation behaviors of DPP-T, DPP-T2 and DPP-T3. The data is in double logarithmic scale. The speed of decaying represents the speed of relaxation of polymer chain at room temperature. The elastic modulus, backbone and side chain glass transition temperature of DPP polymers are shown in (f) and (g).

The representative stress-strain curves of DPP polymeric thin films with varying electron-donating units in the polymer backbone were shown in **Figure 4.1(c)** and **Figure 4.1(d)**. Each polymer was tested for more than six times and the average value of elastic modulus and crack onset strain were summarized in **Table 4.1**. We first discussed the influence of isolated thiophene units on the thin film mechanics, followed by the fused thiophene units. **Figure 4.1(c)** plotted the stress-strain curve of DPP-T, DPP-T2 and DPP-T3 (see **Figure 4.1(a)** for their chemical structure), which provided a close comparison for their mechanical behaviors. With the increasing number of isolated thiophene units on the backbone, the elastic modulus increased from 173 MPa for DPP-T to 281 MPa for DPP-T2, and 319 MPa for DPP-T3 for ~ 90 nm thin films. At first glance, the observation may seem contradictory since the incorporation of thiophene units into the backbone would be expected to increase the backbone flexibility. Donor-acceptor polymers typically have rigid polymer backbones which are less flexible. Here, we measured that DPP-T polymer chain has a persistence length of ~ 9 nm determined by small angle neutron scattering for dilute polymer in deuterated solvents (**Figure C.1**). Previous report by Segalman group suggested that P3HT has more flexibility, coiled chain with persistence length of ~3 nm.[156] Thus inserting more thiophene units would likely to reduce backbone rigidity. This interesting observation of increased elastic

modulus upon incorporating thiophene units was later rationalized by the T_g of DPP polymers. The observed increase in elastic modulus is closely correlated with the increased T_g measured in both thin film and bulk state of conjugated polymers (discussed in more detail in the later part). On the other hand, the stretchability, using crack onset strain as metric, showed less significant difference among three DPP polymers with different amounts of isolated thiophene units. Pseudo-free standing DPP-T thin films on average can be impressively stretched up to 53% of strain while the other two DPP polymers reached 44% of strain before the formation of cracks. Both crack onset strain reached record-high value compared to other pseudo free standing test results reported previously for pure D-A polymeric thin films (see **Table C.4** for a summary of previously reported values). We attribute this observation to the high molecular weight for these three DPP polymers synthesized here, as well as below room temperature backbone T_g.

In addition to the tensile pulling test, stress-relaxation test provided insights into the viscoelastic property of the conjugated polymer, thus was performed on DPP-T, DPP-T2 and DPP-T3 polymers. The polymer film was stretched to 2% strain at the strain rate of 1×10^{-3} s^{-1} to measure the stress relaxation. The stress was recorded as a function of time and plotted in **Figure 4.1(e)**. The Kohlrausch-Williams-Watts (KWW) equation was used to obtain the relaxation time for molecular chains to gain insights into the chain dynamic.[236] Detailed fitting information can be found in **Figure C.2**. The average relaxation time was 116 s, 3563 s, 6058 s for DPP-T, DPP-T2, DPP-T3, respectively. This is in good agreement with the observed trend for T_g, and further supported that the insertion of the thiophene unit will slow the backbone dynamics.

For DPP polymers with fused thiophene rings on the backbone, the increase in elastic modulus was more distinct, from 173 MPa (DPP-T) to 480 MPa (DPP-TTT), as shown in **Figure 4.1(d)**. In the meantime, the decay in crack onset strain was substantial with increased size of fused rings, from 53% to 3%. This phenomenon agreed well with previous research demonstrating that polymers with fused rings have higher stiffness and higher tendency to break upon tensile strain than polymers with isolated rings.[123]

The molecular weight of the conjugated polymer can greatly influence a given polymer's mechanical property.[44,237] Consequently, we also studied thin film mechanical property for three DPP polymers (DPP-T, DPP-T2, and DPP-TT) with a lower molecular weight (M_n = ~ 25 kg/mol), as opposed to the same DPP polymers with M_n around 50 kg/mol as shown in **Figure 4.1**. We found little difference in the value of the elastic modulus on molecular weight, while higher M_n consistently leads to higher crack onset strain, which can be attributed to increased inter-chain entanglements between DPP chains (**Figure C.3**).[44,179] Surpassing the entanglement molecular weight of a given conjugated polymer is important to enhance its crack onset strain. Although we were not able to measure the critical entanglement molecular weight for DPP conjugated polymers, the mechanical tensile test suggested that critical entanglement molecular weight is likely to be below 50 kg/mol, thus significant intermolecular chain entanglements resulted in good deformability of these three samples reported in **Figure 4.1**.

The effect of thermal treatment on the mechanical property was also investigated. **Figure C.4** showed the stress-strain curves for DPP-T, DPP-T2 and DPP-TT polymers before and after thermal annealing at 200 °C for 10 mins. The elastic modulus increased

slightly by ~ 10% while the stretchability decreased by ~ 20%, due to increased degree of crystallinity upon annealing. The detailed analysis on the thin film morphology will be discussed in the following section.

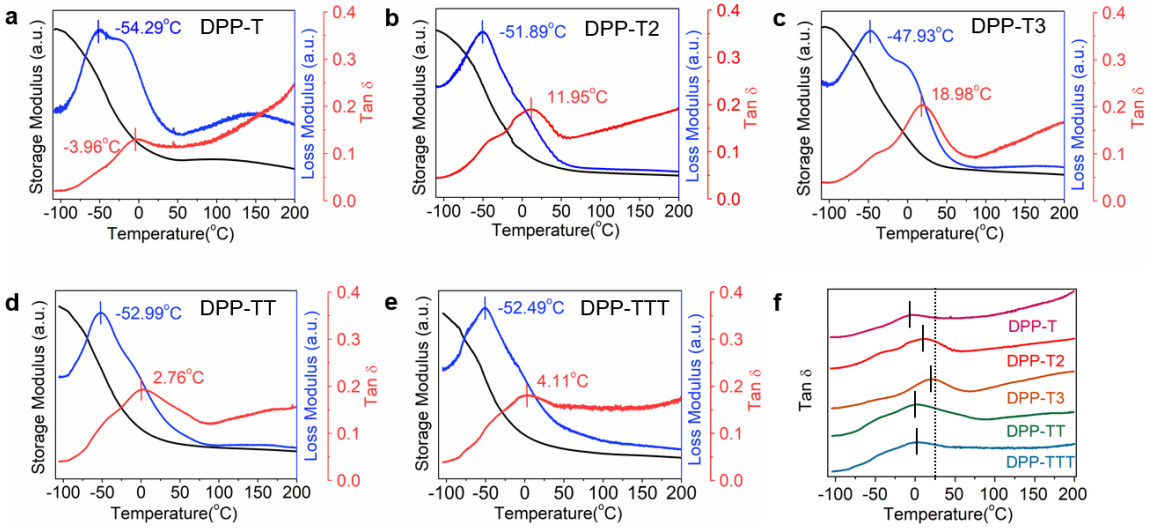

Figure 4.2 *Viscoelastic property of DPP polymers measured by DMA. The storage modulus, loss modulus and tan δ are plotted for (a) DPP-T (b) DPP-T2 (c) DPP-T3 (d) DPP-TT (e) DPP-TTT. The backbone T_g is marked on the transition peak of tan δ. The side-chain T_g is marked on the transition peak of loss modulus. (f) Summary of tan δ curve for five DPP polymers. The vertical dotted line in figure (f) represents the room temperature, or 25 °C.*

To rationalize the change in elastic modulus upon insertion of thiophene building blocks, we measured the T_g for five DPP polymers in both bulk state by DMA and in thin film state by AC chip calorimetry. Previous work indicated the challenge of using DSC to probe weak transitions for conjugated polymers.[238] Thus, we used two techniques that are sensitive to the T_g, and the results were summarized in **Table 4.1**. **Figure 4.2** showed the results for DMA analysis including the T_g of five DPP polymers. Here, we identified the major peak on the tan δ curve as the backbone T_g. We assigned relative weak shoulders around -50 °C to be the T_g of the flexible alkyl side chain, which can be observed in all five polymers. The side chain transition peak was more pronounced as

observed in the loss modulus curve. Only the side chain T_g can be measured by DSC (**Figure C.5**), which agreed with previously reported literature.[226] From **Figure 4.2(a-c)**, we observed a noticeable increase of backbone T_g from -3.96 °C (DPP-T) to 11.95 °C (DPP-T2), and 18.98 °C (DPP-T3) as the number of thiophene units increased (**Table 4.1**). Similarly, when comparing **Figure 4.2(a**, **d**, **e)**, the T_g increased from -3.96 °C (DPP-T) to 2.76°C (DPP-TT), and 4.11 °C (DPP-TTT) as the size of fused ring structure enlarged. The increase in T_g synchronized with the observed increase in elastic modulus. We further used AC-chip calorimetry to characterize the conjugated polymer's T_g in the thin film state. The exact value of T_g is not the same since the glass transition is a kinetic property and highly depends on probing techniques and measurement conditions (e.g., cooling or heating rate). However, the same trend in the probed T_g values was observed using the AC-chip calorimetry (**Figure C.6**). Additionally, we also investigated the molecular weight effect on T_g. DPP polymers with lower molecular weight (~ 25 kg/mol) were tested. The difference in T_g was insignificant with only 3 °C difference being observed (**Figure C.7**), which explained the similar elastic modulus between different molecular weights of polymers observed above. The weak dependence of T_g on molecular weight can be rationalized by the Flory-Fox equation, which predicted this correlation at high molecular weight region.[142,201] Both bulk and thin film techniques suggested the incorporation of the electronic donating group into the polymer structure greatly altered its backbone dynamics, and reflected in their macroscopic mechanical properties.

Although the focus of this paper is not on the electronic property of conjugated polymers, we measured the charge carrier mobility of five samples using thin film

transistors with doped silicon as bottom gate electrode, silicon dioxide as the dielectric layer and evaporated gold as source and drain electrode. We found that all the five polymers showed decent electronic property, ranging from 0.23 ~ 1.09 $cm^2 V^{-1} s^{-1}$ (**Table C.1**). The transfer curve for all the measurements were provided in **Figure C.8**. We also summarized the charge carrier mobility data for previously reported DPP polymers with thiophene units as the donor unit in **Table C.5**. Due to the difference in the molecular weight and processing method, our reported mobility data was not the highest among reported works.

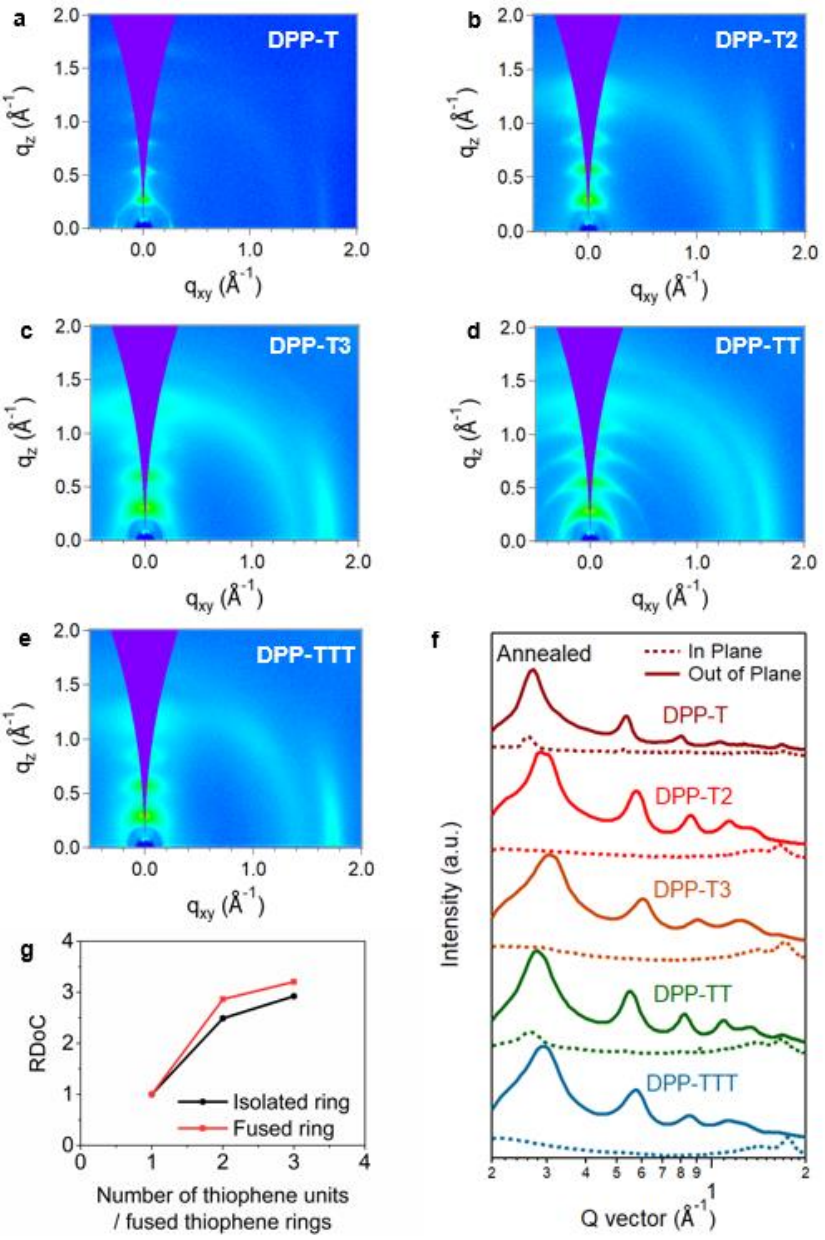

Figure 4.3 *2D GIWAXS pattern of DPP-based polymers after annealing. (a) DPP-T, (b) DPP-T2, (c) DPP-T3, (d) DPP-TT, (e) DPP-TTT. (f) 1D line-cut profiles in both in-plane direction (dotted line) and out-of-plane direction (solid line). (g) RDoC for different polymers with isolated rings (black line) and fused rings (red).*

Table 4.2 *Crystallographic parameters for DPP polymers*

Polymer	Thermal treatment	Lamellar spacing (Å)	Lamellar peak FWHM ($Å^{-1}$)	π-π spacing (Å)	π-π peak FWHM ($Å^{-1}$)
DPP-T	As cast	22.20	0.1106	3.72	0.1799
	Annealed	23.44	0.0249	3.74	0.1315
DPP-T2	As cast	21.89	0.0550	3.74	0.1740
	Annealed	22.20	0.0250	3.77	0.1550
DPP-T3	As cast	20.53	0.0882	3.63	0.2362
	Annealed	20.67	0.0470	3.66	0.1583
DPP-TT	As cast	22.28	0.0519	3.69	0.2331
	Annealed	22.60	0.0367	3.78	0.1194
DPP-TTT	As cast	21.67	0.0833	3.60	0.1397
	Annealed	21.67	0.0430	3.59	0.1233

4.3.2 The relationship between mechanical property and morphology

We used multiple morphology characterization techniques, including GIWAXS, UV-Vis and AFM, to understand the potential correlation between the morphology and mechanical property for the DPP polymers. Firstly, the degree of crystallinity and molecular packing lattice parameter in the crystalline region of five DPP thin films were measured by GIWAXS, before and after thermal annealing. All DPP polymers exhibited semicrystalline structures. The 2D scattering patterns and the 1D line-cut profiles (both in plane and out of plane scattering profile) were shown in **Figure 4.4** for annealed films and **Figure C.9** for as-cast films, respectively. For as-cast polymers, a bimodal orientation, both edge-on and face-on orientation, was shown, as evidenced by (010) π-π stacking peak presented in both in plane and out of plane direction. DPP-T exhibited mostly face-on orientation and less ordered crystalline domain, as inferred from the large full width at half maximum (FWHM) for (100) peak and the absence of high-order

diffraction peaks. In contrast, other polymers showed a preference for edge-on orientation and high-order (h00) peaks. Upon annealing, the fraction of edge-on orientation increased for all polymers, evidenced by much weaker (010) peak along the q_z axis and stronger (010) peak along the q_{xy} axis. Also, improved microstructural ordering was shown, judging from the more intense elliptical shape of (h00) peaks. These observations are similar to previous reports from Zhang *et al*. for DPP-T, DPP-T2, and DPP-TT polymers.[230] The key parameters of chain packing for conjugated polymers were summarized in **Table 4.2**. In this study, the π-π stacking distance showed no obvious trend concerning varied backbone structures, while DPP-TTT has the closest packing distance of 3.59 Å among the five polymers, which could arise from its greater coplanarity due to its large fused ring. On the contrary, the lamellar packing distance showed a clear trend upon systematically varying the main chain structure. With more isolated thiophene units incorporated into the DPP backbone, the d-spacing distance gradually dropped from 23.44 Å for DPP-T to 22.20 Å for DPP-T2, and 20.67 Å for DPP-T3 in annealed samples. Similarly, as the size of fused thiophene rings increases, the lamellar packing distance decreased to 22.60 Å for DPP-TT, and 21.67 Å for DPP-TTT. This is because side chains attached to the DPP moiety can fold into the extra space created by less bulky thiophene units between DPP building blocks (Scheme C.1). A similar observation was reported previously in other conjugated polymer systems.[239,240] The FWHM for the (100) peak increased with the number of thiophene units or the size of fused thiophene rings, which indicated a reduction in the polymer crystallite size. To further quantify the effect of film morphology on mechanical properties, we extracted the relative degree of crystallinity (rDoC) for annealed polymers and plotted in **Figure 4.4**,

detailed procedures to obtain RDoC can be found in **Figure C.10** as well as previous reports by Baker *et al*.[76,241,242] Judged from the (100) pole figures, the relative degree of crystallinity increased in the order of DPP-T < DPP-T2 < DPP-T3, and DPP-T < DPP-TT < DPP-TTT, which is consistent with the trend of elastic modulus. Despite similar RDoC between DPP-T2 and DPP-TT, or between DPP-T3 and DPP-TTT, there is still 50% difference in elastic modulus between two polymers, which could be mostly attributed to the different T_g and backbone rigidity between two polymers. Thus, the RDoC played a secondary role in influencing the mechanical property of the conjugated polymer film, after the T_g.

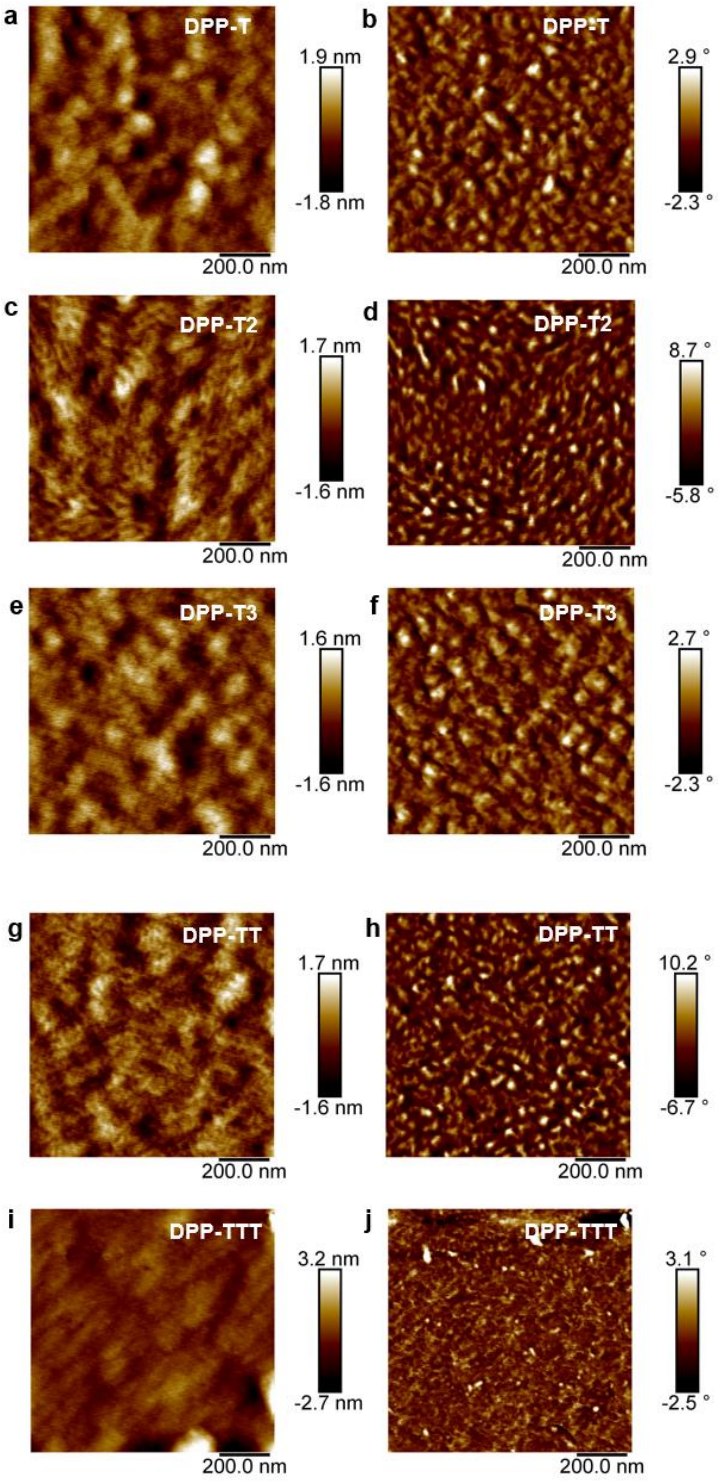

Figure 4.4 *AFM images for annealed polymer films (a,b) DPP-T, (c,d) DPP-T2, (e,f) DPP-T3, (g,h) DPP-TT and (i,j) DPP-TTT. (a, c, e, g, i) are height images, (b, d, f, h, j) are phase images.*

AFM was performed on both as cast (**Figure C.11**) and thermally annealed polymer films (**Figure 4.4**) to study the film morphology using tapping mode. All five samples displayed similar nanofibrillar textures. The film roughness (Ra) for all films was within 1 nm, which can be attributed to their good solubility in chlorobenzene solvent. There is no direct correlation between the mechanical property and surface morphology of conjugated polymers. The UV-Vis absorption spectra were measured in thin film state (**Figure C.12**). It is noted that two absorption bands were presented, corresponding to the π-π* transition (400 to 460 nm) and intramolecular coupling between donor and acceptor units (700 to 850 nm), which is consistent with previous studies on DPP-based conjugated polymers.[226,228] The aggregation behavior was investigated by comparing the relative intensity of peak 0-1 and peak 0-0, the result indicated slight difference in the aggregation behavior for the polymer chain, e.g., DPP-T3 showed 11% decrease in short-range aggregation when compared with DPP-T. The absorption peak positions and peak areas were summarized in **Table C.2** and **Table C.3**, respectively. We did not observe clear correlation between the aggregation state of the DPP polymer films with respective to their mechanical property.

Through the detailed morphological characterization, we found that the crystallinity could increase the fraction of hard-rigid phase in the thin films thus increase their elastic modulus slightly. The degree of order in the amorphous aggregation phase did not influence the apparent elastic modulus which can be attributed to the fact that the probed aggregation order is in the short range (e.g., inter π-π interaction).

4.3.3 Influence of the thiophene block on the backbone T_g

From our experimental results, we found that adding either isolated or fused thiophene rings in the backbone both raised the backbone T_g and consequently the elastic modulus of the polymeric thin film. The glass transition temperature of the DPP polymer upon addition of thiophene building blocks can be estimated by classic Fox equation (Equation 4.1).[243] In this equation, T_g is the glass transition temperature for a given chain, W is the weight fraction of the spicific component in the blend.

$$\frac{1}{T_g} = \frac{W_1}{T_{g,1}} + \frac{W_2}{T_{g,2}} \tag{4.1}$$

Since DPP polymers can be viewed as the DPP unit and the inserted donor unit, the T_g can be treated as the combinatory effect of two individual components. For example, the T_g of DPP-T is -3.96 °C, and the T_g of a polythiophene polymer without side chain was previously determined to be around 120 °C.[162] Upon incorporating one additional thiophene unit, the T_g of DPP-T2 can be calculated to be around 3 °C, and 13 °C for DPP-T3 using Equation 4.1. The calculated result agrees well with experimentally measured T_g for DPP-T2 and DPP-T3. For DPP polymers with fused thiophene rings, we were not able to perform similar calculation since there is no reported T_g of fused thiophene rings.

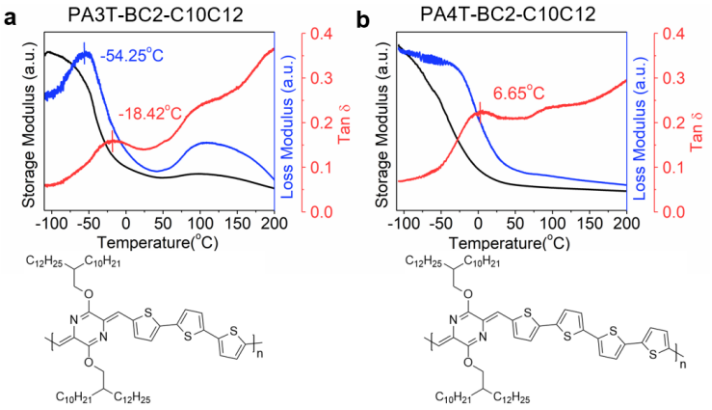

Figure 4.5 *Chemical structures and DMA results for (a) PA3T-BC2-C10C12 and (b) PA4T-BC2-C10C12.*

Besides DPP-based polymer system, the above trend was also observed in the quinoidal *para*-azaquinodimethane (*p*-AQM)-based low-bandgap conjugated polymers.[240] As shown in **Figure 4.5**, the T_g of two polymers (PA3T-BC2-C10C12 and PA4T-BC2-C10C12) with increased number of backbone thiophene units were compared. With one additional thiophene unit inserted into the polymer backbone while maintaining the same side chain length, PA4T-BC2-C10C12 showed 25 °C increase in T_g comparing with PA3T-BC2-C10C12. This observation indicated that the anti-plasticization effect upon inserting thiophene units to the backbone can be a general phenomenon for conjugated polymers.

4.3.4 Engineering low T_g and low modulus DPP polymers

Encouraged by our findings above, we aim to go to the opposite direction by incorporating the low T_g component into the DPP system to reduce its T_g. Another DPP-based polymer was purposely designed and synthesized by incorporating DPP unit with an alkyl chain decorated thiophene unit. The chemical structure and mechanical property of this new polymer (DPP-T3-C8) were shown in **Figure 4.6**. Detailed synthesis of this

polymer can be found in Appendix C. The number average molecular weight of the new DPP polymer is 26.8 kg/mol, with a polydispersity of 2.5. Through introducing additional side chains on the thiophene unit, we effectively increased the weight fraction of the side chain from 58.9% to 64.9%. Consequently, the T_g of DPP-T3-C8 polymer dropped from 18.98 °C for reference polymer DPP-T3 to -11.83 °C. Using this strategy, we were able to reach a record low elastic modulus for DPP polymers down to 150 MPa. Compared to DPP-T3 with a similar molecular weight, the crack onset strain was decreased from 44 % to 35%, representing a 20% of decrease.

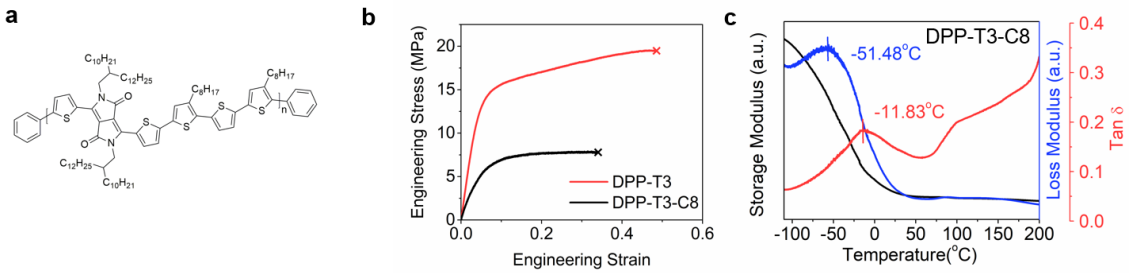

Figure 4.6 *(a) Design of the new DPP-T3-C8 polymer with additional alkyl side chain. (b) Stress-strain curve of the DPP-T3-C8 polymer plotted with the same polymer without side chain. (c) DMA result of DPP-T3-C8 polymer.*

We further surveyed the previously reported work on the DPP polymers with various side chain lengths and listed them in **Table C.5**. There are several popular side chain length choices, 2-hexyloctyl (2-HO), 2-octyldodecyl (2-OD), and 2-decyl dodecyl (2-DD). Those DPP polymers have sixteen carbons, twenty carbons, and twenty-four carbons in the polymer side chain respectively. Using volume fraction of side chain as a measurement metric, the DPP-T3 polymer with three different side chain lengths would have varied weight fractions of the side chain of 55.0% (2-HO), 57.1% (2-OD) and 58.9% (2-DD), respectively. Previously reported DPP-TT polymer, for example, is

mostly focused on the 2-octyldodecyl (2-OD) side chains, thus would result in lower side chain content, high T_g, higher elastic modulus and lower crack onset strain. A systematic study of the side chain length is outside the scope of this work and will be reported in a separate work.

4.4 Conclusions

In summary, we studied the effect of thiophene based electron-rich building block on the thermomechanical property and morphology of semiconducting polymers. Five different DPP-based polymers with isolated thiophene units (DPP-T, DPP-T2, DPP-T3) and fused thiophene rings (DPP-TT, DPP-TTT) were systematically synthesized, their thermomechanical properties were measured and compared. The addition of thiophene units or fused thiophene rings resulted in the increase in the T_g of the polymer measured in both bulk and thin film state and appeared as an increase in its elastic modulus. These behaviors can be related to the addition of high-T_g chemical moieties to the main chain, i.e., reduction in low temperature side chain fraction. This observation can be generally applied to other conjugated polymer systems. Based on the results above, we engineered a new stretchable DPP-based polymer DPP-T3-C8 by increasing the side chain content on the thiophene unit. With the elastic modulus as low as 150 MPa, and T_g of -11.8 °C, the polymer showed 50% decrease in elastic modulus and a stretchability of 35%. Taken together, this study demonstrated that controlling low-T_g side chain content is an efficient way to develop new stretchable conjugated polymers.

CHAPTER V - PREDICTION AND CONTROL OF GLASS TRANSITION TEMPERATURE FOR DONOR–ACCEPTOR POLYMERS

(Adapted from "Zhang, S.; Alesadi, A.; Selivanova, M.; Cao, Z.; Qian, Z.; Luo, S.; Galuska, L.; Teh, C.; Ocheje, M. U.; Mason, G. T.; St. Onge, P. B. J.; Zhou, D.; Rondeau-Gagné, S.; Xia, W.; Gu, X. Toward the Prediction and Control of Glass Transition Temperature for Donor–Acceptor Polymers. *Adv. Funct. Mater.* **2020**, *30* (27), 2002221.")

5.1 Introduction

Past decades have witnessed remarkable progress for performance enhanced organic electronic devices like organic photovoltaics (OPVs) and orgfanic field-effect transistors (OFETs),[9–12] owing to the rapid development of conjugated polymers (CPs), especially recently emerged D-A type CPs.[5,75,205,244] When compared with their inorganic counterparts (e.g. silicon), CPs exhibit solution processability, structural tunability, good electrical performance and mechanical compliance.[45,169,220,221,245–247] Thus, these semiconducting systems have shown great promise in the next-generation electronics through molecular-level engineering, i.e. soft and deformable CPs for wearable and biomedical devices;[169,221] thermal-stable CPs for automotive and aerospace industries.[248,249] A rational design of application-driven CPs requires the new fundamental knowledge to predict, control and manipulate thermomechanical properties of D-A CPs.

Glass transition temperature, or T_g, is an important parameter that characterizes the onset of polymer chain motions. The determination of T_g for a polymer is vital for understanding and controlling over its thermal and mechanical responses. However, the T_g for D-A CPs is hard to detect due to two main reasons. First of all, the only limited

amount of samples (~ 100 mg) is available for a single batch of polymer because of synthetic challenges, which makes a bulk test difficult to perform using oscillatory shear rheometry,[18–20] and dynamic mechanical analysis (DMA).[21,22] Typically, a modified DMA test is applied where the sample is prepared by drop casting polymer solutions onto a glass fiber mesh. Secondly, the semicrystalline nature and rigid polymer backbone of D-A CPs lead to negligible changes in specific heat capacity (ΔC_p) during glass transition, and thus a normal differential scanning calorimetry (DSC) test can hardly detect the backbone T_g.[16,17] To overcome this issue, alternating current (AC)-chip calorimetry[18,19] and fast-scanning DSC[23,250] are applied to determine the T_g of a thin film sample through high frequency scan and heating/cooling rate, respectively. In addition to the thermal property, the understanding of mechanical performance, specifically elastic modulus for D-A CPs still remains challenging. Most recent efforts on investigating the mechanical response of CP thin films were based on the buckling metrology technique using an underlying supporting elastomer layer.[42,109,251] However, a quantitative comparison of reported elastic modulus values from different works is difficult due to the influence of substrate effect, unspecified film thickness and poorly controlled strain rate.[18,137,144] A recently reported pseudo-free standing tensile test or film-on-water (FOW) test has shown great promise in quantifying the mechanical performance of D-A CPs, which provides a substrate-free environment and well-controlled strain rate.[18,53,54] In this work, we use the modified DMA test and AC-chip calorimetry test to separately measure the bulk and thin film T_g. In the meantime, thin film mechanical tests will be performed to further understand the relationship between thermal and mechanical property.

Past efforts on the backbone/side-chain engineering of CPs have demonstrated a qualitative relationship between the polymer structure and the thermal/mechanical properties of CP thin films: stiffer backbones and shorter alkyl side-chains increase both of elastic modulus and T_g of polymers.[45,61,121,252] With the increased number of isolated thiophene units in the backbone of PDPP-based polymers, i.e. from PDPP-T to PDPP-T2 and PDPP-T3, a constant increase in the elastic modulus from 173 to 281 and 319 MPa has been observed from pseudo-free standing tensile test. Their corresponding T_g also rises from -3.96 to 11.95 and 18.98 °C, as tested by DMA.[61] For side-chain engineered isoindigo-based polymers, a steady decrease of elastic modulus from 550 to 250 MPa with increasing alkyl side-chain lengths from C6 to C10 is determined by AFM measurement.[252] Similarly, polythiophenes (P3ATs) with increasing alkyl side-chain lengths have shown lower elastic modulus and T_g, as measured by buckling metrology and DSC, respectively.[121] Such a trend is also demonstrated by a modified coarse-grained model through comparing P3NT and P3DDT, where a reduction in the predicted elastic modulus value from 990 to 780 MPa, and T_g value from 7 °C to -15 °C is shown.[253] Most recent work by Xie *et.al.* shows a simple linear predictive model by connecting the ratio of mobility between conjugated and non-conjugated atoms to CPs' T_g, while the effect of side-chain length on the polymer backbone T_g is not clearly captured.[20] Thus, a quantitative model is in need to predict the thermal and mechanical performances for D-A CPs with various side-chain structures.

Herein, we build a general relationship between the side-chain length, chain flexibility, elastic modulus and T_g to serve for the rational design of new D-A CPs and the prediction of their thermomechanical properties. The PDPP-based D-A CP is utilized

for demonstration due to its high charge mobility.[254] Besides the experimental approaches, coarse-grained molecular dynamics simulation (CG-MD) is utilized to further explore the influence of the segmental structure of D-A CPs on the mechanical properties and T_g at the fundamental molecular level. In particular, coarse-graining provides much improved computational efficiency to study influences of fundamental molecular parameters on the thermomechanical properties of polymers by removing unessential atomistic features of all-atomistic (AA) structures.[255–257]

Both experimental and computational results show a two-stage reduction of elastic modulus and T_g with increasing side-chain length: a rapid near-linear reduction followed by a slowly plateaued region. Next, an empirical mass-per-flexible bond model is proposed to connect the side-chain length to the flexibility of the entire polymer chain, where a linear T_g evolution with increasing chain flexibility is observed. Moreover, a backbone-engineered PDPP-based polymer is designed to elevate backbone T_g, which verifies the observed side-chain length effect as well as the generality of this model. Furthermore, the grafting density effect on T_g is investigated to shed light on the importance of side-chain weight fraction on polymer T_g. This work demonstrates the efficacy of the new model to precisely control the T_g and modulus of PDPP polymers, and provides a rational way to tailor the performance of CPs for their desired applications.

5.2 Experimental

5.2.1 Pseudo-free-standing tensile test

Thin film tensile test is performed by a home-made pseudo-free-standing tensile tester. Details about the tensile stage setup can be referred to our previous publication.[18]

The thin film is first floated on the water surface by dipping into the water to release the PSS (polystyrene sulfonate) layer, then mounted to the aluminum grip of the tensile tester and pulled unidirectionally at a strain rate of $5*10^{-4}$ s^{-1} until the film fractures. The elastic modulus is obtained from the slope of the linear fit of the stress-strain curve using the first 0.5% strain.

5.2.2 Dynamic mechanical analysis (DMA)

A TA Q800 DMA is used to perform DMA measurements by a modified DMA method. Polymer solutions (5 mg/ml) are made and then drop-casted on top of a glass fiber mesh to prepare the samples.[21] The temperature corresponding to the peak of tan δ is determined as the backbone T_g. In strain-controlled mode, temperature ramp experiments are performed at a temperature range of −110 to 150 °C and a heating rate of 3 °C/min with a fixed frequency of 1 Hz. The strain imposed is in the linear regime.

5.2.3 Grazing incidence wide-angle X-ray scattering (GIWAXS)

GIWAXS experiments are performed on beamline 11–3 at the Stanford Synchrotron Radiation Lightsource. Data are collected under helium environment with an incident beam energy at 12.7 keV and an incidence angle of 0.12°. The sample to detector distance is about 300 mm. Diffraction data analysis is performed using the Nika software package for Wavemetrics Igor, in combination with WAXStools.[135,258]

5.2.4 Overview of CG-MD simulations

The force field components of the CG models are defined based on the contributions of the bonded and non-bonded interactions. To capture the non-bonded interactions, standard 12-6 Lennard-Jones (LJ) potential function is utilized:

$$U_{non-bonded} = 4\varepsilon\left[\left(\frac{\sigma}{r}\right)^{12} - \left(\frac{\sigma}{r}\right)^{6}\right] \quad r < r_c \tag{5.1}$$

where σ and ε represent the units of energy and length and the cutoff distance is $r_c = 2.5\sigma$. The cohesive interaction between CG beads is controlled via ε parameter, where for each pair of the CG beads in the backbones $\varepsilon = 1.0$, and for the pairs of chain branching sites and pairs of the side-chains $\varepsilon = 0.5$. All quantities in CG modeling are expressed in reduced (or LJ) units. The potential energy of the bond stretching is defined through a harmonic bonding potential $U_{bond}(r) = K(r - r_0)^2$ where $r_0 = 0.99\ \sigma$ is the equilibrium bond length and $K = 2500\ \ \varepsilon/\sigma^2$ is the stiffness constant, which is consistent with previously investigated branched polymers.[259] The angular potential function which controls the stiffness of the backbone and side-chain is defined via cosine function $U_{angle}(r) = K_\theta[1 + cos(\theta)]$ where K_θ is the angular stiffness constant. For the angles in the backbone, angular stiffness constant is $K_\theta = 1.0\ \varepsilon$, for the angles between chain branching sites and backbone beads $K_\theta = 0.5\ \varepsilon$ and for the angles in the side-chains $K_\theta = 0.2\ \varepsilon$.

All CG-MD simulations of the bulk polymer are performed using the Large-scale Atomic/Molecular Massively Parallel Simulator (LAMMPS) software package.[260] The bulk systems of all models with different grafting densities consist of 100 chains where the backbone of each chain composed of 20 CG beads. All beads of the polymer chain are assumed to have the same mass *m*. Periodic boundary conditions (PBC) are applied in all three directions. An integration time step $\Delta t = 0.005\tau$ where $\tau = \ \sigma(m/\varepsilon)^{1/2}$ is implemented in all the simulations. To equilibrate the system, the total potential energy is first minimized using iterative conjugate gradient algorithm.[261] Then, the equilibration

of the bulk system is continued at the melt state at a high temperature $T = 2.0$ under isothermal-isobaric (NPT) ensemble for the 10^6 time steps with the pressure ramp from the initial 10 to the final 5 in reduced units. Later, the system is further cooled down to the desired temperature with zero pressure for 1.5×10^6 time steps via the NPT ensemble before running for any property calculations. To measure the T_g of the polymer bulk, the simulation is run further under NPT ensemble with zero pressure for a wide range of the temperature. Then, the density of the bulk model is plotted versus the temperature which exhibits two linear regimes and the intersection point of these two lines marks the T_g. The uniaxial tensile simulations are performed to obtain stress-strain relations of bulk polymers at a temperature of 0.2 under a constant strain rate of 5×10^{-4}, where the elastic moduli are determined from the linear slope in the elastic regime up to 3% strain, as shown in the inset of **Figure 5.2 (e)**.

5.3 Results and discussion

5.3.1 Molecular design

In this study, we first aim to achieve fine-tuned thermal and mechanical performances for D-A CPs through side-chain engineering. Four diketopyrrolopyrrole (PDPP)-based polymers are synthesized with systematically increased side-chain lengths from C2C6C8 (2-hexyl decyl) to C2C8C10 (2-octyl dodecyl), C2C10C12 (2-decyl tetradecyl) to C2C12C14 (2-dodecyl hexadecyl) on the DPP core (**Figure 5.1(a)** and **Table D.1**). Next, the side-chain effect on their thermal and mechanical performances are carefully investigated experimentally. To verify the experimental results and gain more insights, CG-MD simulation is employed to probe how side-chain length (M) and grafting density (f) influence mechanical properties and T_g. Informed from the

experiment, a generic bead-spring CG model is employed to preserve the essential structural features of the D-A CPs. Specifically, the CG model of each CP consists of three main components, a linear backbone chain (grey beads), a side-chain branching site (purple beads) and two side-chains connecting the branching site to represent alkyl groups (cyan beads) per grafting (**Figure 5.1(b**)). Specifically, the side-chain length M is represented by the number of cyan beads and grafting density f is determined by the equation:

$$f = \text{number of grafted backbone beads / total number of backbone beads} \quad (5.1)$$

Figure 5.1(b,c) show the snapshots of the polymer chain and the simulation box of the CG polymer model, respectively.

5.3.2 Thermal/mechanical measurements

Firstly, a differential scanning calorimetry (DSC) is utilized to detect the difference in their thermal responses, where the T_g is not evident due to their rigid polymer backbones and insufficient cooling rate, while the melting temperature (T_m) shows a reduction with increasing side-chain length (**Figure D.1**).[16] Such a trend is expected due to the increased weight fraction of low- T_g side-chains in the polymer. Next, a substrate-supported DMA method is utilized to measure polymer T_g followed by previously reported procedures.[21,27,61] The glass transition information is extracted from a tan δ curve, where the main peak close to 0 °C corresponds to backbone relaxation, and the peak shoulder at around -40 °C represents for side-chain T_g (**Figure 5.2(a)** , **Figure D.2**).[21,61] It is observed that the backbone T_g decreases with increasing side-chain length, from 1.88 °C (PDPPT-C2C6C8), to -6.53 °C (PDPPT-C2C8C10), -10.31 °C (PDPPT-

C2C10C12), and -13.26 °C (PDPPT-C2C12C14). Furthermore, an alternating current (AC)-chip calorimetry is applied to measure thin film (around 80 nm) T_g, where the same trend is observed despite different T_g values. This can be attributed to the technique difference and potential confinement effect on T_g measurement between different approaches (**Figure D.3**).[18,26]

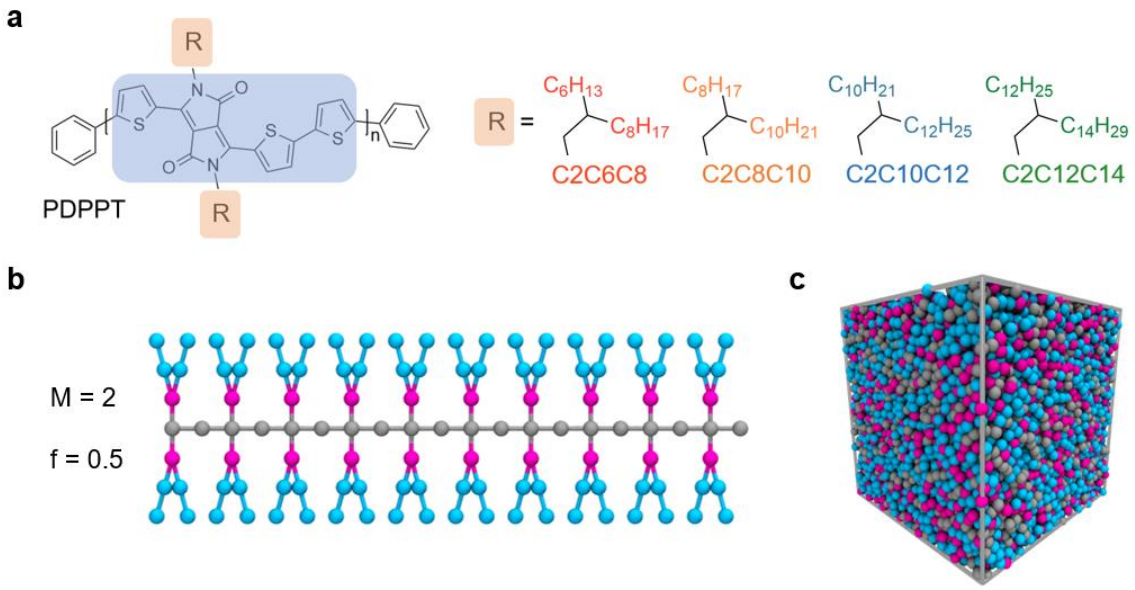

Figure 5.1 *Molecular structure and computational molecular model of PDPPT-based polymers. (a) Chemicals structures of PDPPT-based conjugated polymers. R represents for the side-chain groups attached to the DPP core. (b) Geometrical configuration of simulated polymers with and without branched side-chains. The backbone of all chains is composed of 20 beads (shown in gray). M represents for the number of simulated branched side-chain length (shown in blue). f represents for the grafting density (the branching position is shown in red). (C) A snapshot of coarse-grained model of bulk polymer system.*

The mechanical performance of these polymers is investigated using a pseudo-free standing tensile tester. The polymers are spin coated into thin film state with a similar thickness of 80 nm, then floated on top of the water to avoid the underlying substrate effect, followed by tensile testing at a fixed strain rate of 5×10^{-4} s^{-1}. **Figure 5.2(b)** plots the complete engineering stress-strain curves for all four polymers, which

show a clear difference in their viscoelastic behavior. With increased strain, an elastic region first appears, followed by yielding and strain hardening. Despite slightly different yield strain, the strain-hardening phenomenon for short side-chain polymers is more noticeable with a higher slope, or strain hardening modulus, which can be correlated with their lower chain mobility. What's more, the elastic modulus shows an obvious reduction with increasing side-chain length (**Table D.2**). This phenomenon verifies the direct influence of thermal property on the mechanical response of D-A CPs, shown as a linear relationship between T_g and elastic modulus (**Figure 5.2(c)**). On the other hand, the crack onset strain shows no dependence on the elastic modulus, nor does the side-chain length. We hypothesize that such independence results from their molecular weight difference: For viscoelastic polymers, high mechanical deformation mostly relies on chain sliding, thus the molecular weight plays an important role in determining the extent of elongation.[45] Here, the molecular weights of PDPPT-C2C6C8 (M_n = 88.5 kg/mol) and PDPPT-C2C8C10 (M_n = 76.6 kg/mol) are higher than those of PDPPT-C2C10C12 (M_n = 60.6 kg/mol) and PDPPT-C2C12C14 (M_n = 61.8 kg/mol). Impressively, the PDPPT-C2C8C10 polymer exhibits a record-high crack onset-strain of 105%. To our best knowledge, it is the highest deformability reported for pristine D-A CPs in the literature.

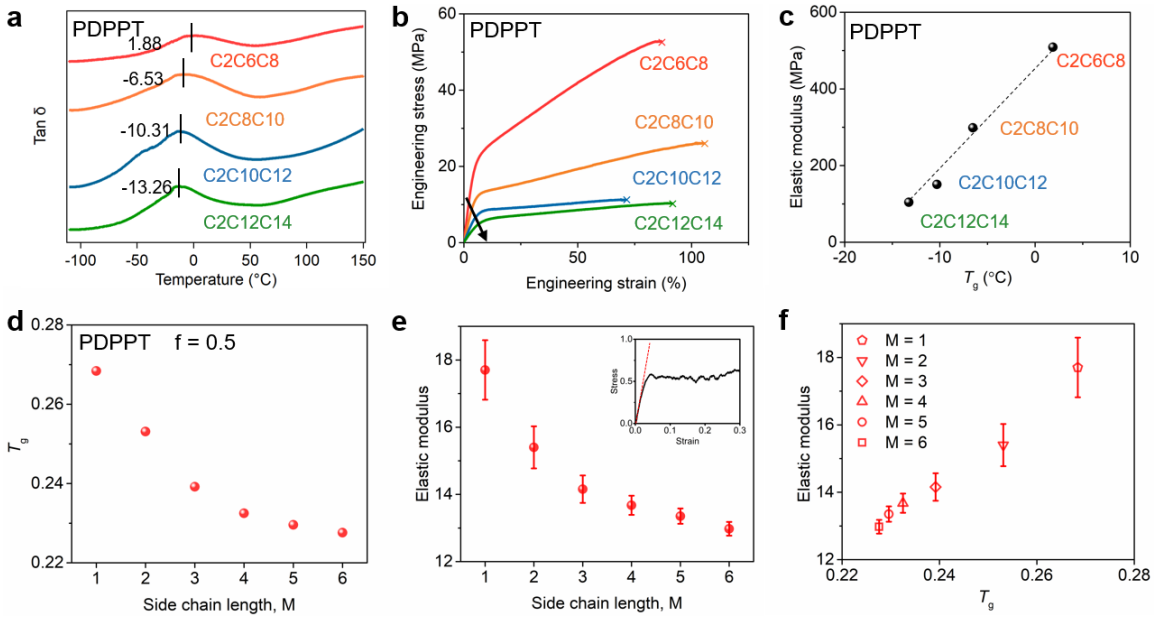

Figure 5.2 *Experimental and simulation results of the thermal and mechanical properties based on PDPP-T polymers with various side-chain lengths. (a-c) Experimental results. (a) Tan δ versus temperature curves extracted from DMA. (b) Engineering stress-strain curves. The arrow direction represents for the decreasing elastic modulus. (c) Summary plot of elastic modulus versus T_g. (d-f) Simulation result. (d) Simulated T_g versus side-chain length M. (e) Simulated elastic modulus versus side-chain length M. Inset shows the stress versus strain curve for M = 2 model. The elastic modulus is extracted from the slope of red dotted line. (f) Simulated elastic modulus versus T_g for polymers with different side-chain lengths. CG-MD simulation results are expressed using the reduced or (LJ) unit.*

5.3.3 Molecular dynamics simulations

Next, we utilize CG-MD simulation to systematically study the mechanical properties and T_g of D-A CPs. As discussed from experimental results, side-chain groups are found to considerably affect the thermomechanical behaviors of polymers. To gain more insights, CG-MD simulations are carried out to investigate the PDPPT models having a grafting density f of 0.5 and side-chain length varying from M = 1 to 6 (**Figure 5.2(d-e)**). **Figure 5.2(d,e)** indicate that the growth of the side-chain length M leads to a sharp decrease in T_g and elastic modulus E of the bulk polymers. It should be mentioned that the results of the elastic modulus are obtained as the average of five different

simulations with independent initial configurations and the error bars mark the standard deviation. For polymer models with a side-chain length $M > 3$, both elastic modulus and T_g of the bulk model tend to reach a plateau – in other words, the reduction rate of these properties decreases with increasing M. **Figure 5.2(f)** plots elastic modulus versus T_g for polymers with varying side-chain lengths, where a near-linear relationship between elastic modulus and T_g can be observed. These results obtained from CG-MD verify the experimental findings, demonstrating that the larger side-chain length leads to a greater reduction in elastic modulus and T_g.

Previous studies have explored the influence of segmental structure and side-chain groups on glass-forming properties of polymers, such as relaxation time, fragility and T_g.[257,262–270] Using the generalized entropy theory (GET), Dudowicz and coworkers[266] have predicted that the stiffnesses of side-chain groups and chain backbone can strongly impact the T_g as well as other characteristic temperatures associated with glass formation of the polymer. For polymers with a flexible backbone and stiff side-chain, the growth of side-chain length is found to increase T_g. However, when flexible side-chains are grafted to relatively stiffer backbones, increasing side-chain length leads to a reduction in T_g. This is largely consistent with the findings of the current study, as the backbone chain of the investigated model system has a relatively higher stiffness compared to the branched side-chains. Similar observations have also been reported in the recent CG-MD study of the star polymers by Fan *et al.*,[271] who showed that increasing the arm length leads to a reduction in T_g as the number of arms exceeding a critical value.

To further explore the influence of the side-chain group on the bulk properties of the current CG polymer model, we next calculate the Debye-Waller factor $\langle u^2 \rangle$, a fast-dynamic property which can be considered as a measure of the local free volume.[272,273] Experimentally, $\langle u^2 \rangle$ can be measured via X-ray and neutron scattering techniques.[274,275] Through MD simulations, $\langle u^2 \rangle$ could be obtained from calculations of mean-squared displacement (MSD) $\langle r^2(t) \rangle = \langle |r_i(t) - r_i(0)|^2 \rangle$ of the CG beads, where $r_i(t)$ is the position of the ith beads at time *t* and $\langle r^2(t) \rangle$ obtained from the average of all the CG beads. Here, $\langle u^2 \rangle$ is defined as the value of MSD at a caging time around 4 for the current model. **Figure 5.5(d)** shows the MSD as a function of time for the models with grafting *f* of 0.35 and different side-chain length at a temperature of 0.2. As it is expected, larger side-chain length *M* exhibits higher MSD values due to the enhanced mobility of chains. Furthermore, **Figure 5.5(e)** shows $\langle u^2 \rangle$ of the models with different grafting density and side-chain length. It is observed that as the fraction of side-chain beads in the bulk polymer model becomes larger, via increasing either *M* or *f*, $\langle u^2 \rangle$ tends to increase – a higher magnitude of $\langle u^2 \rangle$ indicates a greater local free volume associated with segmental mobility. This considerable influence of the grafting density and side-chain length on the T_g can thus be attributed to the enhanced local free volume created by the flexible side-chains according to the well-known free volume argument of Fox and Loshaek.[276] However, this growth of the free volume with *f* and *M* can not be a universal trend for all glassy polymers. As evidenced previously,[266] the relative flexibility of the backbones and side-chain groups governs the side-chain length influence on the free volume and T_g. Current simulation results indicate that the structure of side-chain groups could be interpreted as an important parameter to control the T_g and mechanical properties of the

D-A CPs, which inspires us to propose a physics-based empirical model to predict the T_g of CPs as described next.

5.3.4 Chain flexibility modeling

To quantify the influence of side-chain length on the T_g of D-A CPs, it is vital to understand the interplay between the side-chain length and the polymer chain flexibility. Thus, an empirical mass-per-flexible bond model, first introduced by Di Marzio and Schnider for the prediction of polymer T_g based on the number of mass-per-flexible bond in the repeating unit is employed here, as shown by the following equation:

$$T_g = A\left(\frac{M}{b}\right) + C \tag{5.2}$$

where M is the molecular weight of one repeat unit, b is the number of flexible bonds, A and C are the specific constants representing for the steric hindrance and intermolecular interactions.[277–279] Here, the number of "flexible bond" b, ranging from 0 to 1 will be assigned to each covalent bond in the repeating unit, where 0 represents for an absolutely restricted bond without any rotational or conformational entropy, and 1 stands for a freely rotated bond.

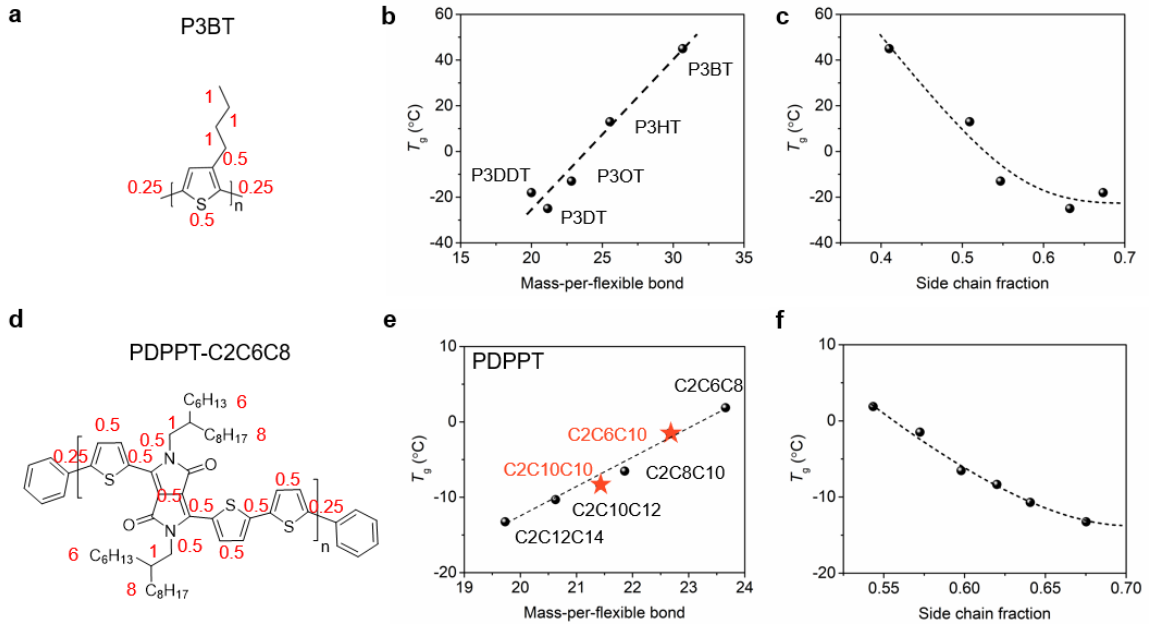

Figure 5.3 *Applying mass-per-flexible bond model to conjugated polymers. (a-c) Polythiophenes. (d-f) PDPPT-based polymers. (a, d) Assignment of number of flexible bonds to polymers. (b, e) T_g over mass-per-flexible bond for polymers with different side-chain lengths. (c, f) T_g over side-chain weight fraction for polymers with different side-chain lengths.*

We first apply the model to the polythiophene polymers with varied side-chain lengths, where the T_g value is obtained from a previous literature.[280] **Figure 5.3(a**) demonstrates the assignment of *b* to different bonds of poly(3-butylthiophene-2,5-diyl) (P3BT). For simplicity, the thiophene ring is given a *b* value of 0.5 due to its limited rotational entropy, so does the single bond connected to the ring structure, while the non-restricted C-C bond on the side-chain has a *b* value of 1. Thus, by plotting $\frac{M}{b}$ with T_g, the influence of chain flexibility on the chain relaxation behavior is obtained, where a linear correlation is shown for polythiophenes (**Figure 5.3(b)** and **Table D.3**). To correlate chain flexibility with side-chain length, **Figure 5.3(c)** plots T_g versus the weight percent of side-chain (wt %), where a two-stage reduction is shown as the side-chain takes up more of the polymer mass and gets closer to unity: a quick T_g drop at lower side-chain

weight fraction followed by a plateau region. This observation is in agreement with the CG-MD simulations above. Using this model, the T_g of PDPPT-based polymers with different side-chain lengths are also plotted versus mass-per-flexible bond in **Figure 5.3(d-e)**, where a similar linear fit is obtained. Next, we aim to apply the model to T_g prediction for new PDPPT-based polymers. Two new polymers with a side-chain length of C2C6C10 (2-hexyl dodecyl) and C2C10C10 (2-decyl dodecyl) are separately synthesized and tested. As shown in **Figure 5.3(e)**, the T_g of both polymers agree with the linear trend (**Figure D.4** and **Table D.4**). **Figure 5.3(f)** shows a steep reduction of T_g with increasing side-chain fraction without obvious saturation, which may suggest that the T_g of PDPPT-based polymers can be further lowered through increasing side-chain length.

5.3.5 Backbone engineering

Besides side-chain engineering, the backbone of CPs is critical for controlling backbone dynamics. Upon introducing an additional high- T_g thiophene unit to the PDPPT backbone, PDPPT2 is purposely engineered for the validation of the proposed model; and to provide a designing method for high- T_g CPs. PDPPT2 with four different side-chain lengths are both experimentally tested and computationally simulated using the same method mentioned above (**Figure 5.4(a, b)**, **Figure D.5**). As shown in **Figure 5.4(c)**, the obtained T_g range expands broadly from 64.69 °C (PDPPT2-C2C6C8) to 25.09 °C (PDPPT2-C2C8C10), 17.22 °C (PDPPT2-C2C10C12) and 1.38 °C (PDPPT2-C2C12C14). This trend follows closely to the simulation result, where the T_g drops with increasing M (**Figure 5.4(d**)). Importantly, the linear T_g -chain flexibility relationship is once again captured by the mass-per-flexible bond model (**Figure 5.4(e**)). The capability

of this model in describing the structure-T_g relationship for different structures of CPs manifests its potential in T_g prediction for other CPs. It is also noticeable that the slope in **Figure 5.4(e)** differs for PDPPT and PDPPT2. Such a difference has been attributed to the intermolecular interactions and structural steric hindrance.[279] However, due to the influence of side-chain length on both intermolecular interactions (π-π stacking distance) and backbone T_g, these contributions are hard to deconvolute (**Figure D.6** and **Table D.5**).

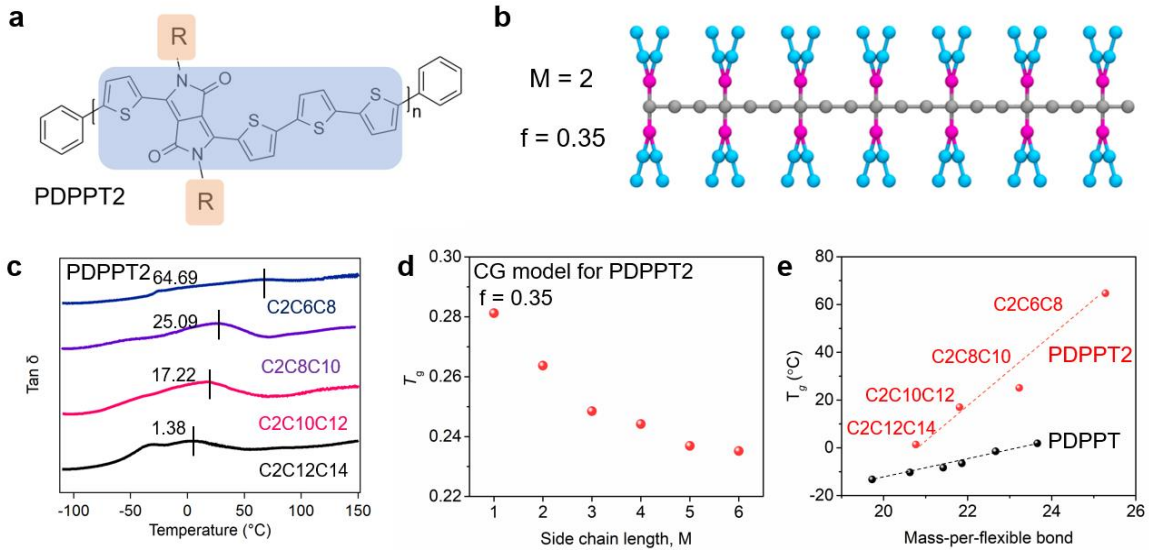

Figure 5.4 *Experimental and simulation results of T_g for PDPP-T2 polymer with various side-chain lengths. (a) Chemical structure. (b) Geometrical configuration of simulated PDPPT2. (c) Tan δ versus temperature curves extracted from DMA. (d) Simulated T_g versus side-chain length M. (e) T_g over mass-per-flexible bond for polymers with different side-chain lengths.*

To facilitate a better understanding, the effect of side-chain grafting density along the polymer backbone is investigated through CG-MD simulations. **Figure 5.5(a)** shows the representative topological configurations of simulated polymer models with varying grafting density *f* by adding more beads in between side-chain substituted backbone beads. Specifically, for *f* = 0.2 model, two potential geometries can be simulated and only

one is shown here due to their similar results (**Figure D.7**). While the trend of T_g reduction with increasing side-chain length holds for all five models, the plateau region for $f = 0.15$ model appears at $M = 3$, but $f = 0.15$ model does not show clear plateau up to $M = 6$ (**Figure 5.5(b)**). Similarly, the T_g drops at different rates with increasing grafting density for various side-chain lengths, where the low-M systems clearly show a steeper reduction but high-M systems are less affected. We attribute these observations to different "saturation limits" of side-chain length fraction for varied systems. In other words, polymer models with larger f (or M) tend to reach the plateaued T_g at smaller M (or f).

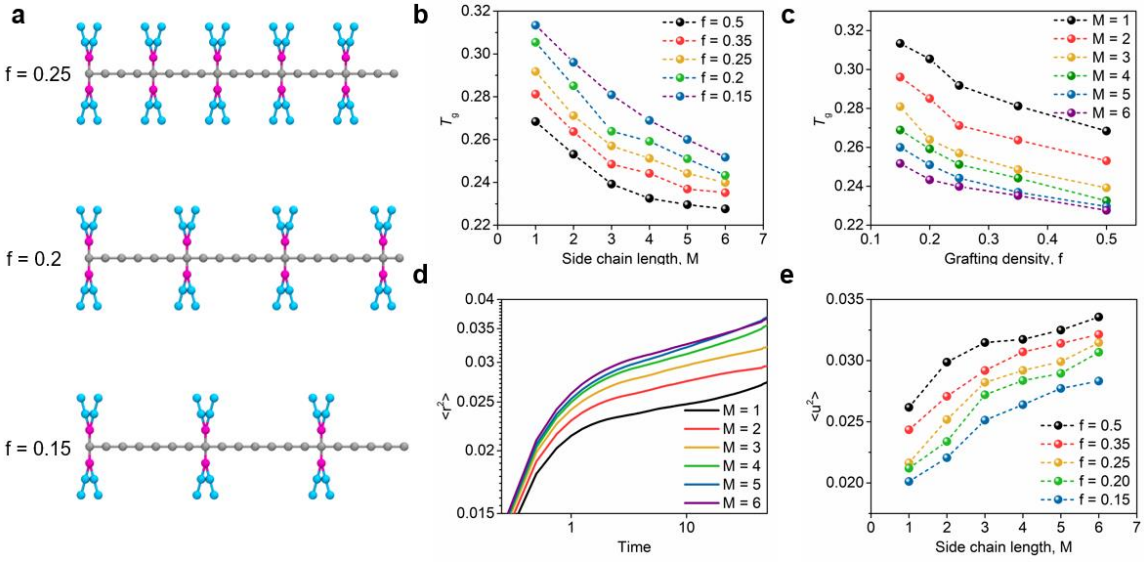

Figure 5.5 *Simulation results of the grafting density effect on the T_g and dynamics of D-A CPs. (a) Topological configuration of simulated polymer chains with different grafting densities. (b) T_g versus side-chain length M for six polymers with different grafting densities f. (c) T_g versus grafting density f for polymers with different side-chain lengths M. (d) Segmental mean-squared displacement (MSD) of the polymer model with f of 0.35 grafting density for different side-chain lengths M. (e) Debye-Waller factor $\langle u^2 \rangle$ versus side-chain length M for polymers with different grafting densities f and side-chain lengths M.*

Here, the quantitative mass-per-flexible bond model demonstrates a linear relationship between chain flexibility and polymer T_g. In the meantime, the CG-MD simulation study shows a two-stage T_g reduction with side-chain fraction until reaching a plateaued T_g. Moreover, as the side chain grafting density increases, the plateaute T_g reduces without a crossing over point. It should be noted that for a polymer with sufficiently long side-chain length, the linear relationship built by the mass-per-flexible bond model may be no longer valid. This is because as the side chain length exceeds a threshold, the side-chain becomes stiff enough that the number of flexible bond per CH_2 moiety on the chain end slowly approaches 0. Similarly, we hypothesize that as the distance between side-chain end and backbone reduces to a certain limit, the rigid backbone could restrict the side-chain flexibility and backbone T_g will be less influenced by side-chain length. Thus it is tricky to attribute the number of the flexible bond to short side-chains as well.

While long and branched side-chains are ususally necessary for solubilization purposes, the proposed empirical model still provides theoretical limits and practical guidance to new polymer designs despite these limitations. For example, the T_g for PDPPT polymer has a lower limit of -37 °C and a high limit of 284 °C. Such understanding can help to guide the material selection for applications from wearable electronics to thermal-stable OPVs. To build a new mass-per-flexible bond model for a different D-A CP system, it is required to experimentally measure the T_g of polymers with several side-chain structures. In the meantime, for backbone engineered polymers with various soft or stiff moieties, the number of flexible bond for the specific moiety can be tuned to fit the linear model. Similar studies along this line can refer to the effective

atomic mobility theory recently proposed by Xie *et al*.[20] For the polymers reported here, although this theory captures the linear relationship between side-chain length and T_g, it does not provide a satisfactory prediction, as shown in **Figure D.8**.

5.4 Conclusions

In summary, we develope a new model for predicting T_g of side-chain engineered D-A CPs, thus controlling their elastic modulus. This model is tested and verified by using both P3ATs and PDPPT-based polymers, where the T_g of newly engineered PDPPT polymers can be predicted. CG-MD simulation further supports the experimental observations on the side-chain length dependence of polymer T_g, and provides insights into the influence of side-chain group and grafting density on the chain mobility. Overall, this work presents multi-perspective T_g -controlling methods, and the polymers engineered here exhibit a wide T_g and elastic modulus span over 80 °C and 400 MPa, respectively. We expect these methods to provide guidance towards the application-driven materials-by-design for D-A CP via molecular engineering, i.e. high T_g and stiff polymers, low T_g and soft polymers; as well as shed light on the future development of newly engineered D-A CPs with tailored thermomechanical performance.

CHAPTER VI - MOLECULAR ORIGIN OF STRAIN-INDUCED CHAIN ALIGNMENT IN PDPP-BASED SEMICONDUCTING POLYMERIC THIN FILMS

(Adapted from "Zhang, S.; Alesadi, A.; Mason, G. T.; Chen, K-L.; Freychet, G.; Galuska, L.; Cheng, Y-H.; St. Onge, P. B. J.; Ocheje, M. U.; Ma, G.; Qian, Z.; Dhakal, S.; Ahmed, Z., Wang, C.; Chiu Y-C.; Rondeau-Gagné, S.; Xia, W.; Gu, X. Molecular origin of strain-induced chain alignment in PDPP-based semiconducting polymeric thin films. *Under Review.* **2021**.")

6.1 Introduction

Flexible and wearable electronics that are conformable to soft surfaces like human skin have raised tremendous research attention.[45,97,220,246,281] Semiconducting polymers are unique species due to their high electrical performance, solution processability, and intrinsic mechanical stretchability.[4–8] Previously, many efforts have been made to improve their charge transport by enhancing the polymer chain alignment.[75–82] Both mechanical stretching and shear coating methods have shown promise in increasing the charge carrier mobility along the alignment direction for semiconducting polymers, especially on traditional conjugated polymers like poly(3-hexylthiophene) (P3HT).[81,82,253,282–285] Strain-induced chain alignment, however, is still less explored for the emerging high-performance donor-acceptor (D-A) type conjugated polymers with much more rigid polymer backbones. The fundamental understanding of the tensile alignment-morphology-performance relationship is vital for future wearable electronics applications.

The deformation mechanism for polymers under tensile draw are well documented in literature.[286–291] However, those knowledges cannot be directly applied to

semi-rigid conjugated polymers. While traditional semicrystalline polymer polyethylene (PE) has a persistence length (l_p) of 9.1 Å that can easily fold, the backbone of conjugated polymers is more rigid with alternating single-and double-bonds.[292] For example, P3HT has an l_p of 3 nm, and it requires 7~8 consecutive thiophene rings in a *sync* conformation to turn 180°.[156,292,293] For D-A polymers with large fused rings in the backbone, they are even harder to bend (*i.e.*, l_p (poly(diketopyrrolopyrrole-co-dithienylethene[3,2-b]thiophene) (PDPPDTT)) ≈ 8 nm).[294,295] Thus, the molecular picture of D-A polymer chains is more likely to be semi-rigid rods that are hard to entangle with each other.[100,296,297] Under the thin-film state, conjugated polymers typically display a complex 3D heterogeneous semicrystalline microstructure with three main characteristic domains: crystalline region, local aggregate, and amorphous region. The crystalline domain consists of layers of lamellae with flexible side chains serving as "spacer" in between. Inside of each lamella is stacked polymer backbones through interchain π-π interaction. Previous studies also suggest these crystalline domains are connected through "tie-chains" that are able to bear load and transport charges.[4,298–300] Local aggregates are also described resulting from intrachain and interchain excitonic coupling, namely J- and H-aggregates, respectively.[301] Furthermore, the amorphous domain containing tie chains, loops, and dangling chain ends is subdivided into mobile and rigid amorphous fractions (MAF, RAF), which can be differentiated through calorimetry methods.[23,302] Thus, multiple techniques are required to deconvolute the contribution from these intertwined domains to understand the effect of macroscopic deformation on thin-film morphologies, as well as final thin-film device performance.

For PE with well-defined crystalline regions, the polymer chain deformation mechanism has been studied through transmission electron microscopy (TEM), small-angle neutron scattering (SANS), and hard X-ray scattering (with photon energy > 8 keV), including both small- and wide-angle X-ray scattering (SAXS/WAXS).[286–291] Specifically, TEM provides local atomic/nanometer-level resolution; WAXS is capable of analyzing averaged crystallite orientation, size, and packing distance at a similar size scale; SANS and SAXS can detect averaged long-range order ranging from 1 nm to hundreds of nm. However, the scattering technique is limited to the detection of ordered crystalline regions. Instead, spectroscopy can detect polymer chains in both amorphous and crystalline regions that are sensitive to atomic-level bond motion, twisting, or orientation based on the specific light characteristics. For example, polarized variable angle spectroscopic ellipsometry (VASE), polarized Infrared (IR) spectroscopy/Raman spectroscopy/Ultraviolet-visible (UV-vis) optical absorption spectroscopy, and near-edge X-ray absorption fine structure (NEXAFS) techniques have been applied to investigate polymer chain orientation upon shear/tensile alignment.[76,80–82,253,282,283,303,304]

To facilitate a better understanding of molecular mechanisms, computational techniques, such as molecular dynamics simulations, have been increasingly utilized to explore complex behaviors of polymers. In particular, coarse-grained molecular dynamics (CG-MD) simulation allows for “bottom-up” investigations of polymer systems over extended spatiotemporal scales by reducing degrees of freedom and elimination of non-essential atomistic details.[253,255,256,305,306] Over the last few decades, the CG-MD approaches have been broadly applied to explore the influences of fundamental molecular parameters on the thermomechanical behaviors of polymers with

different segmental/chain structures at bulk and confined states.[269,307–309] The semi-crystalline morphology of PE under uniaxial tension has been explored via CG-MD methods. It was shown that polymer chains tend to align in the deformation direction, where the large extension and orientation of the chains were found to affect the crystallization and facilitate the primary nucleation.[310] In another study, a chemistry specific CG model was developed to predict the thermomechanical properties of poly(3-hexylthiophene) (P3HT) polymer, where the degree of backbone chain alignment in the bulk state was found to increase with the applied uniaxial strain.[253]

Herein, we performed a detailed study on the chain deformation mechanism for a series of side-chain engineered diketopyrrolopyrrole (DPP)-based semi-flexible D-A polymers. We started with thin-film tensile tests and CG-MD simulations to explore the fundamental mechanism of the macroscopic deformation process. Next, wide/small-angle hard X-ray scattering, wide-angle tender X-ray scattering, polarized UV-vis spectroscopy, NEXAFS, and atomic force microscopy (AFM) were applied to investigate the microstructural chain alignment upon thin-film deformation, which was further confirmed by the CG-MD simulations. Later, organic field-effect transistors (OFETs) were fabricated to test the effect of strain-induced chain alignment on device performance. This work provides the first in-depth molecular picture of the D-A conjugated polymer's under tensile deformation, thus shed light on the future development of deformation semiconducting polymers.

6.2 Experimental

6.2.1 Materials and processing

All four PDPPT-based polymers were synthesized following previously reported methods.[61,230,233] The number-averaged molecular weight was measured by high-temperature gel permeation chromatography (HT-GPC) using trichlorobenzene as the eluent at 160 °C, polystyrene for calibration, viscometer, and light scattering as the detectors. All four polymers were dissolved in chlorobenzene with a concentration of 15 mg/ml upon stirring on the hot plate at 80 ºC overnight. A commercially available water-soluble poly(sodium 4-styrenesulfonate) (PSS) was dissolved in deionized water and coated on the bare silicon wafer with a thickness of 30 nm. Then the solution was spin-coated on the PSS-coated silicon substrate at 1000 rpm/s to form a 100 nm thin-film. Thermally annealed samples were prepared in the glove box through post-heating as-spun films on the hot plate at 200 ºC for 1 h. The film thickness was measured by AFM using step height between film and substrate.

6.2.2 Tensile deformation of 100nm thin-film sample

Dog-bone shaped thin films with a gauge length of 8 mm and 3 mm width were fabricated by laser etching. Next, thin-film dog-bones were floated on top of the water and stretched at a strain rate of $5*10^{-4}$ s^{-1} to a target strain value using a previously described method.[18,54,61] Next, aligned thin-film samples were transferred from the water to a washer to obtain free-standing thin films.

6.2.3 Morphological characterization

Both hard and tender X-ray scattering experiments were performed at NSLS-II Beamline 12-ID.[311] The hard X-ray has an energy of 16.1 keV, while the tender X-ray has energy from 2.45 keV to 2.5 keV with a spacing of 2 eV. The wide-angle X-ray scattering (WAXS) signal was captured by a Pilatus 300K-W detector, consisting of

0.172 mm square pixels in a 1475 × 195 array, mounted at a fixed distance of 0.275 m from the sample position. To cover the range of scattering angles desired, the vertically oriented elongated detector was moved horizontally on a fixed arc at three angles: 0°, 6.5°, and 13°. The images were later visualized in Xi-CAM software and stitched using custom code.[312] The small-angle X-ray scattering (SAXS) signal was obtained simultaneously with the WAXS data with a Pilatus 1M detector. The sulfur fluorescence yield is obtained from the high-q intensity from 2D scattering images. The solid-state UV-vis spectra were recorded on Agilent Cary 5000 using polymer thin films using polarized light with an angle of 0° and 90° to strain direction. The NEXAFS measurement was performed in the advanced light source (ALS) at Lawrence Berkeley National Laboratory using beamline 11.0.1.2. polarized soft X-rays with polarization angles of 0° and 90° to strain direction were used with an energy range from 0.27 keV to 0.4 keV to collect the absorption signal. RSoXS experiments were performed with an X-ray energy of 285.2 eV based on the NEXAFS result. The scattering data was collected with a sample-to-detector distance of 150 mm to give a q range of 0.001–0.015 $Å^{-1}$.

6.2.4 OFET fabrication

A 300 nm SiO_2 layer with capacitance per unit area = 10 nF cm^{-2} as gate dielectric was thermally grown onto the highly n-type doped Si substrates. The wafers were cleaned with compressed nitrogen air. The clean substrates were modified with an OTS self-assembled monolayer. The OTS-modified Si substrates were cut into 1.6 cm × 1.6 cm squares. Next, strain-aligned PDPPT-C2C8C10 polymer thin films were transferred from water to the substrate. The source and drain electrodes were deposited as Cr (5 nm) and Au (70 nm) through a shadow mask. The channel length (L) and width

(W) were 50 and 1000 μm, respectively. For P3HT, polymer solutions (3 mg/ml) were prepared in chloroform. The solution was dropped onto the OTS-modified Si substrate then spin-coated at 1000 rpm for 1 min. The soft PDMS (20:1 base to cross-linker ratio by mass) slabs (4 cm × 0.5 cm) were used to transfer the polymer thin films. The polymer/PDMS active layers were directly laminated onto source/ drain electrode-deposited devices after different tensile strain was applied. All of the electrical characteristics of the stretched polymer active layers were measured with a Keithley 4200 semiconductor parameter analyzer at room temperature under a nitrogen atmosphere.

6.2.5 Simulation overview

The force field parameters of the CG models were determined based on the contributions of the bonded and non-bonded interactions. The non-bonded interactions were implemented via standard 12-6 Lennard-Jones (LJ) potential function, $4\varepsilon\left[\left(\frac{\sigma}{r}\right)^{12}-\left(\frac{\sigma}{r}\right)^{6}\right]$, where σ and ε represented the units of energy and length, and the potential was truncated at a cut-off distance of $r_c = 2.5\,\sigma$. For the CG-MD simulations, all quantities were assumed to be in reduced (or LJ) units. The cohesive energy between particles was regulated via ε parameter, where for each pair of the CG beads in the backbones $\varepsilon = 1.0$, and the pairs of the side groups $\varepsilon = 0.5$. The potential energy of the bond component was defined through a harmonic bonding potential $U_{bond}(r) = K(r - r_0)^2$ where $r_0 = 0.99\,\sigma$ is the equilibrium bond length and $K = 2500\ \varepsilon/\sigma^2$ is the constant, which is consistent with other investigated branched polymers[259]. The angular potentials which control the stiffness of the backbone and side-chain were defined through a cosine function $U_{angle}(\theta) = K_\theta[1 + \cos(\theta)]$ where K_θ stands for the angular stiffness constant. For the

backbone angles, stiffness constant of $K_\theta = 1.0\ \varepsilon$ was assumed where the fused rings were expected to show much higher rigidity comparing to alkyl side groups. For the angles between chain branching sites and backbone beads $K_\theta = 0.5\ \varepsilon$ and for the angles in the side-chain stiffness constant of $K_\theta = 0.2\ \varepsilon$ were defined. All CG-MD simulations were performed using the Large-scale Atomic/Molecular Massively Parallel Simulator (LAMMPS) software package.[260] The bulk systems of the model consisted of 100 chains where the backbone of each chain composed of 30 CG beads, and side-chain lengths of 4 (M = 4) were grafted to the backbone. Periodic boundary conditions (PBC) were applied in all three directions, and an integration time step $\Delta t = 0.001\tau$ was adopted in all simulations. For the equlibration of the system, the total potential energy was first minimized using iterative conjugate gradient algorithm.[261] Then, the equilibration of the bulk polymer model was continued starting at a high temperature $T = 2.0$ under isothermal-isobaric (NPT) ensemble for the 10^6 time steps where the pressure linearly ramped from the initial 10 to the final 5 in reduced units. Next, the model was further cooled down to the desired temperature via NPT under zero pressure for 1.5×10^6 time steps before running for any property calculations. The uniaxial tensile test was performed to obtain the deformation trajectory of the bulk polymer system at a temperature of 0.2 under a constant strain rate of 5×10^{-4}, which is consistent with previously investigated LJ polymer models.[313,314]

6.3 Results and Discussion

6.3.1 Mechanical alignment

In this work, four poly(diketopyrrolopyrrole-co-thiophene) (PDPPT)-based D-A polymers with increasing side-chain lengths from 2-hexyl decyl (C2C6C8) to 2-octyl

dodecyl (C2C8C10), 2-decyl tetradecyl (C2C10C12), and 2-dodecyl hexadecyl (C2C12C14) were synthesized followed by previously reported procedures (**Figure 6.1(a)**).[187] Their molecular weights and polydispersity were summarized in **Table 6.1**. All four polymers were spun cast on the silicon substrate to fabricate thin films with a thickness around 100 nm, followed by tensile testing on the water surface using a previously reported pseudo-free-standing tensile tester, or film-on-water (FOW) tester.[18,54,59,61,187] **Figure 6.1(b)** plotted true stress (σ_T) - true strain (ε_T) curves of the four polymers, with optical images of PDPPT-C2C8C10 thin films at two strains highlighted to show the deformation behavior. It is also observed that polymers with shorter side-chain lengths are easier to deform along the width direction, i.e., a more evident Poisson effect (**Figure 6.1(b)**).

Table 6.1 *Polymer characteristics for four PDPPT-based polymers*

Polymer	M_n (g/mol)[1]	Dispersity[1]	Elastic modulus (MPa)	T_g (°C)
PDPPT-C2C6C8	88.5	4.09	509 ± 17.8	1.88
PDPPT-C2C8C10	76.6	3.27	299 ± 23.3	-6.53
PDPPT-C2C10C12	60.6	2.44	151 ± 21.1	-10.31
PDPPT-C2C12C14	61.8	2.97	104 ± 9.5	-13.26
Note: [1]The number-averaged molecular weight (M_n) and dispersity were obtained through high-temperature gel permeation chromatography, as described in the experimental section.				

All four polymers demonstrated similar viscoelastic stress-strain behaviors with three regions: an initial linear elastic response, mechanical yielding, and strain hardening. Further plastic deformation led to permanent mechanical failure. It was found that polymers with a longer side-chain length exhibited lower elastic modulus (E) due to reduced glass transition temperature (T_g) (**Table 6.1**); fracture strain was not directly affected by the side-chain length while molecular weight effect was more dominant, as

demonstrated in our previous work.[61] The mechanical yielding point was not evident due to the smooth transition in the stress-strain curve and can be extrapolated from the slope difference before and after yielding (**Figure 6.1(b)**). Interestingly, the strain softening behavior was not seen in all four polymers, while it existed in most traditional polymers like polystyrene and PE.[315,316] The strain-softening behavior in polymer glass was attributed to mechanically generated disorder, while for semicrystalline PE, crystallographic deformations like chain slip, martensitic transformation, and potential cavitation are the main causes.[287,289,290] Thus, the lack of strain softening in PDPPTs could result from limited mechanical disorder and different crystallographic deformation from PE.[4]

Importantly, strain hardening was observed with continuously increased slope at around ε_T > 0.35, while increased side-chain length led to a less obvious hardening behavior. The degree of strain hardening could be represented by strain hardening modulus G_R, which can be affected by the distance between T_g and testing temperature (T - T_g), the entanglement density of the amorphous phase, and the existence of highly stretched and oriented chains.[315,317,318] Meanwhile, the degree of crystallinity was found to play a negligible role in strain hardening modulus (G_R) of semicrystalline polymers.[315,318,319] Since D-A polymer chains are relatively rigid, the traditional Gaussian network theory of entropic elasticity cannot be applied here. Instead, we performed temperature-dependent FOW tensile tests on PDPPT-C2C8C10 at 20 ºC, 30 ºC, 40 ºC, and 50 ºC to investigate the temperature effect (**Figure E.1(a)**). The role of crystallinity was analyzed through testing thermally annealed PDPPT-C2C8C10 under three temperatures (80 ºC, 140 ºC, and 200 ºC) (**Figure E.1(b)**). It can be found that the

strain hardening region was slightly affected at a higher testing temperature, while the degree of crystallinity showed negligible influence. Thus, we attribute the various strain hardening behavior of these four side-chain engineered polymers to the entanglement density difference: the entanglement density of amorphous chains decreases with increased volume taken by the solubilizing side chains.

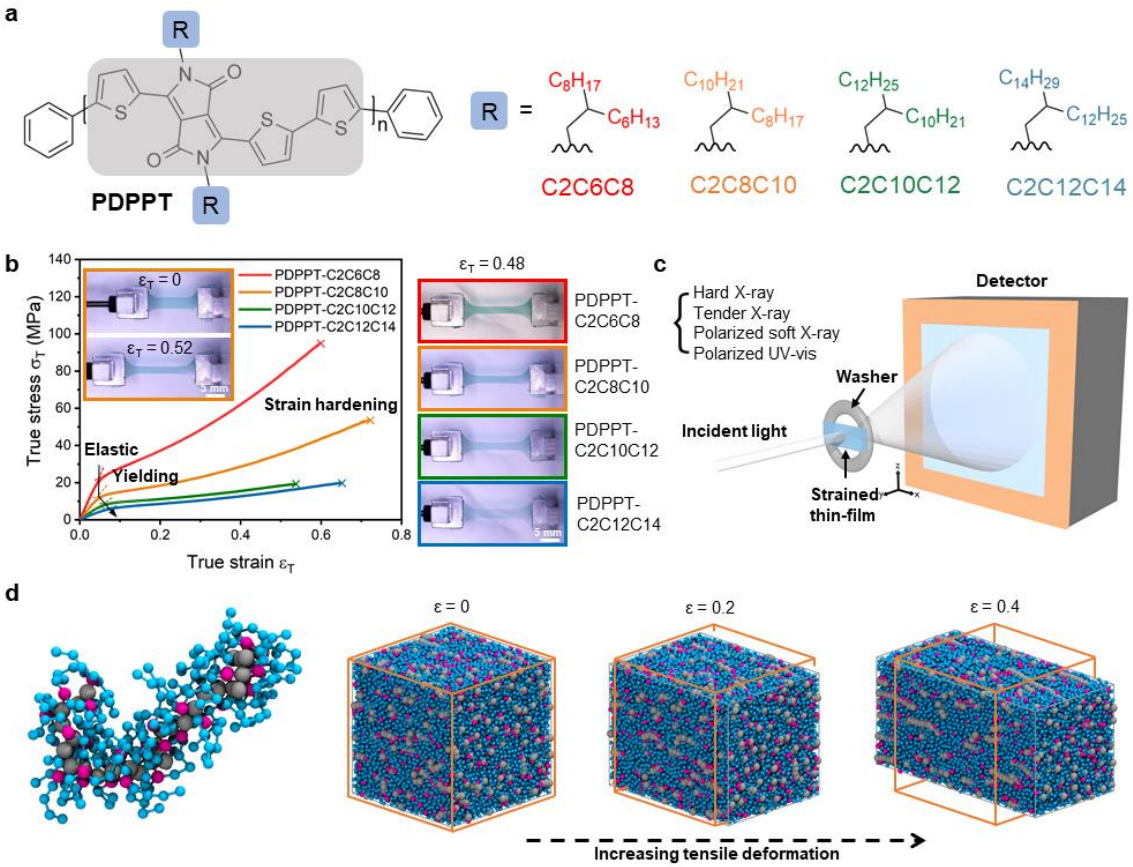

Figure 6.1 *Molecular picture and characterization methods for PDPPT-based polymers (PDPPT-C2C6C8, PDPPT-C2C8C10, PDPPT-C2C10C12, PDPPT-C2C12C14). (a) Schematics of PDPPT polymers with different side-chain structures. (b) True stress-strain curves for four polymers and representative optical images under different strain. (c) Schematic of multimodal morphological characterization tools on tensile strained free-standing thin films. (d) Snapshots of a single representative chain and the CG bulk polymer model under deformation.*

6.3.2 Morphological measurements

After strain alignment, multimodal characterization methods were applied to aligned thin films to understand the molecular-level chain alignment mechanism in a transmission geometry (**Figure 6.1(c)**). The sample was transferred from the water onto a hollow metal washer, followed by air drying (**Figure E.2**). In parallel with experiments, CG-MD simulations of tensile deformation were carried out to explore the chain alignment of conjugated polymers in a bulk system. **Figure 6.1(d)** showed a representative CG model of polymer chain informed from PDPP and several snapshots of the deformed simulation box at different strains.

Based on the above mentioned three tensile test regions, the molecular orientation was investigated by several morphological characterization tools at five true strains: $\varepsilon_T =$ 0, 0.18, 0.34, 0.47, 0.59. Transmission wide/small-angle hard/tender X-ray scattering, polarized UV-vis absorption spectroscopy/transmission NEXAFS, and atomic force microscopy (AFM) were applied to detect different regions of interest in the polymer thin-film. Namely, bulk averaged crystallite orientation; bulk averaged whole chain orientation; and chain orientation on thin-film surface. To provide a fair comparison of chain alignment and anisotropy determined by different techniques, a two-dimensional (2D) Herman's orientation parameter *f* was introduced by prescribing that chain orientation takes place in a 2D plane, owing to the semi-rigid nature of PDPPT polymer chains:[78]

$$f = 2 < \cos^2\theta > -1 \tag{6.1}$$

where θ is the angle between polymer chain orientation and deformation direction. For clarity purposes, the molecular orientation of PDPPT-C2C8C10 polymer was first discussed, followed by comparisons with the other three polymers.

6.3.2.1 Wide/Small-angle hard X-ray scattering

The X-ray scattering technique was applied to detect the amount, size, and orientation of crystallites within the illumination volume (blue color in **Figure 6.2(a)**). The x-axis stands for the strain direction. Typically, three representative packing directions that are orthogonal to each other can be differentiated: (100) lamellar packing, commonly known as the distance between layered side-chain regions; (010) π-π packing, the distance between adjacent stacked polymer backbones; (001) backbone packing, the distance between two alternating electron donors/acceptors along a polymer backbone. Additionally, an amorphous halo was commonly observed for conjugated polymers. While its origin was still unknown, past works attributed it to an averaged intermolecular distance of amorphous polymer chains or unoriented alkyl side-chain packing.[320,321] A comprehensive understanding of crystallite orientation requires an analysis of all the peaks above.

Figure 6.2(b) showed 2D scattering patterns from wide-angle hard X-ray scattering (16.1 keV) for five PDPPT-C2C8C10 ~ 100 nm thin-film samples under various strains. Two sector-averaged 1D plots along the meridian and equatorial directions were integrated to understand the peak evolution (**Figure 6.2(c, d)**). It should be noted that all curves were vertically shifted for a clear demonstration. Along both directions, the scattering vector q position for (100) and (010) peak only slightly shifted, signifying unchanged packing distances within crystallites (**Table 6.2**). Along the equatorial direction, both (100) and (200) peak intensity diminished with increasing strain, corresponding to a higher fraction of crystallites with (010)/(001) plane perpendicular to the z-axis (Type I and II crystallites). The coherence length along the

equatorial direction continuously decreased from 9.76 Å to 6.24 Å while slightly increased from 9.90 Å to 10.50 Å along the meridian direction, representing crystallite rotation and crystallographic deformation along the tensile direction, i.e., crystallite breakage and slip (**Table 6.2**). Meanwhile, (001) and (001') backbone packing peak started to appear from ε_T = 0.18 at q = 0.41 Å^{-1} (or d-spacing of 15.32 Å) and q = 2 Å^{-1} (or d-spacing of 3.14 Å), indicating the distance between two DPP acceptors and two thiophene donors, respectively. The increased signal strength of (001) and (001') peaks upon alignment signified straightened polymer backbone along the strain direction in the crystalline region (Type I and III crystallites). On a different note, the (010) peak became more evident with strain along the equatorial direction, representing the formation of crystallites with backbones perpendicular to the strain direction (Type II and IV crystallites). Next, pole figure analysis was performed on (100), (010) peak, and the amorphous halo to provide a quantitative comparison of molecular orientation, where 0º and -90 º corresponded to the equatorial and meridian directions, respectively (**Figure 6.2(e)** and **Figure E.3**). The (100) pole figure analysis proved the above discussion where the population of crystallites with (100) peak seen in the meridian direction increased, and those with (100) peak shown in the equatorial direction decreased with strain. On the other hand, the population of crystallites with (010) peak displayed in the meridian direction increased while those with (010) peak resided in the equatorial direction stayed at almost the same level. This observation proved the existence of more Type III crystallites. Based on the pole figure, Herman's orientation parameter *f* was calculated and plotted in **Figure 2(f)** by using Equation 6.1 and Equation 6.2:

$$< \cos^2\theta > = \frac{\int_0^{\frac{\pi}{2}} I(\theta) \cos^2\theta \, d\theta}{\int_0^{\frac{\pi}{2}} I(\theta) \, d\theta} \quad (6.2)$$

where θ is the azimuthal angle, $I(\theta)$ represent the scattering intensity at θ. From (100) peak, it was seen that the alignment of crystallites increased linearly with strain up to ε_T = 0.47, followed by a slower increase in *f* until 0.65, indicating highly oriented crystallites. On the other hand, the (010) peak only showed a low *f* value of 0.2 at the maximum strain ε_T = 0.59, which can be potentially correlated with the backbone slippage along (100)/(001) plane due to the weak π-π interaction. Such phenomenon has also been proposed in the alignment of bulk P3HT sample.[283] Interestingly, the anisotropy of the amorphous peak followed closely with the (010) peak, which suggested the origin of the amorphous halo to be randomly oriented π-π stacking behavior between polymer backbones.

Small-angle hard X-ray scattering was also conducted to investigate the distance between crystallites. However, unlike previous observations on P3HT, where a long period of 11.5 nm was captured, we did not observe any peak in SAXS images (**Figure E.4**).[283] This observation could result from a low degree of crystallinity of PDPPT-based polymers. However, the absolute degree of crystallinity measurement is rather complicated due to the fast crystallization rate for conjugated polymers, which is not within the scope of the current work.

Table 6.2 *Crystallographic information for PDPPT-C2C8C10 extracted from wide-angle hard X-ray scattering*

Strain (ε_T)	Equatorial direction					Meridian direction			
	(100)			(010)	(001)	(100)			(010)
	q (Å^{-1})	FWHM (Å^{-1})	Coherence length (Å)[1]	q (Å^{-1})	q (Å^{-1})	q (Å^{-1})	FWHM (Å^{-1})	Coherence length (Å)[1]	q (Å^{-1})
0	0.290	0.071	9.762	1.652	N/A	0.285	0.070	9.902	1.633
0.18	0.287	0.080	8.664	1.650	0.411	0.289	0.068	10.19	1.641
0.34	0.285	0.102	6.795	1.638	0.411	0.290	0.068	10.19	1.650
0.47	0.283	0.111	6.244	1.634	0.412	0.289	0.064	10.83	1.667
0.59	0.282	0.131	5.291	1.626	0.416	0.291	0.066	10.50	1.667

Note: [1]The coherence length τ is calculated by the Scherrer equation: $\tau = (K \cdot \lambda)/(\beta \cdot \cos\theta)$, where K = 0.9, λ = 0.77 Å for X-ray energy of 16.1 keV, β is the FWHM, θ is the Bragg angle.

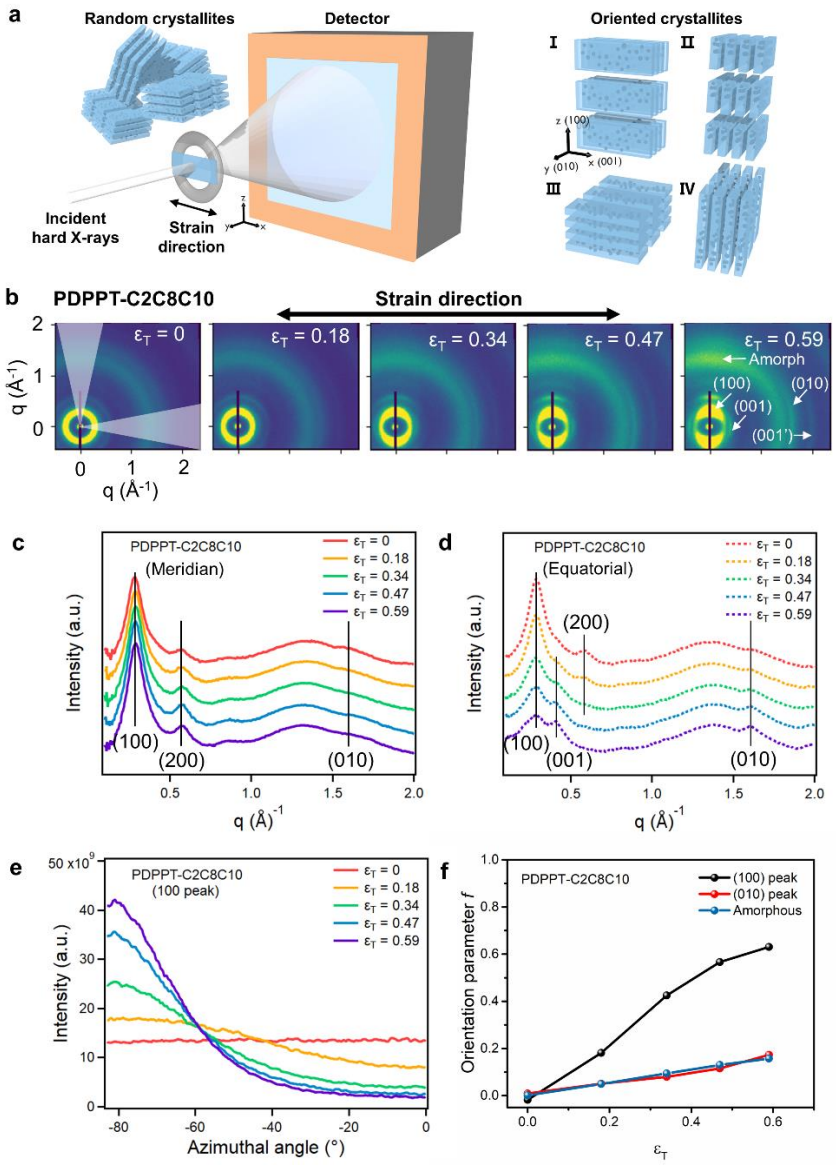

Figure 6.2 *Wide-angle hard X-ray scattering experiment on PDPPT-C2C8C10 polymer under various strain. (a) Schematic of the experimental setup. Incident X-ray transmits through polymer thin films, where the detector collects the scattering signal from crystalline regions. Four preferable crystallite orientations under deformation are also shown on the right. (b) Representative 2D scattering patterns and characteristic crystallographic peaks. (c) Sector averaged 1D integration along the meridian direction and (d) equatorial direction. (e) Pole figure analysis based on (100) peak. (f) Herman's orientation parameter f versus strain based on (100) peak, (010) peak, and amorphous halo.*

6.3.2.2 Wide-angle anomalous tender X-ray scattering

The crystallite orientation detected by hard X-rays comes from a combination of backbone and side-chain scattering. In order to differentiate the contribution from each component, wide-angle tender X-ray scattering experiments with energy near the sulfur K-edge (around 2.47 keV) were performed to investigate backbone orientation in polymer crystallites (**Figure 6.3(a)**). Since sulfur atoms only reside in the backbone, the scattering signal contribution from the backbone and side-chain can be deconvoluted through data collection at different energies across the S-edge. A range of energy from 2.45 keV to 2.5 keV was used on each sample. As the energy moved through the sulfur edge, an increase in the background intensity, mainly located at high q, was observed. This intensity variation corresponds to the fluorescence yield of the sulfur atom (**Figure 6.3(b)**). For PDPPT-C2C8C10 with/without strain, the fluorescence yield NEXAFS spectrum only differed slightly. It is also worthwhile to note that the thickness effect on absorption is negligible here (< 0.3%). It was shown that below 2.47 keV (pre-edge), the fluorescence was minimal; from 2.47 to 2.474 keV, sulfur only slightly absorbed; from 2.476 to 2.478 keV (on-edge), a dramatic increase in fluorescence showed up, followed by a plateau at higher energies (post-edge).

Characteristic 2D scattering patterns of strain aligned PDPPT-C2C8C10 thin films under X-ray energy of 2.478 keV were displayed in **Figure 6.3(c)**. Due to the limited detector size and high X-ray wavelength, only (100) peak was collected through stitching multiple scattering images. Again, the sector averaged integration was performed along the meridian and equatorial directions to compare the peak evolution (**Figure 6.3(d)**). Similar to section **6.3.2.1**, the orientation parameter *f* under five energies from 2.47 to 2.478 keV was summarized in **Figure 6.3(e)** through pole figure analysis

(**Figure E.5, E.6**). Generally, the chain orientation at all energies increased with ε_T in a similar fashion to the wide-angle hard X-ray scattering. Specifically, the orientation parameter *f* at 2.47 keV energy for all five strains is nearly identical to that of 16.1 keV, which is expected due to limited resonant effect in the pre-edge region. For 2.472 keV and 2.474 keV, only highly strained samples show a slight difference in *f*. The non-zero *f* value for the undeformed sample at both 2.476 keV and 2.478 keV is not fully understood at this stage, which could relate to different bonding orientations from sulfur atoms upon spin-cast. However, such ambiguity does not affect the understanding of *f* evolution under strain. Notably, at 2.478 keV, where the fluorescence from sulfur reached a maximum, the backbone orientation signal is predominant. Upon deformation, the orientation parameter *f* only increased by 0.23 under a strain ε_T = 0.59, which is surprising since the orientation of crystallite changed by 0.65. The origin of such a drastic difference could come from the following sources: the PDPPT polymer backbone torsion and twisting lead to a broad distribution of sulfur atoms; the lamellar in crystallites slide past each other along the (010)/(001) plane through soft and mobile side chains upon deformation.

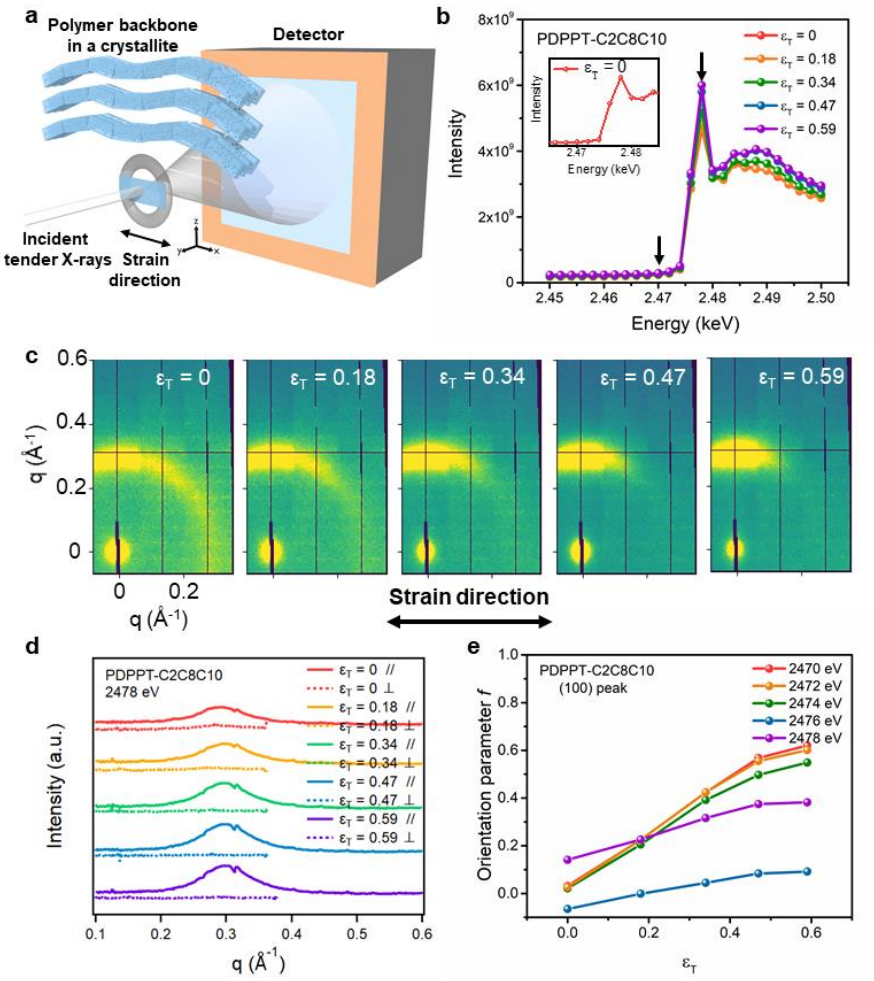

Figure 6.3 *Wide-angle tender X-ray scattering experiment for PDPPT-C2C8C10 polymer under various strain. (a) Schematic of the experimental setup. Incident tender X-ray transmits through polymer thin films, and the detector collects the scattering signal from the sulfur atom on the polymer backbone in crystallites. (b) The plot of background scattering intensity at various incident X-ray energies, indicating the fluorescence yield of sulfur atom at different energies, which corresponds to the sulfur absorption. The inset shows a zoom-in plot at 0% strain. The absorption starts from 2470 eV and the maximum absorption is shown at 2478 eV. (c) 2D scattering patterns at 2478 eV. (d) Sector averaged 1D integration along the meridian direction (//) and equatorial direction (⊥) at 2478 eV. (e) Herman's orientation parameter f versus strain based on (100) peak at various X-ray energies.*

6.3.2.3 Polarized UV-vis optical absorption spectroscopy

Since the orientation of polymer crystallites upon deformation only represents a fraction of the entire polymer film, it is also essential to understand the deformation

mechanism for amorphous polymer chains. A polarized optical spectroscopy technique was commonly performed to investigate polymer chain orientation based on the absorption anisotropy along/perpendicular to the strain direction.[81] Such anisotropy can be quantified by dichroic ratio *R*, which is the ratio of peak absorbance parallel and perpendicular to the polarized light. In this case, 2D Herman's orientation parameter *f* can be calculated as:

$$f = \frac{R-1}{R+1} \tag{6.3}$$

Polarized UV-vis absorption spectroscopy was widely applied to study the orientation of conjugated polymer chains due to their characteristic emission peaks.[78,81,322,323] Previously developed HJ-aggregate model successfully described the competition between intra- and inter-molecular coupling, which is sensitive to the nature and magnitude of disorder and leads to different J- and K-aggregate behaviors.[301,324] **Figure 6.4(a)** showed a schematic of the test setup, where the polarized light parallel and perpendicular to the strain direction can capture the alignment of the entire chain in the film. The absorption spectrum for PDPPT-C2C8C10 thin films under strain was plotted in **Figure 6.4(b)**, where the 0→0 and 0→1 transition occurred at 820 nm and 760 nm, respectively. Surprisingly, the degree of orientation for the whole chain was limited with an *f* of 0.14 at ε_T = 0.59, which suggested the averaged anisotropy for strain-aligned polymer chains was relatively low (**Figure 6.4(c)**). Considering the high level of strain applied to the thin-film, such low orientation implied that the deformation process for free-standing thin films involved substantial chain slippage. Film-on-elastomer method was also applied to align PDPPT-C2C8C10 thin films, an orientation parameter *f* of 0.36 was detected at the same strain (ε_T = 0.59) (**Figure E.7**). Such difference in *f* is expected

due to different deformation mechanisms and Poisson's effects for thin films bonded to PDMS versus free-standing polymers.[98] This result is comparable to other D-A polymers like a near-amorphous D-A polymer indacenodithiophene-co-benzothiadiazole IDTBT (f = 0.22) and a relative crystalline P3HT (f = 0.5) polymer with more than 50% crystallinity.[82,323,325,326] Again, this observation highlighted the importance of amorphous chain slippage in semicrystalline conjugated polymers.

6.3.2.4 Transmission NEXAFS

Transmission NEXAFS technique was applied to supplement UV-vis spectroscopy by detecting the polymer backbone rotation for the entire chain. While tender X-rays were used to probe the sulfur K-edge, soft X-rays near the carbon K-edge (0.27-0.34 keV) can detect absorption signals based on the chemical environment of the carbon atom. Specifically, for conjugated polymers with multiple ring structures in the backbone, the C=C 1s→π* transition is a signature fingerprint that indicates the orientation of aromatic planes. **Figure 6.4(d)** demonstrated two orthogonal electric field vectors $\vec{E}$ for linearly polarized soft X-ray beam, as well as the 1s→π* transition dipole moment $\vec{O}$ perpendicular to the plane of the aromatic ring. The resonance intensity detected on the photodetector is proportional to the overlap between these two vectors:

$$I \propto |\vec{E} \cdot \vec{O}|^2 \propto \cos^2\theta \tag{6.4}$$

where θ is the angle between $\vec{E}$ and $\vec{O}$. Thus, the dichroism of such transition can be used to determine the molecular orientation.[327,328] It should be noted that the orientation determined here only considers polymer chains with an aromatic plane parallel to the film thickness direction.

Figure 6.4(e) plotted the 1s→π* transition peak for strained PDPPT-C2C8C10 thin films, while the complete NEXAFS spectrum with an energy ranging from 0.27 keV to 0.4 keV was plotted in **Figure E.8** followed by previously reported procedures.[327] The parallel/perpendicular direction was referring to the angle between $\vec{E}$ and strain ε_T (**Figure 6.4(d)**). From the anisotropic peak resonance energy at 285.2 eV, an orientation parameter *f* can be calculated by $R = \frac{I_\perp - I_\parallel}{I_\perp + I_\parallel}$ (**Figure 6.4(f)**). Upon strain alignment, f continuously increased with ε_T from 0.09 to a moderate value of 0.53 at ε_T = 0.59, indicating an efficient backbone rotation mechanism, i.e., the majority of aromatic planes on the polymer chain rotated with its normal $\vec{O}$ perpendicular to strain. Two primary rotation modes were drawn in **Figure 6.4(f)** ($\vec{E} \parallel \varepsilon_T$ and $\vec{E} \perp \varepsilon_T$). For polymer chains in the crystalline region, mode I corresponds well to an increased population of Type III crystallites, while mode II is less preferred as judged by the (100) lamellar packing direction. For the amorphous domain, mode I represents slowly aligned polymer chains, while a high fraction of mode II can contribute to the low degree of anisotropy found in UV-vis measurement. Resonant soft X-ray scattering (RSoXS) experiments were also performed under two orthogonal polarization angles at 285.2 eV. There appears to be some increasing anisotropic features that are more visible at the 90° polarization angle ($\vec{E} \perp \varepsilon_T$) with increasing stretching, which could be associated with the chain alignment potentially reflected in the scattering at low q region (**Figure E.9**). Further investigations are warranted to explore the chain alignment with RSoXS technique.

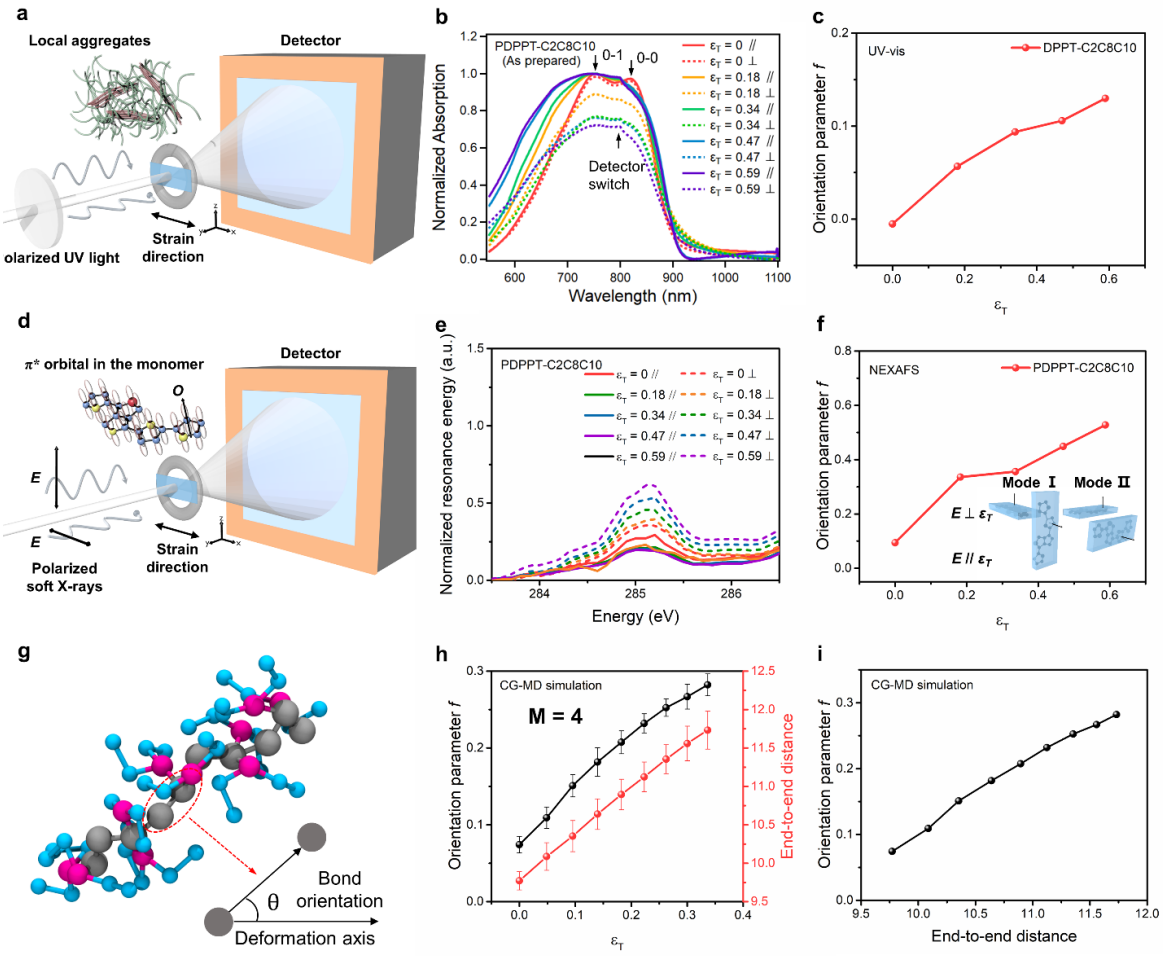

Figure 6.4 *Characterization of chain orientation through UV-vis spectroscopy, NEXAFS and CG-MD simulation. (a-c) UV-vis absorption spectroscopy for PDPPT-C2C8C10 polymer under various strains. (a) Schematic of incident polarized UV light transmitted through polymer thin films. (b) 1D UV-vis absorption plot at different wavelengths. (c) Herman's orientation parameter f under strain. (d-f) NEXAFS experiment for PDPPT-C2C8C10 polymer under various strains. (d) Schematic of incident polarized soft X-rays transmitted through polymer thin films. E represents the electric field direction, and O represents the normal direction of the aromatic plane. (e) Normalized resonance energy under different incident energies for E // ε_T, and E ⊥ ε_T direction. The peak at around 285.2 eV represents the 1s to π* transition. (f) Herman's orientation parameter f under strain. The inset shows two backbone rotation modes (I and II) under strain. (g-i) CG-MD simulation for the M = 4 model, where M represents for simulated side-chain length. (g) Schematic of a single polymer chain with a defined angle between the bond direction and deformation direction. (h) Herman's orientation parameter f and end-to-end distance under strain. (i) Relationship between Herman's orientation parameter and end-to-end distance.*

6.3.2.5 AFM

The film surface morphology was investigated through AFM height images (**Figure E.10**). Similar to previous publications, fiber-like structures can be observed all over the surface, while small, randomly shaped aggregates are also presented.[232] However, the fiber orientation was not extracted due to the high surface roughness, while the aggregates showed evident deformation with their shapes being elongated along the stretching direction. This observation provides direct visual evidence for thin-film alignment.

6.3.3 CG-MD simulation

By employing the CG-MD modeling, the orientation of the polymer chains was characterized by a 3D Herman's function:

$$f = \frac{3<\cos^2\theta>-1}{2} \tag{6.5}$$

where θ is the formed angle between the bond vector in the polymer chain (backbone) and the deformation axis (**Figure 6.4(g)**). The CG model is discussed in detail in our experimental section. The orientation factor *f* can be defined as an average of all CG backbone "bond" vectors orientation values in the bulk simulation. Besides the orientation parameter, the end-to-end distance of the polymer backbone during deformation was examined. Here, the molecular orientation of the CG model was presented for the CG bulk polymer model with a side-chain length (M) of 4 at different strains. **Figure 6.4(h)** indicated that, as the tensile strain increases, the backbone chains tended to align in the deformation axis and exhibited a higher orientation parameter. Expectedly, the increase of orientation parameter was accompanied by the increase in the end-to-end distance, as shown in the right axis of **Figure 6.4(h)**. Meanwhile, the orientation parameter and end-to-end distance exhibited a near-linear correlation

(**Figure 6.4(i)**). The current results are also consistent with the previous CG-MD study on the P3HT polymer, where the backbone chains were found to align in the deformation axis by increasing the tensile strain.[253]

6.3.4 OFET performance upon strain alignment

To further understand the effect of strain-alignment on electrical performance, organic field-effect transistor (OFET) devices were fabricated with strained PDPPT-C2C8C10 films. The PDPPT-C2C8C10 films were strained on the water surface and transferred onto an octadecyltrichlorosilane (OTS)-coated substrate before the fabrication of OFET devices (**Figure E.11** and **Table E.1**).[329] It is noticed that the charge mobility did not show any obvious improvements, with an averaged value from 0.025 to 1.1 cm^2 V^{-1} s^{-1} along the parallel direction and 0.045 to 1.1 cm^2 V^{-1} s^{-1} along the perpendicular direction at various strains. More importantly, no apparent anisotropy in the charge mobility was noticed. This observation is in line with previous studies where OFET devices were fabricated using strain-aligned D-A polymer thin films on the PDMS dielectric.[323,330] However, it is different from a previous study on tensile-aligned P3HT study, where a small reduction in mobility from 0.05 to 0.01 cm^2 V^{-1} s^{-1} in the perpendicular direction and a slight increase from 0.05 to 0.1 cm^2 V^{-1} s^{-1} in the parallel direction was observed, resulting in an anisotropy around 5 at ε_T = 0.59.[81] To verify our findings, we performed similar measurements on strain-aligned P3HT on PDMS support, where the charge mobility dropped consistently along both parallel and perpendicular directions without showing clear anisotropy (**Figure E.12** and **Table E.2**). Such difference could be due to several reasons. Firstly, the previous work used a much shorter channel length (5 um) when compared with ours (50 um). Thus, the scale of strain-

alignment could be a localized effect and could be averaged out on a macroscopic electrical performance. Secondly, the improvement in charge mobility could fall into the error bar in our experiments. In addition, the charge mobility values under strain can be affected by coherence length and orientation, as well as backbone alignment. For PDPPT-C2C8C10 polymer, the coherence length decreased with strain; the backbone alignment in the crystalline domains was relatively weak due to potential crystallographic slip. All these phenomena can result in the absence of significant charge mobility improvements.

6.3.5 Side-chain length effect

The side-chain effect was also investigated by performing the measurements described in the previous section on the other three PDPPT-based polymers with side chains of C2C6C8, C2C10C12, and C2C12C14. Previous works have shown that side-chain length can significantly affect the thin-film microstructure (crystallographic packing, aggregation behavior, degree of crystallinity) and device performance.[94,97,134,323,331–333] From hard X-ray scattering, we observed a similar influence on unstrained samples, i.e., longer side chains led to higher lamellar packing distance and less clearly defined (010) peak (**Table 6.2**, **Figure E.13-E.14** and **Table E.3-E.5**). However, the side-chain length effect on crystalline domain orientation upon strain was not reported for D-A polymers. Our observation showed the *f* value for (100), (010), and amorphous peak at each strain was very close for all three polymers with longer side-chain lengths, while PDPPT-C2C6C8 displayed a higher degree of alignment for (010) and amorphous peak (**Figure 6.5(a-c)**, **Figure E.15**). This interesting behavior is attributed to the preferred edge-on morphology for PDPPT-C2C6C8 upon casting on the silicon substrate, while all other three polymers show a bimodal morphology, as

reported in our previous publication.[187] Once the thin-film being floated from the substrate, the predominant edge-on polymer chains with aromatic planes perpendicular to the substrate were susceptible to in-plane strain due to lamellar rotation (i.e., Type IV to III crystallite). Similarly, the backbone orientation in polymer crystallites measured by tender X-ray scattering showed negligible dependence on the side-chain length (**Figure 6.5(d)** and **Figure E.16-E.21**). To further understand the crystallinity effect, both hard and tender X-ray scattering were performed on thermally annealed PDPP polymer thin films at 200 °C (**Figure E.22-E.25** and **Table E.6-E.8**). For annealed PDPPT-C2C8C10, the (100) coherence length extended, corresponding to an increase in crystallite size and quality. However, the degree of alignment is much lower than as-cast thin films before ε_T = 0.47, then reached to a similar level. This can be explained by the high entropic and enthalpic penalty to reorient large crystallites at an early stage. Similar behavior can also be observed in other PDPP polymers with longer side chains. Interestingly, the degree of crystallite alignment decreased with increased side-chain length for annealed samples, which implied easier crystallographic slippage with the help of longer branched side chains.

On the other hand, the whole chain orientation detected by UV-vis spectroscopy presented slight dependence on side-chain length, where polymers with longer side chains exhibited a slightly higher degree of orientation in the later stage of alignment (**Figure 6.5(e)** and **Figure E.26**). This could result from the low T_g and "lubrication effect" from longer side chains that lowered the energetic penalty barrier required for chain alignment in the amorphous phase. On the other hand, polymers with longer side-chain length were more reluctant to rotate due to the steric effect, as evidenced by

NEXAFS (**Figure 6.5(f)** and **Figure E.8**). On a macroscopic scale, AFM showed limited influence of side-chain length on the backbone rotation behavior and fiber-like structure alignment (**Figure E.27**).

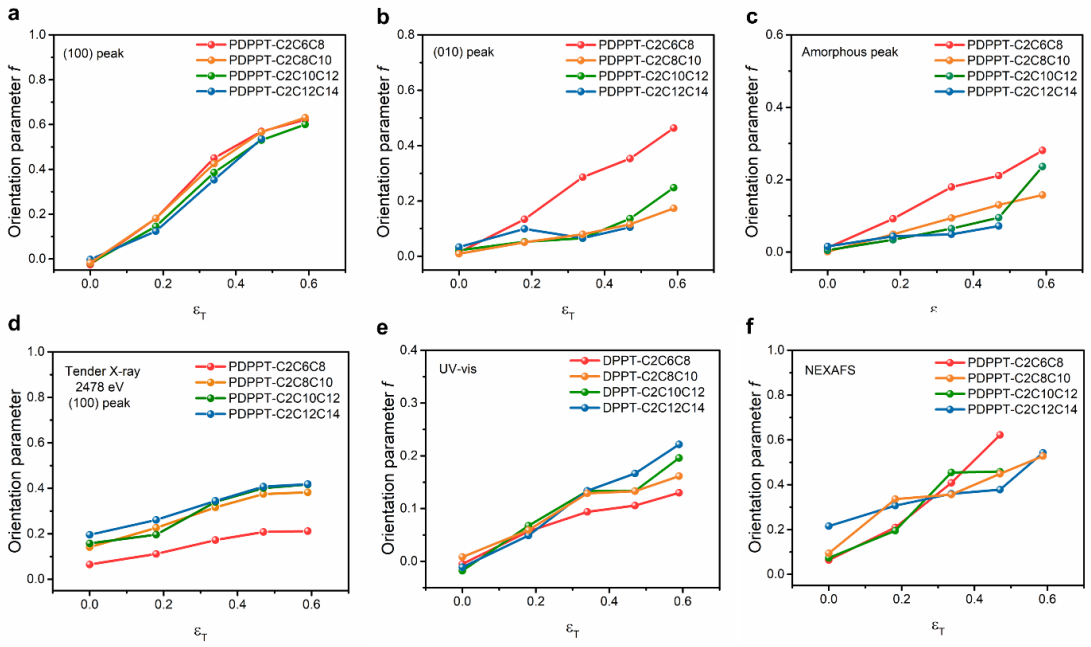

Figure 6.5 *Side-chain length effect on Herman's orientation parameter f detected by different techniques for PDPPT-based polymers. (a) (100) peak, (b) (010) peak, and (c) amorphous halo from wide-angle hard X-ray scattering. (d) (100) peak from wide-angle tender X-ray scattering at 2478 eV. (e) UV-vis absorption spectroscopy. (f) NEXAFS.*

6.3.6 Discussion

Herein, we discuss the deformation mechanism of D-A polymers, and contrast to conventional PE polymers. For the past decades, the chain deformation mechanism of semicrystalline PE has been thoroughly investigated.[286–291] Detailed studies based on both tensile and compression tests had shown that the deformation came from a synergic contribution of both rubbery amorphous domains and hard crystalline domains. The initial deformation mostly relies on amorphous components, such as interlamellar shear, interlamellar separation, and lamellar stack rotation, which are reversible to a large

extent. Followed by the elastic response, mechanical yielding and strain softening occur due to crystallographic deformations.[287,289,290] The further alignment would cause cavitation, lamellae fragmentation, and fibrillation together with the strain hardening behavior.[315,318,319] The degree of crystallinity was demonstrated to significantly affect the contribution from crystalline and amorphous domains to deformation. For polythiophenes with semi-flexible backbones, the molecular picture upon deformation was somewhat different. In case of P3HT and poly(3-dodecylthiophene) (P3DDT), while no strain softening, cavitation, or fibrillation were observed, crystallographic deformation still existed.[18,44] Chen *et al.* proposed the deformation of P3HT associated with crystallographic slip along (010)/(001) direction, while side-chain length could change the slip direction to (100)/(001) for (P3DDT).[283]

In this work, the molecular picture of PDPPT-based polymers is vastly different from PE due to their rigid backbones.[61,334] Unlike the traditional chain folding model in polymer crystallites, the DPP-based polymer chains are much harder to bend. A brush-like lamellar structure is usually formed through weak intermolecular π-π stacking between backbones and van der Waals interaction between side chains, as evidenced by scanning tunneling microscopy (STM).[89,90] **Figure 6.6** showed the proposed chain alignment mechanism under three stages of strain (I for the elastic deformation under low strain, II for intermediate strain, and III for large strain) and molecular orientation discussed above. Our previous work had demonstrated significant hysteresis behavior for both P3HT and PDPPT-based polymer even before ε_T = 0.03, thus the initial elastic deformation in region I was much shorter than that of PE.[18] During the entire plastic deformation process, continuous lamellar stack rotation happened with the emergence of

four main types of strain-aligned crystallites: More Type I and III crystallites with their backbone parallel to the strain direction and a small portion of narrowly dispersed Type II and IV crystallites with their backbone perpendicular to the strain direction (**Figure 6.2(a)**). Within the crystalline domain, the limited degree of alignment for both (010) peak and the polymer backbone suggested potential slippage along both (100)/(001) and (010)/(001) planes, respectively.[283] In the meantime, NEXAFS captured apparent backbone rotation behavior, suggesting the aromatic plane preferred to lie parallel to the strain direction (**Figure 6.4(f)**). Despite the highly oriented crystallites, UV-vis showed that the whole chain alignment was very limited, due to considerable chain slippage in the amorphous region. **Figure 6.6(b)** showed the schematic snapshots of chain deformation for each stage. Stage I represented for undeformed film, stage II mainly involved crystallites rotation with amorphous chain slippage. At stage III, the extent of lamellar rotation almost reached a plateau with an $f = 0.65$, while both backbone rotation and whole chain alignment did not show evident saturation, corresponding to slowly aligned amorphous chains. The side-chain length effect on different crystallographic slip mechanisms shown in P3HT and P3DDT was not clearly seen in PDPPTs. The pole figure analysis for (100), (010), and amorphous peak presented a similar crystallographic rotation and slippage mechanism for polymers with different side-chain lengths, while longer side chains provided a stronger lubrication effect and allowed a higher *f* for the whole chain at a high strain.

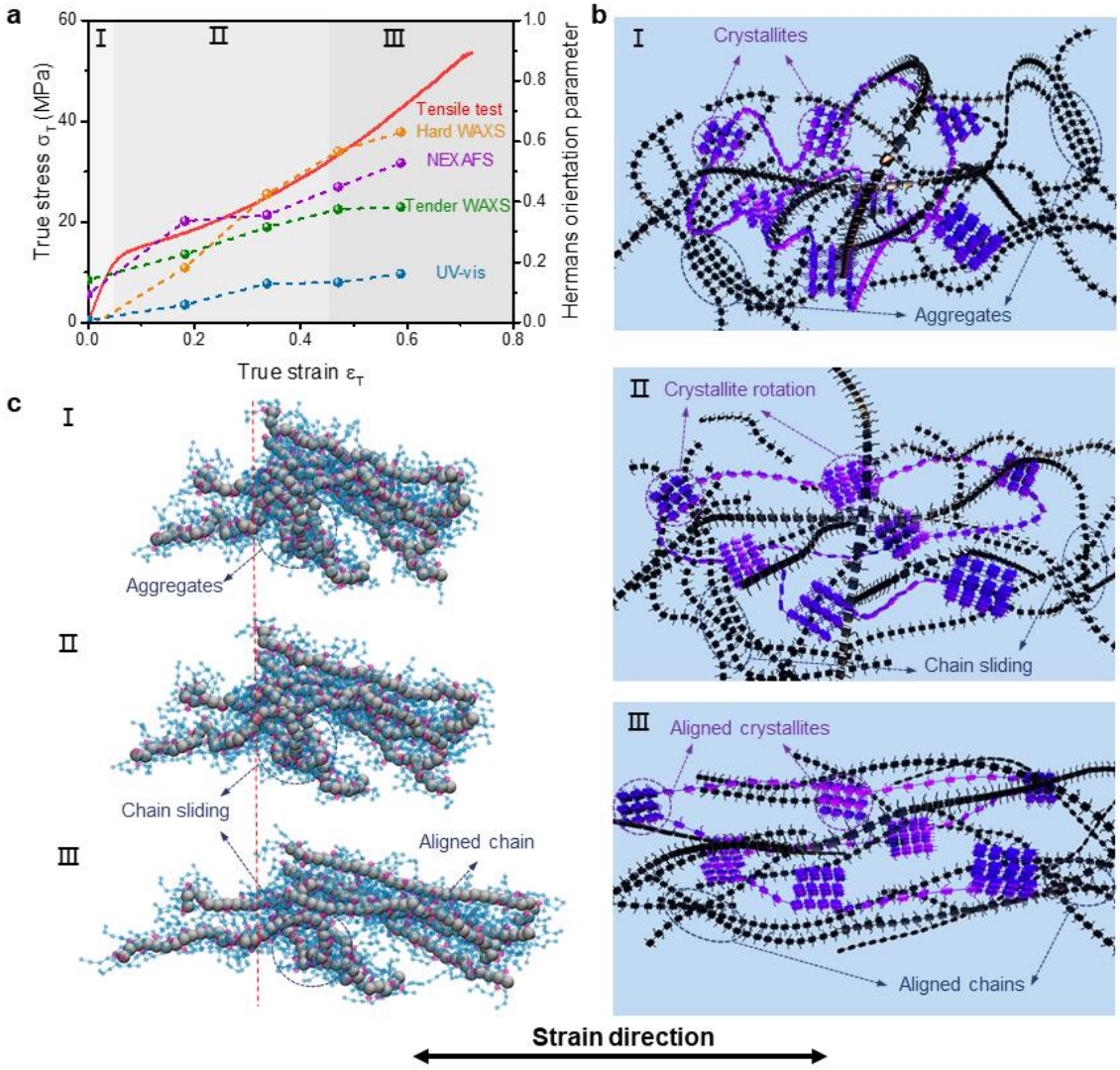

Figure 6.6 *Chain alignment mechanism for PDPPT-based polymers. (a) Stress-strain response and summarized Herman's orientation parameter for PDPPT-C2C8C10 polymer under three stages of strain. I: Initial deformation; Stage II: Medium strain; Stage III: High degree of alignment. (b) Schematic snapshots of deformation mechanisms under three stages showing crystallite orientation, chain alignment, and chain sliding. (c) Snapshots of polymer conformations showing the chain alignment and sliding during deformation in the bulk CG-MD simulations.*

To further explore our experimental results via MD simulations, a CG model was utilized to mimic the essential structural features of the PDPPT-based polymer chain. It is to be noted that only amorphous chains were studied to provide the fundamental

understanding. **Figure 6.6(c)** showed different snapshots of a group of adjacent chains through the tensile simulation. Simulation snapshots were presented for different applied strains of 0, 0.2, and 0.4 that were consistent with the probed three regions of stress-strain behavior obtained from the experimental results. Prior to deformation, a random orientation of the polymer chains is observed. As the strain increases to 0.2 (region II), the applied deformation caused polymer chain-sliding, and chain-torsional motions ended in a higher alignment of the backbones in the deformation axis. As the tensile simulation proceeded and reached the strain of 0.4, chains were largely extended and oriented to the deformation direction (region III), where backbone-sliding was found less restricted, and sliding motion became smoother due to the plastic behavior of the bulk system. This trend was presented quantitatively in **Figure 6.4(h)**, where extended chains at higher strains were found to have larger orientation parameters and end-to-end distances. The simulation result of the backbone orientation is in line with our experimental results, where the alignment slowly plateaus with increased deformation.

Except for mechanical stretching, another common technique to align polymer chains is through mechanically shearing the polymer solution on a substrate. In this technique, the final chain orientation can be affected by many more parameters.[75] First, the choice of polymer/solvent combination greatly affects the amount of pre-aggregated polymer chains. Next, the substrate temperature and coating speed can directly change the evaporation speed of the solvent, thus the range of evaporative and Landau-Levich regimes. Also, previous reports showed that the nano-grooved blade/substrate could improve the orientation of polymer chains.[32,76] However, the backbone orientation with respect to coating direction was closely connected with the backbone rigidity and the

formation of the lyotropic liquid crystal phase, while the degree of crystallinity played a minor role.[78–80,87] Additionally, a strong gradient of alignment was found along the film thickness direction with the highest degree of alignment at the liquid/air surface or the nano-grooved surface. Overall, shear-alignment can introduce highly oriented chains during solution-film evaporation and endows high mobility anisotropy after film formation. In comparison, strain-alignment is directly performed in a thin-film state with disordered morphology. The alignment process and the degree of alignment strongly depend on the microscopic picture of polymer chains and crystallographic structure. Although the charge mobility may not greatly improve after stretching, the conductivity has shown strong improvement through doping of tensile drawn conjugated polymers, where the influence of morphological disorder and grain boundaries could be mitigated.[335]

6.4 Conclusions

In summary, we systematically explored the chain alignment mechanism of PDPPT-based polymers and the structure-morphology-electrical performance relationship. Two primary strain-induced alignment mechanisms were addressed: highly oriented crystalline domains and substantial chain slippage in the amorphous domain. Specifically, the lamellar rotation was determined to be the main pathway for crystallite orientation, coupled with potential crystallographic slippage resulting in a lower degree of backbone alignment. In the amorphous region, chain slippage was enabled by long and branched side chains. Meanwhile, the backbone rotation was identified as part of the whole chain deformation, with their aromatic planes rotated towards the parallel-to-strain direction. All these microscopic behaviors lead to an isotropic charge carrier mobility in

the OFET device. We believe such a fundamental understanding of the chain deformation mechanism for PDPPT-based polymers can serve as a platform and provide more insights into the semi-rigid D-A polymer design for the application of stretchable electronics. As discussed above, the ability to design and synthesis new polymers that can easily slide past one another using backbone and sidechain engineering can be very important for making future stretchable electronics.

CHAPTER VII - TACKY ELASTOMERS TO ENABLE TERA-RESISTANT AND AUTONOMOUS SELF-HEALING SEMICONDUCTOR COMPOSITES

(Adapted from "Zhang, S.; Cheng, Y.; Galuska, L.; Roy, A.; Lorenz, M.; Chen, B.; Luo, S.; Li, Y.; Hung, C.; Qian, Z.; St. Onge, P. B. J.; Mason, G. T.; Cowen, L.; Zhou, D.; Nazarenko, S. I.; Storey, R. F.; Schroeder, B. C.; Rondeau-Gagné, S.; Chiu, Y.; Gu, X. Tacky Elastomers to Enable Tear-Resistant and Autonomous Self-Healing Semiconductor Composites. Adv. Funct. Mater. 2020, 30 (27), 2000663.")

7.1 Introduction

Decades of development of new organic semiconductors has boosted electronic performance (e.g. charge carrier mobility) to be comparable to their inorganic counterparts, like amorphous silicon.[4–8] Semiconducting polymers are known for their chemical tunability, solution processability, and mechanical deformability, which makes them promising candidates for flexible or deformable electronic devices.[45,97,220,246] In the past, researchers have focused on engineering semiconducting polymers with lower elastic modulus and maximized deformability through modifying their molecular structures, for example, through backbone/side-chain engineering, and introduction of cross-linkable moieties to polymer side chains and/or intermolecular hydrogen bonding to the backbone/side chain.[94,97,105,134,323,331–333] However, the mechanical performance of fully conjugated semiconducting polymers is limited due to their intrinsic rigid backbone and synthetically limited molecular weight, leading to a generally high elastic modulus (> 100 MPa) as compared to human skin (e.g. ~ 0.1 MPa), low deformability (< 200% of strain) and strong hysteresis under cyclic stretching.[45,61,97,336] This causes a great mismatch in mechanical properties between the wearable device and human skin. The

buckling and delamination of the thin film device from soft skin can potentially be an issue.

Another promising method to achieve both high electrical and mechanical properties for a given semiconducting polymer is through physical blending with mechanically soft and deformable elastomers.[19,32,131–133,337–340] A blend of poly(3-hexylthiophene) (P3HT) and styrene-ethylene-butylene-styrene (SEBS) elastomer showed a relatively low charge transport mobility around 2×10^{-3} cm^2 V^{-1} s^{-1} at 50% strain, with a high fracture strain around 300%.[133] Similarly, commercially available crosslinked polydimethylsiloxane (PDMS) elastomer (Sylgard 184) has also been used as the elastomer matrix in semiconducting polymer blend systems.[131] Most recently, Xu *et al.* introduced a conjugated polymer/elastomer phase separation-induced elasticity (CONPHINE) method to blend different polydiketopyrrolopyrrole (PDPP)-based conjugated polymers with SEBS, thereby obtaining a high and stable charge mobility above 1 cm^2 V^{-1} s^{-1} under 100% strain.[19] However, the maximum deformability of these early composites was restricted due to limited ultimate strain of the elastomer component: 300% strain for pristine SEBS and 400% strain for pristine PDMS.[133] Even for systems with a highly extensive elastomeric phase, failure of the conjugated polymer phase is hard to avoid due to the rapid propagation of intrinsic defects during the tensile drawing at stress concentrated point near the crack tip. In order to achieve mechanically and electronically robust composite, it is necessary to substantially suppress crack initiation and propagation, together with healing of the crack region; thus a tear-resistant and self-healable polymeric semiconductor material is required.[341–343]

7.2 Experimental

7.2.1 Pseudo-free-standing Thin Film Tensile Test

Thin film tensile tests were performed on a water surface through pseudo-free-standing tensile tester. Details of the tensile stage setup can be found in our previous publication.[18] Briefly, the polymer thin films (~ 50 nm) were patterned into dog-bone shape by ultra-fast laser patterning, floated on top of water, and unidirectionally deformed at a strain rate of 0.125 s^{-1} until film fracture. At least six independent specimens were measured for each sample to provide statistically averaged mechanical property. The elastic modulus was obtained from the slope of the linear fit of the elastic region of the stress-strain curve using the first 1% strain.

7.2.2 Device Fabrication and Characterization

FET devices were fabricated on highly doped n-type Si (100) wafers with octadecyltrimethoxysilane (OTS)-modified SiO_2 (capacitance per unit area Ci = 10 nF cm^{-2}). The organic semiconducting thin films were spun-cast on SiO_2/Si substrates at a spinning rate of 1000 rpm for 60 s from prepared polymer solutions in chlorobenzene (5 mg/ml) at 70 °C. The films were thermal annealed at 170 °C for 1 h inside a N_2-filled glove box. Top-contact gold electrodes (50 nm) were subsequently deposited by evaporation through a shadow mask with the channel length (L) and width (W) defined as 50 and 1000 μm, respectively. All the measurements of transistors were conducted using a Keithley 4200 semiconductor parameter analyzer (Keithley Instruments Inc., Cleveland, OH, USA) under dry N_2 (glove box) and ambient atmosphere at room temperature.

7.2.3 Atomic Force Microscopy with Nanoscale Infrared Spectroscopy (Nano-IR AFM)

All measurements were performed using Bruker Anasys nanoIR3 system equipped with HyperSpectra QCL (800-1800 cm^{-1}) laser source. Tapping mode AFM and AFM-IR measurements were done with gold coated Si probes (PR-EX-TnIR-A probes, nominal diameter ~25 nm). For spectral measurements, data spacing was set to 4 cm^{-1}. Acquired spectra were smoothed using Savitzky-Golay (3,5) filter.

7.2.4 Oxygen and Water Vapor Permeability Measurements

The oxygen permeability of BR and PDMS films was measured at 23°C, 0% RH, and 1 atm partial oxygen pressure difference using a commercially manufactured diffusion apparatus OX-TRAN® 2/21 ML (MOCON). BR film with area of 50 cm^2 was tested using pure oxygen gas. PDMS film was masked with aluminum foil with inner hole size of 5 cm^2 and tested using 4% oxygen/nitrogen to avoid the saturation of oxygen sensor. The oxygen transmission rate of PDMS was then normalized to 100% O_2. The permeability of oxygen for BR and PDMS films was determined as 1.753 and 5498.0 $cc/cm/(m^2/day/atm)$ respectively. Water vapor permeability test of both BR and PDMS films was conducted via dry cup test (ASTM D1653 – 13) in a humidity chamber at 20°C and 94% relative humidity.

7.2.5 Time-of-flight Secondary Ion Mass Spectrometry (TOF-SIMS)

TOF-SIMS experiments were performed on an IONTOF TOF.SIMS 5 platform (IONTOF GmbH, Münster, Germany), equipped with a 30 keV maximum energy bismuth liquid metal ion source (LMIS) and an argon gas cluster ion source (GCIS). The instrument was used for dual beam depth profiling with a Bi_3^+ analysis beam (0.48 nA DC beam current) and a 10 keV Ar_{2550}^+ sputter beam (68 pA beam current). The LMIS was operated in Fast Imaging mode to enable high lateral resolution chemical imaging at

nominal mass resolution. Depth profiles were acquired in positive ion mode with non-interlaced cycles of 2 analysis frames (128×128 pixels, random scan pattern, 25 µm × 25 µm) and 1 sputter frame (800 µm × 800 µm). The depth profiling data sets were cropped to 19 µm × 19 µm lateral dimensions and integrated over one spatial dimension for the 2D representation in **Figure 7.3(l)**, **F39**.

7.2.6 Resonant Soft X-ray Scattering (RSoXS)

RSoXS data was collected at beamline 11.0.1.2 of the Advanced Light Source, Lawrence Berkeley National Laboratory. X-ray energy of 286.8 eV was chosen based on Near Edge X-ray Absorption Fine Structure (NEXAFS) spectroscopy for two individual components to maximize the scattering contrast between conjugated polymers and elastomer matrix. Scattering data were collected with a sample-to-detector distances of 150 mm to give a q range of 0.001–0.020 $Å^{-1}$. Data analysis was also performed using a modified Nika package supported in the Igor Pro environment.

7.2.7 Grazing Incidence Wide Angle X-ray Scattering (GIWAXS)

Grazing incidence wide-angle X-ray scattering (GIWAXS) of conjugated polymer thin film was carried out at the Stanford Synchrotron Radiation Lightsource (SSRL) on beamline 11-3. Data were collected under helium environment with an incident beam energy at 12.7 keV and an incidence angle of 0.12°. The sample to detector distance was about 250 mm. Diffraction data analysis was performed using Nika software package for Wavemetrics Igor, in combination with WAXStools. The relative degree of crystallinity (RDoC) was calculated through pole figure analysis followed by previously reported methods.[76]

7.2.8 UV-Vis-NIR Absorption Spectroscopy

The UV-Vis-NIR spectra for composite films were recorded on Agilent Cary 5000 using polymer thin films deposited on glass slides.

7.2.9 Alternating Current (AC) Chip Calorimetry

The glass transition temperature of the polymeric thin film was measured by an AC chip calorimeter. Thin film samples were floated off a Si substrate and then transferred to the sensor XI392 (Xensor integrations, NL), containing a large smooth heated area (100 μm × 100 μm). The experiments were performed at a frequency of 10 Hz and a heating/cooling rate of 1 °C/min. Each sample was scanned three times under a protecting nitrogen atmosphere. The amplitude of the complex differential voltage as a function of measuring temperature was obtained. The glass transition temperature was determined as the half-step temperature of the amplitude as previous reported.[26]

7.2.10 Differential Scanning Calorimetry (DSC)

DSC measurement of PDPPTVT was performed on Mettler-Toledo DSC 3+ equipped with FRS 6+ sensor. Dry nitrogen gas with a flow rate of 50 ml/min was used as inert atmosphere. Heat-cool-heat cycle with heating/cooling rate of 30 °C/min was applied to enhance the thermal transition signal. In addition, physical aging experiment was carried out at -10 °C for 2 hrs for the confirmation of T_g around 17 °C.

7.3 Result and Discussion

In this study, we report a new semiconducting composite using butyl rubber (BR) as the elastomer matrix due to its outstanding elasticity (low persistence length of 5.2 Å), strong adhesion and excellent barrier properties to both oxygen and water.[344] We hypothesize these properties will endow new performances to conjugated polymer composite system, such as resistance to crack propagation, self-healing property, and

ambient-stability. A p-type donor-acceptor (D-A) semiconducting polymer, poly(2,5-bis(2-decyltetradecyl)-3,6-di(thiophen-2-yl)diketopyrrolo[3,4-c]pyrrole-1,4-dione-*alt*-thienovinylthiophene (PDPPTVT) was chosen as a model system for the demonstration of our concept of fracture resistant and healable composite film, owing to its high charge transport mobility (**Figure 7.1(a, b)** and **Table F.1**).[254] The blend ratio between donor polymers and elastomer matrix is critical for device morphology, and consequently device performance. To optimize the blend ratio between PDPPTVT and BR, we first measured the mechanical properties of the composite film with a pseudo-free standing tensile tester, where a dog-bone shaped thin film (60 nm) was prepared and stretched at a strain rate of 0.125 s^{-1} uniaxially on top of a water surface.[18,54] As the fraction of BR was increased, the semiconducting polymer composite showed a significant drop in elastic modulus and great improvement in crack onset strain, especially when the BR phase became the continuous phase, above a volume fraction of about 50% ((**Figure 7.1c, d**) and **Table F.2**). In contrast to the low deformability of pristine PDPPTVT film, the composite film with a blend weight ratio of 1:8.5 for conjugated polymer:elastomer exhibited a record-low modulus of 1 MPa and record-high fracture strain exceeding 800%, which was shown to deform into a high aspect ratio polymer fiber under uniaxial loading (**Figure F.1**). **Figure 7.1(e)** compared the current system to several recently reported highly deformable and soft fully conjugated polymers (open symbol), non-conjugated polymers (half-filled symbol), and polymer composites (filled symbol); the data clearly demonstrate the outstanding mechanical performance for the current system, which displays the lowest modulus and highest deformability of all systems (**Table F.3**).[19,96,105,127,133,134,210,345–347]

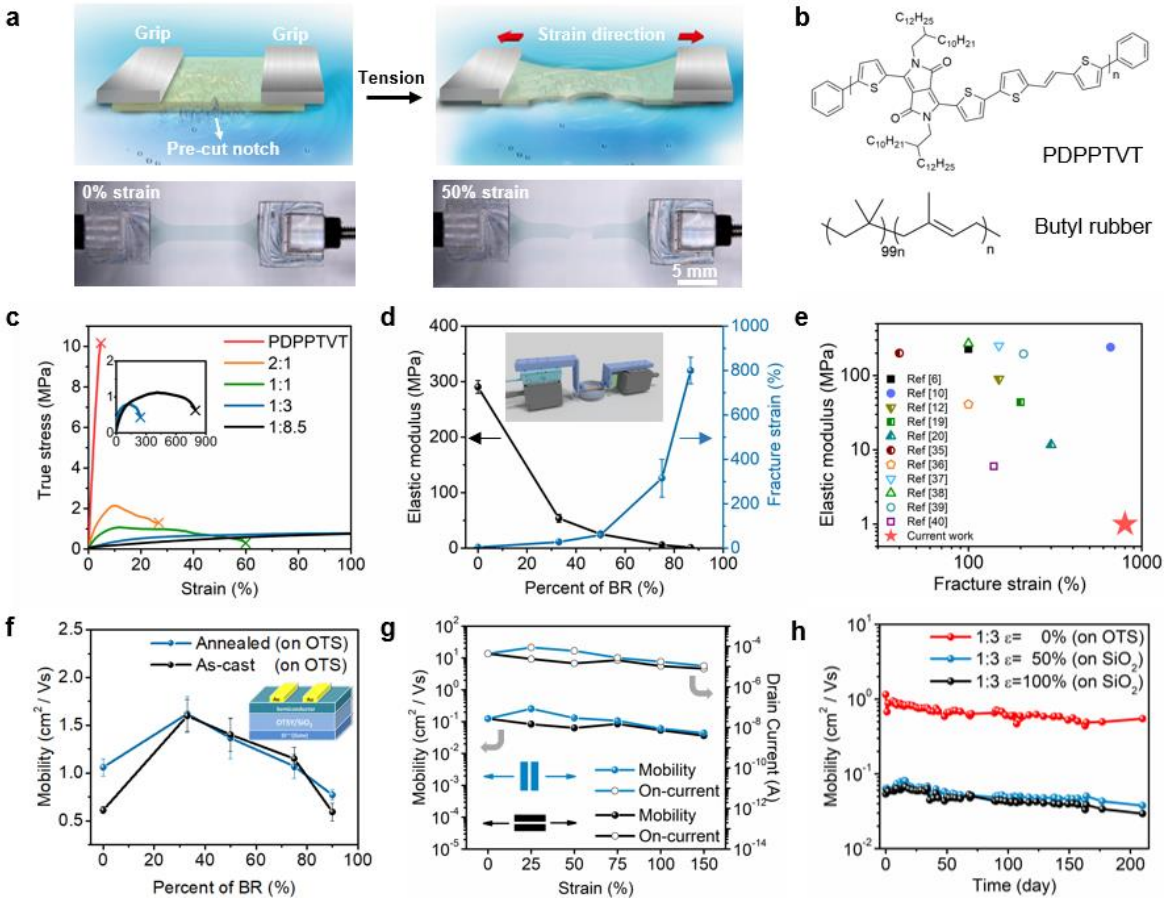

Figure 7.1 *Mechanical and electrical performances for PDPPTVT/BR composite film. (a) 3D schematic illustration and optical images of notched 2:3 PDPPTVT/BR composite film before and after tensile deformation on water surface. (b) Chemical structures for PDPPTVT and BR. (c) Stress-strain curves for different blend ratios of PDPPTVT/BR. Inset: Stress-strain curves for 1:3 and 1:8.5 blend. (d) Elastic modulus and crack onset strain for different blend ratios of PDPPTVT/BR. The inset shows the scheme of tensile testing setup. (e) Comparison of the mechanical performance of the current system to previously reported semiconducting polymeric materials. (f) Charge carrier mobility of OFET devices made using different blend ratios of PDPPTVT/BR. (g) Charge carrier mobility and drain current of 1:3 PDPPTVT/BR composite film upon stretching in parallel and in perpendicular to charge transfer direction at different strain without annealing. (h) Time-dependent charge mobility of OFET devices for 1:3 PDPPTVT/BR composite films.*

Next, we demonstrated the tear-resistance of the new composite film using edge-notched dog-bone-shaped thin film samples with a notch size that is one third of the original width (2 mm). As expected, the notched pristine PDPPTVT broke at a very early

stage. At a low BR content (33% weight fraction), the notch of composite film propagated quickly, leading to catastrophic fracture of the composite film below 25% strain (**Figure F.2(a)**); however, the notched 2:3 composite film withstood 50% strain, with the notch becoming quickly blunted and propagating slowly (**Figure 7.1(a)**). For 1:3 and 1:8.5 blend ratios, thin films did not fail even at 100% strain (**Figure F.2(b-c)**). This observation was attributed to an ideal morphology with BR as the continuous matrix phase, low T_g and highly entangled BR network. Upon uniaxial loading, BR polymer chains are likely to aligned along the loading direction and redistributed the stress at the notch tip, thus the crack propagation was hindered. In the meantime, highly entanglement BR polymer chains could delay the chain slippage and scission, thus preventing the system from catastrophic failure at the pre-cut notch. To further highlight the unique crack-resistance of BR, a control sample was fabricated using a pre-notched PDPPTVT/PDMS composite film at 1:3 blend ratio. This PDMS-based control showed rapid crack propagation and film failure at < 25% strain (**Figure F.2(d)**). The results above showed that highly flexible BR can greatly improve the mechanical property of the conjugated polymer, enabling the composite film to achieve a record-high crack on-set strain, record-low elastic modulus, and outstanding tear resistance behavior.

The electrical performance of the composite film was also investigated through the fabrication of thin film organic field-effect transistors (OFETs). Shown in **Figure 7.1(f)**, the charge carrier mobility of thin films at different blend ratio was between 0.5 and 1.5 $cm^2\ V^{-1}\ s^{-1}$ (**Figure F.3-F.4** and **Table F.4**). The relative insensitivity of charge carrier mobility to PDPPTVT/BR blend ratios can be understood through the unique fibril morphologies dispersed in the elastomer matrix as discussed later. Next, we performed

strain-dependent electrical property measurements for both of 1:3 and 1:8.5 PDPPTVT/BR composite films, following a previously reported transfer method.[97] The thin film was first transferred onto the PDMS substrate and stretched to a desired strain before fabricating into an OFET device on a heavy doped Si substrate with a 300 nm SiO_2 gate dielectric layer. The mobility stayed within the same order of magnitude upon 150% strain along two charge transport directions (e.g., from 0.12 to 0.06 $cm^2 V^{-1} s^{-1}$ for 1:3 composite film and from 0.16 to 0.12 $cm^2 V^{-1} s^{-1}$ for 1:8.5 composite film), demonstrating its strong strain-insensitive electrical performance (**Figure 7.1(g**), **Figure F.5-F.9** and **Table F.5-F.6**). Since the electrical performance of organic semiconductors typically degrades rapidly with the presence of oxygen and water, we also explored the stability under ambient environmental conditions of OFET devices made from the new composite films.[348,349] Both 1:3 and 1:8.5 PDPPTVT/BR composite films were tested under different degrees of strain (0%, 50% and 100%), and the charge carrier mobility showed limited degradation (within 40%) after being stored under ambient conditions for over 150 days (**Figure 7.1(h**), **Figure F.10, F.11**). We attributed to the excellent oxygen and water barrier resistance of BR. When compared with pristine PDMS elastomer, the oxygen and water permeability of pristine BR were 3136 and 56 times lower, measured by gas diffusion test and dry cup test (ASTM D1653-13), respectively (**Table F.7**).

The self-healing performance of PDPPTVT/BR composite film was tested at room temperature through the pseudo-free-standing tensile tester (**Figure 7.2(a**)). Two pieces of 2:3 composite polymer thin films with a size of 4 mm (length) × 4.7 mm (width) × 60 nm (thickness) were fabricated and floated on water. They were firstly compressed for 20% strain, then left for two seconds before being stretched (**Figure**

7.2(b)). It is observed that the two films adhered to each other autonomously within seconds during compression; the healed film could be strained past its original length by nearly 150%. When subjected to an identical test, a PDPPTVT polymer control did not show any sign of self-healing performance due to the loss of adhesion force (**Figure 7.2(c)**). This observation indicated that BR matrix provides room temperature self-healing mechanically properties for ultrathin films. Furthermore, using the same 2:3 composite film, we demonstrated that the electrical property can be restored (healed), as shown in **Figure 7.2(d)**. The edges of two separate pieces of films were physically compressed on top of a water surface, followed by transferring the film onto a SiO_2 substrate for transistor testing. Through landing probes on different electrodes, the electrical properties of the following film areas were measured: within pristine films, within self-healed region, and across the self-healed region. Both SEM and AFM showed good contact of two films with similar morphology, along with well-defined self-healing boundaries (**Figure 7.2(e,f)** and **Figure F.12**). The hole mobility for Film I, Film II, and healed region was 0.093, 0.088, and 0.084 $cm^2 V^{-1} s^{-1}$, respectively (**Figure F.13** and **Table F.8**). To observe the electrical properties across the whole self-healed region, the charge mobility was extracted purposely from Electrode 4 to Electrode 8, as illustrated in **Figure 7.2(d)**, a long channel length fully crossing the self-healing region; the data showed that charge mobility was maintained within the same order of magnitude, averaging 0.043 $cm^2 V^{-1} s^{-1}$.[350] It is worth noting that, the transfer curve trace from the self-healing region (Electrode 1 to Electrode 2) in **Figure F.14** displayed little resistance enhancement at OFF current (red line curve), while the negative shift in threshold voltage caused lower ON current at the gate voltage of - 60 V due to the effect of longer channel

length (Film I to Film II, green line curve). Furthermore, the self-healed composite film was strained at 50% for 1 cycle, 50 cycles, 100 cycles and 500 cycles. AFM 3D images clearly showed intact self-healed regions, while the charge mobilities of all probed regions were kept on the same order of magnitude before and after strain (**Figure 7.2(g)**, **Figure F.15-F.22** and **Table F.9-F.12**). These results verified that the composite film is self-healable both mechanically and electrically.

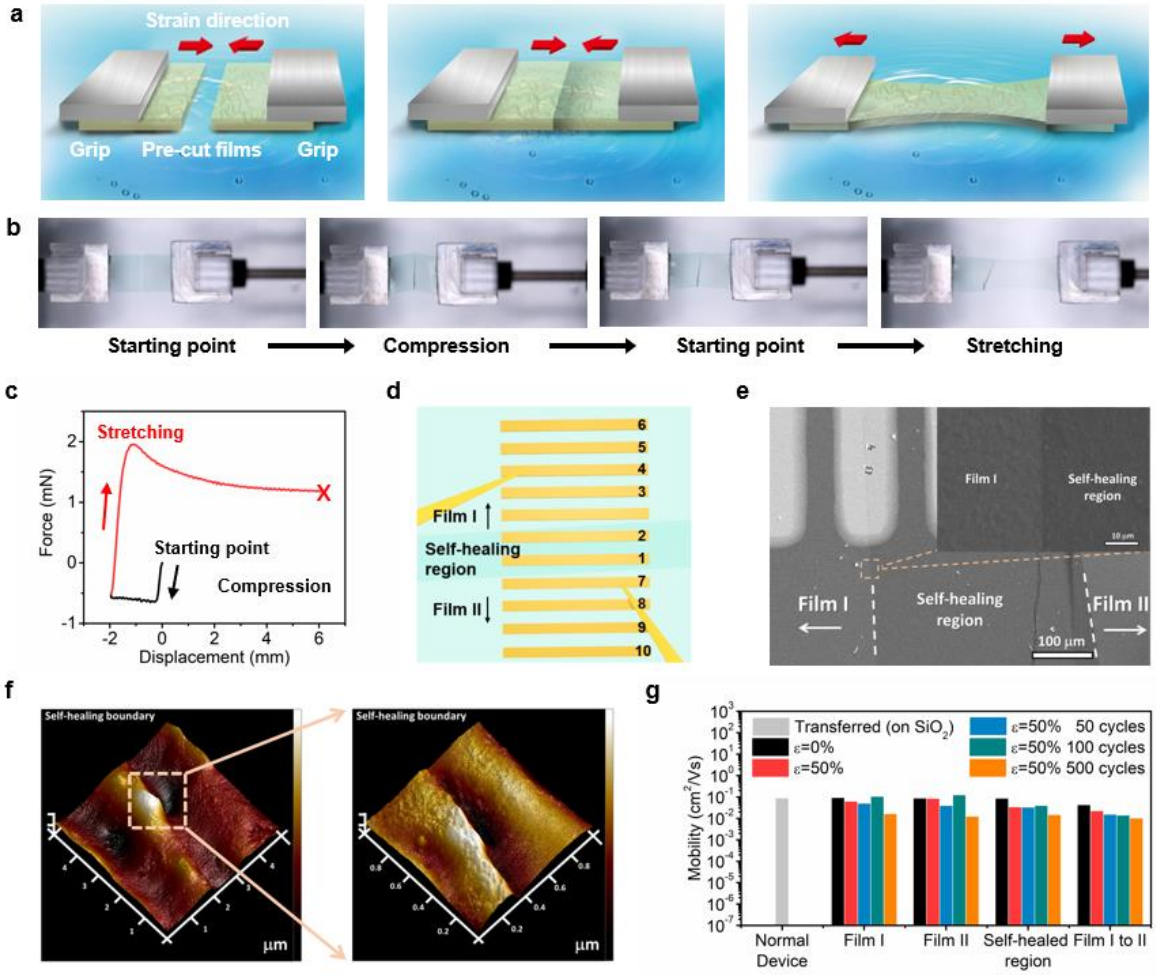

Figure 7.2 *Characterization of self-healing behavior for PDPPTVT/BR semiconducting composites. (a) 3D schematic demonstrating the self-healing process. Two pre-cut films were floated on water upon compression. (b) Optical images of self-healing behavior for 2:3 PDPPTVT/BR composite film. Two films were first compressed at 20% to allow adhesion and later immediately stretched for 150% of the original length (4 mm). (c) Force-displacement plot of 2:3 PDPPTVT/BR composite film during deformation process as described in (b). (d) Schematic illustration of the OFET device fabricated by self-*

healed film. (e) SEM image on the self-healable region of the OFET device. (f) AFM 3D images showing the self-healing boundary of 2:3 PDPPTVT/BR film. (g) Summary of charge carrier mobility for self-healed 2:3 PDPPTVT/BR composite films measured at different electrodes before and after strain for various cycles.

The observed self-healing performance results from the following three procedures: the compression of two separate films allows for close contact of both BR chains and PDPPTVT chains; the tackiness of BR enables two films to attach with each other; the fast segmental motion of low T_g BR polymer chains under room temperature leads to the reconstruction of conjugated PDPPTVT polymer chains, thus they can come back into contact. Together with PDPPTVT chains in contact upon compression, the conducting pathway for intermolecular hopping is built. We performed additional test to replace one side of PDPPTVT/BR composite to the PDPPTVT/polystyrene film, and healing ability drops evidently. Compared with previously reported conjugated polymer/elastomer composites, the PDPPTVT/BR composite film discussed above is the softest and most deformable system with tear-resistant and self-healable performances reported to date.

To demonstrate the general applicability of this method to create self-healable films, poly(3-hexylthiophene) (P3HT) and P3HT/BR composite films were also prepared and compared for their room temperature self-healing ability. For the neat P3HT film, upon compressing between two separate edges, the film did not heal itself, while the 2:3 composite film healed autonomously on the water surface upon close contact (**Figure F.23**). For the 2:3 P3HT/BR composite film, similar morphologies of the self-healing boundary were shown when compared with non-strained films upon 50% strain for 500 stretching cycles, while the charge mobility was slightly affected (**Figure F.24-F.34** and

Table F.13-F.17). This illustrated the capability of the proposed method in introducing self-healable performance to other conjugated polymer systems.

To fully understand the observed mechanical and electrical properties of the semiconductor composite, detailed thermal and morphological studies were performed. The glass transition temperature of different blend ratios of thin films was determined by alternating current (AC)-chip calorimetry. Two clear transitions at -57 °C and 10 °C were observed, attributed to backbone transitions for BR and PDPPTVT, respectively (**Figure F.35**).[16,26,351] The sub-room temperature T_g of BR directly contributed to the high polymer chain flexibility and mobility at the room temperature, leading to a record-low elastic modulus for the composite film. Additionally, the combined tackiness and fast chain mobility allows the polymer composite to heal autonomously at room temperature. Exploration of the thin film morphology for different blend ratios of PDPPTVT/BR began with chemical imaging on the film surface using atomic force microscopy in combination with infrared-spectroscopy (AFM-IR, Anasys nanoIR-3) (**Figure 7.3(a-k)** and **Figure F.36**).[352] Through comparison of IR absorption spectra of the two component polymers, two distinct characteristic absorption wavelengths, 1664 cm^{-1} (C=O stretching vibration in amide) and 1462 cm^{-1} (CH_3 torsional vibration) respectively, were chosen to selectively distinguish between the PDPPTVT and BR phase, respectively (**Figure 7.3(b-c)**). Firstly, AFM tapping mode was applied to obtain the phase images (**Figure 7.3(d-g)**). Next, the IR laser with the characteristic wavelength was aligned and focused at the gold coated AFM tip for a second scan. Upon absorption of the characteristic IR light, a thermal expansion would occur in the corresponding polymer phase, which was recorded by the change of tapping frequency of AFM tip, while the

specific location was marked by a color (the green color for the PDPPTVT phase and red for the BR phase (**Figure 7.3(h-k)**). Due to the similar surface energy of two polymer components (PDPPTVT and BR) and high aggregation tendency of PDPPTVT polymer chains, a hieratical structure of PDPPTVT aggregates in BR matrix was formed at different blend ratios (**Figure F.37** and **Table F.18**).

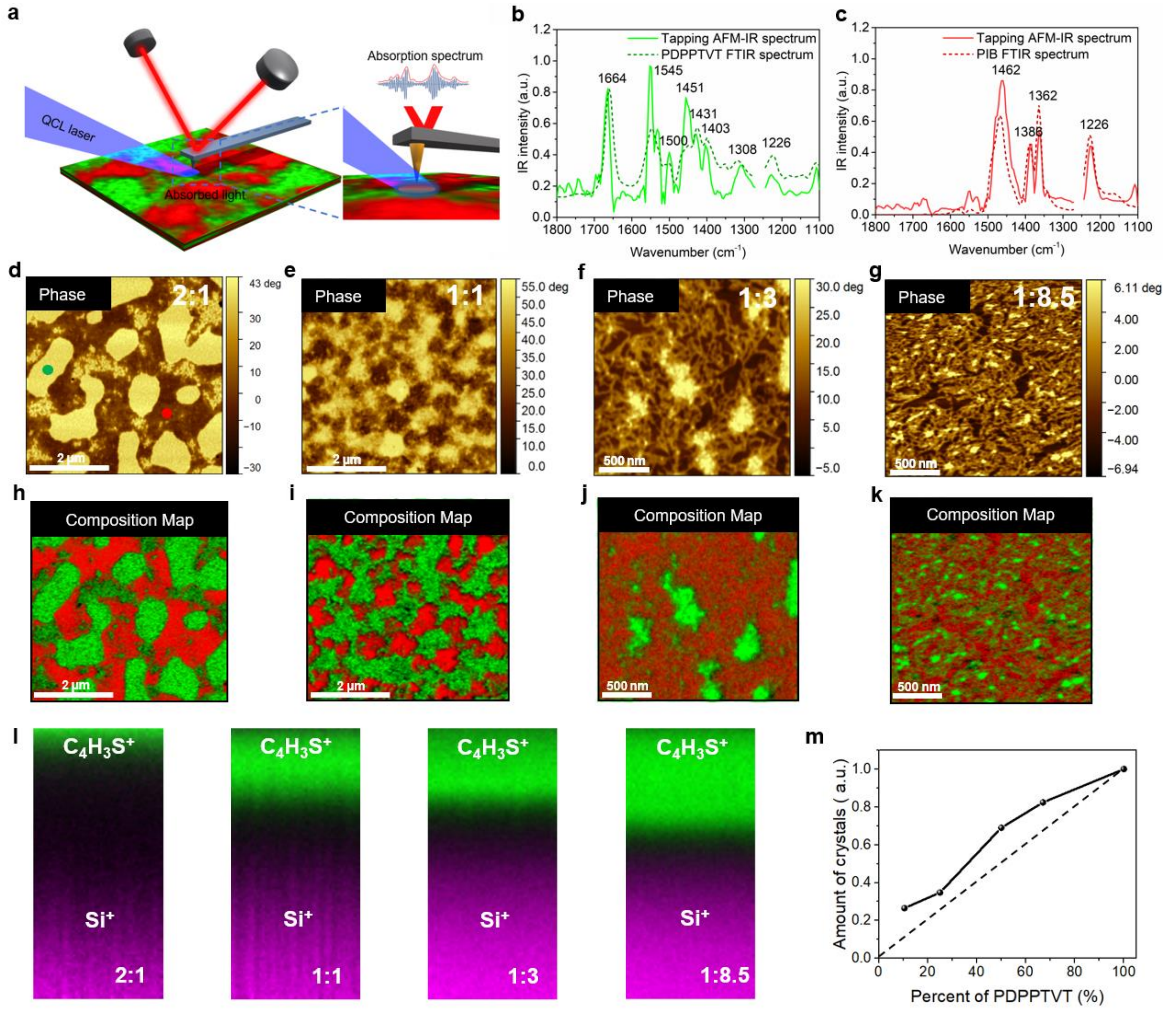

Figure 7.3 *Morphological characterization of different blend ratios of PDPPTVT/BR systems. (a-k) Nano IR-AFM test. (a) 3D schematic of the working principle for the IR-AFM system. (b, c) IR absorption spectrum of PDPPTVT and BR polymer taken by the IR-AFM and FTIR. The characteristic IR absorption peaks selected for PDPPTVT and BR are 1664 cm^{-1} and 1462 cm^{-1}, respectively. (d-g) AFM phase images for different blend ratios of PDPPTVT/BR composite film. (h-k) IR-AFM overlay images highlighting the distributions of PDPPTVT and BR (green color represents for PDPPTVT at 1664 cm^{-1} and red color represents for BR at 1462 cm^{-1}). (l) TOF-SIMS chemical depth profiling*

overlay (19 μm lateral field of view × 200 erosion frames) for samples with different blend ratios of PDPPTVT/BR composite film. The composition of $C_4H_3S^+$ (from PDPPTVT) is marked with green color and Si^+ (from Si wafer) is marked with purple color. (m) Relative degree of crystallinity for different blend ratios of PDPPTVT-BR based on (100) lamellar peak.

For 2:1 composite film, PDPPTVT formed micrometer size aggregates across the surface. As the BR content exceeded 50%, the size of aggregates was greatly reduced and a mesh-like network comprising of interpenetrating PDPPTVT fibrils started to appear together with sparsely dispersed large PDPPTVT aggregates. At 1:8.5 blend ratio, the large aggregates almost fully disappeared and well dispersed PDPPTVT fibrils were observed to be scattered across the film. Due to the high deformability of the fibril-like geometry, these findings line up well with the greatly improved fracture strain as well as the high electrical performance of the conjugated polymer composites even under a high fraction of BR. The phase separation behavior was further studied by resonant soft X-ray scattering (RSoXS) (**Figure F.38**), an inverse phase characterization technique that is sensitive to chemical composition. For 2:1, 1:1 and 1:3 blend systems, two regions of interest were observed from the 1D scattering profile, including a phase separation size of greater than 600 nm and a much smaller phase separation size around 60 nm, corresponding to the distance between large PDPPTVT aggregates and small fibers, respectively; these observations indicated that the PDPPTVT formed a unique hierarchical structure. However, only the small-scale phase separation was observed for the 1:8.5 blend, which can be attributed to the absence of large PDPPTVT aggregates, as seen in the AFM-IR measurement (**Figure 7.3(g,k)**). Overall, AFM-IR showed that at high BR content, conjugated polymers are dispersed as individual fibril structure within the continuous BR matrix.

Vertical phase separation was probed by elemental mapping using time-of-flight secondary ion mass spectrometry (TOF-SIMS) along the film thickness direction, where $C_4H_3S^+$ and Si^+ were characteristic signals originating from PDPPTVT and the Si substrate, respectively (**Figure 7.3(l)** and **Figure F.39**). At 2:1 ratio, PDPPTVT was shown to be mostly concentrated on the top surface of the 50 nm thin film. As the weight percent of BR increased, PDPPTVT tended to become better dispersed in the polymer composite. For 1:8.5 composite film, PDPPTVT was evenly mixed across the thickness direction. This observation implied that a higher proportion of BR leads to better dispersion of PDPPTVT fibers, providing uniform film deformation and water/oxygen stability and resulting in greater deformability. The grazing-incidence wide angle X-ray scattering (GIWAXS) experiment further confirmed the stable charge carrier mobility of the composite film, showing that PDPPTVT maintained its crystallization ability in different composite films, as evidenced by the clear (100) lamellar peak in the out-of-plane direction and near-linear decrease of relative degree of crystallinity (RDoC) with increasing percentage of BR in the composite film (**Figure 7.3(m)** and **Figure F.40**). Ultraviolet-visible (UV-Vis) spectroscopy demonstrated limited difference in these composite films except for an increase in the intensity of the 0-0 transition peak with increasing BR content, which demonstrates enhanced aggregation through phase separation while maintaining the crystallization ability (**Figure F.41** and **Table F.19**). In summary, detailed morphological characterizations suggested that the composite film with a high blend ratio produced a continuous PDPPTVT fibrillar structures embedded in the BR matrix, resulting in excellent mechanical property and stable electrical performance. Further morphological control methods including varying temperature

and/or additive conditions are also promising, although they are not under the scope of current work.[353]

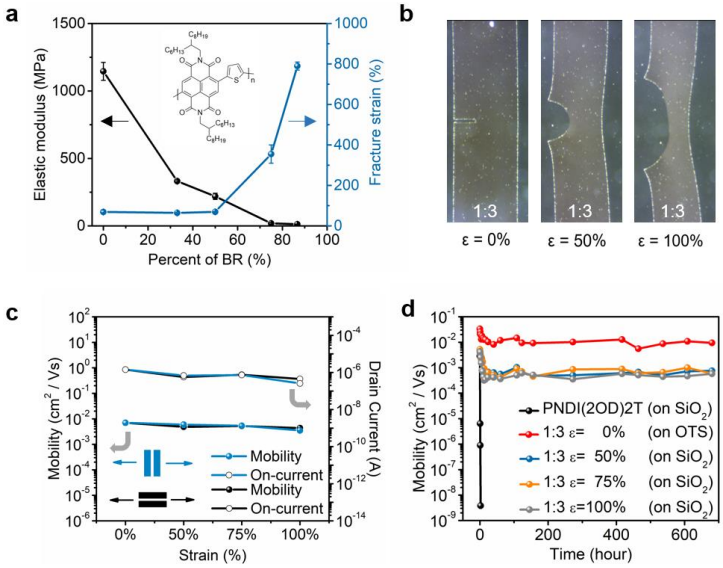

Figure 7.4 *Mechanical and electrical performance of PNDI(2OD)2T/BR composite films. (a) Elastic modulus and crack onset strain for different blend ratios of PNDI(2OD)2T/BR. (b) Optical images of notched 1:3 composite film under stretching at different degrees of strain. (c) Charge carrier mobility and drain current of OFET devices made by 1:3 ratio of PNDI(2OD)2T/BR blend system under various degrees of strain. (d) Time-dependent charge mobility of OFET devices for 1:3 ratio PNDI(2OD)2T/BR blend system under various degrees of strain.*

In addition to the p-type DPP-based D-A polymers, the same blending method was applied to three well-known semiconducting polymers, P3HT, poly(2,5-bis(3-hexadecyllthiophen-2-yl)thieno[3,2-b]thiophene) (PBTTT) and an air-sensitive n-type polymer, poly{[N,N'-bis(2-octyldodecyl)naphthalene-1,4,5,8-bis(dicarboximide)-2,6-diyl]-alt-5,5'-(2,2'-bithiophene)} (PNDI(2OD)2T).[354,355] All three composite films demonstrated a dramatic improvement in mechanical performance (lower modulus, better deformability and crack-resistance) when using BR as the matrix phase (**Figure 7.4(a, b)**, **Figure F.42, F.43** and **Table F.20**). In addition, the charge transport properties of pristine PNDI(2OD)2T and the 1:3 PNDI(2OD)2T/BR composite films were tested in the

ambient environment to further validate their superior oxygen/water stability. The mobility of pristine PNDI(2OD)2T dropped by 6 orders of magnitudes within 2h in air due to oxygen doping; in comparison, the 1:3 composite film was electronically stable for 2 months, even under 100% strain (**Figure 7.3(e)**, **Figure F.44, F.45** and **Table F.21**). The initial decrease in charge mobility of the pristine PNDI(2OD)2T presumably resulted from oxygen diffusion into the dielectric layer, which was significantly delayed by the existence of BR in the composite film.[14] These results illustrate that using BR as the elastomer matrix for deformable and healable composites can be widely applied to a variety of semiconducting polymers, especially those with known sensitivity to oxygen and/or water. On a broader scale, such method also shows a great potential in fabricating novel stretchable conductive nanocomposites.[356]

7.4 Conclusions

In summary, we have demonstrated the use of BR as a new matrix polymer for the preparation of semiconducting composites that display unprecedented mechanical and electrical performance, including record low modulus, record high deformability, and resistance to crack-propagation, as well as strain-insensitive electronic property, autonomous healable and ambient-stable charge carrier mobility for both n-type and p-type D-A polymers. Developing new elastomers for conjugated polymer composite can facilitate future developments towards more robust flexible and deformable electronics for wearable applications.

CHAPTER VIII – FUTURE DIRECTIONS

To conclude, this dissertation focuses on investigating the structure-thermal/mechanical property-morphology relationship for DPP-based semiconducting polymers through pseudo-free standing tensile tests, AC-chip calorimetry measurement, substrate-supported DMA tests, molecular dynamics simulations, and multimodal morphological characterizations. These studies here mark the beginning of the investigations on more structurally complicated high-performing CP thin films through the combination of experimental and computational methods.

Firstly, the exploration of film-on-water tensile tests is only at its initial stage. Up until now, only a few metal and polymer samples have been investigated to a less extent; more complicated methods like temperature-dependent mechanical tests have not been reported. Future studies can also be expanded to functional materials like metal-organic frameworks (MOFs)[357–361] and 2D materials like graphene.[39,362–365] Specifically, studies on the fracture behavior of these materials still lack in the current literature. Furthermore, only water has been utilized as the liquid supporting layer until now. The selection of a variety of liquids and the detailed characterization of the thin-film-liquid interface, *i.e.*, solvent infiltration, surface relaxation, and the effect of temperature, will provide a more in-depth understanding of thin-film mechanics. In a broader context, free-standing tensile tests enabled by liquid removal can serve as a universal method for multimodal characterizations through the combination of spectroscopy and scattering techniques.

Next, while a general T_g prediction model is built for DPP-based polymers with various alkyl side-chain lengths, the effect of side-chain branching position, different types of heteroatom-containing side-chains, and asymmetrical side-chains have not been

carefully studied yet. Similarly, the size and geometric effect of fused rings in the polymer backbone still needs systematically designed experiments to provide further understanding. Meanwhile, the proposed techniques and methodologies here are also transferrable to study the thermal properties of other semiconducting polymer systems, *i.e.*, naphthalene diimide (NDI)-based and isoindigo (IID)-based CPs. A more generally applied T_g prediction model is promising with sufficient experimental results and the assistance of molecular dynamics simulation or all atomistic simulations. More importantly, understanding the interplay between the side-chain and backbone dynamics in both solution- and solid-state is vital for the design of new semiconducting polymers with desired molecular structures.

Finally, physical blending is an economical and efficient way to achieve mechanically and electronically high-performing semiconducting polymer systems. It is crucial to ensure a stable polymer thin-film morphology under large-scale processing conditions like roll-to-roll printing. Thus, it is promising to take advantage of thermally stable semiconducting polymer composites, solution printing methods, and multimodal in-situ characterization techniques to promote the commercialization of organic electronic devices.

APPENDIX A

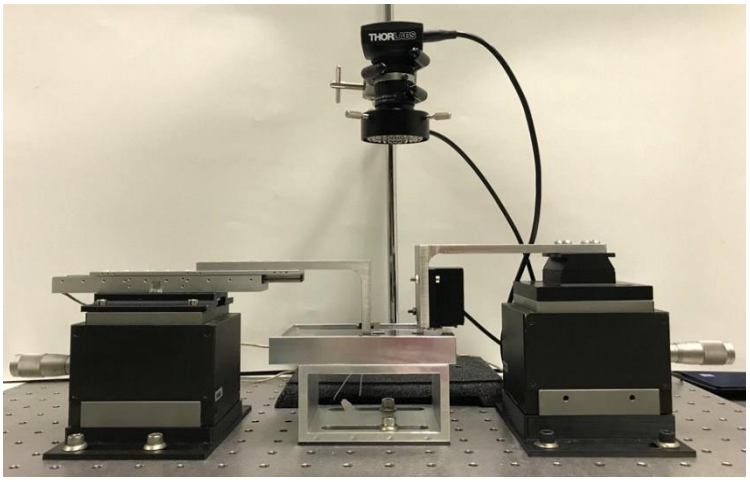

Figure A.1 *Schematic illustration of tensile tester set-up for floated ultrathin film. A pre-patterned dog-bone shaped film floating on the surface of water was attached by two aluminum grips coated with silicone rubber.*

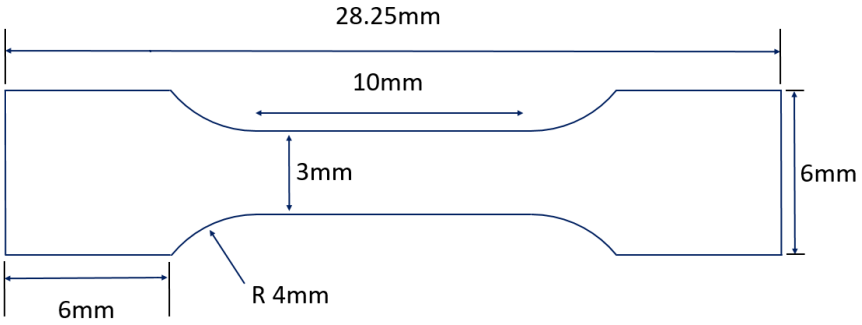

Figure A.2 *The design of the dog-bone shaped etch mask.*

Figure A.3 *Patterning organic electronic thin films into dog-bone shape. (a) Dog-bone shaped PDMS masks were placed on top of semiconducting polymer/PSS bilayer film. (b) After plasma etching, dog-bone patterns from the etch mask were transferred to under lying bilayer polymeric films. (c) Dog-bone shaped bilayer films after removing the PDMS masks from Si substrate.*

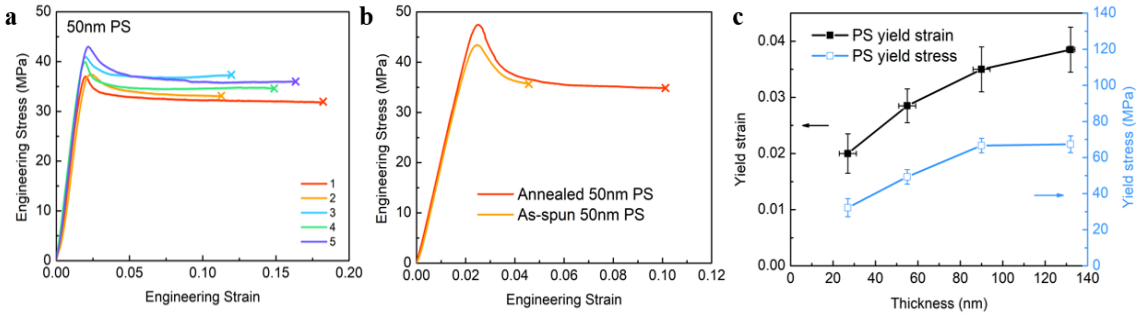

Figure A.4 *(a) Stress-strain curves for five independent measured PS thin films with 50nm thickness. (b) Stress-strain curves for as-spun PS film and for film with subsequently annealed film at 120°C for overnight. The PS samples were 50 nm thick (c) Yield strain and yield stress versus thickness curves for PS films.*

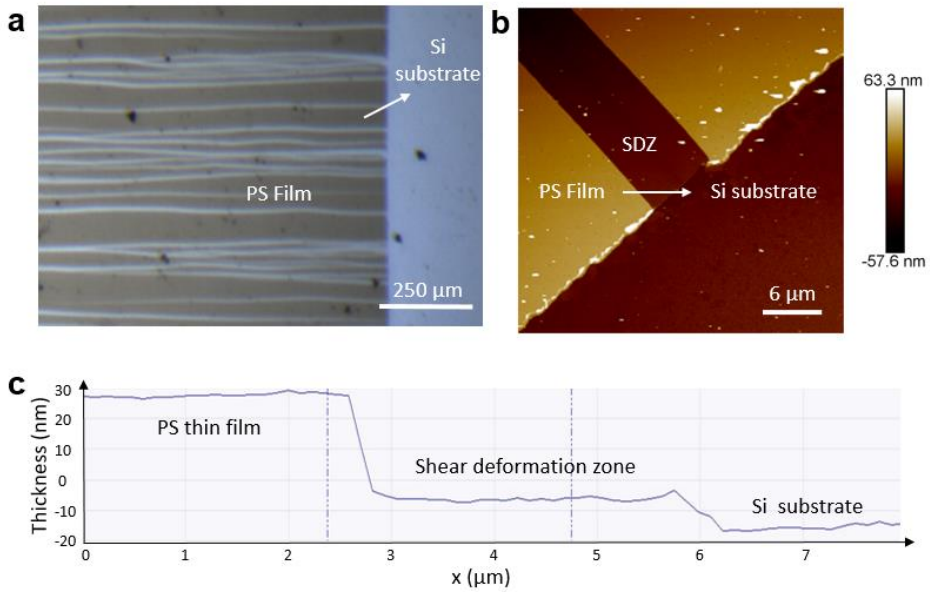

Figure A.5 *(a) Optical microscope image of stretched PS (20% strain) on Si substrate. After stretch, the PS film was picked up by a silicon wafer. The bright horizontal lines on PS film represent for the shear deformation zone (SDZ). (b) AFM height image of the edge of PS film using tapping mode, the arrow represents for scanning direction of the tip. (c) Height profile along the scanning direction shown in (b), PS film has a thickness of ~ 45 nm, SDZ has a thickness of ~ 8 nm.*

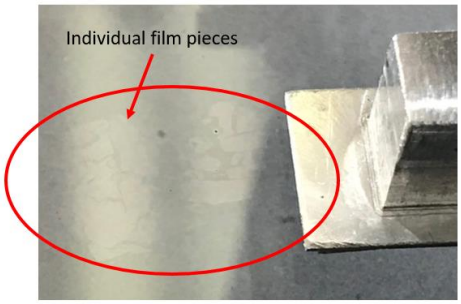

Figure A.6 *Photograph of broken 23 nm thick DPP-TVT film on water surface.*

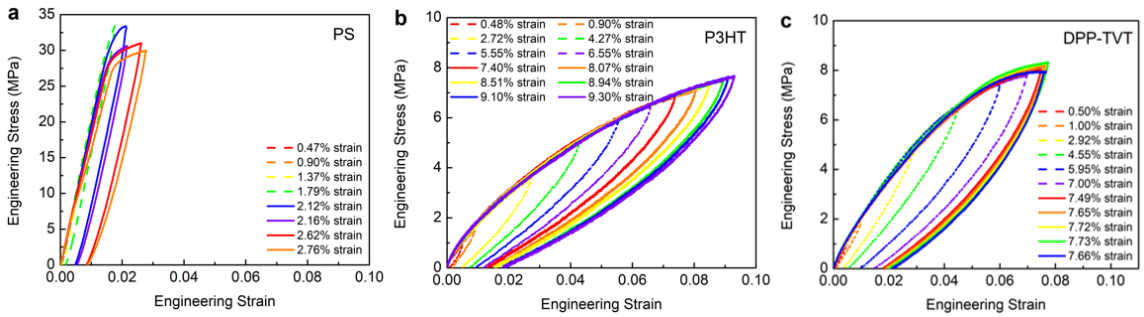

Figure A.7 *Hysteresis tests plotted as stress-strain curves for (a) PS, (b) P3HT and (c) DPP-TVT.*

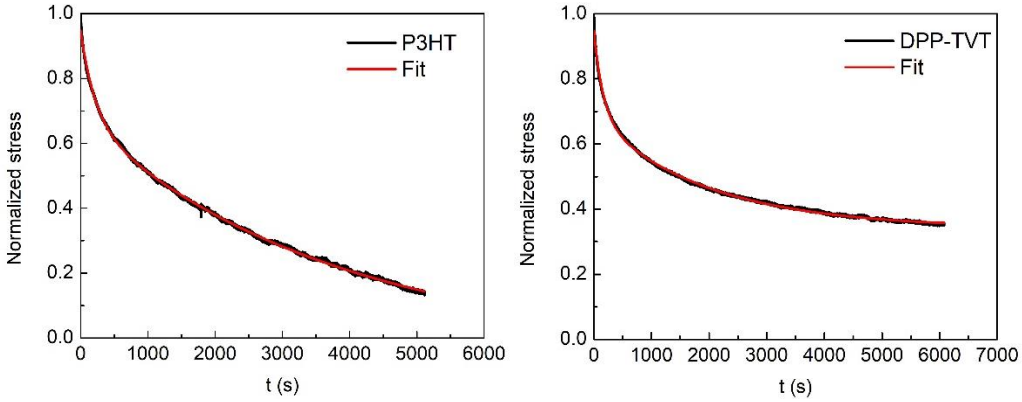

Left: P3HT: $\boldsymbol{\sigma = 0.271 * e^{-\frac{t}{216}} + 0.712 * e^{-\frac{t}{3709}} - 0.035}$

Right: DPP-TVT: $\boldsymbol{\sigma = 0.263 * e^{-\frac{t}{162.6}} + 0.342 * e^{-\frac{t}{1949}} + 0.342}$

Figure A.8 *Two Maxwell models in series were fitted to the stress relaxation curves of P3HT and DPP-TVT. The fast drop within 500s is mostly from the relaxation of the shorter and more mobile chains in the conjugated polymer, which is contributed from the first component of the equation. The second component of the equation contributes to a slower relaxation process, which might due to impediments from entangled network.*

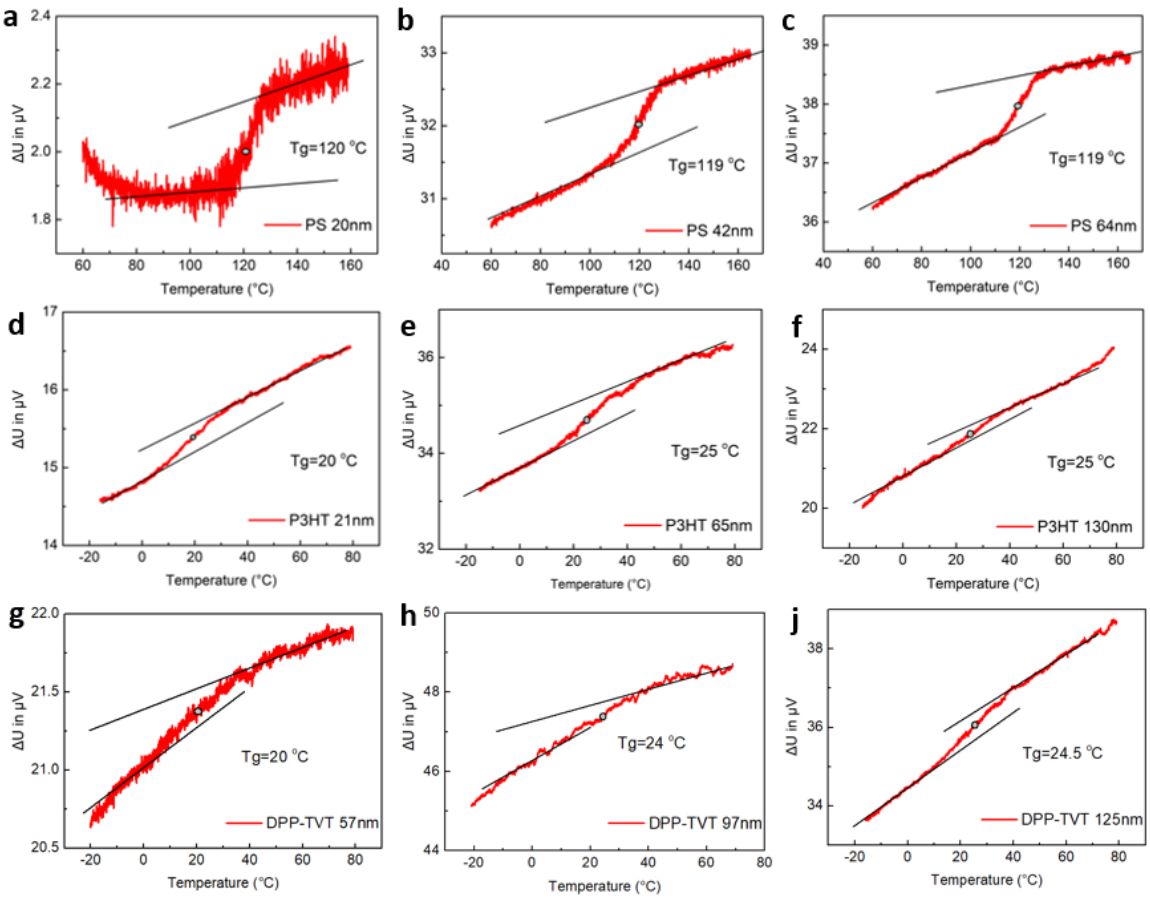

Figure A.9 *Calorimetric ac-chip measurement cooling curves for (a-c) PS, (d-f) P3HT and (g-j) DPP-TVT films with different thicknesses. It is shown that the T_g of PS, P3HT and DPP-TVT is 120 °C, 25 °C and 24°C, respectively. Due to a relative high frequency (10 Hz) of ac-chip, the measured T_g is typically ~ 20 °C higher than that measured by normal differential scanning calorimetry (DSC).*

Table A.2 *Summary Table for peak positions of P3HT and DPP-TVT in GIWAXS*

P3HT	**Out of Plane**			**In Plane**		
q (Å^{-1})	0% strain	10% strain	20% strain	0% strain	10% strain	20% strain
(100)	0.365	0.343	0.33	0.337	0.342	0.344
(200)	0.713	0.685	0.668	\	0.67	0.682
(300)	1.075	1.051	1.059	\	1.08	1.059
(010)	1.47	1.541	1.545	1.535	1.55	1.573

DPP-TVT	**Out of Plane**			**In Plane**		
q (Å^{-1})	0% strain	10% strain	20% strain	0% strain	10% strain	20% strain
(100)	0.248	0.25	0.245	\	\	\
(200)	0.483	0.486	0.486	\	\	\
(300)	\	0.828	0.741	\	\	\
(010)	\	\	\	1.598	1.6	\

APPENDIX B

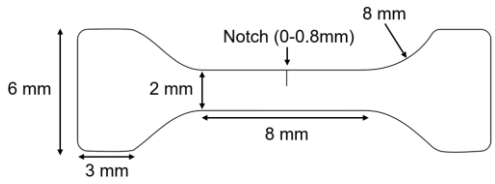

Figure B.1 *Dimension of dog-bone shaped thin film sample for Begley-Landes method.*

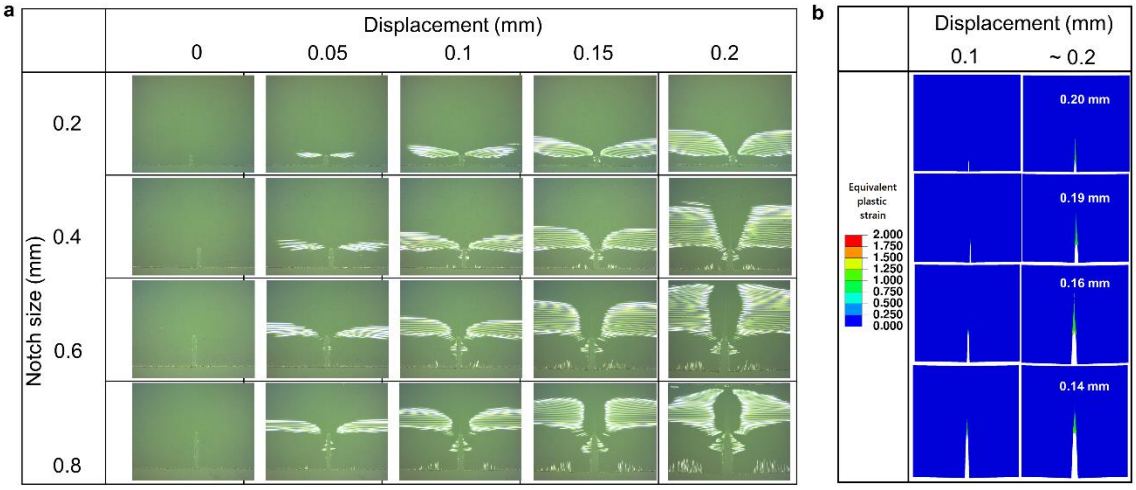

Figure B.2 *Optical and simulation images of 80 nm thick polystyrene film (173 kg/mol) with various notch sizes at different displacement. (a) Optical images. (b) Finite element simulation results of equivalent plastic strain distribution.*

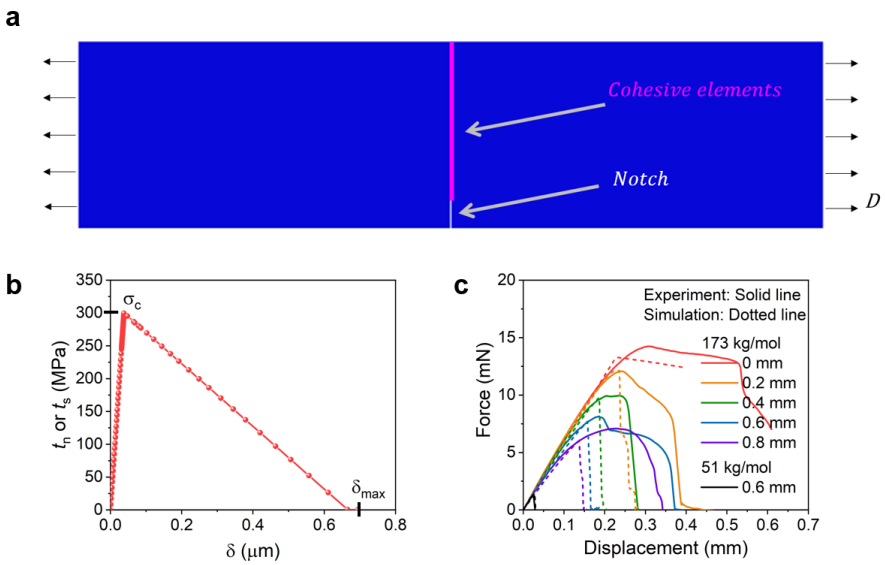

Figure B.3 *Finite element simulation with Gent model. (a) Crack growth resistance curve (R-curve) for Gent model of initial modulus, 15 MPa with different parameters of J_m. (b) Force-displacement curves of PS with an initial notch of 0.6 mm for each Gent model with corresponding values of J_m.*

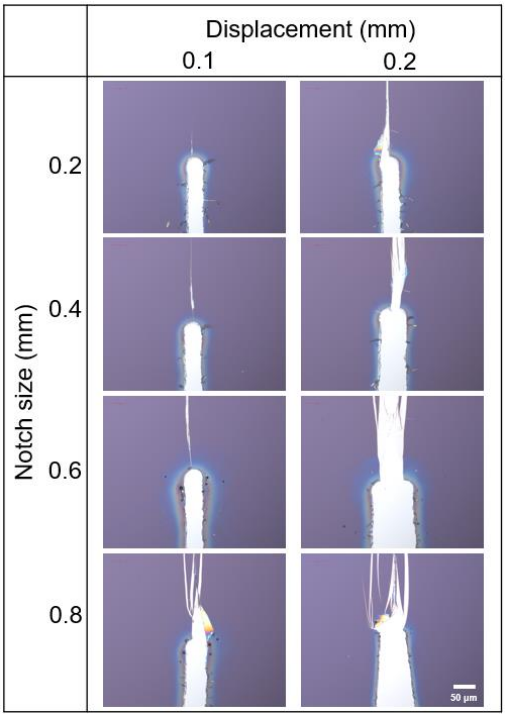

Figure B.4 *Optical microscope images of the notch tip for 86 nm 173 kg/mol PS thin films sitting on top of silicon substrate. The white band-like region on the bottom represents for crack propagation and the formation of shear deformation zone.*

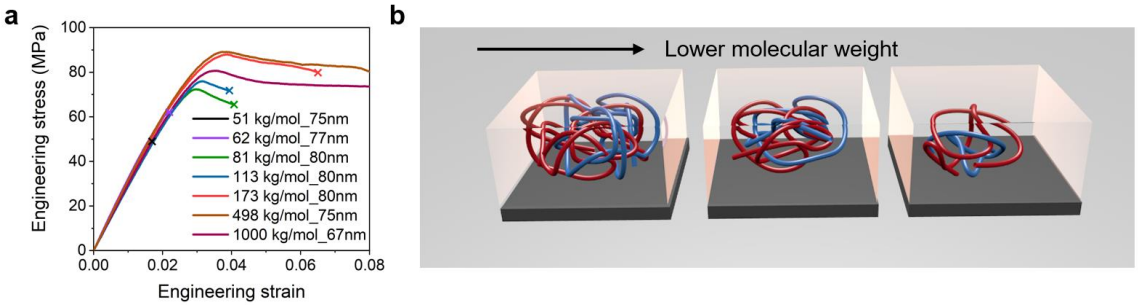

Figure B.5 *(a) Engineering stress-strain curves of polystyrene thin films with various molecular weights at a similar thickness around 80 nm. (b) 3D scheme showing molecular weight effect on the number of chain entanglements at the same film thickness.*

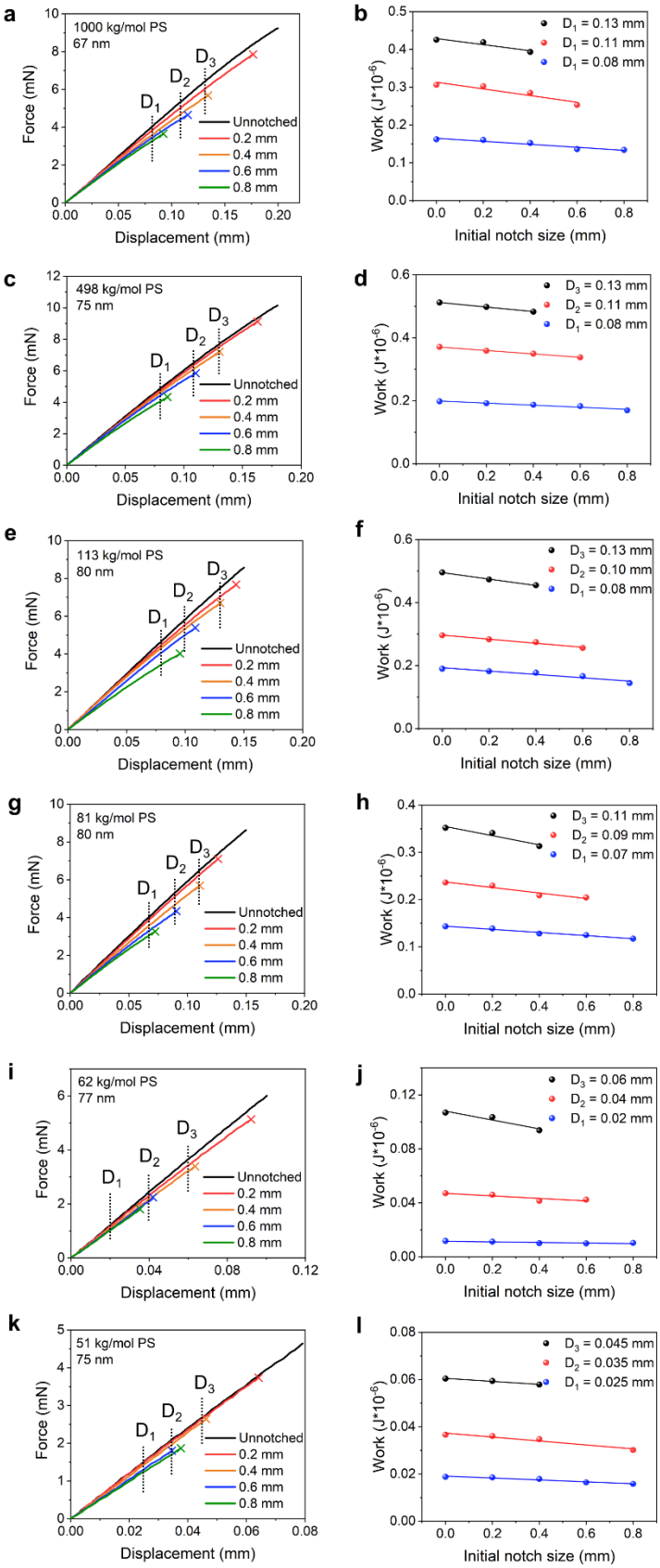
a
1000 kg/mol PS
67 nm
D1
D2
D3
Unnotched
0.2 mm
0.4 mm
0.6 mm
0.8 mm
Force (mN)
Displacement (mm)
b
D1 = 0.13 mm
D1 = 0.11 mm
D1 = 0.08 mm
Work (J*10-6)
Initial notch size (mm)
c
498 kg/mol PS
75 nm
d
D3 = 0.13 mm
D2 = 0.11 mm
D1 = 0.08 mm
e
113 kg/mol PS
80 nm
f
D3 = 0.13 mm
D2 = 0.10 mm
D1 = 0.08 mm
g
81 kg/mol PS
80 nm
h
D3 = 0.11 mm
D2 = 0.09 mm
D1 = 0.07 mm
i
62 kg/mol PS
77 nm
j
D3 = 0.06 mm
D2 = 0.04 mm
D1 = 0.02 mm
k
51 kg/mol PS
75 nm
l
D3 = 0.045 mm
D2 = 0.035 mm
D1 = 0.025 mm

Figure B.6 *Tensile test for PS with various crack lengths under different molecular weights. (a, b) 1000 kg/mol. (c, d) 498 kg/mol. (e, f) 113 kg/mol. (g, h) 81 kg/mol. (i, j) 62 kg/mol (l, l) 51 kg/mol. (a, c, e, g, i, k) force-displacement curves for various notch lengths. (b, d, f, h, j, l) the work done for propagating the notch with different notch sizes was calculated using the area under the force-displacement curve with selected displacement value.*

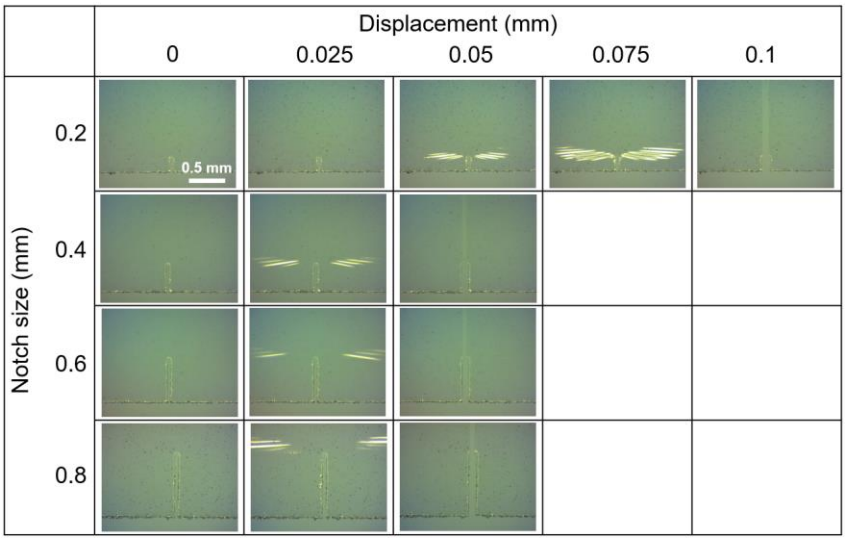

Figure B.7 *Optical images of 75 nm thick polystyrene film (51 kg/mol) with various notch sizes at different displacement.*

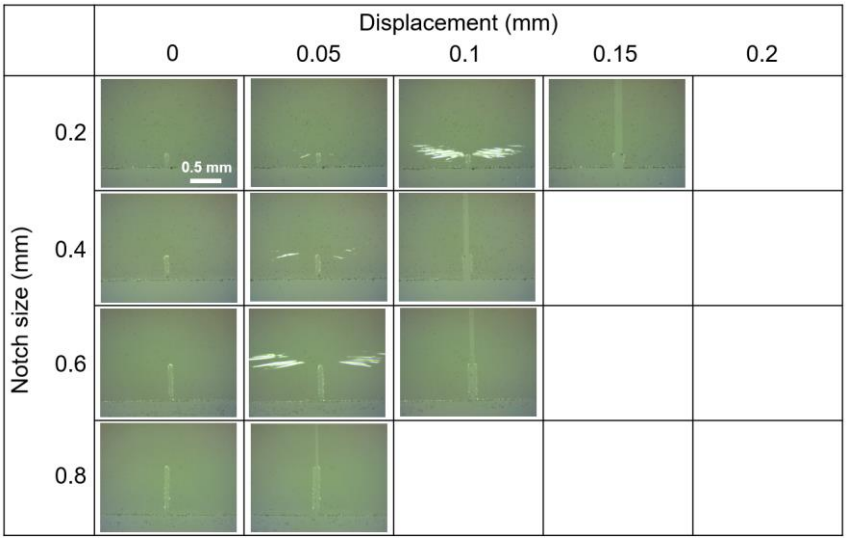

Figure B.8 *Optical images of 77 nm thick polystyrene film (62 kg/mol) with various notch sizes at different displacement.*

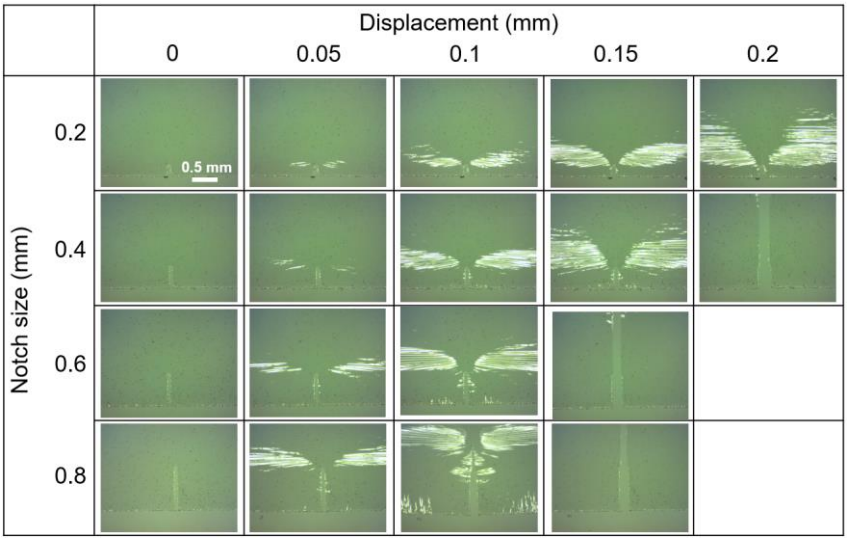

Figure B.9 *Optical images of 80 nm thick polystyrene film (81 kg/mol) with various notch sizes at different displacement.*

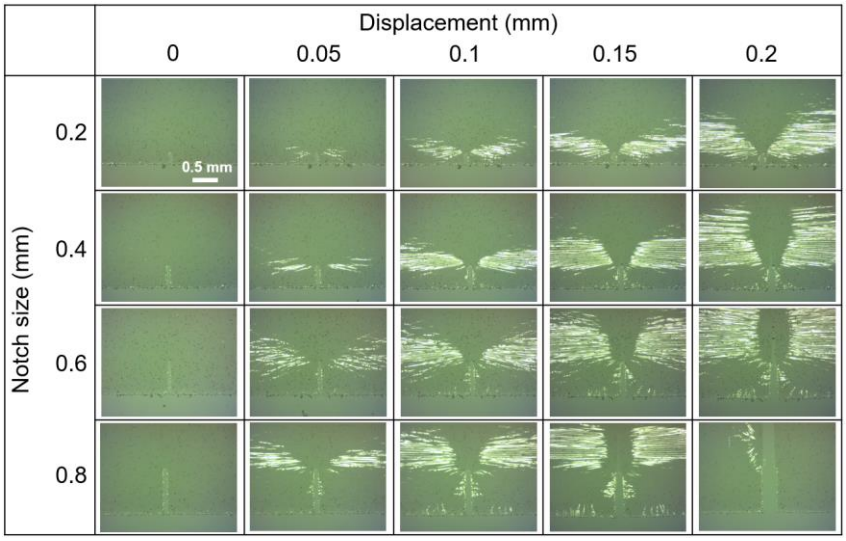

Figure B.10 *Optical images of 80 nm thick polystyrene film (113 kg/mol) with various notch sizes at different displacement.*

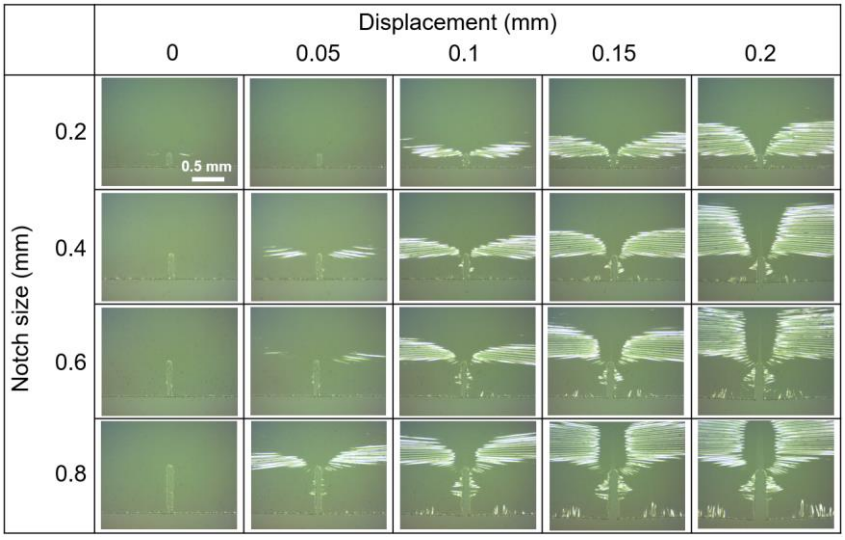

Figure B.11 *Optical images of 75 nm thick polystyrene film (498 kg/mol) with various notch sizes at different displacement.*

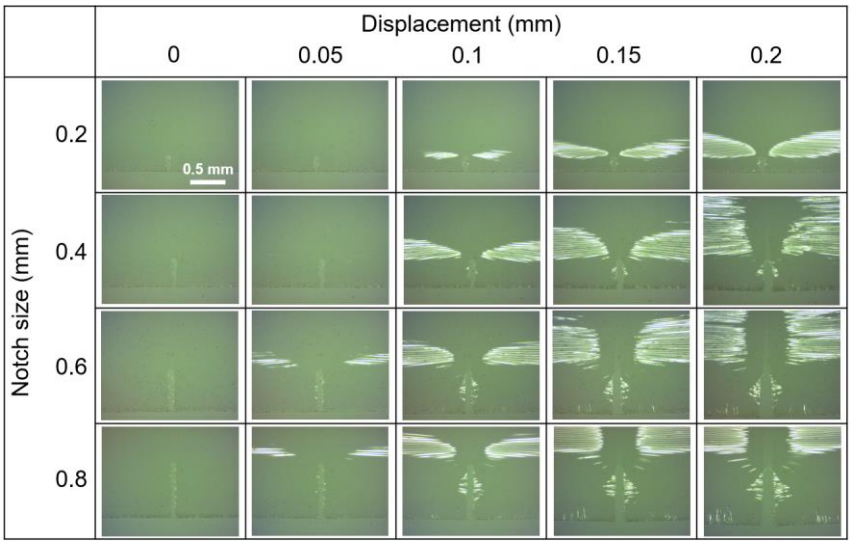

Figure B.12 *Optical images of 67 nm thick polystyrene film (1000 kg/mol) with various notch sizes at different displacement.*

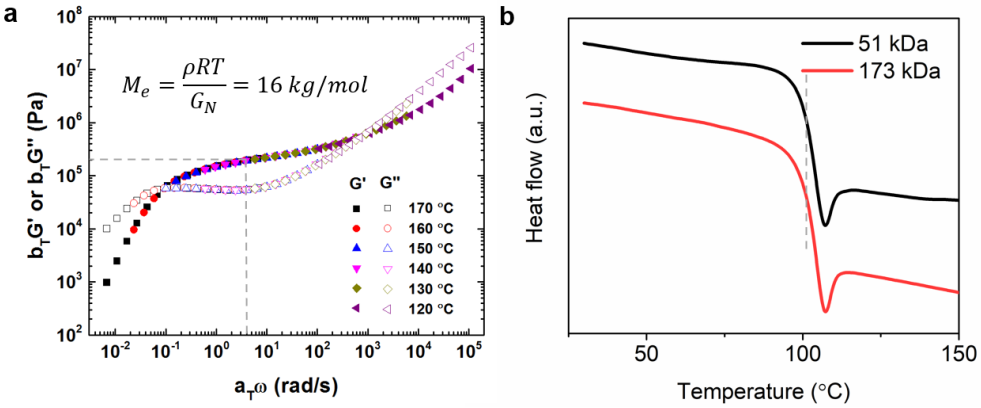

Figure B.13 *(a) Dynamic moduli (G' and G'') master curves of 173 kg/mol PS at a reference temperature of 150 ºC. The dashed horizontal line indicates the rubbery plateau modulus GN of 0.21 MPa. The entanglement molecular weight of 16 kg/mol was obtained with the equation in the plot. (b) DSC curves from the reheating scan with a heating rate of 10 ºC/min for 51 kg/mol and 173 kg/mol PS after cooling from 150 ºC at the same rate.*

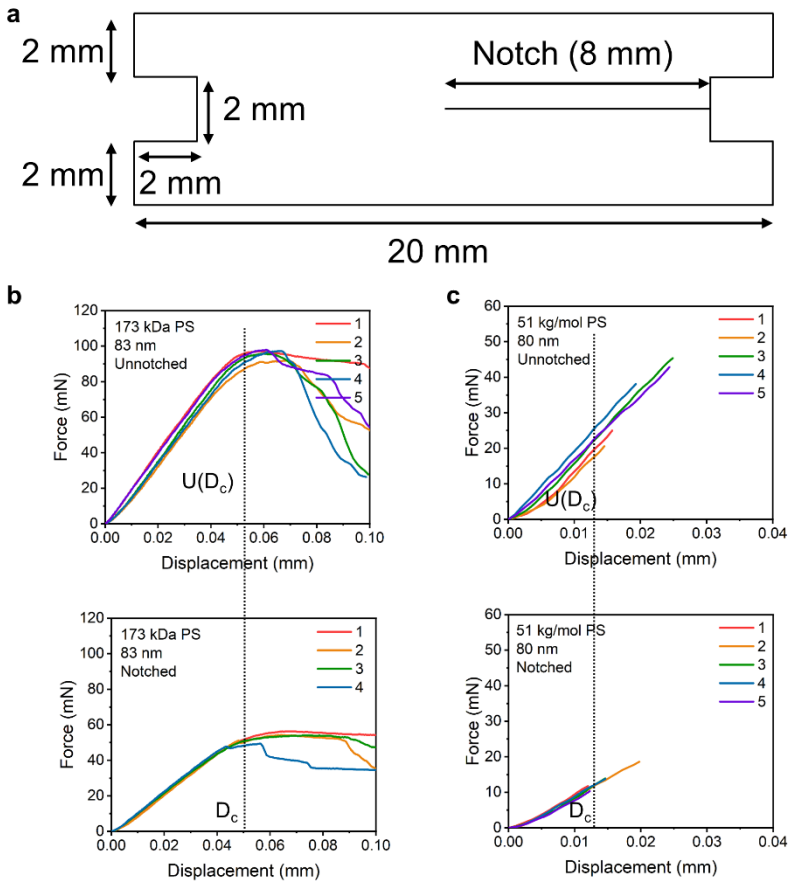

Figure B.14 *Pure shear test for 173 kg/mol and 51 kg/mol PS. (a) Sample geometry for pure shear test. (b, c) Five representative force-displacement curve for both unnotched and notched (b) 173kg/mol PS samples and (c) 51 kg/mol PS samples.*

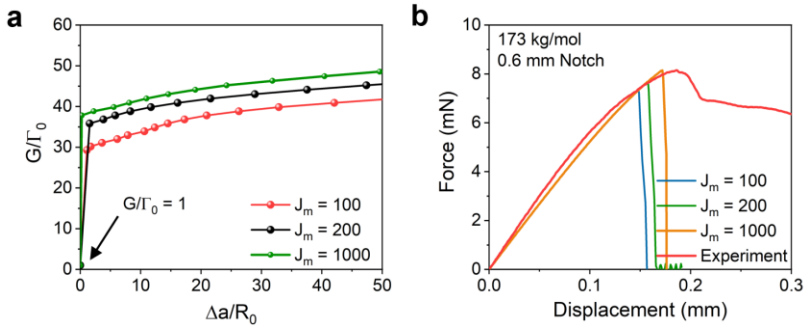

Figure B.15 *Effect of the stretching limit parameter J_m in the finite element simulations on the fracture behavior of 173 kg/mol PS. (a) Crack growth resistance curve (R-curve) from the K-field zone method, and (b) force-displacement curves of dog-bone shaped PS samples with an initial notch of 0.6 mm for different J_m.*

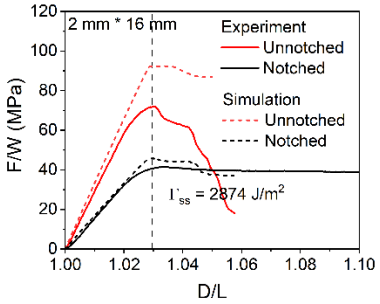

Figure B.16 *Pure shear test simulation for samples with the same* dimension as the experiment. A lower steady-state fracture energy of 2874 J/m2 is measured.

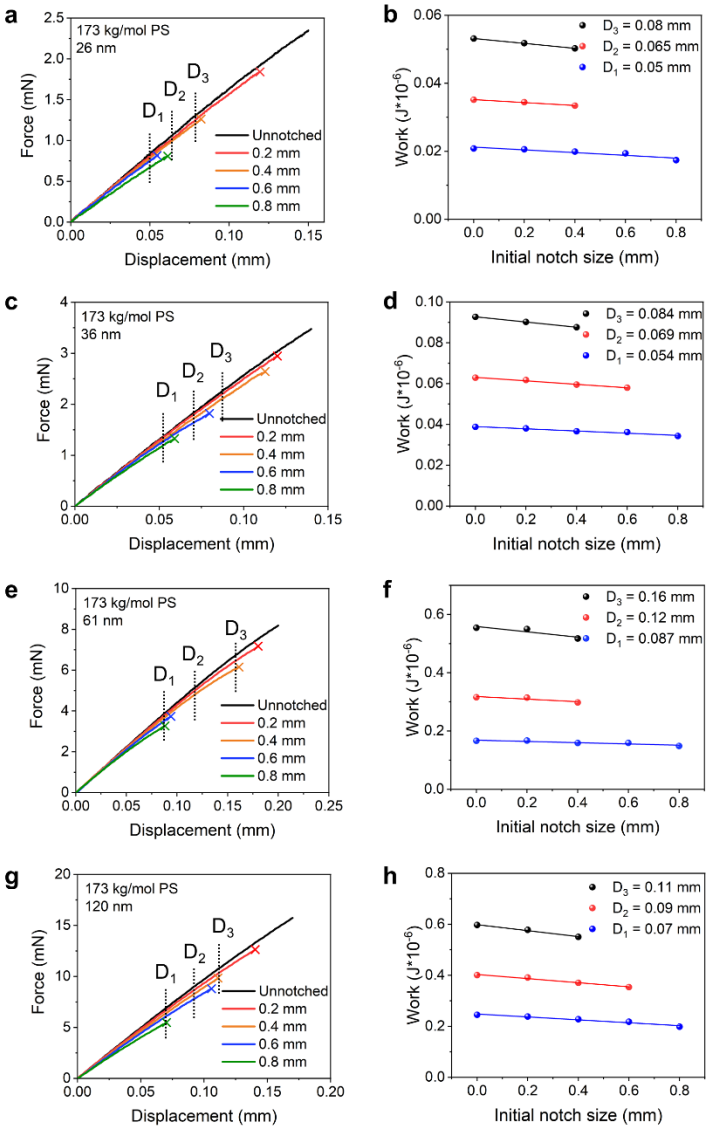

Figure B.17 *Tensile test for 173 kg/mol PS with various crack lengths under different film thicknesses. (a, b) 26 nm. (c, d) 36 nm. (e, f) 61 nm. (g, h) 120 nm. (a, c, e, g) force-displacement curves for various notch lengths. (b, d, f, h) the work done for propagating the notch with different notch sizes was calculated using the area under the force-displacement curve with selected displacement value.*

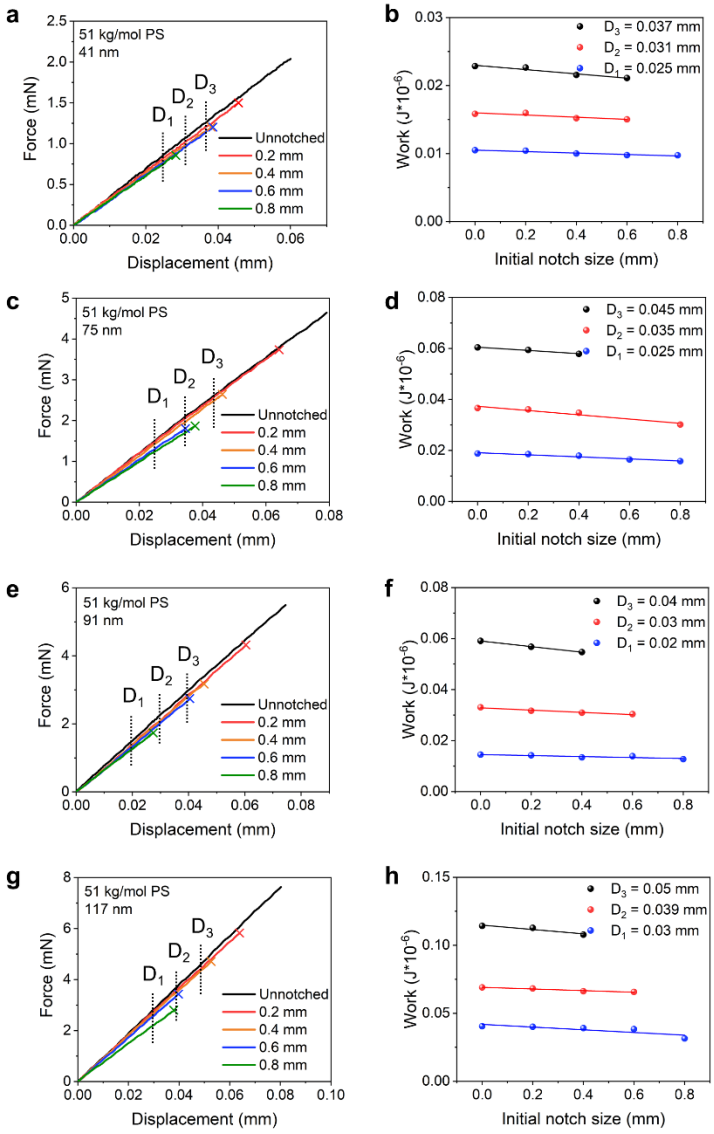

Figure B.18 *Tensile test for 51 kg/mol PS with various crack lengths under different film thicknesses. (a, b) 41 nm. (c, d) 75 nm. (e, f) 91 nm. (g, h) 117 nm. (a, c, e, g) force-displacement curves for various notch lengths. (b, d, f, h) the work done for propagating the notch with different notch sizes was calculated using the area under the force-displacement curve with selected displacement value.*

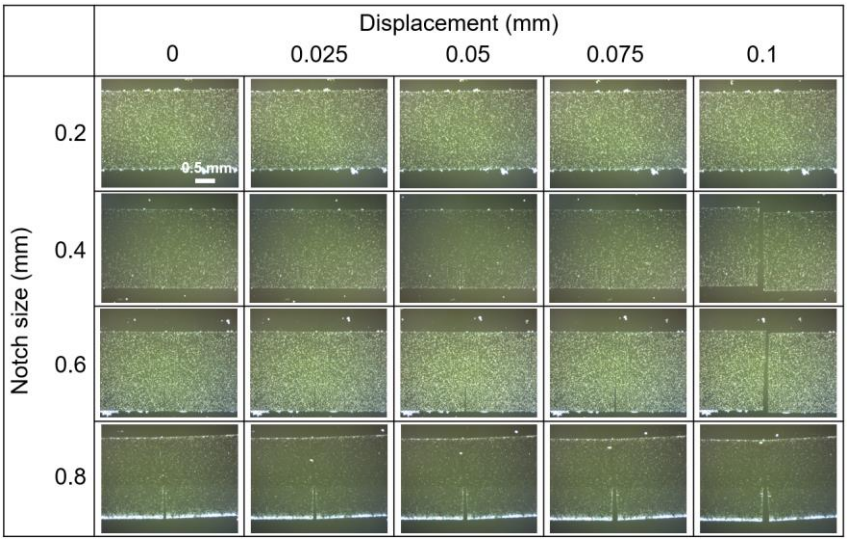

Figure B.19 *Optical images of 26 nm thick polystyrene film (173 kg/mol) with various notch sizes at different displacement.*

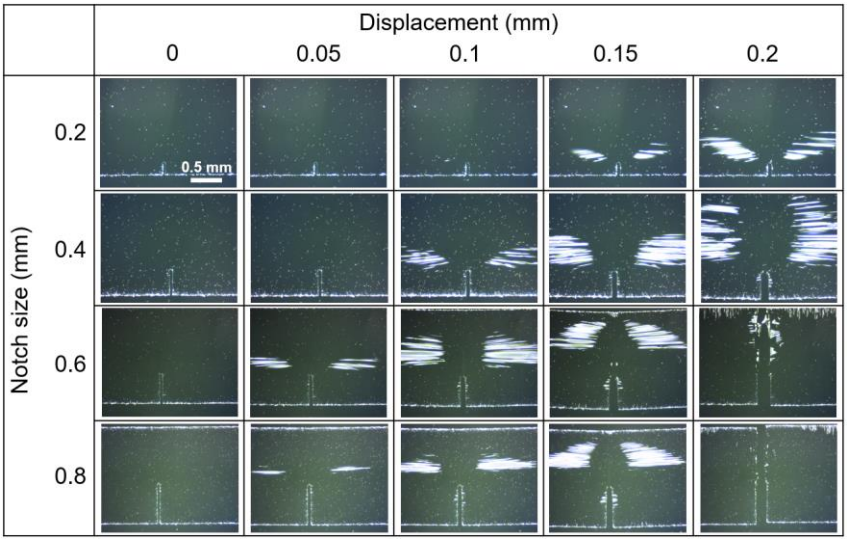

Figure B.20 *Optical images of 36 nm thick polystyrene film (173 kg/mol) with various notch sizes at different displacement.*

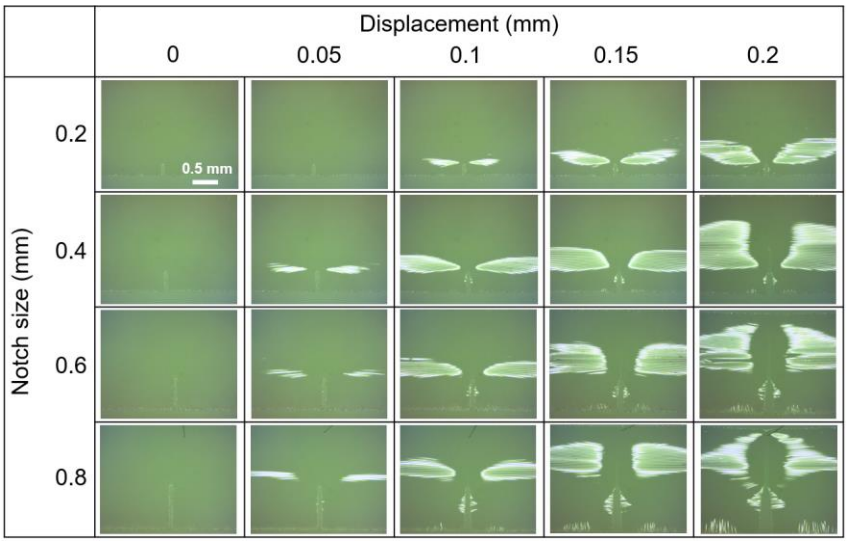

Figure B.21 *Optical images of 61 nm thick polystyrene film (173 kg/mol) with various notch sizes at different displacement.*

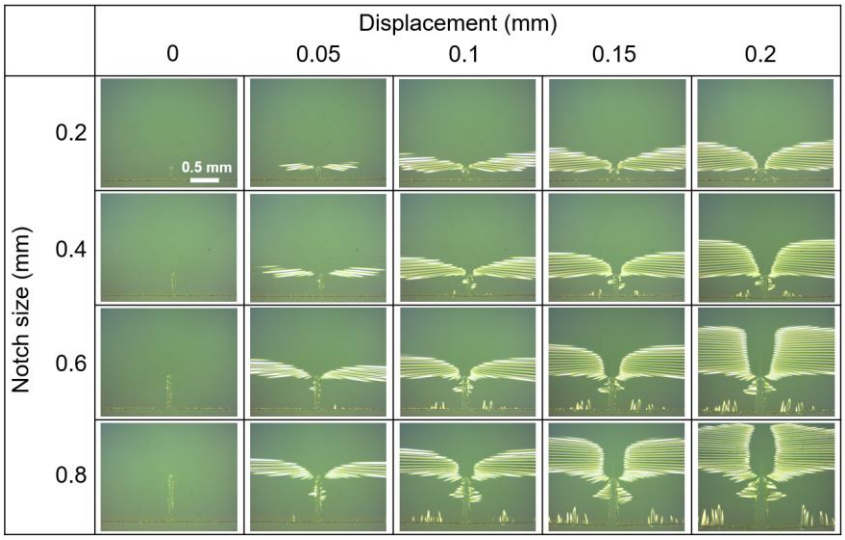

Figure B.22 *Optical images of 120 nm thick polystyrene film (173 kg/mol) with various notch sizes at different displacement.*

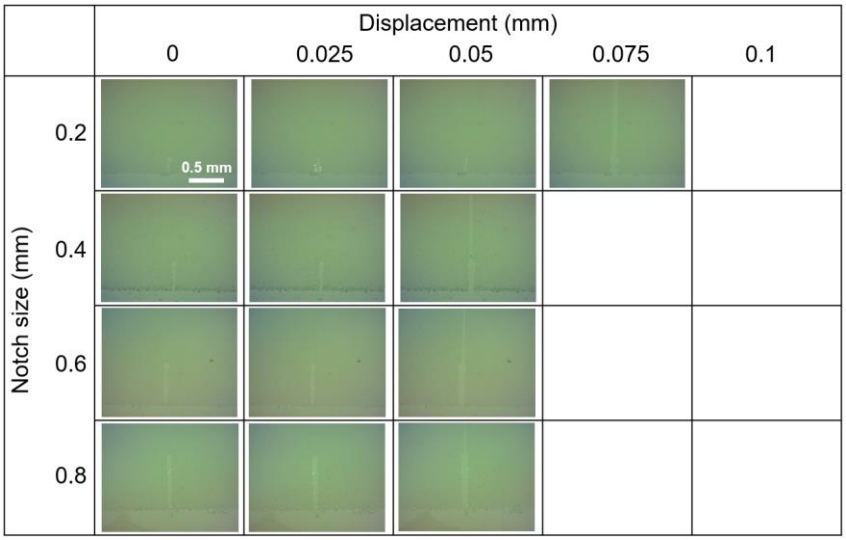

Figure B.23 *Optical images of 41 nm thick polystyrene film (51 kg/mol) with various notch sizes at different displacement.*

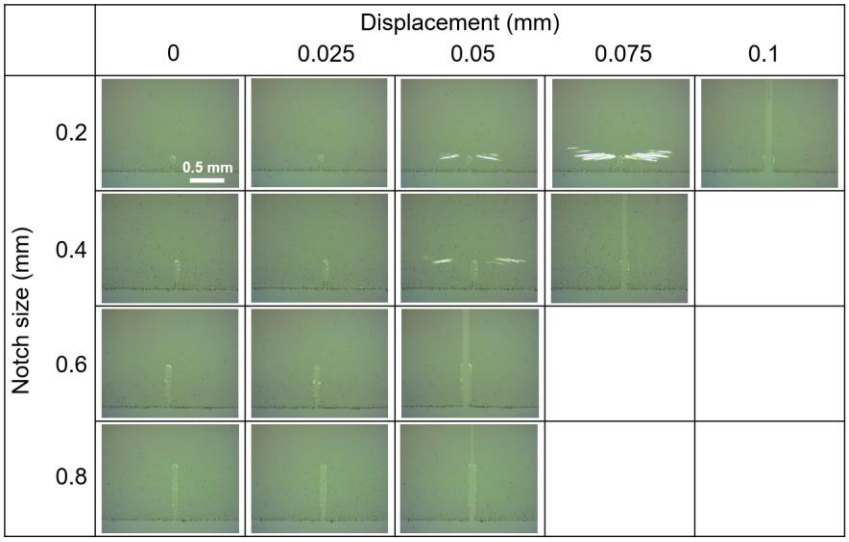

Figure B.24 *Optical images of 91 nm thick polystyrene film (51 kg/mol) with various notch sizes at different displacement.*

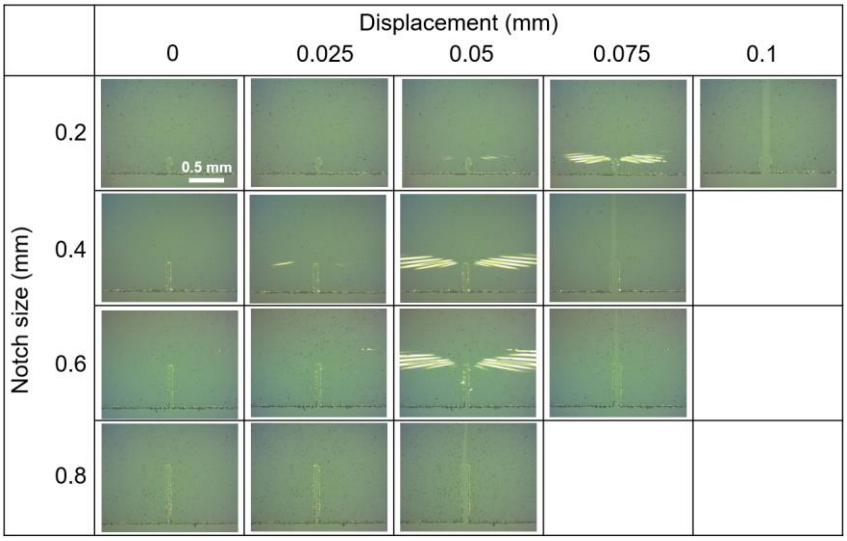

Figure B.25 *Optical images of 117 nm thick polystyrene film (51 kg/mol) with various notch sizes at different displacement.*

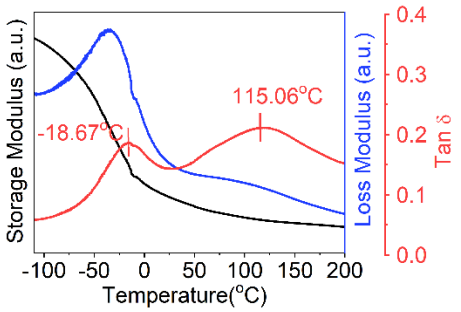

Figure B.26 *Dynamic mechanical analysis for PNDI(2HD)T sample. The backbone glass transition temperature is at 115 °C, the side-chain glass transition temperature is at -19 °C.*

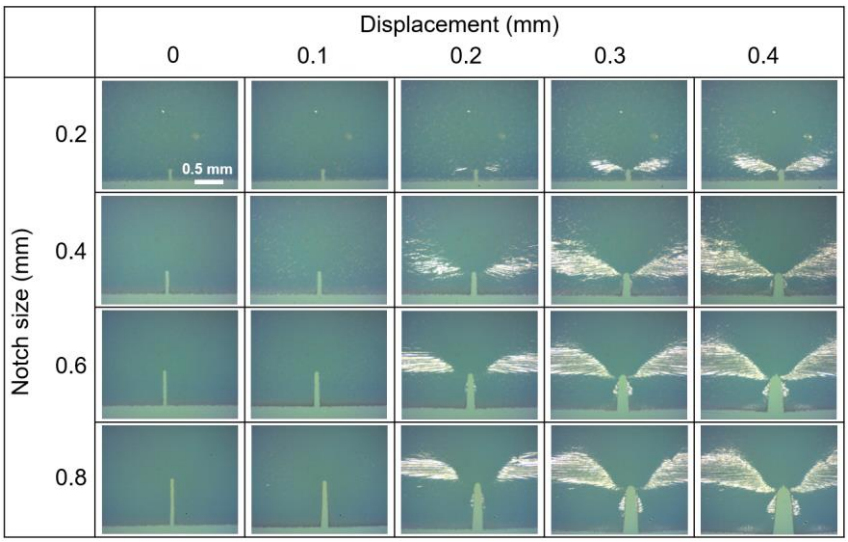

Figure B.27 *Optical images of 58 nm thick PNDI(2HD)T film with various notch sizes at different displacement.*

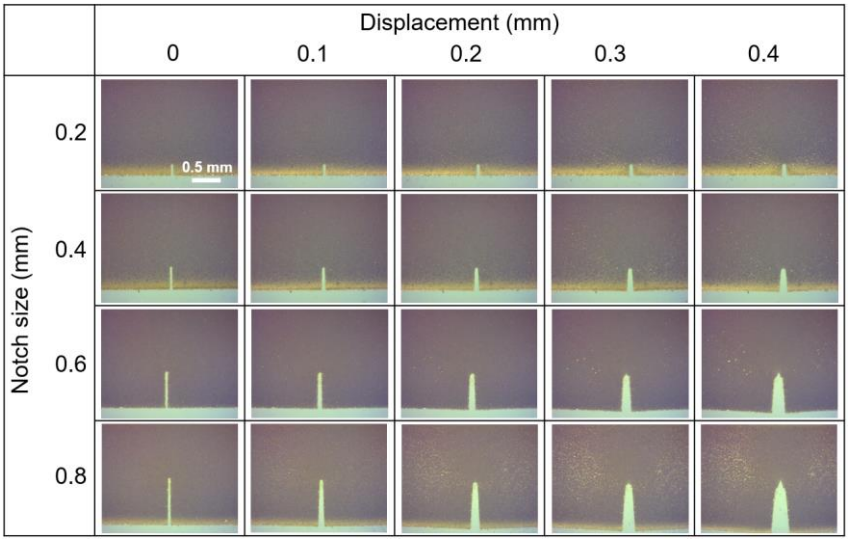

Figure B.28 *Optical images of 51 nm thick P3HT film with various notch sizes at different displacement.*

APPENDIX C

Materials

Commercial reactants were used without further purification unless stated otherwise. All the solvents used in these reactions were distilled prior to use. Tris(dibenzylideneacetone)dipalladium(0)-chloroform adduct ($Pd_2(dba)_3$•$CHCl_3$) was purchased from Sigma Aldrich and recrystallized following a reported procedure.[366] 3,6-bis(5-bromothiophen-2-yl)-2,5-bis(2-decyltetradecyl)-2,5-dihydropyrrolo[3,4-*c*]pyrrole-1,4-dione[367] and trimethyl(4-octylthiophen-2-yl)stannane[368] were synthesized according to literature. PDPP-T2,[369] PDPP-TT,[369] PDPP-TTT,[235] PDPP-T,[370] and PDPP-T3[224] were prepared according to previous reports from the literature.

Measurements and Characterization

Nuclear magnetic resonance (NMR) spectra were recorded on a Bruker 300 MHz. The spectra for all polymers were obtained in deuterated 1,1,2,2-tetrachloroethane (TCE-d_2) at 120 °C. Chemical shifts are given in parts per million (ppm). The number average molecular weight (M_n) and dispersity ($Đ$) values were determined using size exclusion chromatography (SEC) operating at 160 °C using 1,2,4-trichlorobenzene [stabilized with 125 ppm of butylated hydroxytoluene (BHT)] in an Agilent PL-GPC 220 High Temperature SEC system equipped with a set of four PLgel 10 μm MIXED-B columns. The polymer samples were dissolved at 1-2 mg mL^{-1} concentration in 1,2,4-trichlorobenzene while shaking for 2 h at 150 °C. All molecular weight and dispersity values are reported against polystyrene (PS) standards.

Synthetic pathway to PDPP-T3-C8

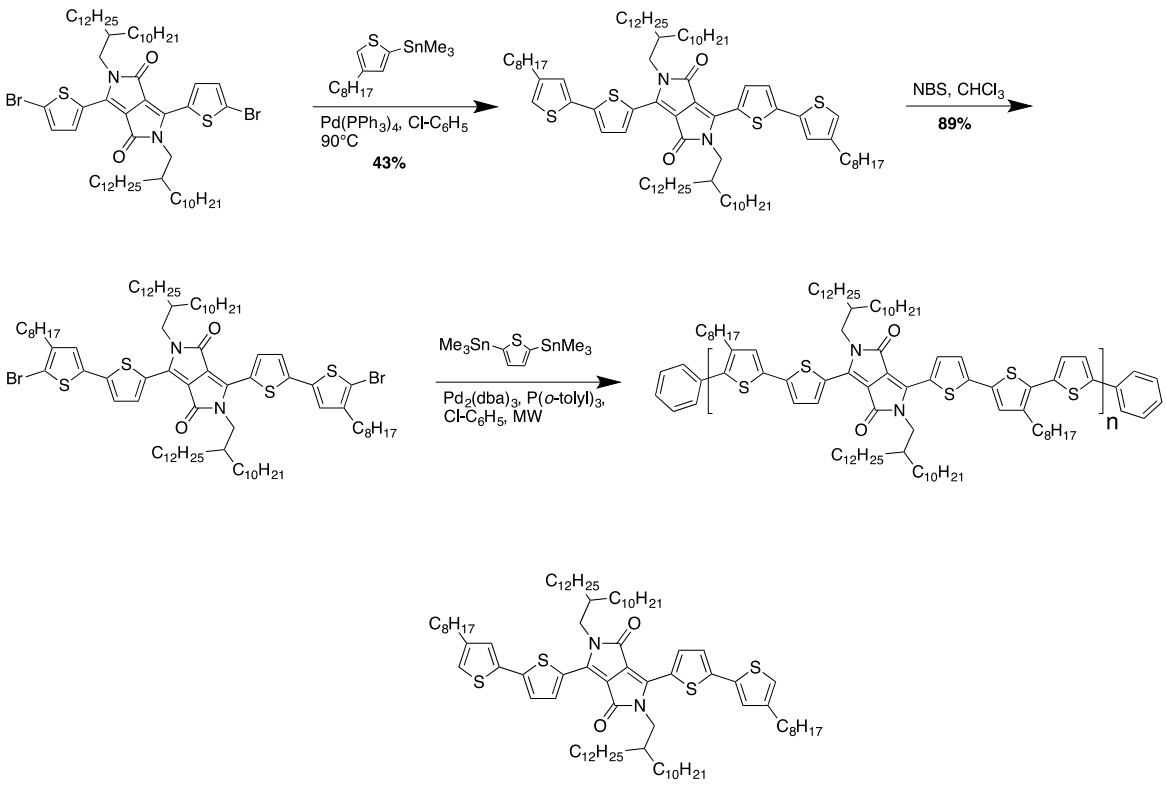

Compound 1

A purged and flame-dried round-bottom flask equipped with a magnetic stir bar was charged with 3,6-bis(5-bromothiophen-2-yl)-2,5-bis(2-decyltetradecyl)-2,5-dihydropyrrolo[3,4-c]pyrrole-1,4-dione (250 mg, 0.22 mmol), trimethyl(4-octylthiophen-2-yl)stannane (167 mg, 0.46 mmol), anhydrous chlorobenzene (3.4 mL) and $Pd(PPh_3)_4$ (25.5 mg, 0.02 mmol). The solution was stirred at 90°C temperature overnight. Upon completion, the reaction was diluted in CH_2Cl_2, washed with H_2O and washed with brine. The organic layer was subsequently dried with Na_2SO_4 and the solvent was removed under reduced pressure. The crude mixture was purified by flash chromatography on silica gel using 20% CH_2Cl_2 in Hexanes as the eluent to afford compound **1** as a purple-blue amorphous powder (130 mg, 43% yield). ^{1}H NMR (300MHz, $CDCl_3$, 298 K): 8.88 (br s, 2H), 7.28 (s, 2H), 7.15 (br s, 1H), 6.91 (br s, 2H), 4.03 (d, *J* = 9.0 Hz, 4H), 2.60 (t, *J*

= 7.5 Hz, 4H), 1.97 (br s, 2H), 1.61-1.64 (m, 4H), 1.43-1.21 (m, 96H) 0.88 (t, *J* = 4.5 Hz, 18H); ^{13}C NMR (300 MHz, $CDCl_3$, 298K): 161.72, 144.69, 143.16, 139.51, 136.57, 135.87, 127.92, 126.48, 124.46, 121.04, 108.32, 46.35, 37.97, 31.98, 31.42, 30.46, 30.12, 29.72, 29.43, 26.46, 22.74, 14.17; HRMS (ESI-ToF) calcd for $[M+H]^+$ 1361.9798, found 1361.9872.

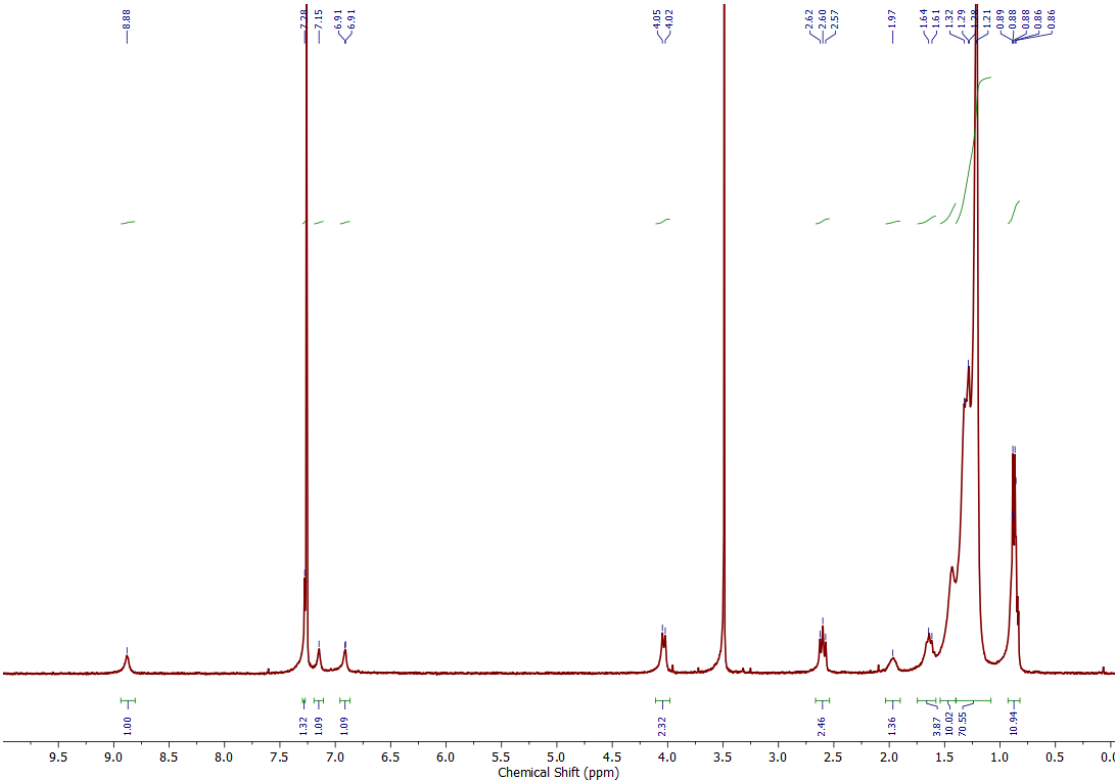

^{1}H NMR spectra of compound **1** in $CDCl_3$

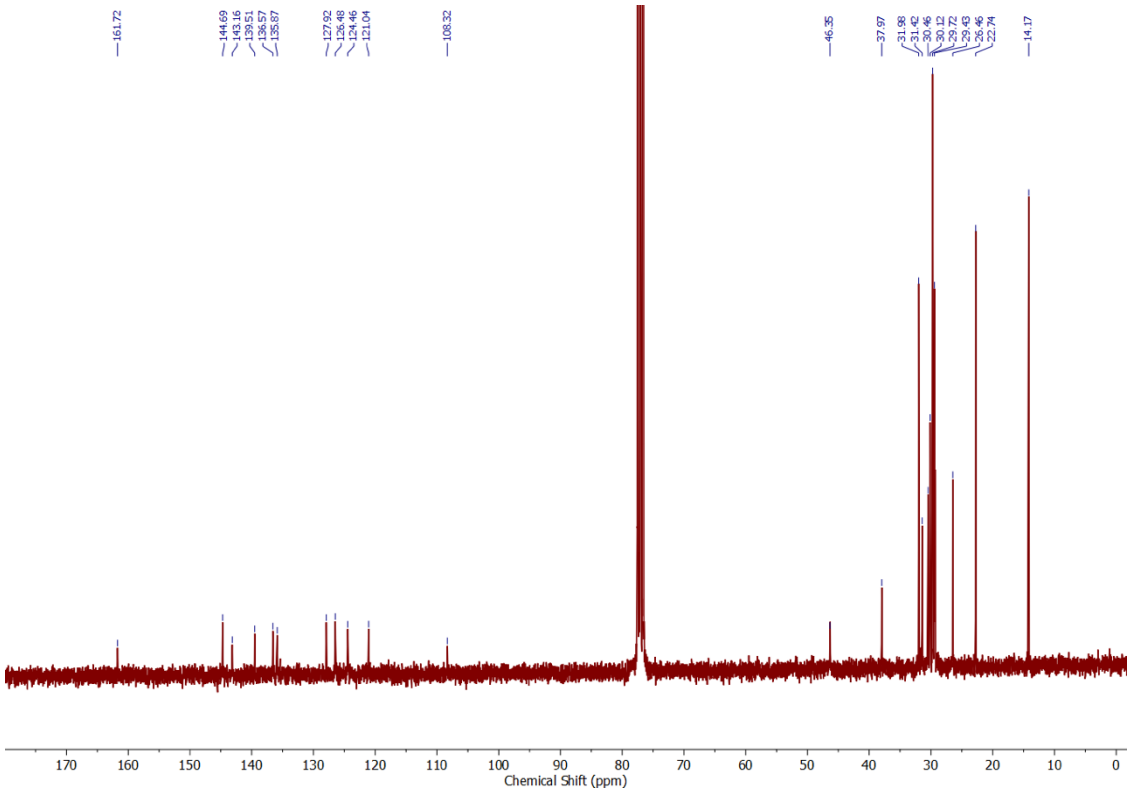

^{13}C NMR spectra of compound **1** in $CDCl_3$

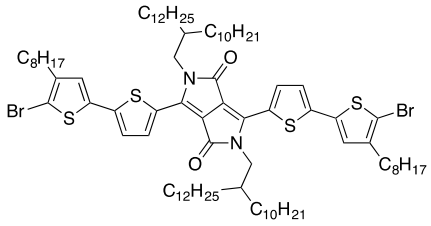

Compound 2

A round-bottom flask equipped with a magnetic stir bar was charged with **1** (100 mg, 0.07 mmol) and anhydrous $CHCl_3$ (3.2 mL). *N*-Bromosuccinimide (30 mg, 0.18 mmol) was then added in one portion and stirred at room temperature overnight. The reaction was checked by TLC and terminated once no more mono-brominated species

were observed. Upon completion, the reaction was quenched with water, dried with Na_2SO_4, and the solvent was removed under reduced pressure to afford monomer **2** as a dark blue-purple solid (100 mg, 89% yield). ^{1}H NMR (300MHz, $CDCl_3$, 298 K): 8.83 (d, *J* = 3.0 Hz, 2H), 7.21 (d, *J* = 6.0 Hz, 2H), 7.00 (s, 2H), 4.03 (t, *J* = 10.5 Hz, 4H), 2.56 (t, *J* = 9.0 Hz, 4H), 1.94 (s, 2H), 1.59-1.64 (m, 4H), 1.21-1.30 (m, 96H), 0.87 (t, *J* = 4.5 Hz, 18H); ^{13}C NMR (300 MHz, $CDCl_3$, 298K): 161.64, 143.60, 141.92, 139.40, 136.43, 135.65, 128.26, 125.79, 124.58, 110.02, 108.52, 46.34, 37.96, 31.98, 31.41, 30.11, 29.73, 29.43, 26.45, 22.74, 14.16; HRMS (ESI-ToF) calcd for $[M+H]^+$ 1517.8008, found 1517.8057.

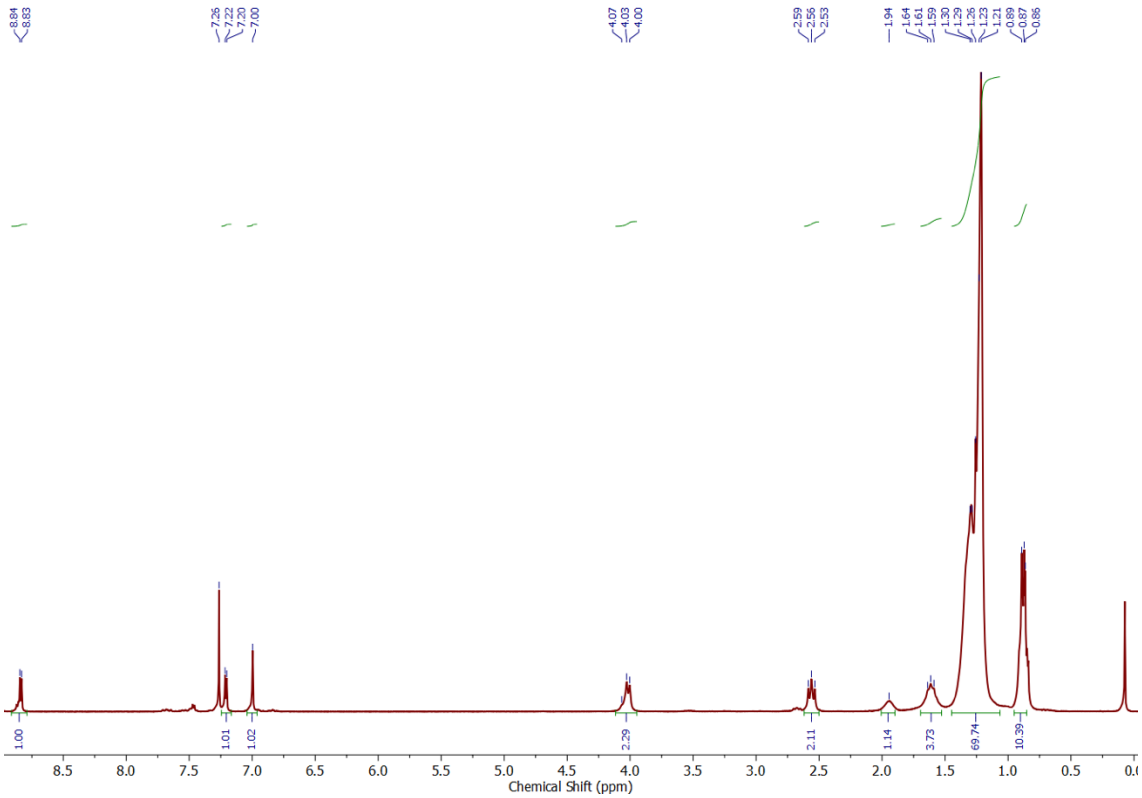

^{1}H NMR spectra of compound **2** in $CDCl_3$

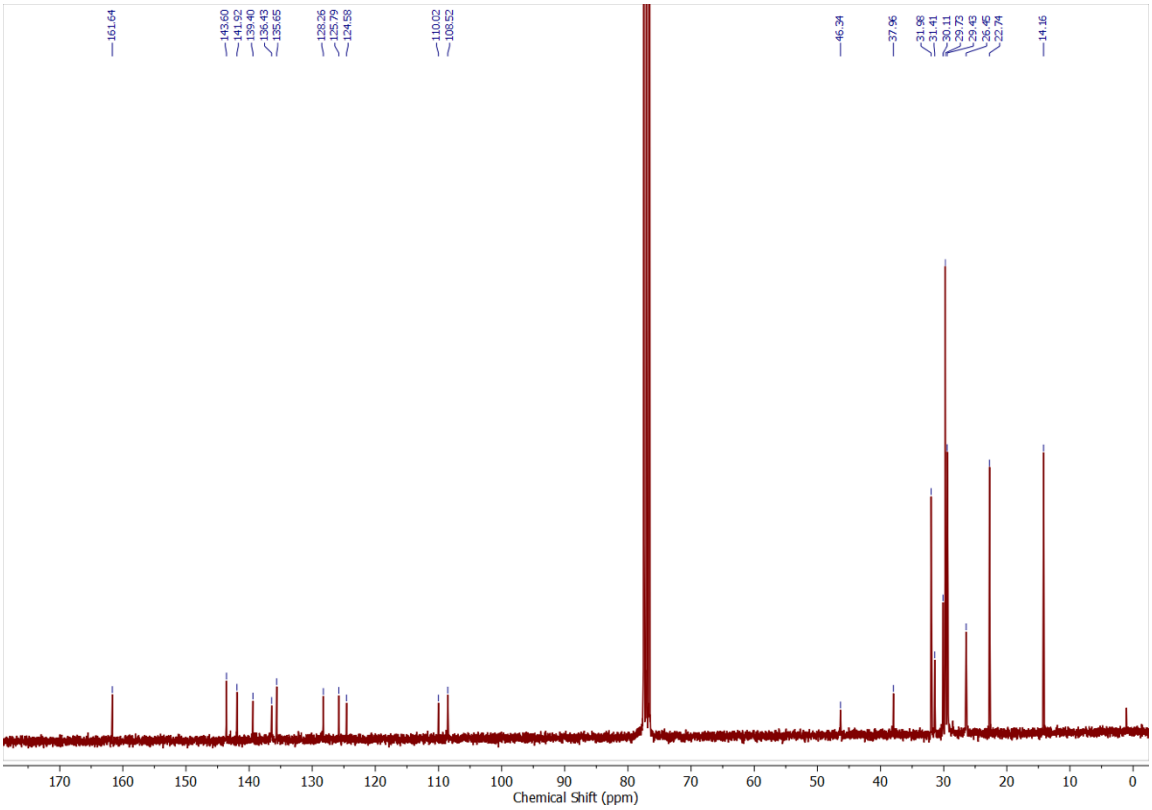

^{13}C NMR spectra of compound **2** in $CDCl_3$

PDPP-T2-C8

A microwave vessel equipped with a stir bar was charged with compound **2** (92.7 mg, 0.061 mmol), 2,5-bis(trimethylstannyl)thiophene (25.0 mg, 0.061 mmol), and chlorobenzene (3.1 mL). The solution was then bubbled with N_2 gas for 30 minutes, followed by addition of $Pd_2(dba)_3$ (1.12 mg, 0.001 mmol) and P(*o*-tolyl)$_3$ (1.67 mg, 0.006 mmol). The vessel was then immediately sealed with a snap cap and microwave irradiated under the following conditions with ramping temperature (Microwave Setup: Biotage Microwave Reactor; Power, 300 W; Temperature and Time, 2 minutes at 100 ^{o}C, 2 minutes at 120 ^{o}C, 5 minutes at 140 ^{o}C, 5 minutes at 160 ^{o}C, and 40 minutes at 180 ^{o}C;

Pressure, 17 bar; Stirring, 720). After completion, the polymer was end-capped with trimethylphenyltin (14.7 mg, 0.061 mmol) and bromobenzene (9.60 mg, 0.061 mmol). The reaction was then cooled to room temperature and precipitated in methanol and the solid was collected by filtration into a glass thimble. The contents of the thimble were then extracted in a Soxhlet extractor with methanol, acetone, hexane and finally chloroform. The chloroform fraction was concentrated and reprecipitated in methanol, followed by filtration and drying under vacuum. Molecular weight estimated from high temperature GPC: M_n = 26.8 kg/mol, M_w = 66.2 kg/mol, PDI = 2.5.

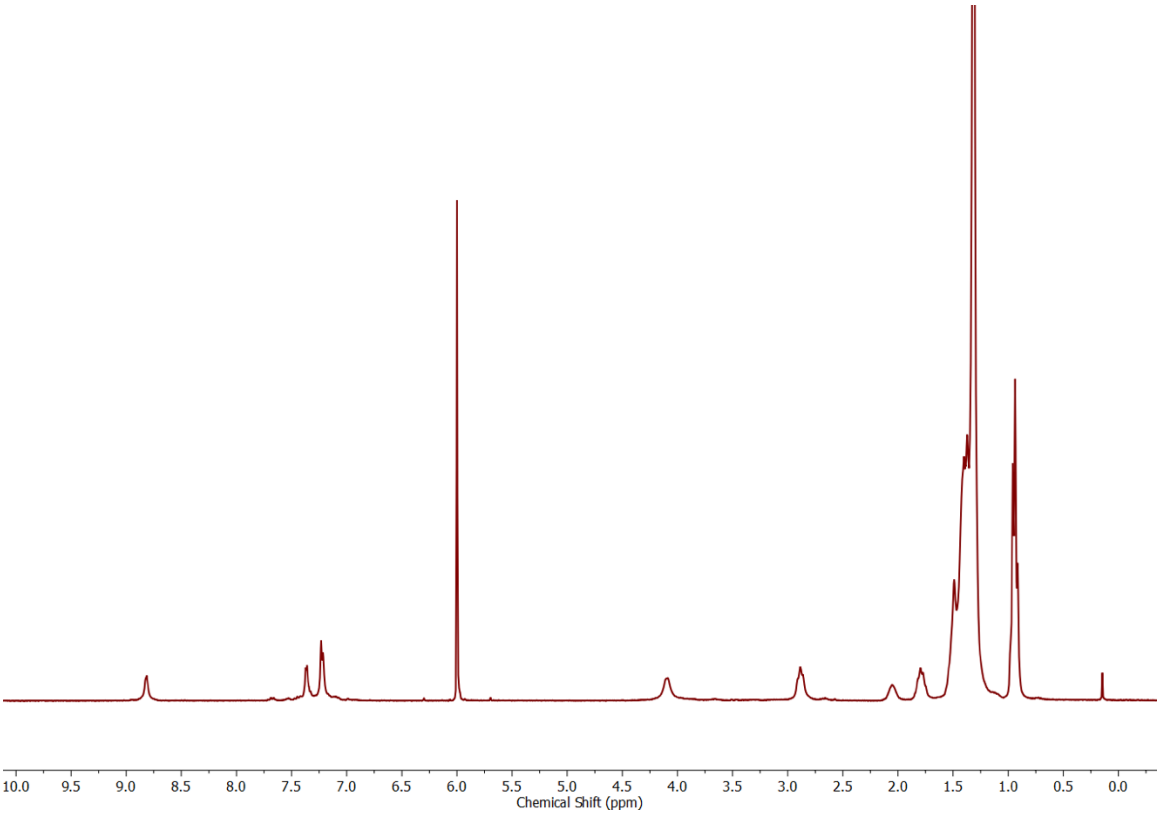

^{1}H NMR spectrum of **P1** in 1,1,2,2-tetrachloroethane-d_2 at 120 °C

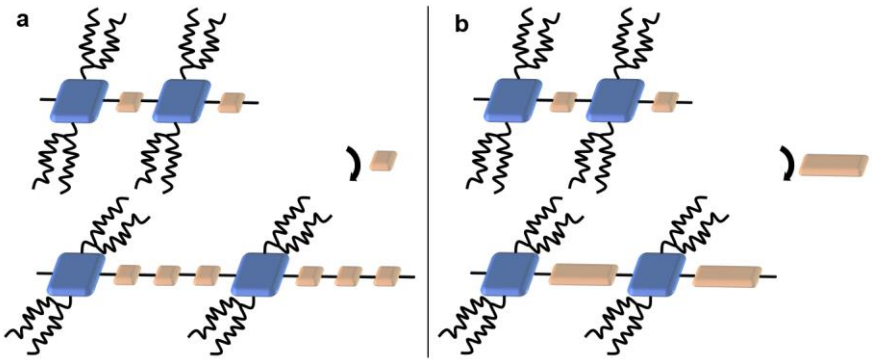

Scheme C.1 *The blue cube represents for DPP unit, the yellow cube represents for thiophene unit. (a) introducing more thiophene units or (b) introducing larger thiophene rings creates more space for the side chains to fold.*

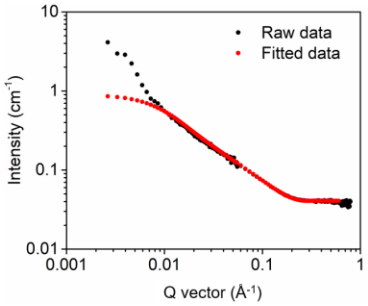

Figure C.2 *Neutron scattering raw curve (black dot) and fitted curve (red dot) for DPP-T polymer. A flexible cylinder model was used to fit the data using a q range from 0.008 Å-1 to 0.9 Å-1 due to the strong aggregation behavior shown at low q. the contour length and persistence length were fitted to be 216 Å and 90 Å, respectively. The radius of the fitted cylinder was determined to be 13 Å.*

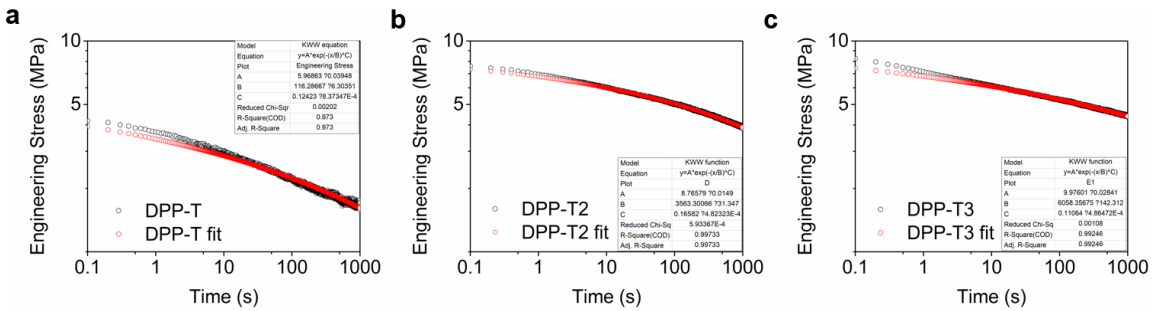

Figure C.3 *Fitted stress relaxation curves for (a) DPP-T (47 kg/mol), (b) DPP-T2 (44 kg/mol), (c) DPP-TT (51 kg/mol). The relaxation time, denoted as B in the equation above, can be obtained. They are 116 s for DPP-T, 3563 s for DPP-T2, and 6058 s for DPP-T3, respectively.*

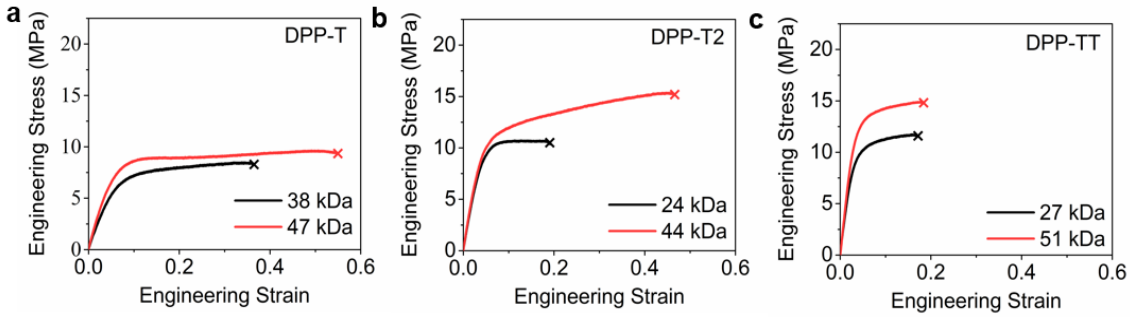

Figure C.4 *Comparison of stress-strain curves for DPP polymers with different molecular weights. The molecular weight is listed in the plot. The data is plotted (a) DPP-T, (b) DPP-T2, and (c) DPP-TT respectively. The curve is a representative curve among six individual tests. Lower molecular weight DPPs consistently fractures earlier than higher molecular weight of DPP film upon tensile strain.*

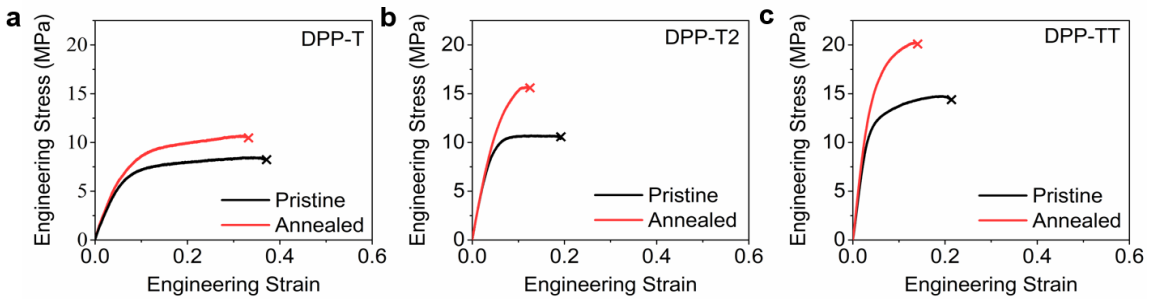

Figure C.5 *Comparison of stress-strain curves of as deposited and after annealing for (a) DPP-T (38 kg/mol), (b) DPP-T2 (24 kg/mol), and (c) DPP-TT (51 kg/mol). The annealing process was performed at 200 °C for 10 mins. Annealed films showed slightly increased elastic modulus and drop in the crack onset strain.*

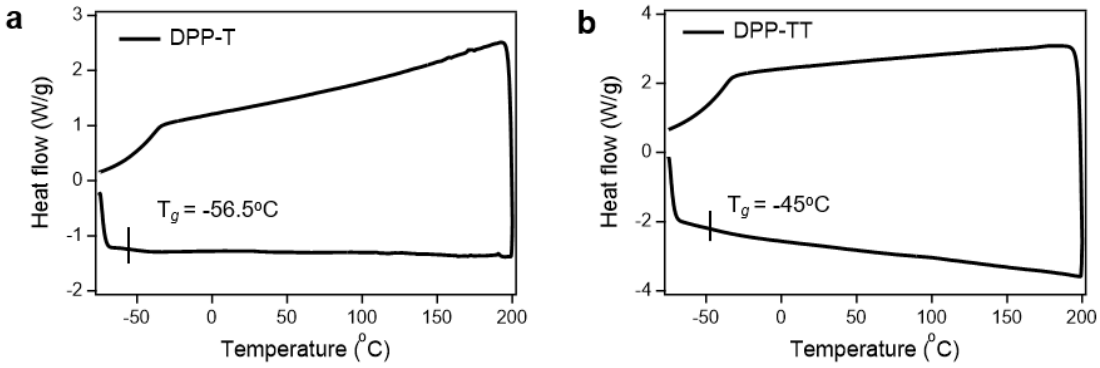

Figure C.6 *The polymer was first heated from -75 °C to 200 °C at a rate of 10 °C/min. Later, the polymer was held for 10 mins before cooling down to -75 °C at the same rate. No obvious backbone T_g was observed, the side chain T_g was noted in the curve.*

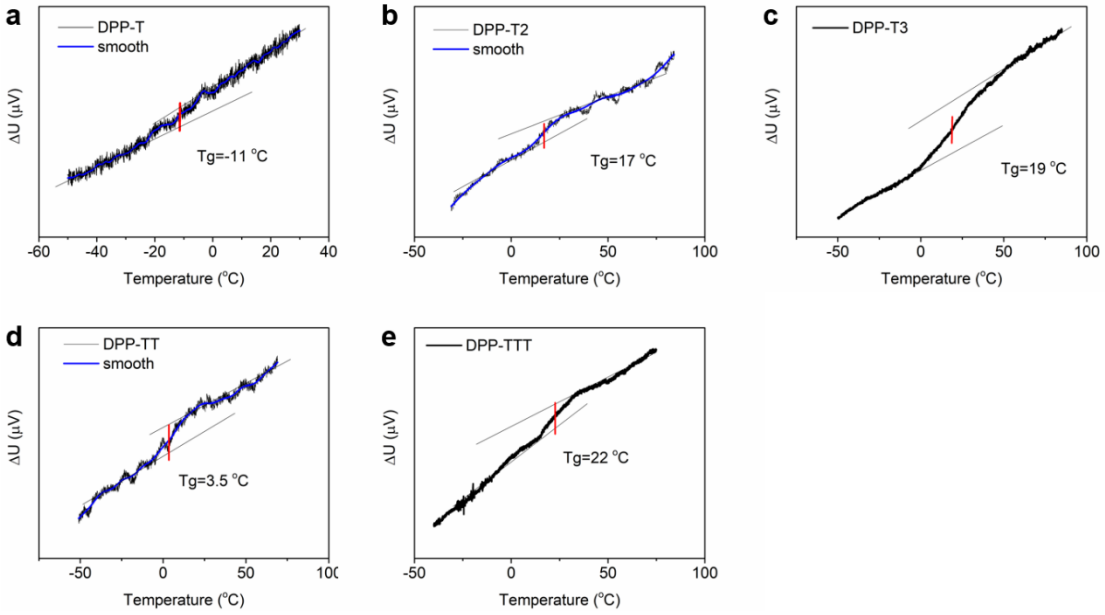

Figure C.7 *AC-chip calorimetry data for (a) DPP-T, (b) DPP-T2, (c) DPP-T3, (d) DPP-TT, (e) DPP-TTT. The T_g is defined as the half-step temperature of the amplitude of the complex differential voltage.*

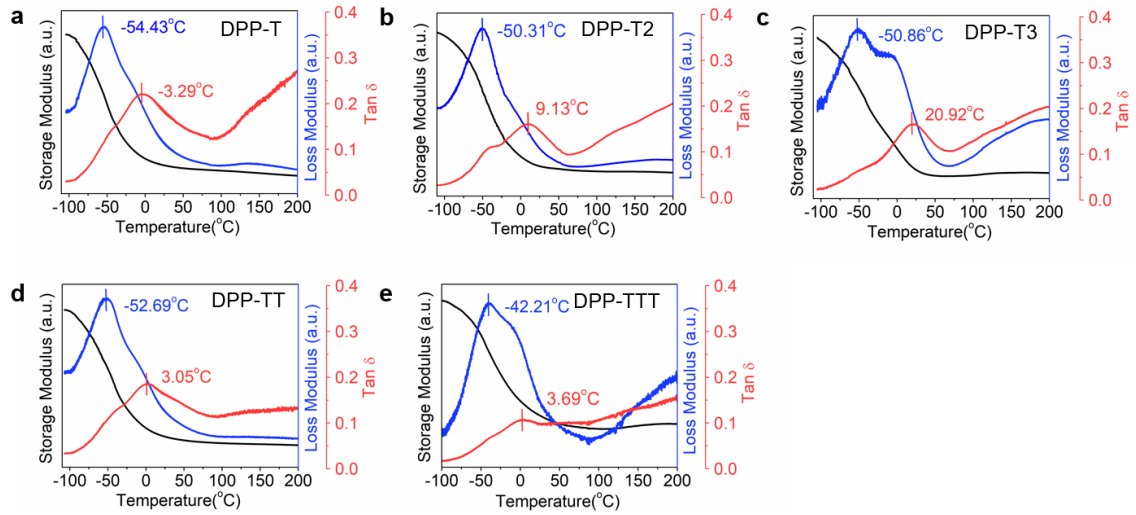

Figure C.8 *The experiment is performed on the batch of DPP films with lower molecular weight for (a) DPP-T (38 kg/mol), (b) DPP-T2 (24 kg/mol), (c) DPP-T3 (27 kg/mol), (d) DPP-TT (27 kg/mol), and (e) DPP-TTT (15 kg/mol).*

FET Device Fabrication and Characterization

FET devices were fabricated on highly doped n-type Si (100) wafer with octadecyltrimethoxysilane (OTS) modified SiO_2 (capacitance per unit area Ci = 10 nF cm^{-2}).[329] The organic semiconducting thin films were spun-cast on SiO_2/Si substrates at a spinning rate of 1000 rpm for 60 s from prepared polymer solutions in chlorobenzene (5 mg/ml) at 70 °C. The films were thermal annealed at 170 °C for 1 h inside of a N_2-filled glove box. Top-contact gold electrodes (50 nm) were subsequently deposited by evaporation through a shadow mask with the channel length (L) and width (W) defined as 50 and 1000 μm, respectively. All the measurements of the transistors were conducted using a Keithley 4200 semiconductor parameter analyzer (Keithley Instruments Inc., Cleveland, OH, USA) under dry N_2 (glove box) and ambient atmosphere at room temperature. The transistor property is given below.

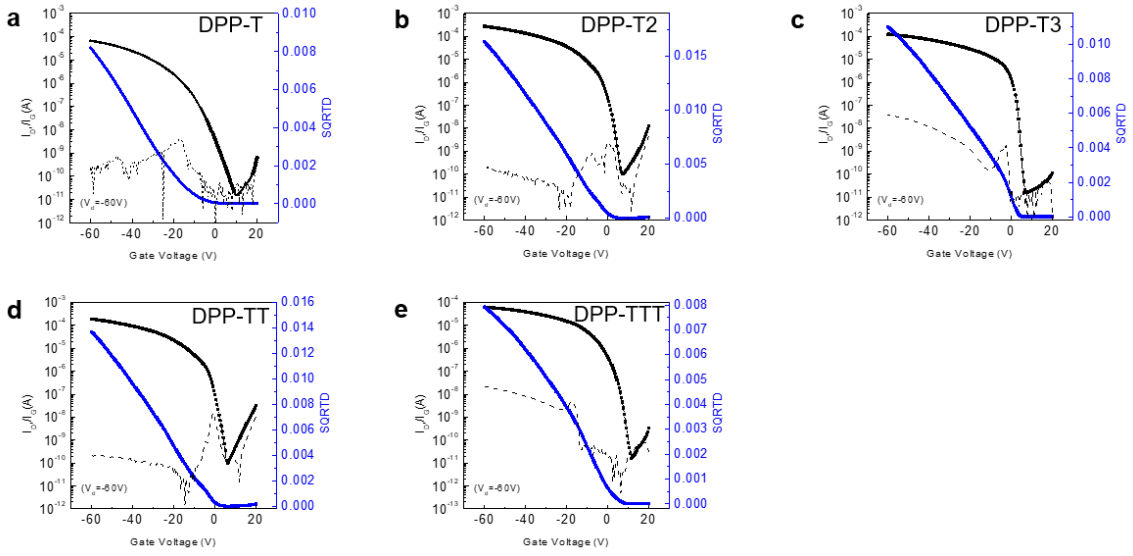

Figure C.9 *Transfer curves of DPP-based polymer thin films were shown here for (a) DPP-T (b)DPP-T2 (c) DPP-T3 (d) DPP-TT (e) DPP-TTT.*

Table C.2 *Parameters extracted from the polymer OFETs.*

Polymer	Width/Length	Max μ_{hole} ($cm^2 V^{-1} s^{-1}$)	Average μ_{hole} ($cm^2 V^{-1} s^{-1}$)	I_{ON}/I_{OFF}	Vt_sat
DPP-T	20	0.30	0.29	$>10^6$	-8.92
DPP-T2	20	1.13	1.09	$>10^6$	-20.69
DPP-T3	20	0.23	0.21	$>10^6$	-23.26
DPP-TT	20	1.04	1.02	$>10^4$	-15.48
DPP-TTT	20	0.65	0.64	$>10^4$	-1.68

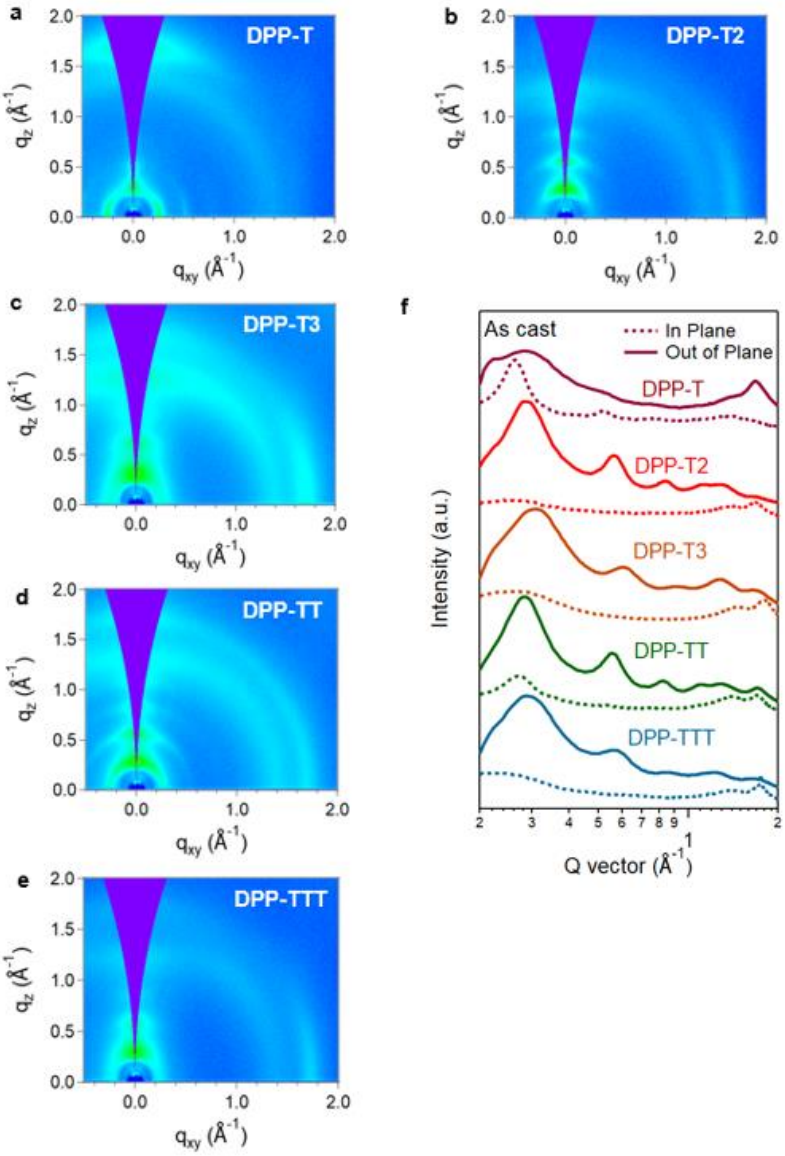

Figure C.10 *2D GIWAXS of DPP-based polymers before annealing. (a) DPP-T, (b) DPP-T2, (c) DPP-T3, (d) DPP-TT, (e) DPP-TTT. (f) 1D line-cut profiles in both in-plane direction (dotted line) and out-of-plane direction (solid line).*

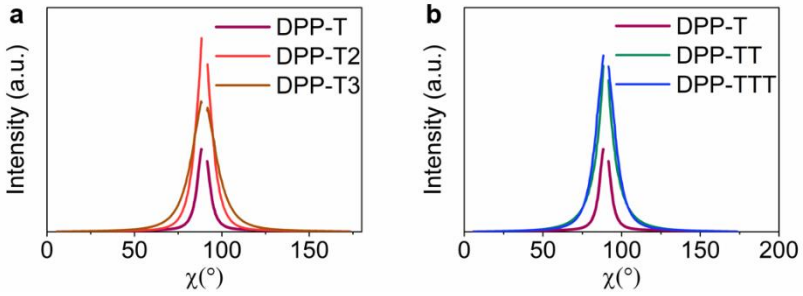

Figure C.11 *Pole figures for the (100) scattering peak for (a) DPP polymers with isolated thiophene units and (b) DPP with fused thiophene units. The intensity of (100) peak was normalized by exposure time, sample thickness and beam path length, later geometrically corrected orientation distribution function, or sin(χ)I(χ), was performed to obtain the relative orientation of the crystallite. The relative degree of crystallinity is obtained by integrating the area below each curve.*

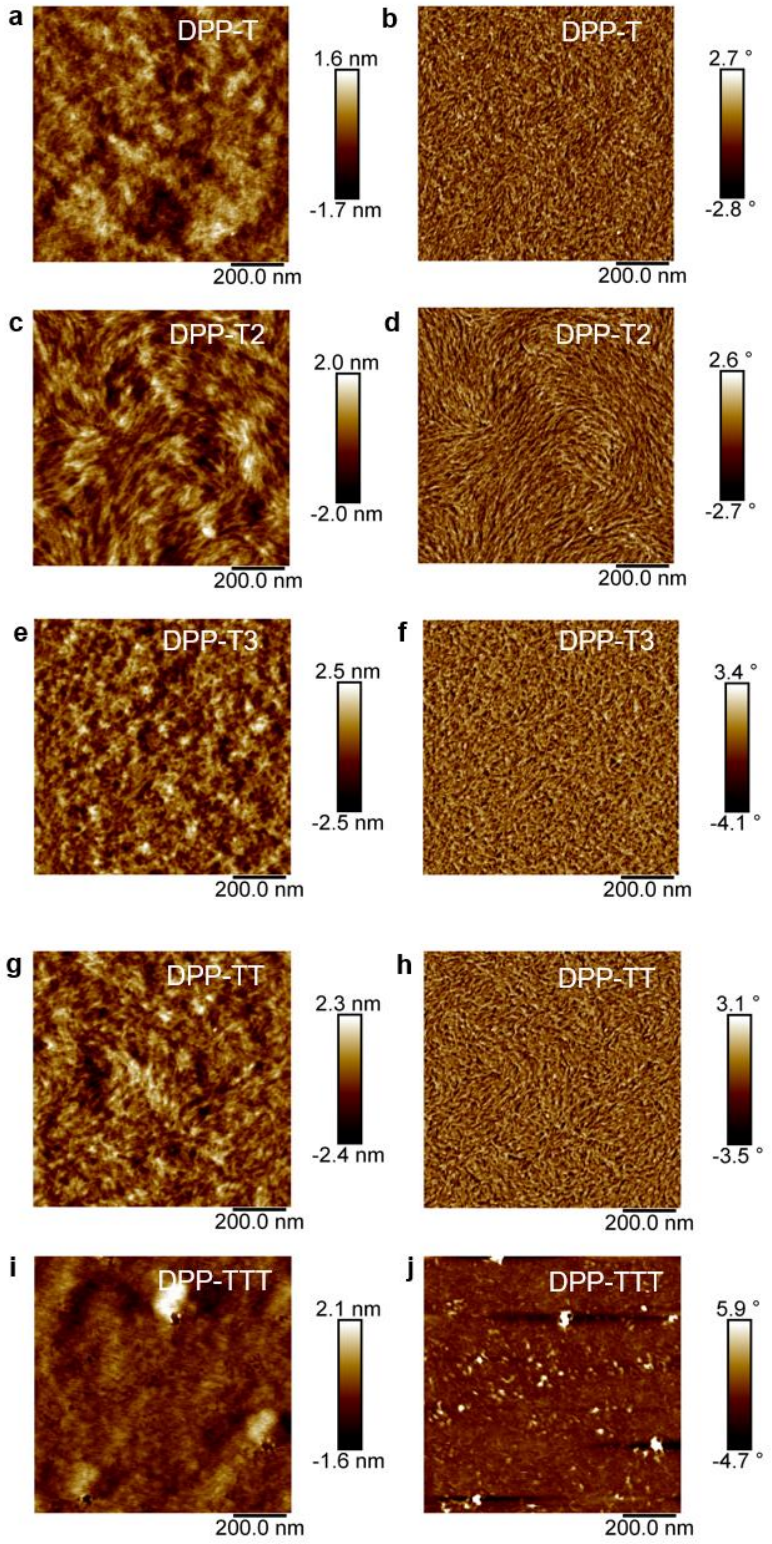
a
DPP-T
1.6 nm
-1.7 nm
200.0 nm
b
DPP-T
2.7 °
-2.8 °
200.0 nm
c
DPP-T2
2.0 nm
-2.0 nm
200.0 nm
d
DPP-T2
2.6 °
-2.7 °
200.0 nm
e
DPP-T3
2.5 nm
-2.5 nm
200.0 nm
f
DPP-T3
3.4 °
-4.1 °
200.0 nm
g
DPP-TT
2.3 nm
-2.4 nm
200.0 nm
h
DPP-TT
3.1 °
-3.5 °
200.0 nm
i
DPP-TTT
2.1 nm
-1.6 nm
200.0 nm
j
DPP-TTT
5.9 °
-4.7 °
200.0 nm

Figure C.12 *AFM height images (a,c,e,g,i) and phase images (b,d,f,h,j) for as-cast polymer films, (a,b) DPP-T, (c,d) DPP-T2, (e,f) DPP-T3, (g,h) DPP-TT and (i,j) DPP-TTT.*

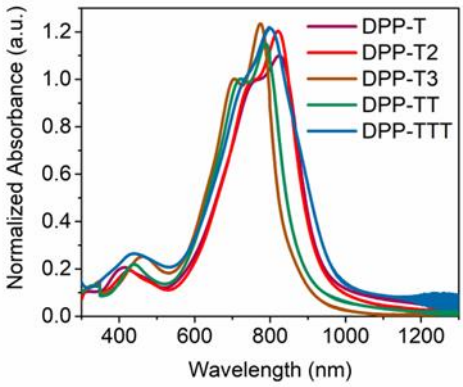

Figure C.13 *Normalized thin film UV-vis absorption spectra of DPP polymer thin film deposited on glass.*

Table C.3 *Peak positions of UV-vis spectra.*

	Peak position (nm)		
Polymer	π-π* transition	0-1 transition	0-0 transition
DPP-T	404	757	840
DPP-T2	432	740	821
DPP-T3	457	702	777
DPP-TT	436	717	788
DPP-TTT	435	700	800

Table C.4 *Peak areas of UV-vis spectra.*

	Peak area			
Polymer	π-π* transition	0-1 transition	0-0 transition	Percent of aggregation
DPP-T	15.73	201.54	25.28	0.125
DPP-T2	19.59	213.71	25.46	0.119
DPP-T3	29.07	191.58	21.36	0.111
DPP-TT	20.67	201.37	18.72	0.092
DPP-TTT	n/a	n/a	n/a	n/a

Table C.5 *Mechanical data summary for pseudo-free standing tensile test data*

Polymer type	Polymer name	M_n/PDI	Thickness (nm)	Elastic modulus (MPa)	Crack onset strain	Ref
Polythiophene	P3HT	15.0/-	200	0.2	4.5%	[44]
		40.0/-	200	0.26	13.0%	
		6.03/-	200	0.26	58.7%	
		80.0/-	200	0.27	95.6%	
	P3HT 98% Regioregularity	20.3/1.08	100	0.29	0.6%	[103]
	P3HT 86% Regioregularity	20.8/1.23	100	0.14	0.9%	
	P3HT 80% Regioregularity	13.6/1.42	100	0.11	1.3%	
	P3HT 75% Regioregularity	12.3/1.44	100	0.07	2.4%	
	P3HT 64% Regioregularity	9.2/1.33	100	0.013	5.3%	
	P3HT	19.6/2.74	80	0.14	80.0%	[18]
	P3HT	16.4/1.06	-	0.46	1.0%	[371]
Copolymer	P3HT-co-polythiophene（RP33)	16.1/1.15	-	1.05	3.0%	
	P3HT-co-polythiophene（RP25)	16.1/1.1	-	0.65	2.2%	
	P3HT-co-polythiophene（RP17)	16.2/1.1	-	0.42	1.9%	
	P3HTT-co-DPP (10% T-6-T)	29.0	-	0.23	25.0%	[372]
	P3HTT-co-DPP (10% T-8-T)	19.7	-	0.14	32.0%	
	P3HTT-co-DPP (10% T-10-T)	14.0	-	0.13	24.0%	
	P3HTT-co-DPP (20% T-10-T)	12.4	-	0.32	22.0%	
	P3HTT-co-DPP (30% T-10-T)	9.8	-	0.33	18.0%	
	P3HTT-co-DPP (40% T-10-T)	12.2	-	0.75	10.0%	
	DPP-co-PCL (T-0)	19.1	100-200	0.24	13.0%	[347]
	DPP-co-PCL (T-25)	21.8	100-200	0.17	15.0%	
	DPP-co-PCL (T-50)	25.7	100-200	0.20	87.0%	

	DPP-co-PCL (T-75)	22.9	100-200	0.20	208.0 %	
	DPP-co-PCL (TT-0)	24.2	100-200	0.52	3.0%	
	DPP-co-PCL (TT-50)	25.9/4.1	100-200	0.25	80.0%	
Donor-Acceptor homopolymer	PBDTTTPD:P(NDI2HD-T) blend (1:1.5 ratio)	22.0/2.0 48.0/2.1	130	0.43	7.0%	[102]
	PTB7	123.0/2.5	100	0.44	27.0%	[60]
	PTB7-Th	23.0/2.2	90-110	0.88	13.0%	[373]
	P(NDI2HD-T)	38.0/2.3	90-110	0.62	15.8%	
	F8BT	10.0/3.2	130	1.00	9.0%	[68]
	PTB7-Th	-	-	-	16.0%	
	P3BT	-	-	-	22.0%	
	A5D7	-	-	-	28.0%	
	DPP-TVT	46.9/2.1	80	0.16	20.0%	[18]

Table C.6 *Previously reported charge mobility data summary for DPP-based Polymers*

Polymer	Side chain on the DPP unit [a]	M_n/M_w (kg/mol)	μ_{hole} ($cm^2 V^{-1} s^{-1}$)	Ref
DPP-T	C2C6C8	54/170	0.04	[229]
	C2C6C8	10/24	0.05	
	C2C8C10	104/310	0.6	[230]
	C2C8C10	53/236	2.4	[374]
	C2C6C8	33/94	0.3	[239]
	C2C8C10	34/205	1.57	
	C5C8C10	51/116	6.00	[375]
DPP-T2	C2C8C10	55/175	0.2	[230]
	C2C8C10	59/197	1.04	[231]
	C2C8C10	25/61	0.97	[376]
		21/51	0.39	
	C2C8C10	40/128	3.57	[377]
	C2C10C12	55/171	2.65	
	C4C10C12	63/263	5.18	
	C2C8C10	34/-	1.14	[378]
		64/-	2.44	
		40/-	3.57	
	C5C8C10	15/30	4.00	[375]
DPP-TT	C2C8C10	15/39	0.38	[230]
	C2C6C8	20/80	0.79	[239]
	C2C8C10	42/182	1.93	
	C2C810	50/194	1.36	[379]
	C2C8C10	90/212	0.94	[380]
	C2C6C8	9/35	0.03	[233]
	C2C8C10	110/500	10.5	[381]
	C2C8C10	21/72	-	[234]
DPP-TTT	C2C8C10	10/52	0.75	[235]
	C2C8C10	137/424	0.23	[382]

[a] The following acronyms are for branched alkyl chains: CaCbCc. a represents for the number of carbon before branching point, b and c represent for the number of carbon in the alkyl chain.

APPENDIX D

Materials

Commercial reactants were used without further purification unless stated otherwise. All the solvents used in these reactions were distilled prior to use. Tris(dibenzylideneacetone)dipalladium(0)-chloroform adduct ($Pd_2(dba)_3$•$CHCl_3$) was purchased from Sigma Aldrich and recrystallized following a reported procedure.[366] 2-decyltetradecanol, 2-octyldodecanol, 2-dodecylhexadecanol, 2-hexyldecanol and 2-hexyldodecanol were purchased commercially (TCI America) and were converted to the corresponding alkyl halides following a previously reported procecure.[383] Diketopyrrolopyrrole monomers, bearing different side chains, were prepared by alkylation in basic conditions as previously reported.[367] The various PDPPT polymers were synthesized using the general procedure for Stille polymerization, according to previous reports from the literature.[384]

General procedure for Stille polymerization

A microwave vessel equipped with a stir bar was charged with Diketopyrrolopyrrole monomers (1 equivalent) 2,5-bis(trimethylstannyl)thiophene (1 equivalent) and chlorobenzene (0.05 M). The solution was then bubbled with N_2 gas for 30 minutes, followed by addition of $Pd_2(dba)_3$ (10 mol%) and P(*o*-tolyl)$_3$ (10 mol%). The vessel was then immediately sealed with a snap cap and microwave irradiated under the following conditions with ramping temperature (Microwave Setup: Biotage Microwave Reactor; Power, 300 W; Temperature and Time, 2 minutes at 100 ^oC, 2 minutes at 120 ^oC, 5 minutes at 140 ^oC, 5 minutes at 160 ^oC, and 40 minutes at 180 ^oC; Pressure, 17 bar;

Stirring, 720). After completion, the polymer was end-capped with trimethylphenyltin and bromobenzene. The reaction was then cooled to room temperature and precipitated in methanol and the solid was collected by filtration into a glass thimble. The contents of the thimble were then extracted in a Soxhlet extractor with methanol, acetone, hexane and finally chloroform. The chloroform fraction was concentrated and reprecipitated in methanol, followed by filtration and drying under vacuum.

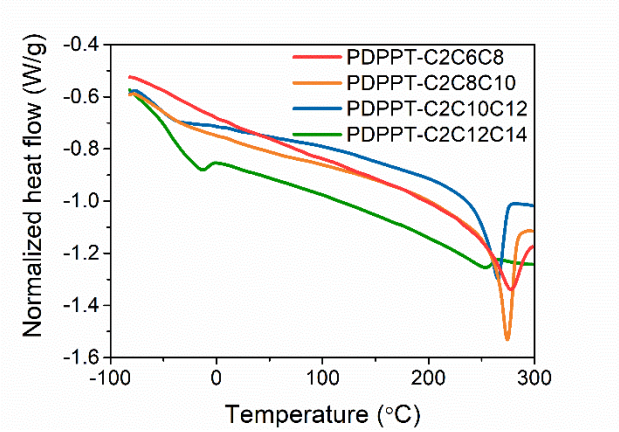

Figure D.1 *DSC result for PDPPT-based polymers with four different side chain lengths.*

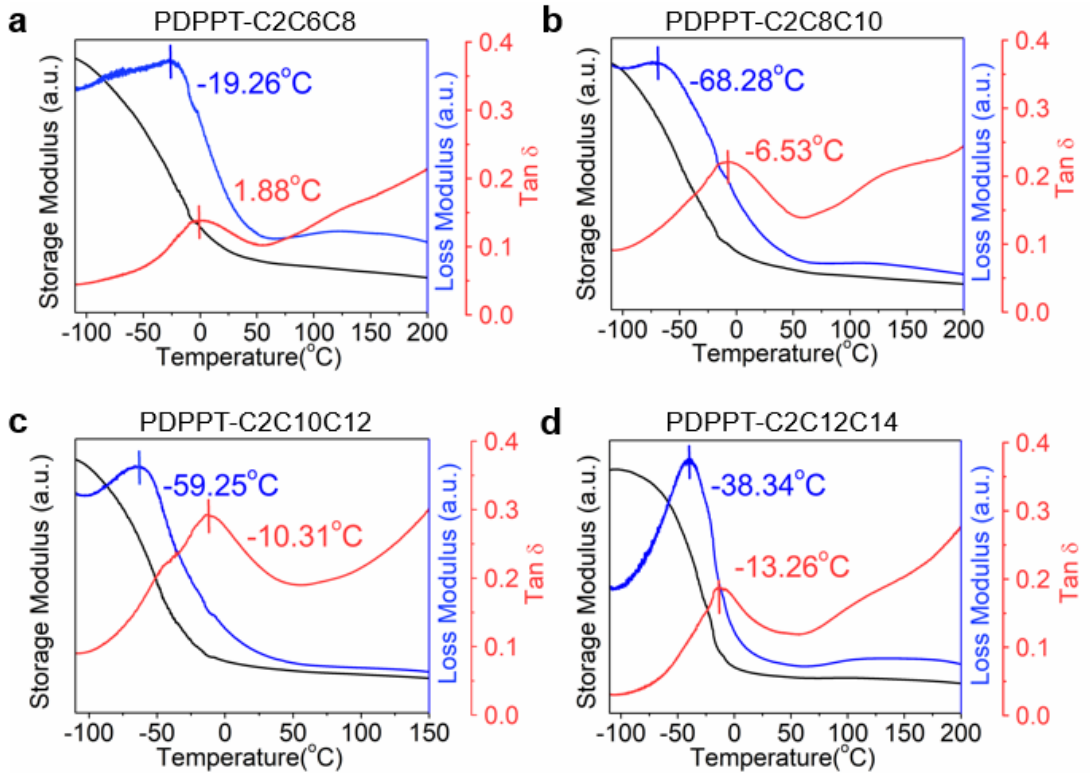

Figure D.2 *DMA result for PDPPT-based polymers with four different side chain lengths. (a) PDPPT-C2C6C8, (b) PDPPT-C2C8C10, (c) PDPPT-C2C10C12, (d) PDPPT-C2C12C14.*

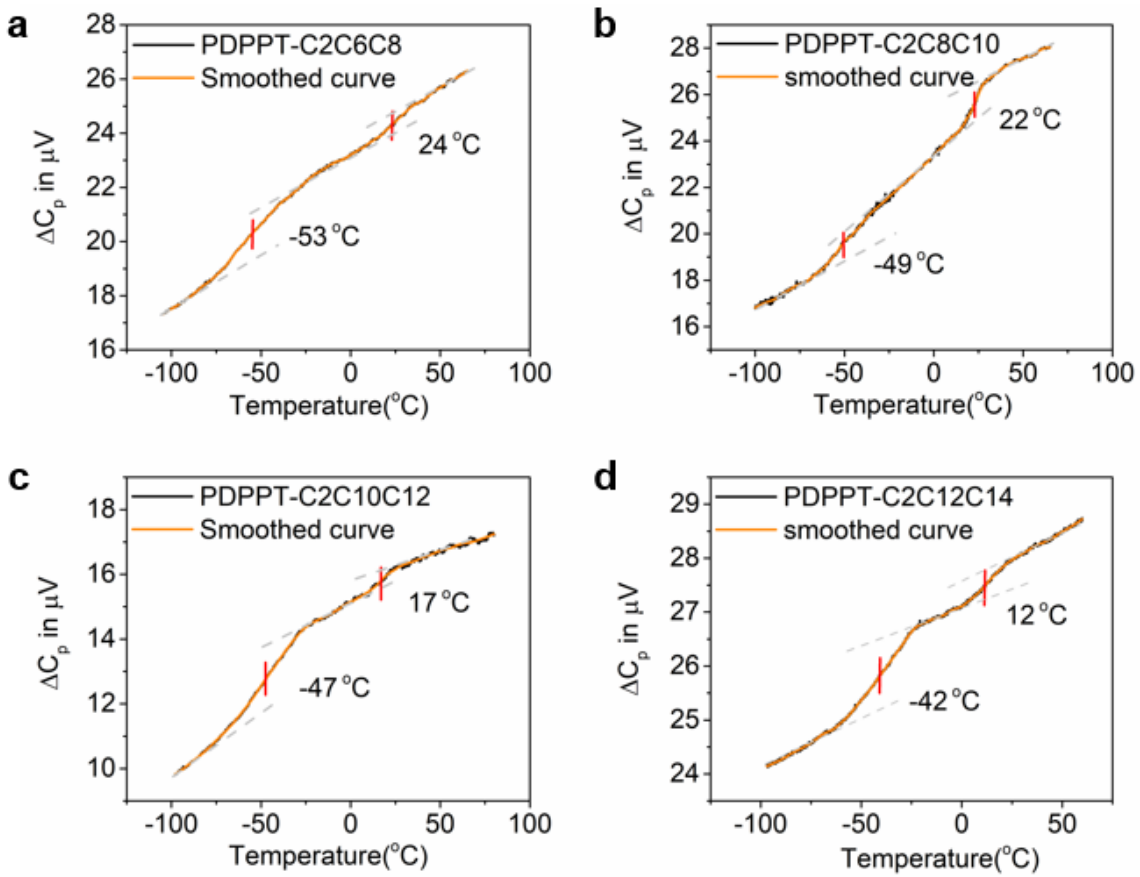

Figure D.3 *AC-chip result for PDPPT-based polymers with four different side chain lengths. (a) PDPPT-C2C6C8, (b) PDPPT-C2C8C10, (c) PDPPT-C2C10C12, (d) PDPPT-C2C12C14.*

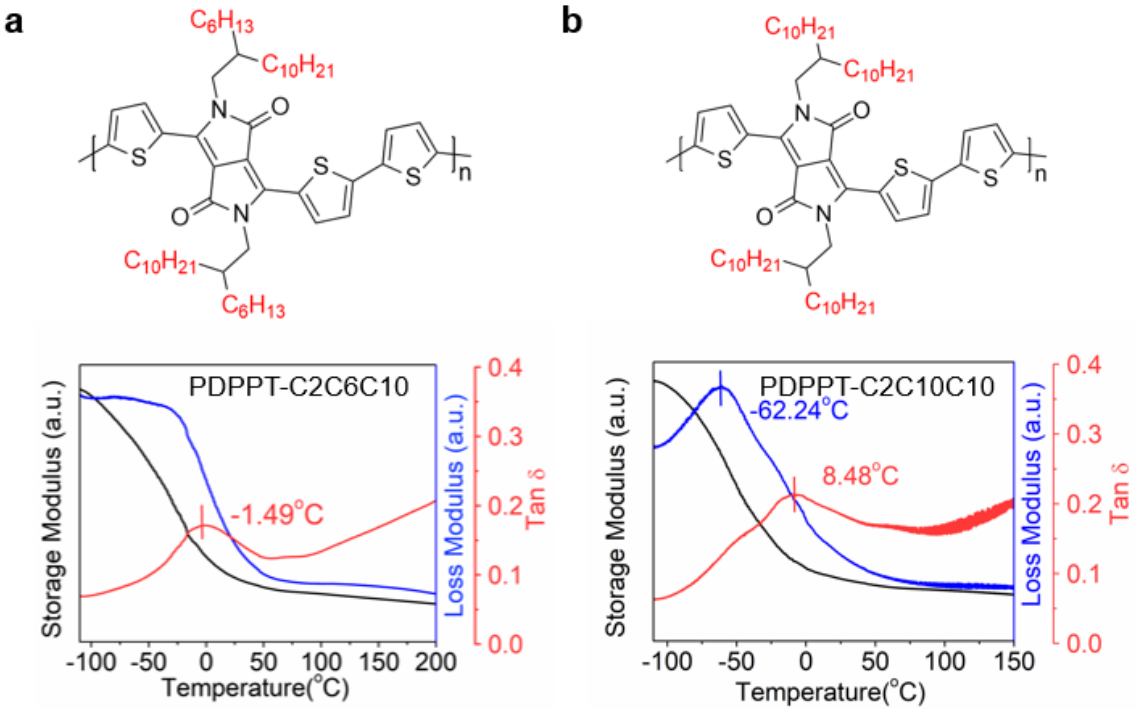

Figure D.4 *DMA result for (a) PDPPT-C2C6C10 and (b) PDPPT-C2C10C10.*

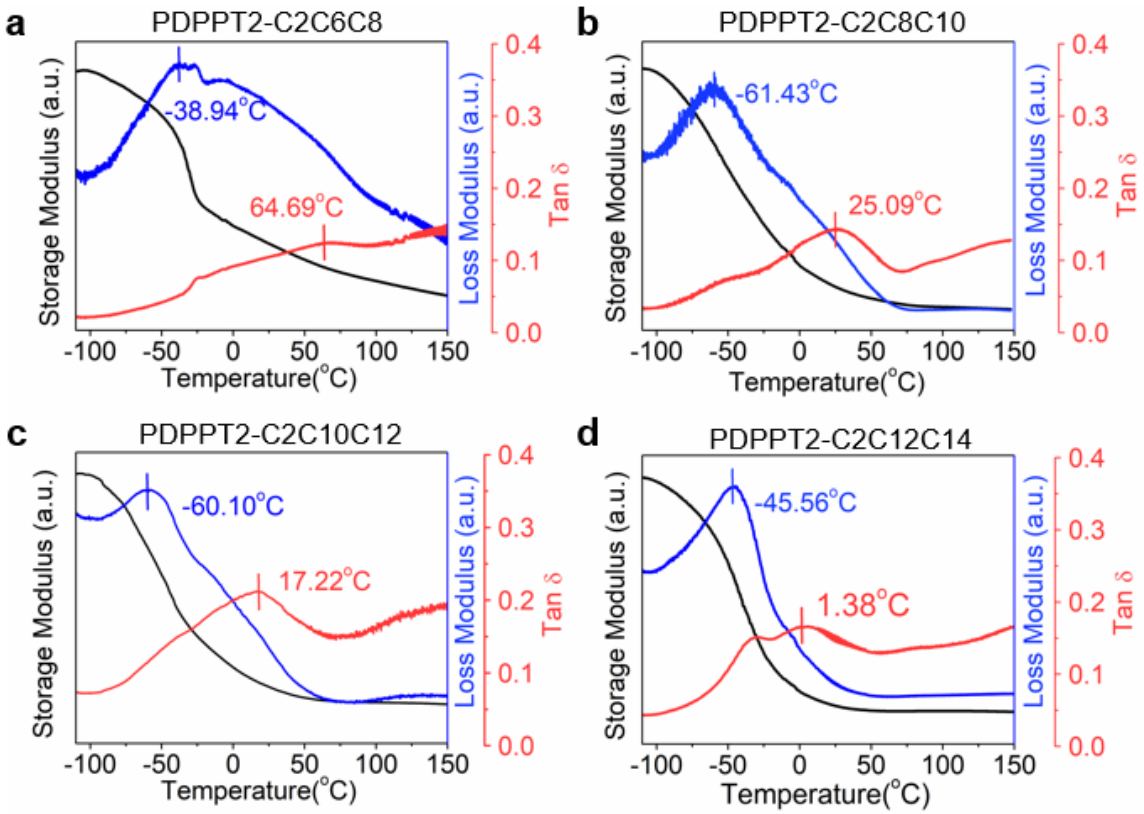

Figure D.5 *DMA result for PDPPT2-based polymers with four different side chain lengths. (a) PDPPT2-C2C6C8, (b) PDPPT2-C2C8C10, (c) PDPPT2-C2C10C12, (d) PDPPT2-C2C12C14.*

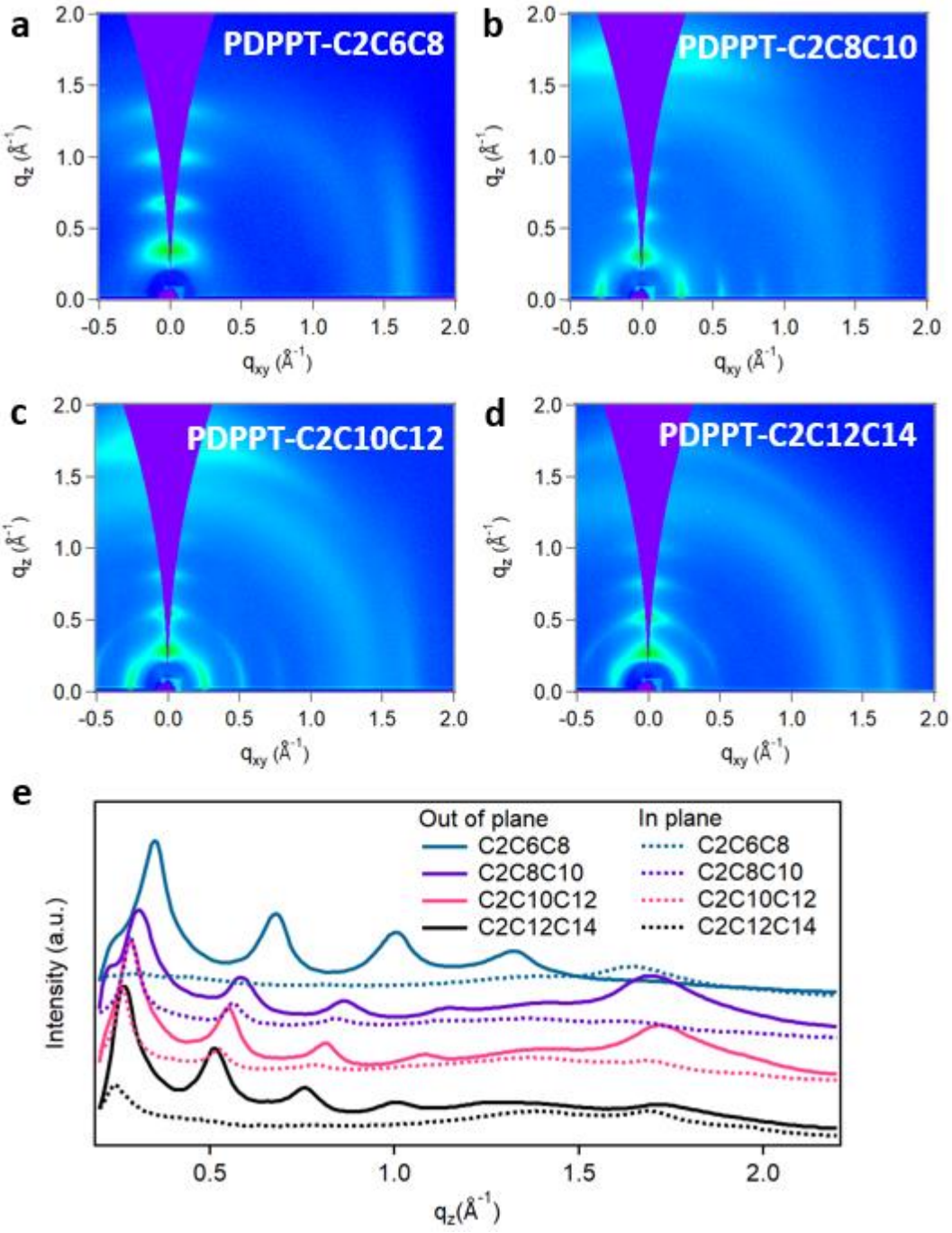

Figure D.6 *GIWAXS (a-d) 2D patterns (e) and 1D reduction plot for (a) PDPPT-C2C6C8, (b) PDPPT-C2C8C10, (c) PDPPT-C2C10C12, (d) PDPPT-C2C12C14.*

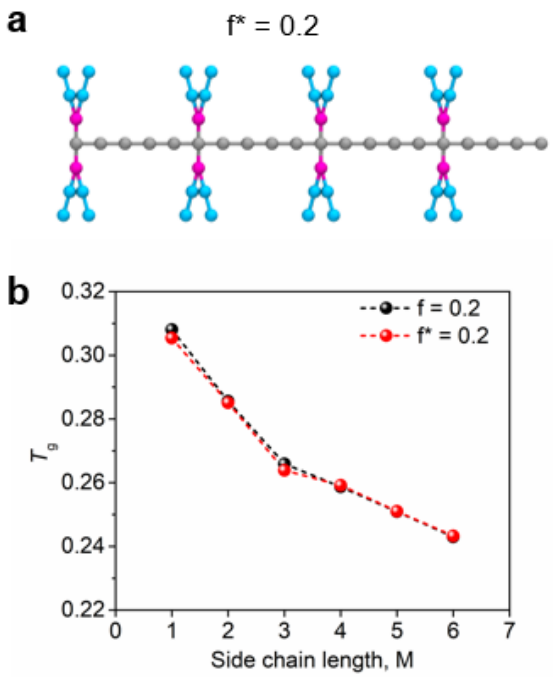

Figure D.7 *(a) Topological configuration of another polymer model with a grafting density of 0.2. (b) Comparison of side-chain length effect on T_g for two different configurations having a same grafting density of 0.2.*

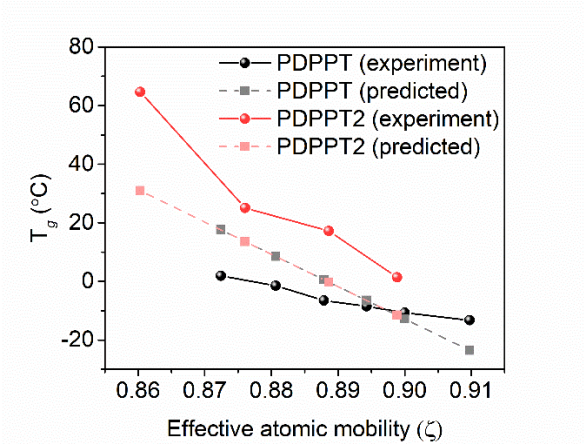

Figure D.8 *Comparison between the experimental T_g and predicted T_g for PDPPT-based and PDPPT2-based polymers with the effective atomic mobility model. ζ is the sum of effective atomic mobilities of individual bonds in the repeating unit.*

Table D.2 *Molecular weight of synthesized polymers.*

Polymer	Molecular weight M_n (kg/mol)	Dispersity
PDPPT-C2C6C8	88.5	4.09
PDPPT-C2C8C10	76.6	3.27
PDPPT-C2C10C12	60.6	2.44
PDPPT-C2C12C14	61.8	2.97
PDPPT-C2C6C10	24.3	1.77
PDPPT2-C2C6C8	58.1	2.26
PDPPT2-C2C8C10	99.1	1.76
PDPPT2-C2C10C12	21.9	1.45
PDPPT2-C2C12C14	44.2	3.96

Table D.3 *Elastic modulus of PDPPT-based polymers.*

Polymer	Elastic modulus (MPa)
PDPPT-C2C6C8	509±17.8
PDPPT-C2C8C10	299±23.3
PDPPT-C2C10C12	151±21.1
PDPPT-C2C12C14	104±9.5

Table D.4 *Mass-per-flexible bond model for P3ATs.*

Polymer	Mass (g/mol)	Flexible bond	M/F	T_g (°C)
P3BT	138	4.5	30.66	45
P3HT	166	6.5	25.53	13
P3OT	194	8.5	22.82	-13
P3DT	222	10.5	21.14	-25
P3DDT	250	12.5	20.00	-18

Table D.5 *Mass-per-flexible bond model for PDPP-based polymers.*

Polymer	Mass (g/mol)	Flexible bond	M/F	T_g (°C)
PDPPT-C2C6C8	828	35	23.66	1.88
PDPPT-C2C6C10	884	39	22.67	-1.49
PDPPT-C2C8C10	940	43	21.86	-6.53
PDPPT-C2C10C10	996	47	21.19	-8.48
PDPPT-C2C10C12	1052	51	20.63	-10.31
PDPPT-C2C12C14	1164	59	19.73	-13.26
PDPPT2-C2C6C8	910	36	25.28	64.69
PDPPT2-C2C8C10	1022	44	23.23	25.09
PDPPT2-C2C10C12	1134	52	21.81	17.22
PDPPT2-C2C12C14	1246	60	20.77	1.38

Table D.6 *Summarized peak positions of GIWAXS 1D plot for PDPPT-based polymers.*

Polymers	Peak positions q ($Å^{-1}$)				
Out of plane direction	(100)	(200)	(300)	(400)	(010)
PDPPT-C2C6C8	0.35	0.68	1.00	1.31	
PDPPT-C2C8C10	0.31	0.59	0.86	1.14	1.70
PDPPT-C2C10C12	0.29	0.55	0.81	1.07	1.73
PDPPT-C2C12C14	0.27	0.51	0.75	1.01	1.74
In plane direction	(100)	(200)	(300)	(400)	(010)
PDPPT-C2C6C8	N/A	N/A	N/A	N/A	1.65
PDPPT-C2C8C10	0.28	0.56	0.84	1.12	1.64
PDPPT-C2C10C12	0.26	0.52	0.78	1.05	1.69
PDPPT-C2C12C14	0.24	0.48	N/A	N/A	1.69

APPENDIX E

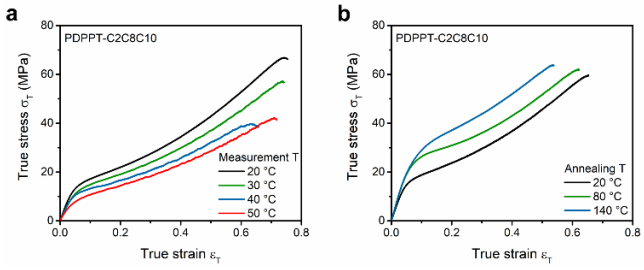

Figure E.1 *Temperature- and crystallinity-dependent stress-strain behavior of PDPPT-C2C8C10 polymer. (a) True stress-strain curves at four different measurement temperatures: 20, 30, 40, and 50 ºC. (b) True stress-strain curves for thermal annealed polymer thin films: 20, 80, and 140 ºC for 30 mins.*

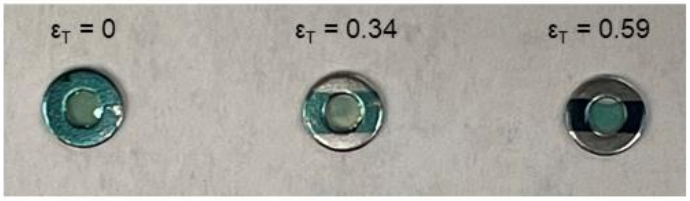

Figure E.2 *Representative optical images of strain-aligned PDPPT-C2C8C10 polymer thin films on top of hollow washers.*

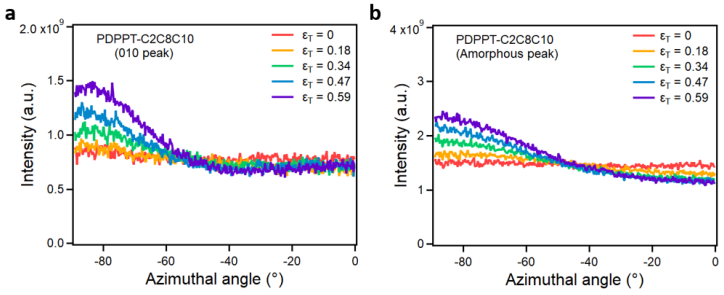

Figure E.3 *Pole figure analysis for strained PDPPT-C2C8C10 polymer based on wide-angle hard X-ray scattering result. (a) (010) peak, (b) Amorphous peak.*

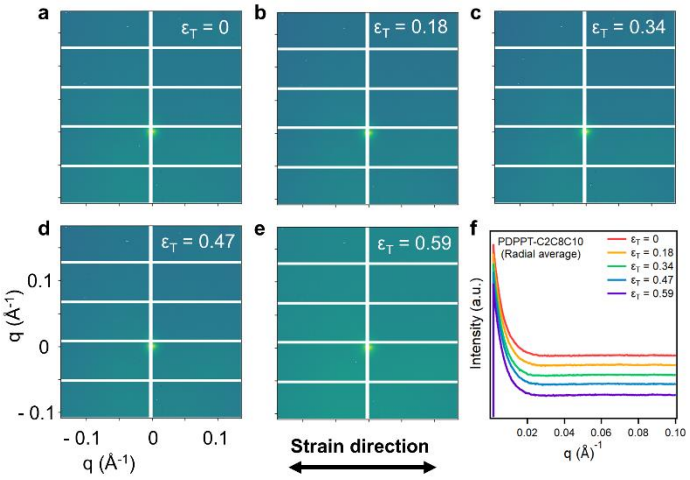

Figure E.4 *Small-angle hard X-ray scattering result for PDPPT-C2C8C10 polymer. (a-e) 2D scattering patterns for thin-films under various degrees of strain, (f) 1D radial averaged intensity versus q plot.*

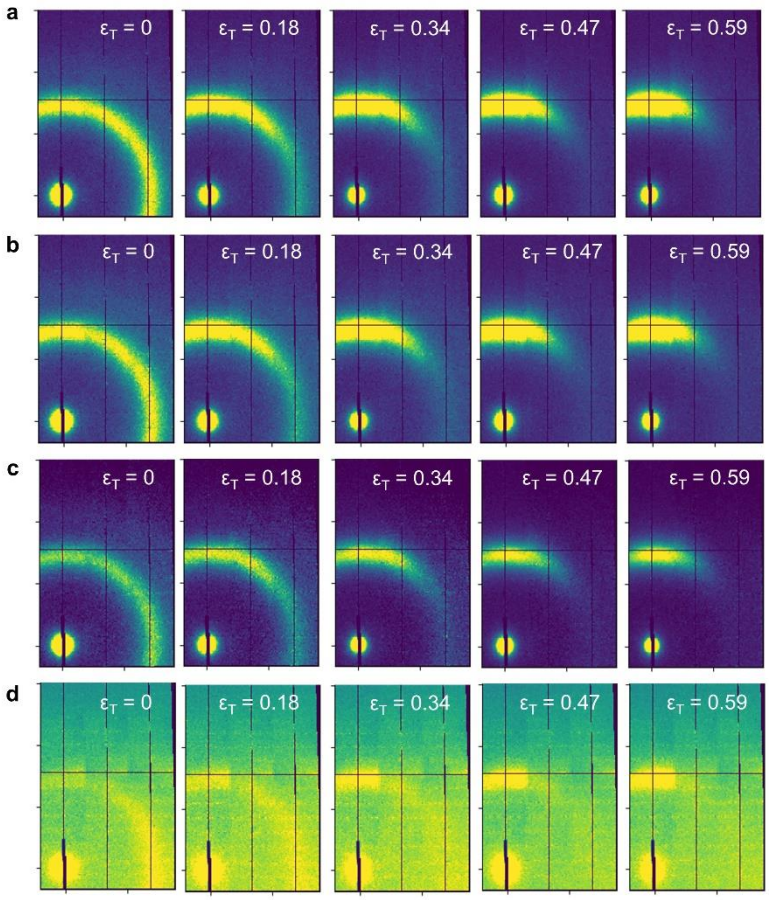

Figure E.5 *Wide-angle tender X-ray scattering 2D patterns of strained PDPPT-C2C8C10 thin films at different energies (a) 2.47 keV, (b) 2.472 keV, (c) 2.474 keV, (d) 2.476 keV.*

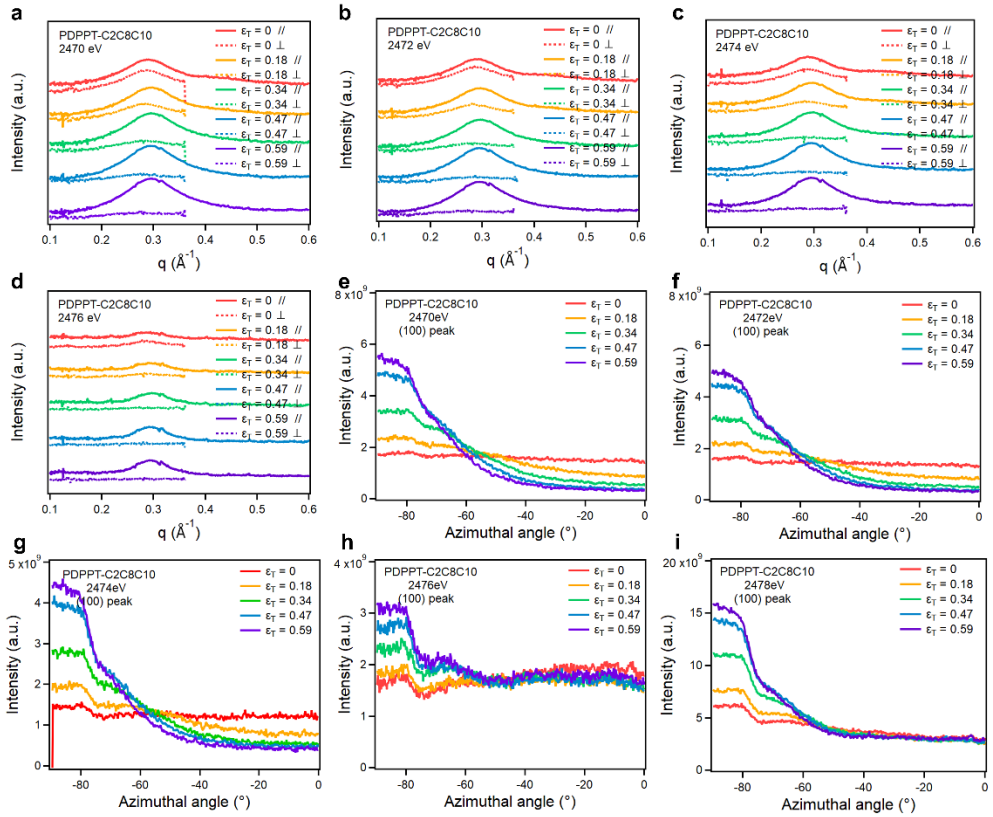

Figure E.6 *Sector averaged (a-d) and (100) pole figure analysis (e-i) for strained PDPPT-C2C8C10 thin films from tender X-ray scattering at different energies (a, e) 2.47 keV, (b, f) 2.472 keV, (c, g) 2.474 keV, (d, h) 2.476 keV, (i) 2.478 keV.*

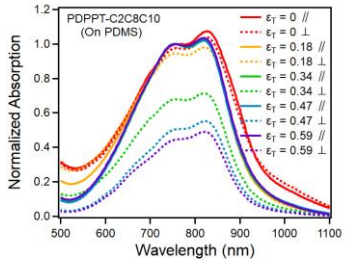

Figure E.7 *UV-vis absorption spectroscopy result for strained PDPPT-C2C8C10 thin films supported on the PDMS substrate.*

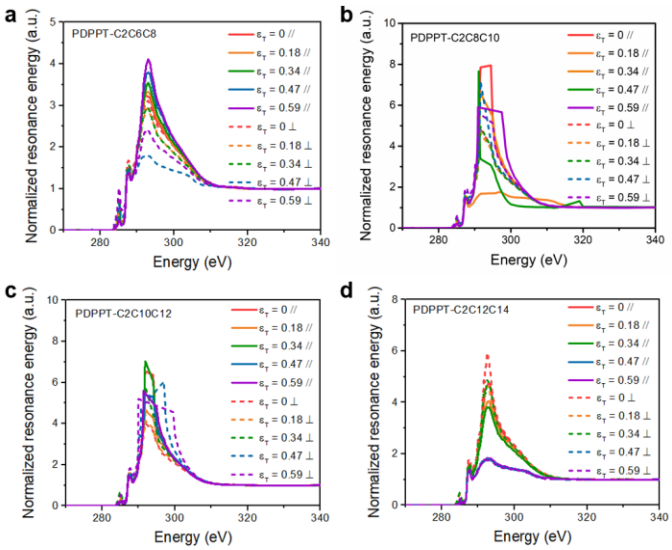

Figure E.8 *NEXAFS plots for (a) PDPPT-C2C6C8, (b) PDPPT-C2C8C10, (c) PDPPT-C2C10C12, (d) PDPPT-C2C12C14. The pre-edge (270-280 eV) intensity was set to 0, and post-edge (320-340 eV) intensity was normalized to 1.*

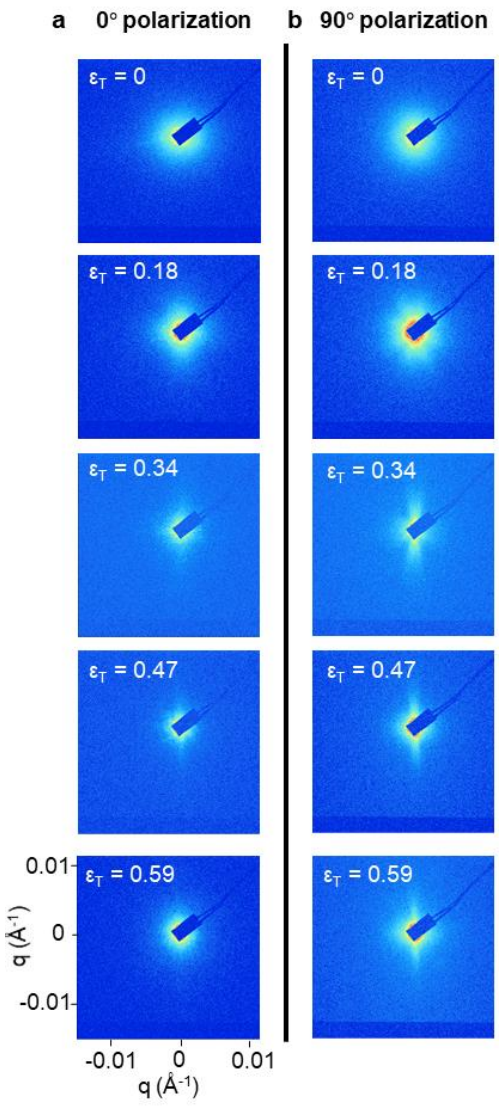

Figure E.9 *RSoXS 2D images for PDPPT-C2C8C10 under polarized X-ray at 285.2 eV. (a) 0° polarization angle (b) 90 ° polarization angle.*

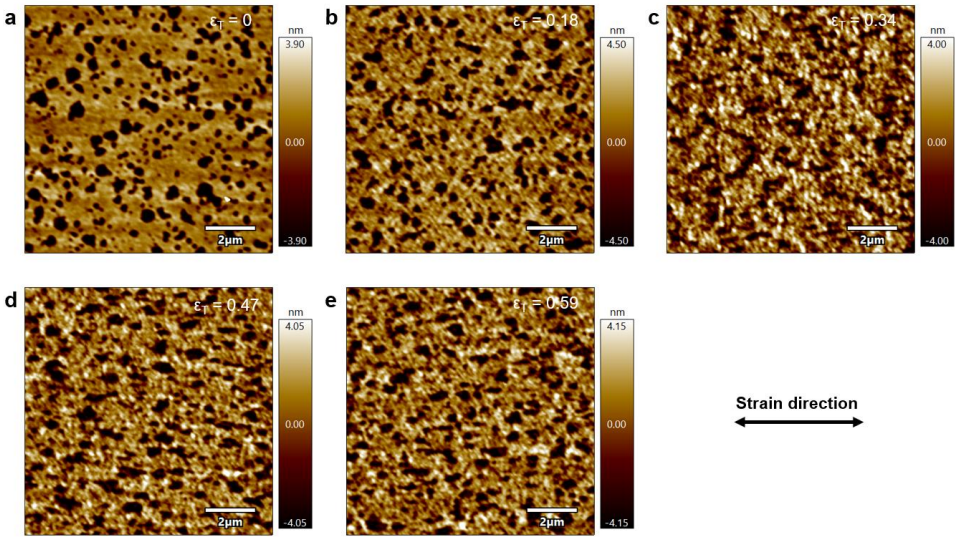

Figure E.10 *AFM height images for strained PDPPT-C2C8C10 films (a) $\varepsilon_T = 0$, (b) $\varepsilon_T = 0.18$, (c) $\varepsilon_T = 0.34$, (d) $\varepsilon_T = 0.47$, (e) $\varepsilon_T = 0.59$.*

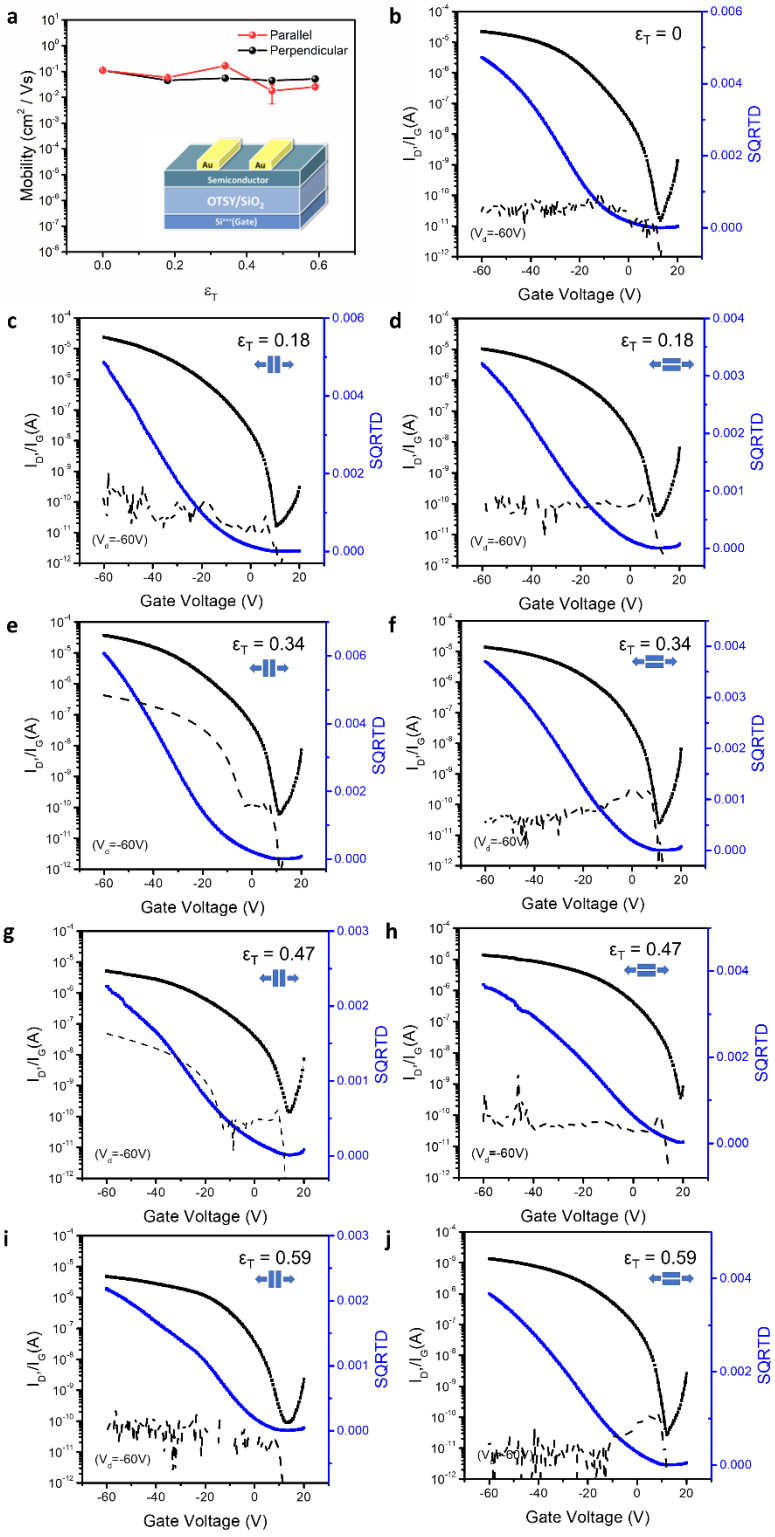
a
Parallel
Perpendicular
Mobility (cm² / Vs)
Au
Au
Semiconductor
OTSY/SiO2
Si+++(Gate)
εT
b
εT = 0
c
εT = 0.18
d
εT = 0.18
e
εT = 0.34
f
εT = 0.34
g
εT = 0.47
h
εT = 0.47
i
εT = 0.59
j
εT = 0.59
ID/IG(A)
SQRTD
Gate Voltage (V)
(Vd=-60V)

Figure E.11 *Charge carrier mobility and representative transfer curves for PDPPT-C2C8C10 polymer thin films under different strain along two charge transport directions. (a,b) $\varepsilon_T = 0$, (c,d) $\varepsilon_T = 0.18$, (e,f) $\varepsilon_T = 0.34$, (g,h) $\varepsilon_T = 0.47$, (i,j) $\varepsilon_T = 0.59$.*

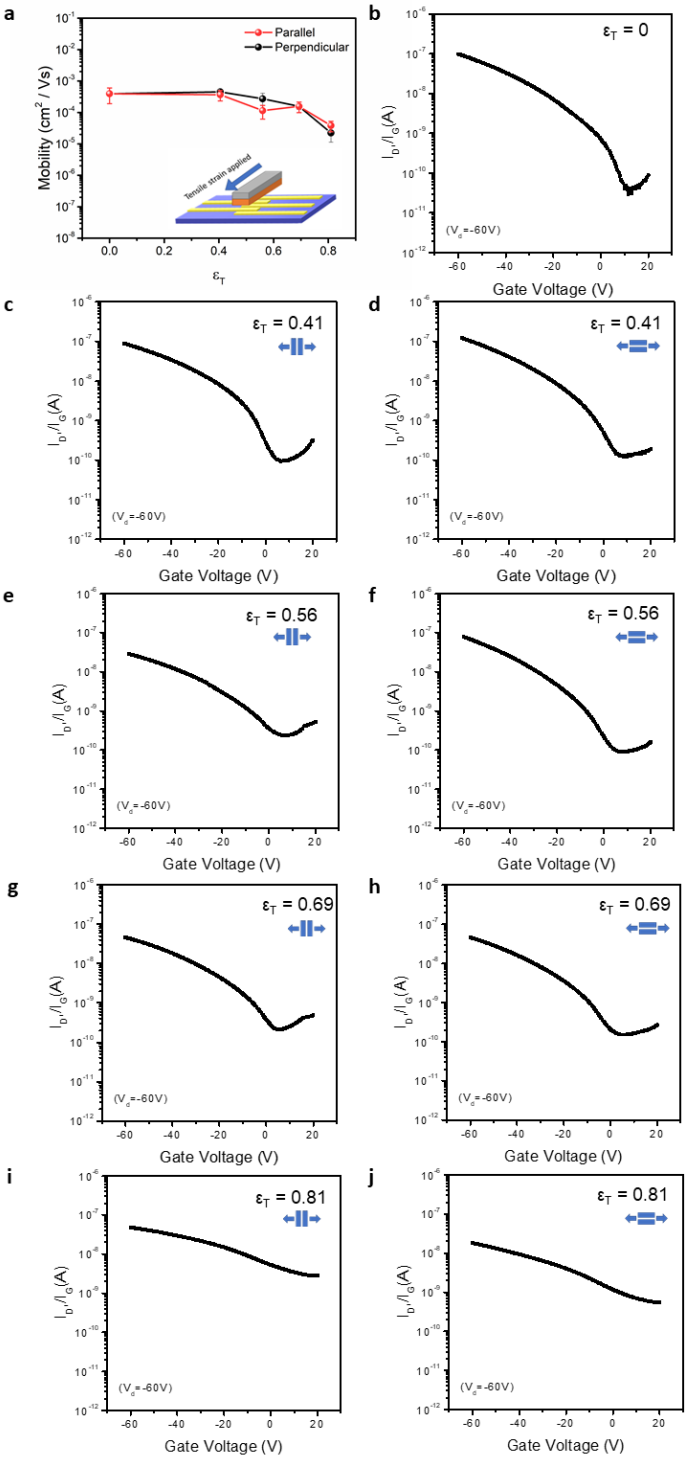

Figure E.12 *Charge* carrier mobility and representative transfer curves for PDMS-supported P3HT polymer thin films under different strain along two charge transport directions. (a,b) εT = 0, (c,d) εT = 0.41, (e,f) εT = 0.56, (g,h) εT = 0.69, (i,j) εT = 0.81.

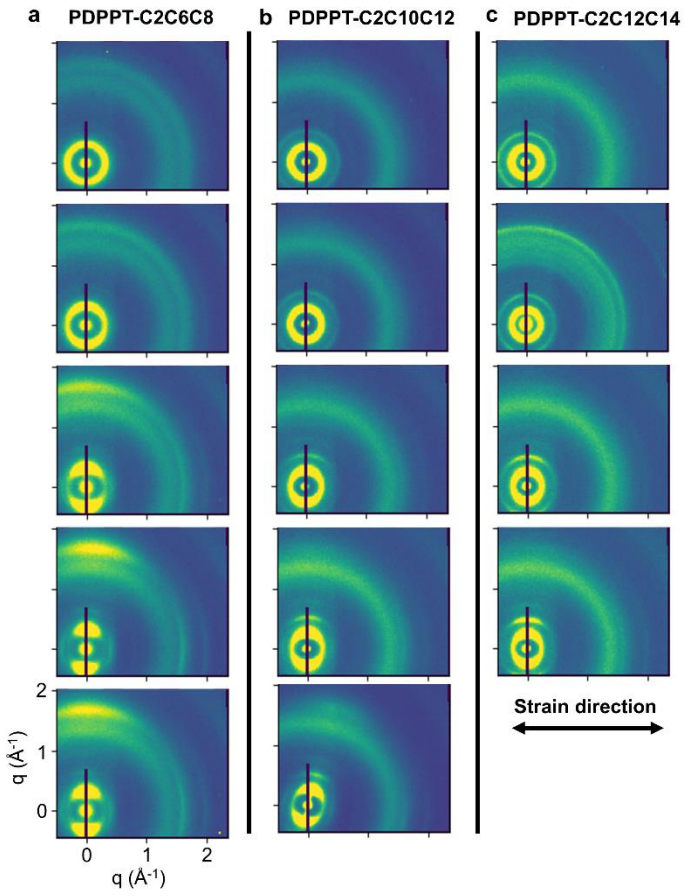

Figure E.13 *Wide-angle hard X-ray scattering 2D patterns for (a) PDPPT-C2C6C8, (b) PDPPT-C2C10C12, (c) PDPPT-C2C12C14 under various strains.*

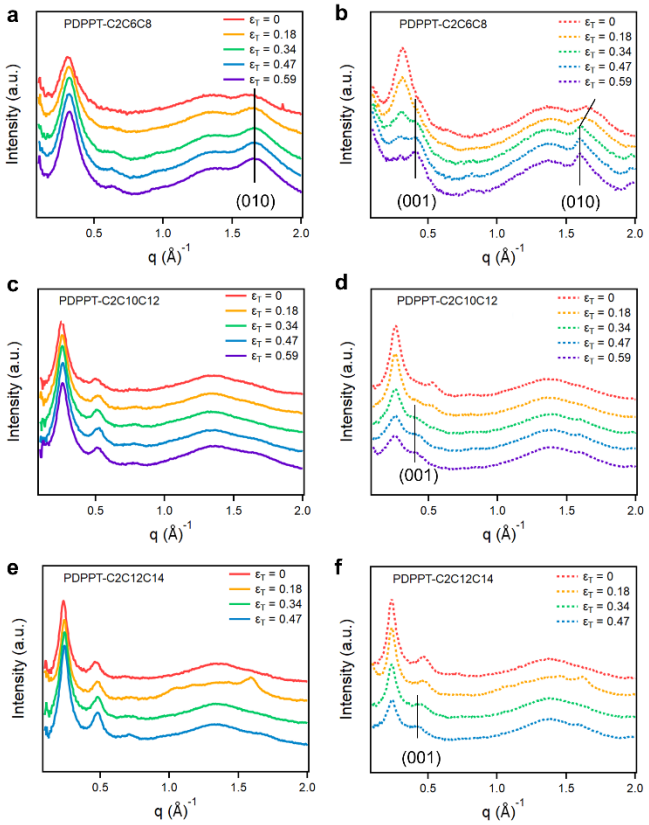

Figure E.14 *Wide-angle hard X-ray scattering sector averaged integration along meridian direction (a, c, e) and equatorial direction (b, d, f) for (a, b) PDPPT-C2C6C8, (c, d) PDPPT-C2C10C12, (e, f) PDPPT-C2C12C14 under various strains.*

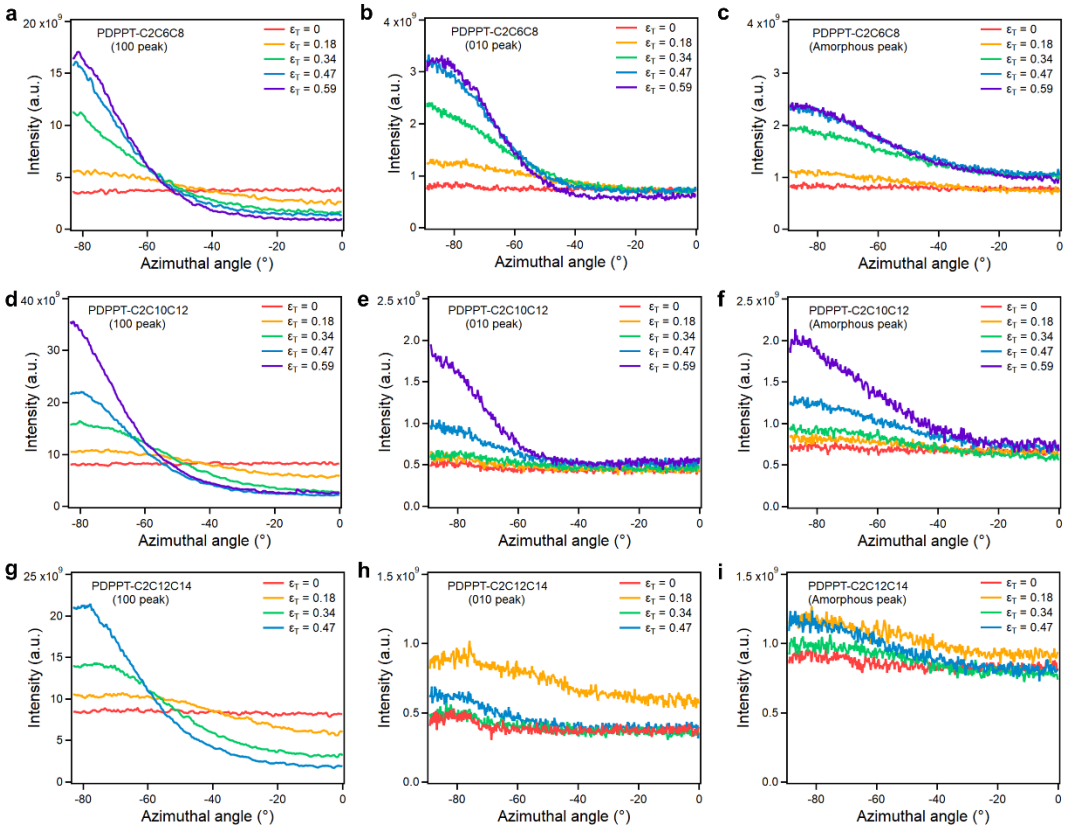

Figure E.15 *Wide-angle hard X-ray scattering pole figure analysis of (100) peak (a, d, g), (010) peak (b, e, h) and amorphous peak (c, f, i) for (a, b, c) PDPPT-C2C6C8, (d, e, f) PDPPT-C2C10C12, (g, h, i) PDPPT-C2C12C14 under various strains.*

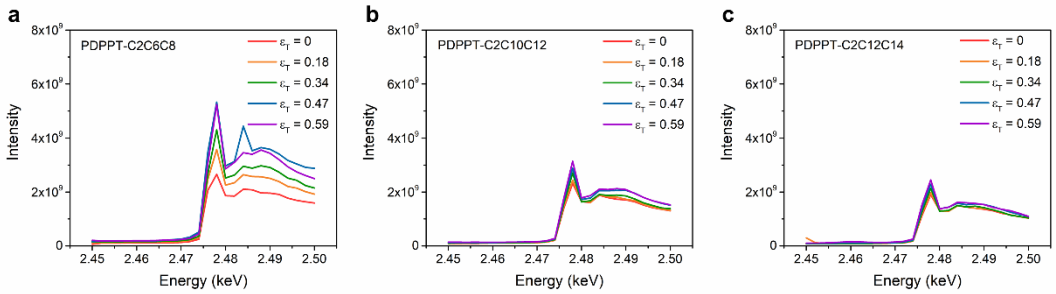

Figure E.16 *Tender X-ray fluorescence yield near the sulfur edge energy for strained polymer samples (a) PDPPT-C2C6C8, (b) PDPPT-C2C10C12, (c) PDPPT-C2C12C14.*

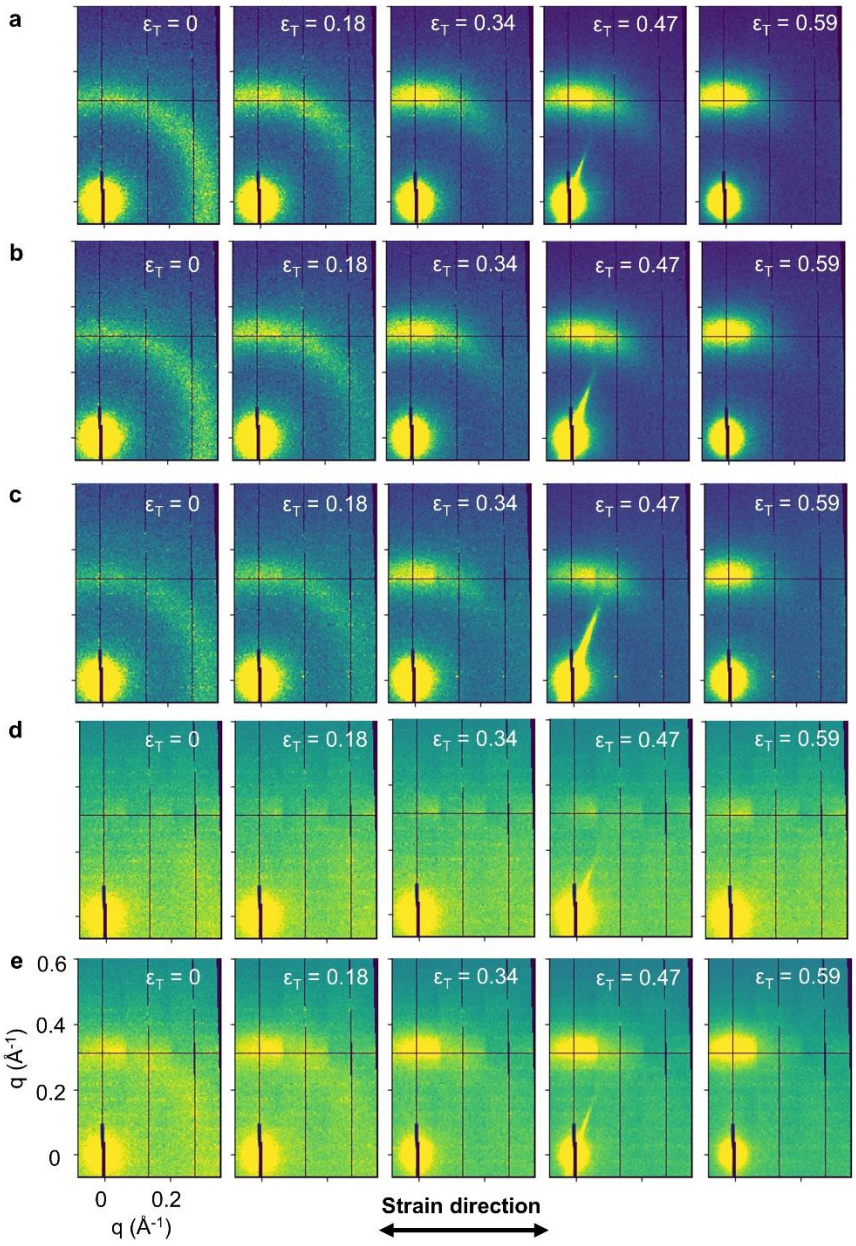

Figure E.17 *Wide-angle tender X-ray scattering 2D patterns of strained PDPPT-C2C6C8 thin films at different energies (a) 2.47 keV, (b) 2.472 keV, (c) 2.474 keV, (d) 2.476 keV, (e) 2.478 keV.*

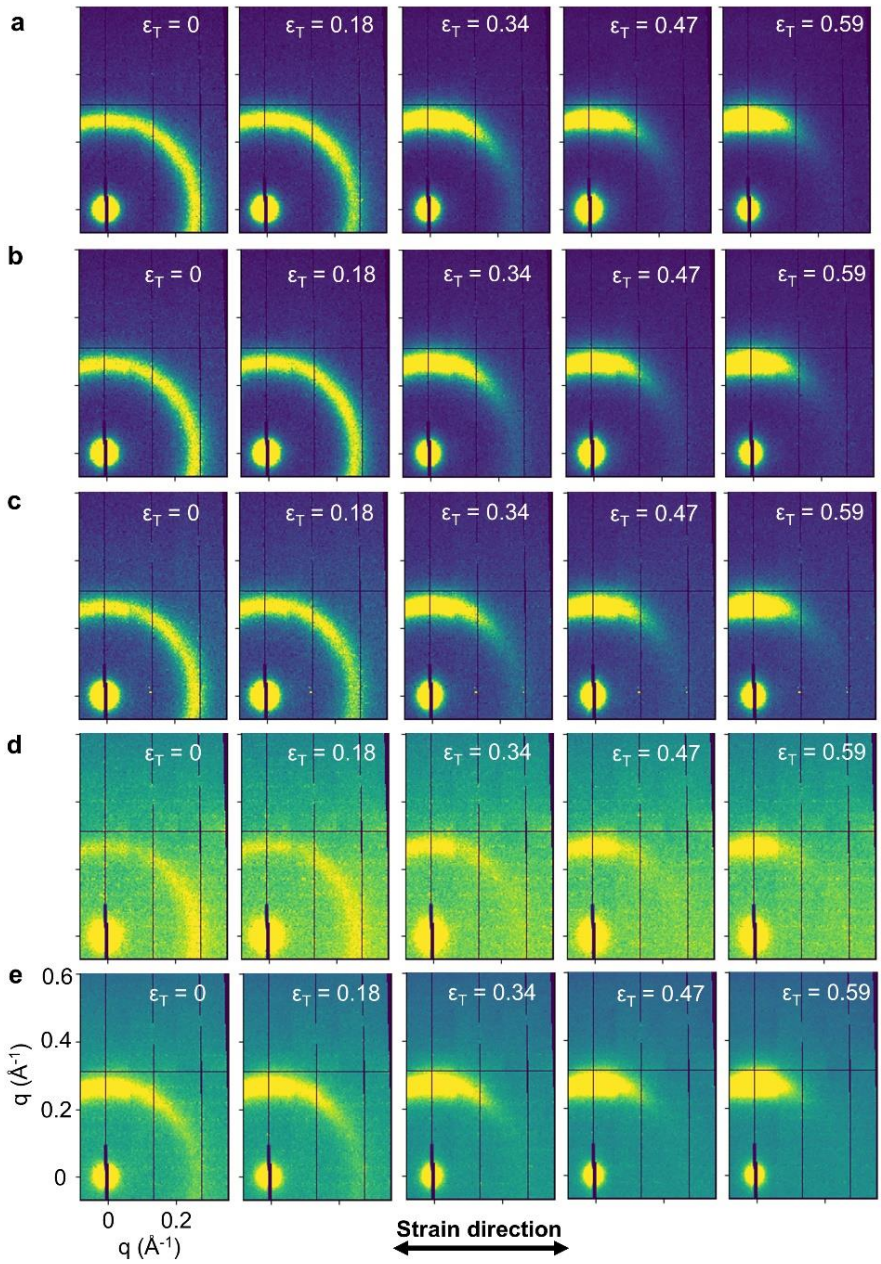

Figure E.18 *Wide-angle tender X-ray scattering 2D patterns of strained PDPPT-C2C10C12 thin films at different energies (a) 2.47 keV, (b) 2.472 keV, (c) 2.474 keV, (d) 2.476 keV, (e) 2.478 keV.*

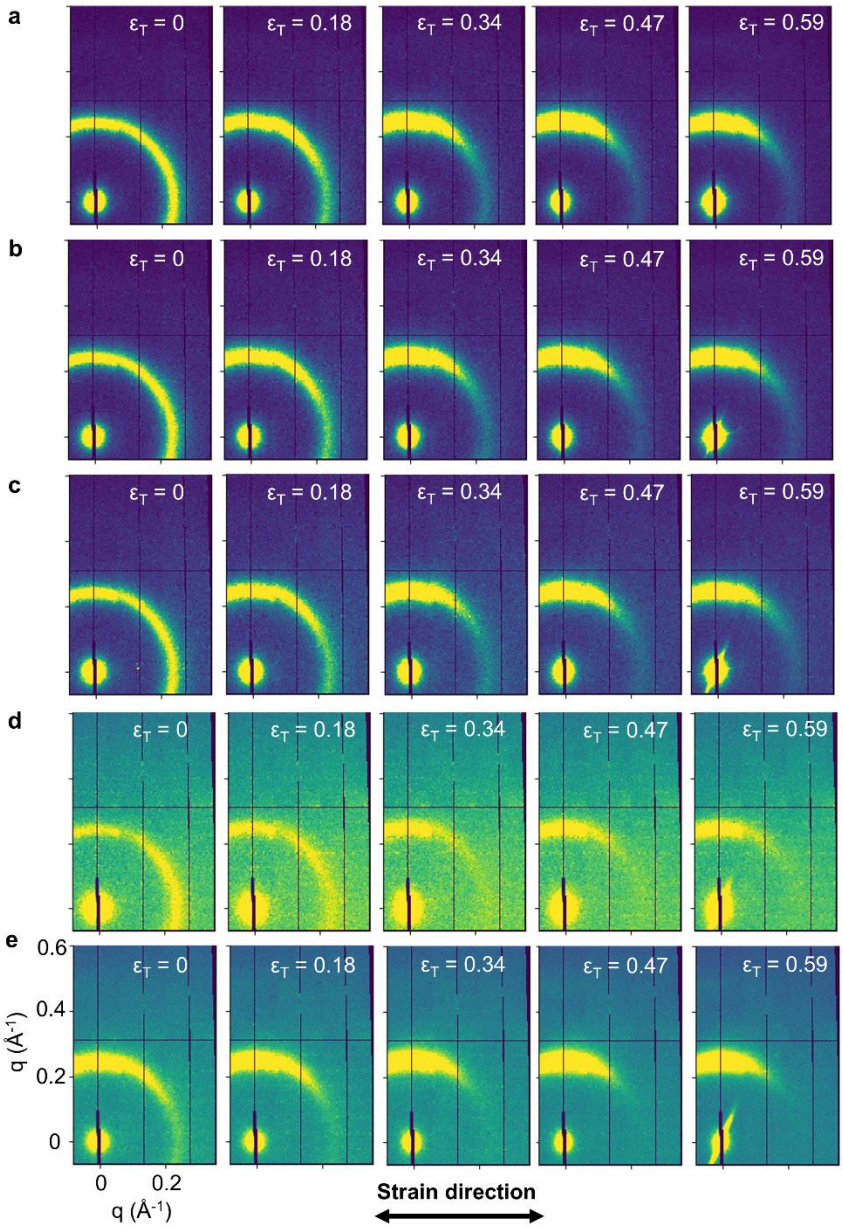

Figure E.19 *Wide-angle tender X-ray scattering 2D patterns of strained PDPPT-C2C12C14 thin films at different energies (a) 2.47 keV, (b) 2.472 keV, (c) 2.474 keV, (d) 2.476 keV, (e) 2.478 keV.*

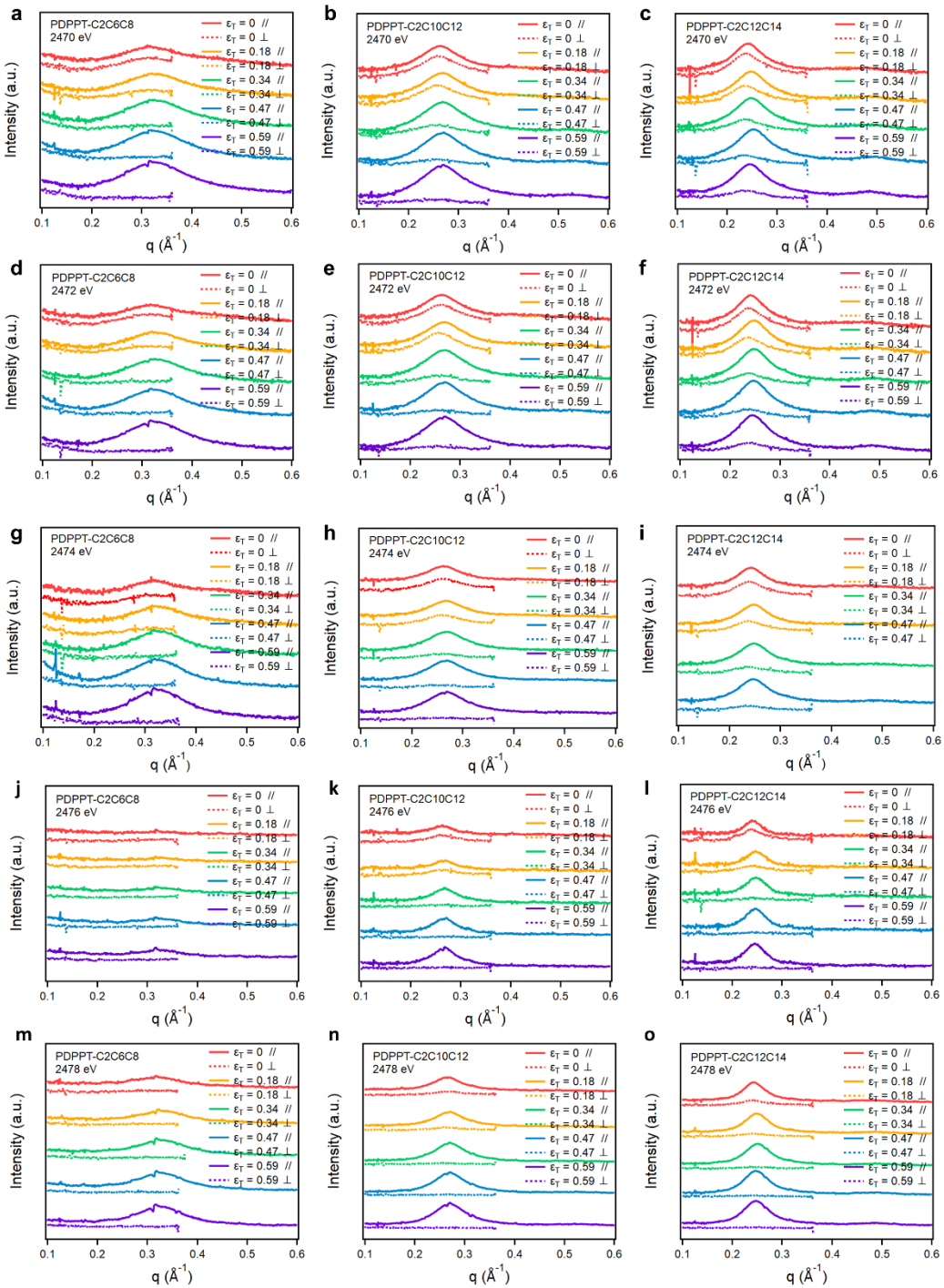

Figure E.20 *Wide-angle tender X-ray scattering sector averaged integration of strained (a, d, g, j, m) PDPPT-C2C6C8, (b, e, h, k, n) PDPPT-C2C10C12, (c, f, i, l, o) PDPPT-C2C12C14 thin films at different energies (a-c) 2.47 keV, (d-f) 2.472 keV, (g-i) 2.474*

keV, (j-l) 2.476 keV, (m-o) 2.478 keV. The parallel symbol (//) represents meridian direction and perpendicular symbol (⊥) represents equatorial direction.

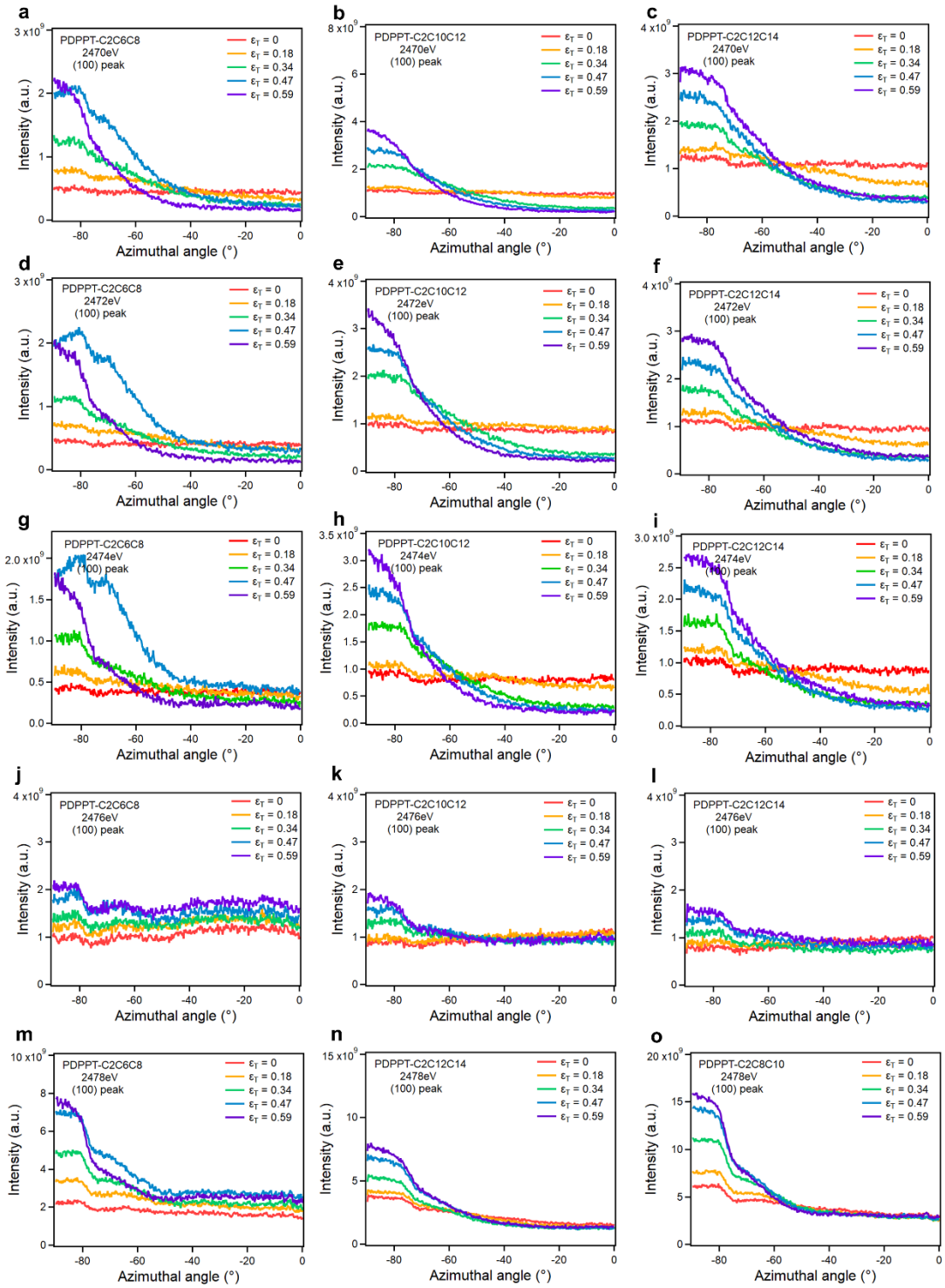

Figure E.21 *Wide-angle tender X-ray scattering (100) pole figure analysis of strained (a, d, g, j, m) PDPPT-C2C6C8, (b, e, h, k, n) PDPPT-C2C10C12, (c, f, i, l, o) PDPPT-C2C12C14 thin films at different energies (a-c) 2.47 keV, (d-f) 2.472 keV, (g-i) 2.474 keV, (j-l) 2.476 keV, (m-o) 2.478 keV.*

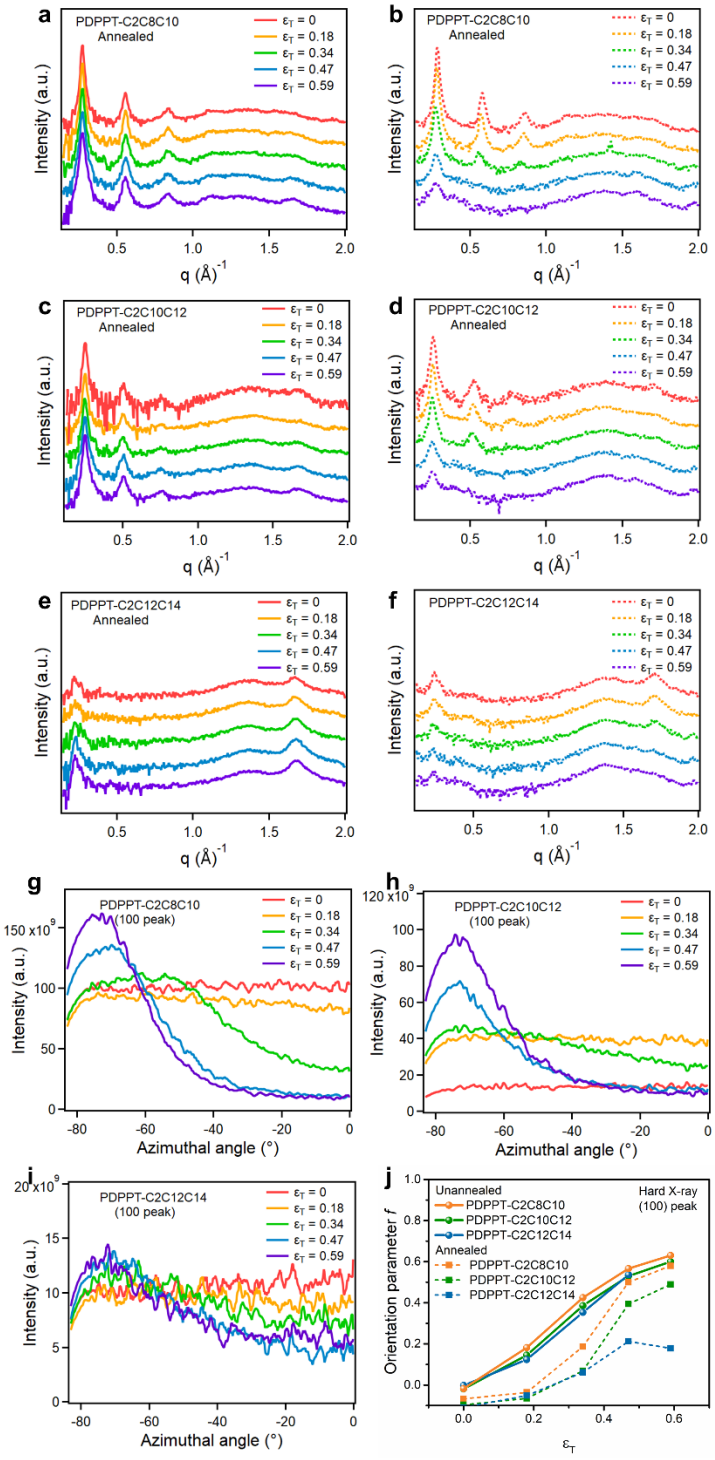

Figure E.22 *Wide-angle hard X-ray scattering on annealed PDPP polymers. (a-h) Sector averaged integration along meridian direction (a, c, e) and equatorial direction (b, d, f)*

for (a, b) PDPPT-C2C8C10, (c, d) PDPPT-C2C10C12, (e, f) PDPPT-C2C12C14 under various strains. (g-i) Pole figure analysis on the (100) peak for (g) PDPPT-C2C8C10, (h) PDPPT-C2C10C12, (i) PDPPT-C2C12C14. (j) Comparison of orientation parameter before and after thermal annealing.

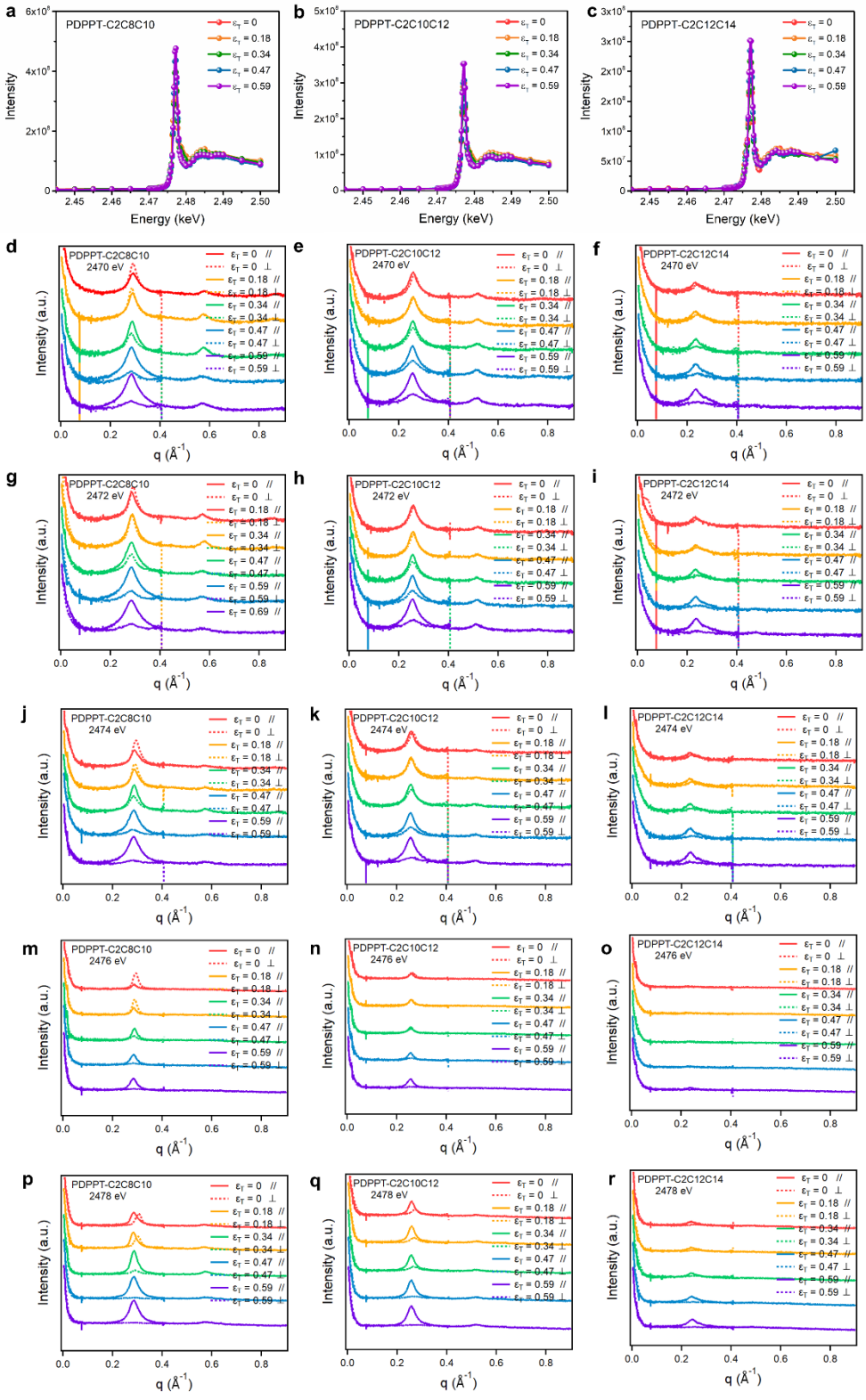
a
PDPPT-C2C8C10
b
PDPPT-C2C10C12
c
PDPPT-C2C12C14
Intensity
Energy (keV)
d
e
f
g
h
i
j
k
l
m
n
o
p
q
r
2470 eV
2472 eV
2474 eV
2476 eV
2478 eV
Intensity (a.u.)
q (Å^{-1})

Figure E.23 *Wide-angle tender X-ray scattering and fluorescence on annealed samples. (a-c) Tender X-ray fluorescence yield near the sulfur edge energy. (d, g, j, m, p) PDPPT-C2C8C10, (e, h, k, n, q) PDPPT-C2C10C12, (f, i, l, o, r) PDPPT-C2C12C14 thin films under various strains at different energies (d-f) 2.47 keV, (g-i) 2.472 keV, (j-l) 2.474 keV, (m-o) 2.476 keV, (p-r) 2.478 keV. The parallel symbol (//) means meridian direction and perpendicular symbol (⊥) means equatorial direction.*

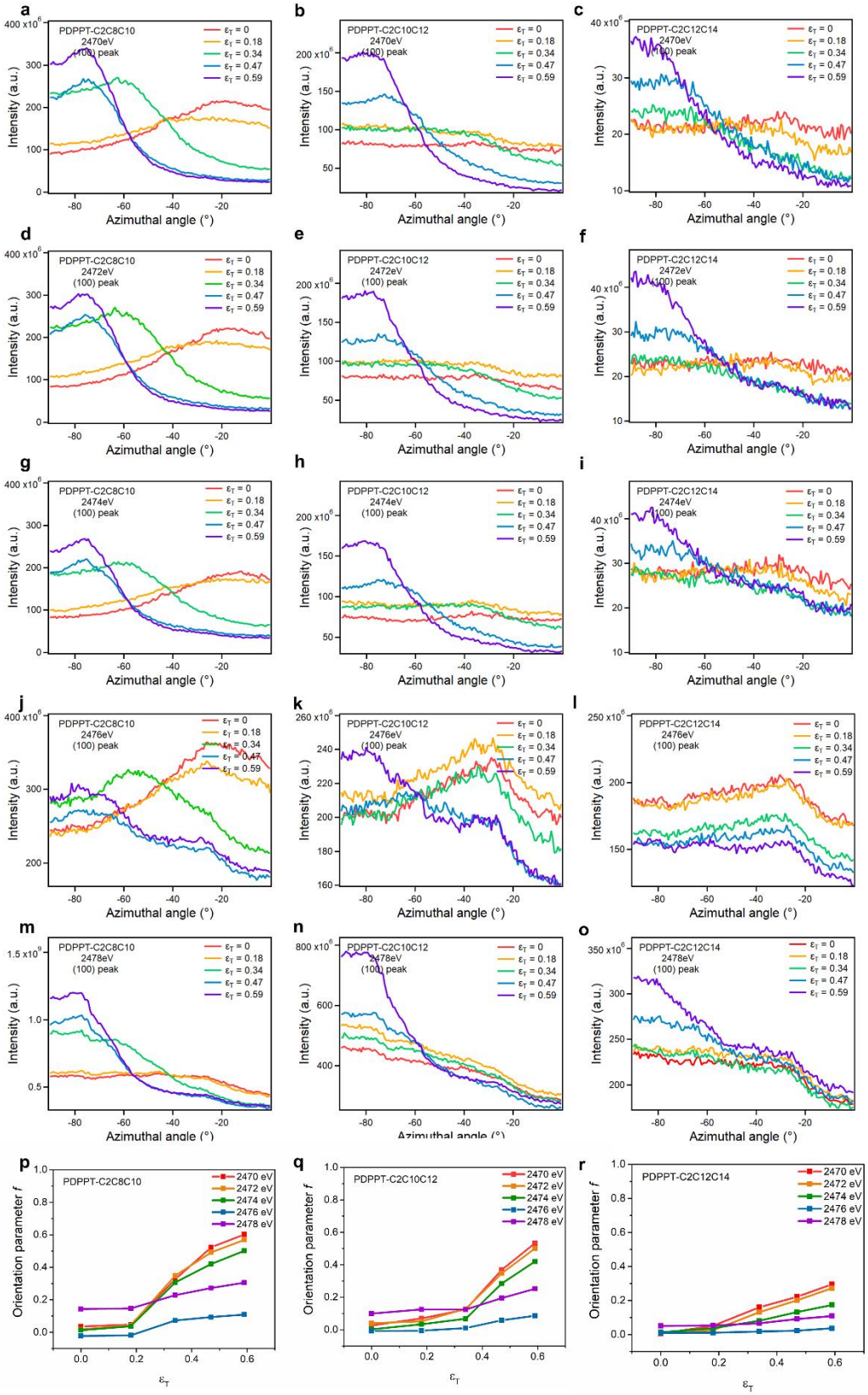
a
PDPPT-C2C8C10
2470eV
(100) peak
b
PDPPT-C2C10C12
2470eV
(100) peak
c
PDPPT-C2C12C14
2470eV
(100) peak
d
PDPPT-C2C8C10
2472eV
(100) peak
e
PDPPT-C2C10C12
2472eV
(100) peak
f
PDPPT-C2C12C14
2472eV
(100) peak
g
PDPPT-C2C8C10
2474eV
(100) peak
h
PDPPT-C2C10C12
2474eV
(100) peak
i
PDPPT-C2C12C14
2474eV
(100) peak
j
PDPPT-C2C8C10
2476eV
(100) peak
k
PDPPT-C2C10C12
2476eV
(100) peak
l
PDPPT-C2C12C14
2476eV
(100) peak
m
PDPPT-C2C8C10
2478eV
(100) peak
n
PDPPT-C2C10C12
2478eV
(100) peak
o
PDPPT-C2C12C14
2478eV
(100) peak
Intensity (a.u.)
Azimuthal angle (°)
εT = 0
εT = 0.18
εT = 0.34
εT = 0.47
εT = 0.59
p
PDPPT-C2C8C10
q
PDPPT-C2C10C12
r
PDPPT-C2C12C14
2470 eV
2472 eV
2474 eV
2476 eV
2478 eV
Orientation parameter f
εT

Figure E.24 *Wide-angle tender X-ray scattering (a-o) pole figure analysis and (p-r) orientation parameter summary of annealed (a, d, g, j, m, p) PDPPT-C2C8C10, (b, e, h, k, n, q) PDPPT-C2C10C12, (c, f, i, l, o, r) PDPPT-C2C12C14 thin films under various strains at different energies (a-c) 2.47 keV, (d-f) 2.472 keV, (g-i) 2.474 keV, (j-l) 2.476 keV, (m-o) 2.478 keV.*

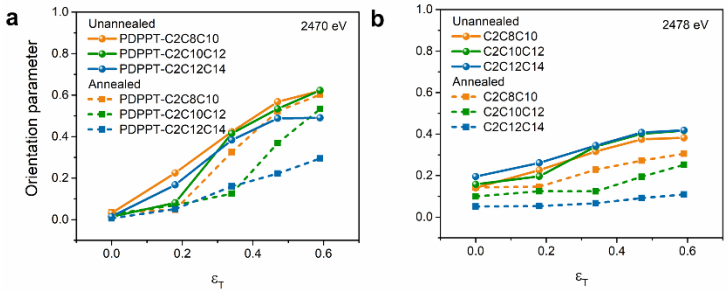

Figure E.25 *Comparison of orientation parameter from tender X-ray scattering before and after thermal annealing at (g) 2.47 keV and (h) 2.478 keV.*

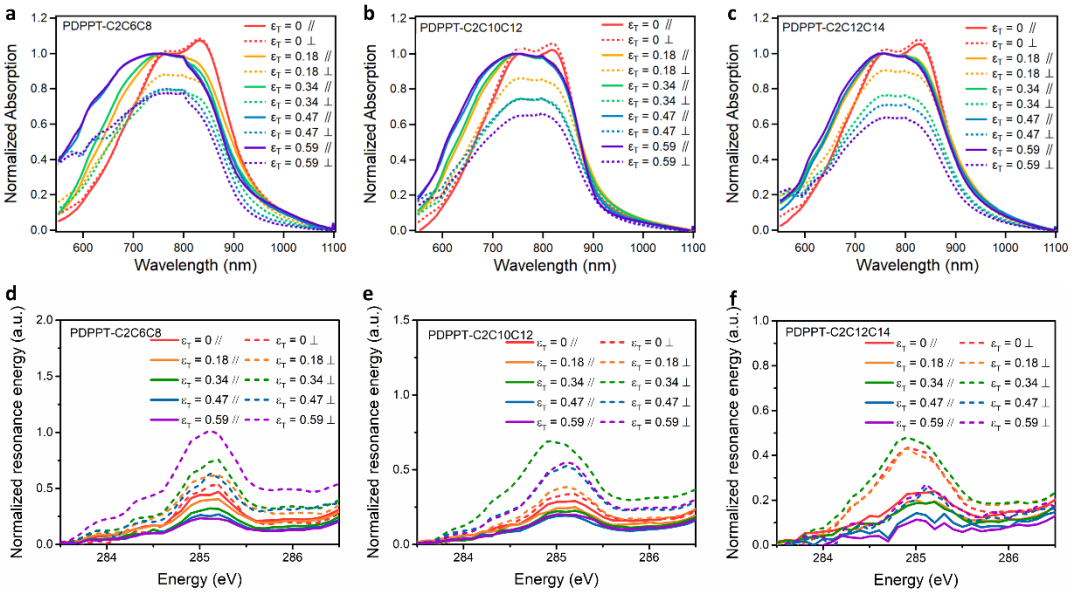

Figure E.26 *Polarized UV-vis absorption spectroscopy (a-c) and polarized transmission NEXAFS results (d-f) of strained (a, d) PDPPT-C2C6C8, (b, e) PDPPT-C2C10C12, (c, f) PDPPT-C2C12C14 thin films. The parallel symbol (//) represents meridian direction and perpendicular symbol (⊥) represents equatorial direction.*

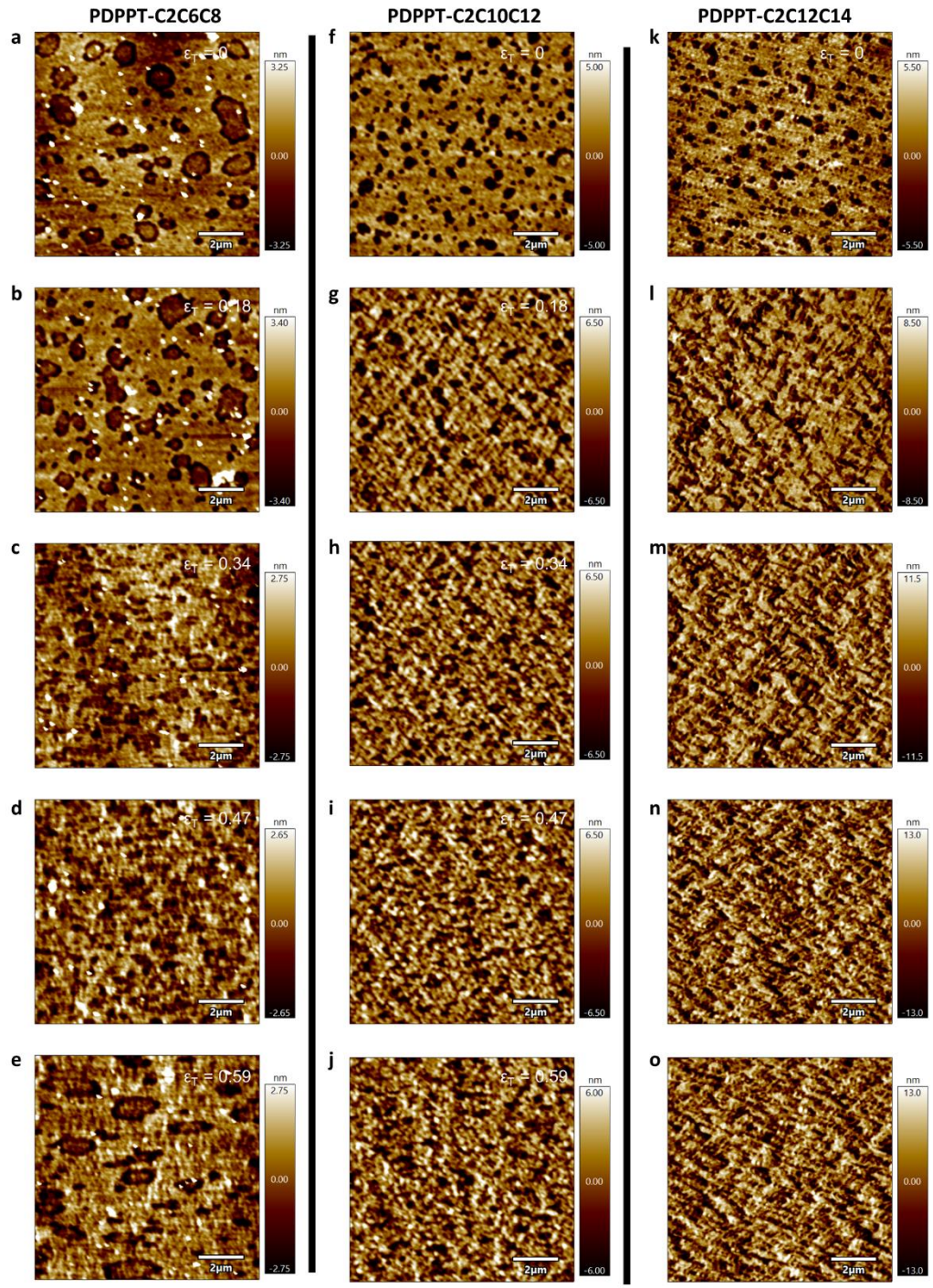

Figure E.27 *AFM height images for strained (a-e) PDPPT-C2C6C8, (f-j) PDPPT-C2C10C12, (k-o) PDPPT-C2C12C14 films.*

Table E.2 *Summary of OFET device performance for PDPPT-C2C8C10 under deformation.*

	Strain (ε_T)	W/L	μ_{max} ($cm^2\ V^{-1}\ s^{-1}$)	μ_{ave} ($cm^2\ V^{-1}\ s^{-1}$)	on/off	Vt_sat (V)
Parallel	0	20	1.61E-01	1.11E-01± 0.0085	1.98E+06	-11.97
	0.18	20	6.75E-02	5.85E-02± 0.0039	6.60E+05	-11.94
	0.34	20	1.80E-01	1.68E-01± 0.008	4.06E+05	-5.70
	0.47	20	3.32E-02	1.80E-02± 0.0124	2.52E+04	9.48
	0.59	20	3.04E-02	2.53E-02± 0.0035	3.18E+04	2.23
Perpendicular	0	20	1.61E-01	1.11E-01± 0.0085	1.98E+06	-11.97
	0.18	20	5.26E-02	4.51E-02± 0.0054	3.09E+05	-3.46
	0.34	20	5.96E-02	5.52E-02± 0.0051	4.34E+05	0.12
	0.47	20	4.93E-02	4.45E-02± 0.0032	3.95E+05	4.28
	0.59	20	5.50E-02	5.14E-02± 0.004	5.75E+05	-2.56

Table E.3 *Summary of OFET device performance for PDMS supported P3HT under deformation.*

	Strain (ε_T)	W/L	μ_{max} ($cm^2\ V^{-1}\ s^{-1}$)	μ_{ave} ($cm^2\ V^{-1}\ s^{-1}$)	on/off	Vt_sat (V)
Parallel	0	20	7.33E-04	3.95E-04 ± 0.0002	1.39E+03	-15.96
	0.41	20	5.68E-04	3.66E-04 ± 0.00013	1.93E+03	-10.88
	0.56	20	1.87E-04	1.14E-04 ± 0.000053	3.42E+02	-4.06
	0.69	20	2.51E-04	1.56E-04 ± 0.000057	9.86E+02	-7.61
	0.81	20	5.65E-05	3.83E-05 ± 0.000014	1.66E+01	20.85
Perpendicular	0	20	3.97E-04	3.95E-04 ± 0.0002	1.39E+03	-15.96
	0.41	20	4.71E-04	4.51E-04 ±0.000024	6.69E+02	-17.68
	0.56	20	3.70E-04	2.72E-04 ± 0.00013	6.83E+02	-14.69
	0.69	20	1.79E-04	1.56E-04 ±0.000032	3.57E+02	-12.92
	0.81	20	3.13E-05	2.24E-05 ± 0.000011	4.39E+01	8.93

Table E.4 *Crystallographic information for PDPPT-C2C6C8 extracted from wide-angle hard X-ray scattering*

Strain (ε_T)	Equatorial direction				Meridian direction			
	(100)			(010)	(100)			(010)
	q ($Å^{-1}$)	FWHM ($Å^{-1}$)	Coherence length (Å)	q ($Å^{-1}$)	q ($Å^{-1}$)	FWHM ($Å^{-1}$)	Coherence length (Å)	q ($Å^{-1}$)
0	0.321	0.105	13.21	1.696	0.315	0.104	13.34	1.667
0.18	0.322	0.128	10.84	1.673	0.321	0.100	13.87	1.673
0.34	0.336	0.229	6.058	1.645	0.322	0.096	14.45	1.684
0.47	0.382	0.211	6.576	1.634	0.322	0.097	14.30	1.678
0.59	0.409	0.140	9.912	1.623	0.323	0.099	14.01	1.683

Table E.5 *Crystallographic information for PDPPT-C2C10C12 extracted from wide-angle hard X-ray scattering*

Strain (ε_T)	Equatorial direction			Meridian direction		
	(100)			(100)		
	q (Å^{-1})	FWHM (Å^{-1})	Coherence length (Å)	q (Å^{-1})	FWHM (Å^{-1})	Coherence length (Å)
0	0.262	0.058	23.91	0.257	0.055	25.21
0.18	0.261	0.062	22.37	0.262	0.055	25.21
0.34	0.261	0.082	16.91	0.262	0.053	26.16
0.47	0.258	0.101	13.73	0.264	0.055	25.21
0.59	0.259	0.100	13.87	0.264	0.057	24.33

Table E.6 *Crystallographic information for PDPPT-C2C12C14 extracted from wide-angle hard X-ray scattering*

Strain (ε_T)	Equatorial direction			Meridian direction		
	(100)			(100)		
	q (Å^{-1})	FWHM (Å^{-1})	Coherence length (Å)	q (Å^{-1})	FWHM (Å^{-1})	Coherence length (Å)
0	0.239	0.041	33.82	0.236	0.041	33.82
0.18	0.240	0.043	32.25	0.241	0.040	34.67
0.34	0.240	0.056	24.76	0.243	0.041	33.82
0.47	0.240	0.060	23.11	0.243	0.040	34.67

Table E.7 *Crystallographic information for thermally annealed PDPPT-C2C8C10 extracted from wide-angle hard X-ray scattering*

Strain (ε_T)	Equatorial direction			Meridian direction		
	(100)			(100)		
	q (Å^{-1})	FWHM (Å^{-1})	Coherence length (Å)	q (Å^{-1})	FWHM (Å^{-1})	Coherence length (Å)
0	0.286	0.02	69.34	0.275	0.018	77.04
0.18	0.283	0.02	69.34	0.275	0.016	86.67
0.34	0.276	0.029	47.82	0.275	0.02	69.34
0.47	0.278	0.043	32.25	0.276	0.023	60.30
0.59	0.278	0.055	25.21	0.275	0.025	55.47

Table E.8 *Crystallographic information for thermally annealed PDPPT-C2C10C12 extracted from wide-angle hard X-ray scattering*

Strain (ε_T)	Equatorial direction			Meridian direction		
	(100)			(100)		
	q (Å^{-1})	FWHM (Å^{-1})	Coherence length (Å)	q (Å^{-1})	FWHM (Å^{-1})	Coherence length (Å)
0	0.259	0.025	55.47	0.248	0.023	60.29
0.18	0.257	0.024	57.78	0.247	0.024	57.78
0.34	0.253	0.03	46.22	0.247	0.025	55.47
0.47	0.253	0.046	30.14	0.247	0.025	55.47
0.59	0.254	0.047	29.50	0.248	0.024	57.78

Table E.9 *Crystallographic information for thermally annealed PDPPT-C2C12C14 extracted from wide-angle hard X-ray scattering*

Strain (ε_T)	Equatorial direction			Meridian direction		
	(100)			(100)		
	q (Å^{-1})	FWHM (Å^{-1})	Coherence length (Å)	q (Å^{-1})	FWHM (Å^{-1})	Coherence length (Å)
0	0.239	0.034	40.78	0.234	0.07	19.81
0.18	0.239	0.034	40.78	0.233	0.058	23.91
0.34	0.237	0.056	24.76	0.241	0.087	15.94
0.47	0.23	0.034	40.78	0.23	0.03	46.22
0.59	0.233	0.046	30.14	0.232	0.044	31.51

APPENDIX F

Materials

Commercial reactants were used without further purification unless stated otherwise. All the solvents used in these reactions were distilled prior to use. Tris(dibenzylideneacetone)dipalladium(0)-chloroform adduct ($Pd_2(dba)_3$•$CHCl_3$) was purchased from Sigma Aldrich and recrystallized following a reported procedure.[366] P(DPPTVT) was prepared according to previous reports from the literature.[159] Number average molecular weight (M_n), weight average molecular weight (M_w), and polydispersity index (PDI) were evaluated by high temperature size exclusion chromatography (SEC) using 1,2,4-trichlorobenzene and performed on a EcoSEC HLC-8321GPC/HT (Tosoh Bioscience) equipped with a single TSKgel GPC column (GMH_{HR}-H; 300 mm × 7.8 mm) calibrated with monodisperse polystyrene standards.

Butyl rubber (EXXON™ Butyl 068) was donated by ExxonMobil Corporation and used as received. Characterization via GPC/MALLS indicated that Butyl 068 has a number average molecular weight (M_n) of 3.37 x 10^5 g/mol and a dispersity (Đ) of 1.29. ^{1}H NMR analysis showed that the mole fraction of isoprene (IP) comonomer units in the copolymer, FIP, was equal to 0.0108.

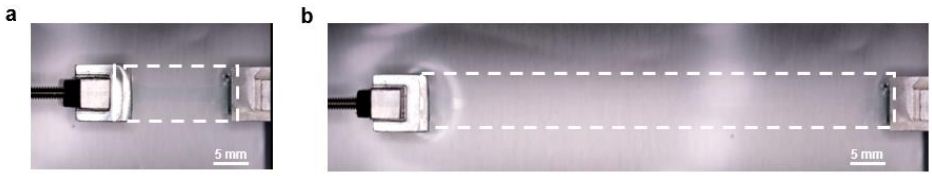

Figure F.1 *Optical images of 1:8.5 blend ratio of PDPPTVT/BR under deformation. (a) starting point (b) after being deformed to 800% strain.*

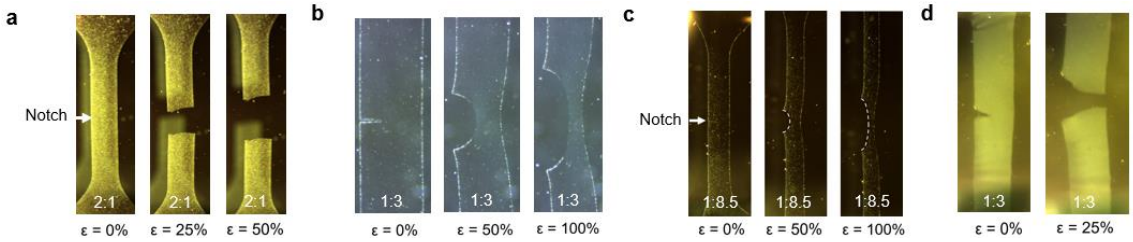

Figure F.2 *(a) 2:1 blend ratio of PDPPTVT/BR (b) 1:3 blend ratio of PDPPTVT/BR (c) 1:8.5 blend ratio of PDPPTVT/BR (d) 1:3 blend ratio of PDPPTVT/PDMS.*

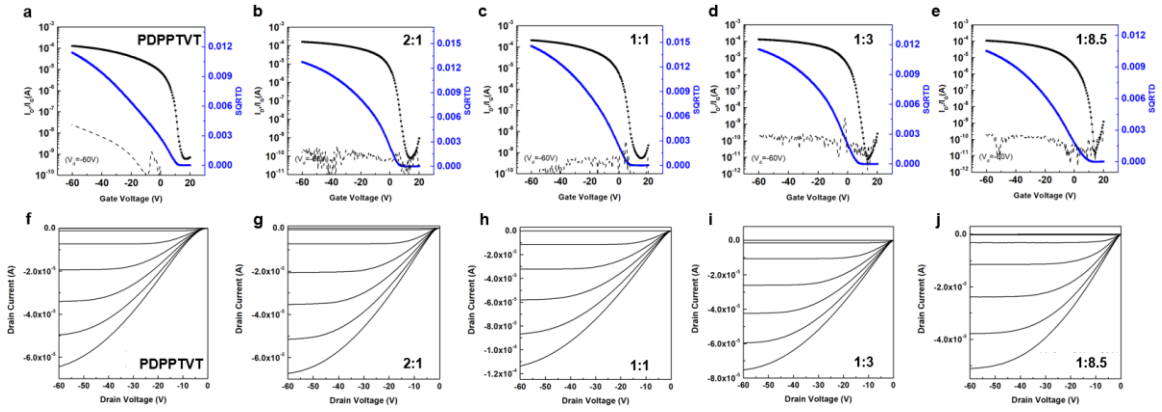

Figure F.3 *Representative transfer curves (a-e) and output curves (f-j) for different blend ratios of PDPPTVT/BR blend systems without annealing. (a, f) PDPPTVT (b, g) 2:1 ratio (c, h) 1:1 ratio (d, i) 1:3 ratio (e, j) 1:8.5 ratio.*

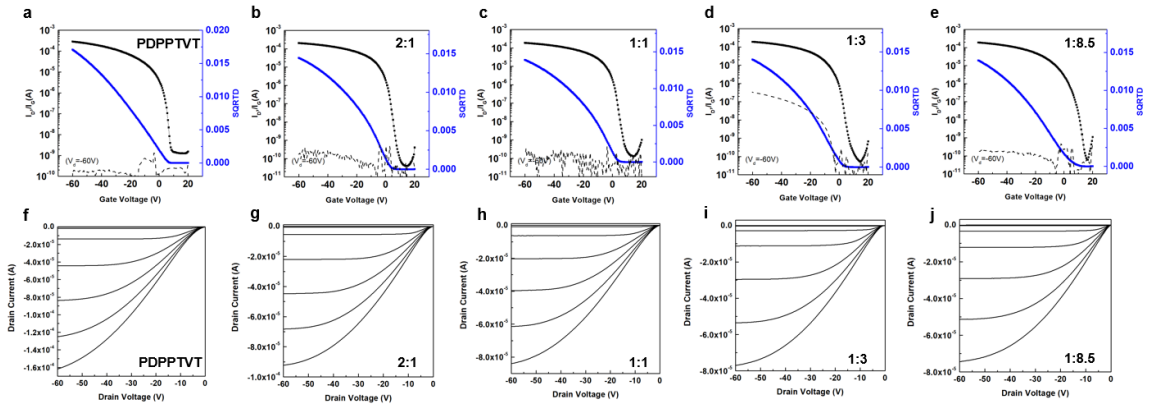

Figure F.4 *Representative transfer curves (a-e) and output curves (f-j) for different blend ratios of PDPPTVT/BR blend systems upon annealing under vacuum at 170 °C. (a, f) PDPPTVT (b, g) 2:1 ratio (c, h) 1:1 ratio (d, i) 1:3 ratio (e, j) 1:8.5 ratio.*

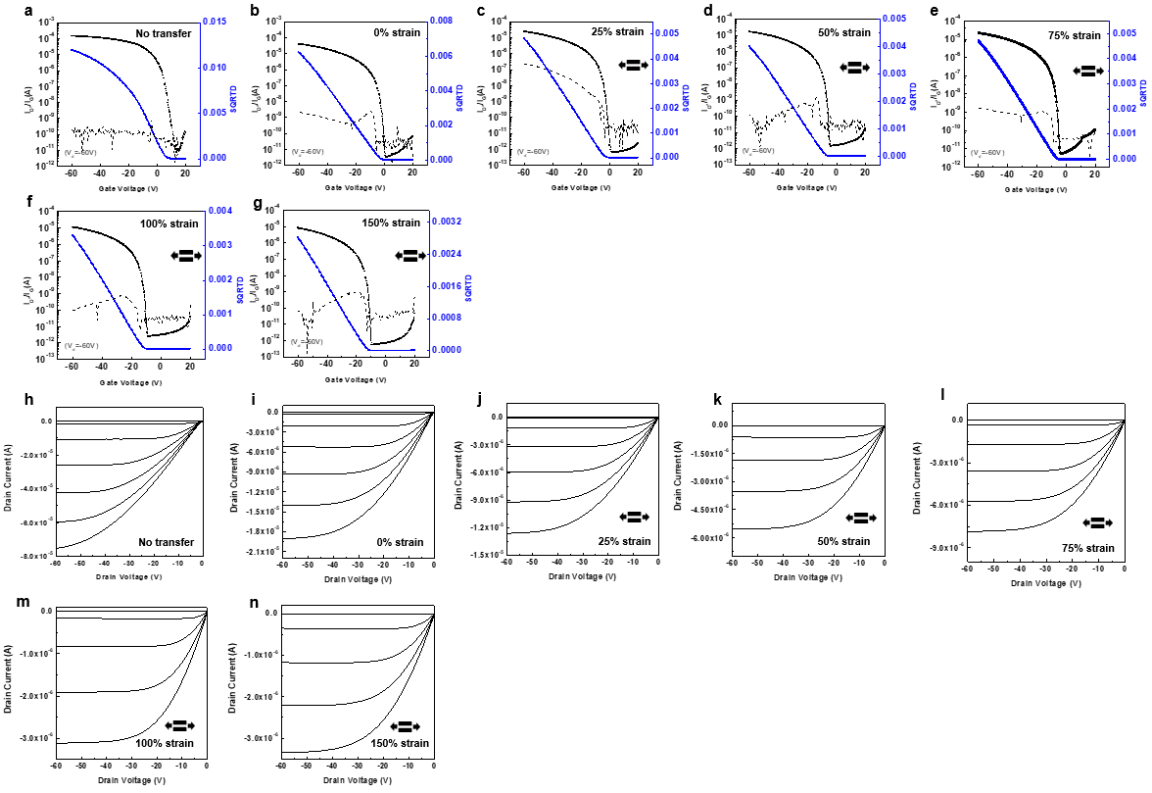

Figure F.5 *Representative transfer curves (a-g) and output curves (h-n) for 1:3 PDPPTVT/BR blend systems upon stretching in perpendicular to charge transfer direction at different degrees of strain without annealing. (a,h) no transfer (b,i) 0% strain after transfer (c,j) 25% strain after transfer (d,k) 50% strain after transfer (e,l) 75% strain after transfer (f,m) 100% strain after transfer (g,n) 150% strain after transfer.*

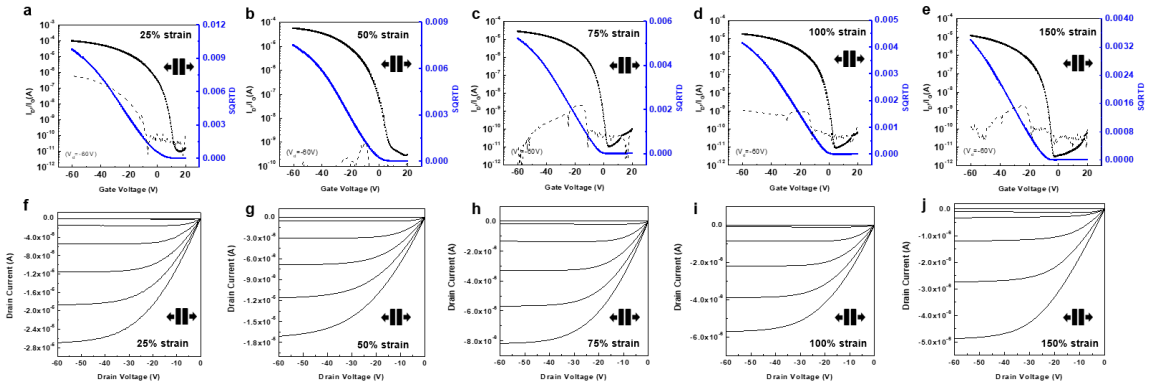

Figure F.6 *Representative transfer curves (a-e) and output curves (f-j) for 1:3 PDPPTVT/BR blend systems upon stretching in parallel to charge transfer direction at different degrees of strain without annealing. (a,f) 25% strain after transfer (b,g) 50% strain after transfer (c,h) 75% strain after transfer (d,i) 100% strain after transfer (e,j) 150% strain after transfer.*

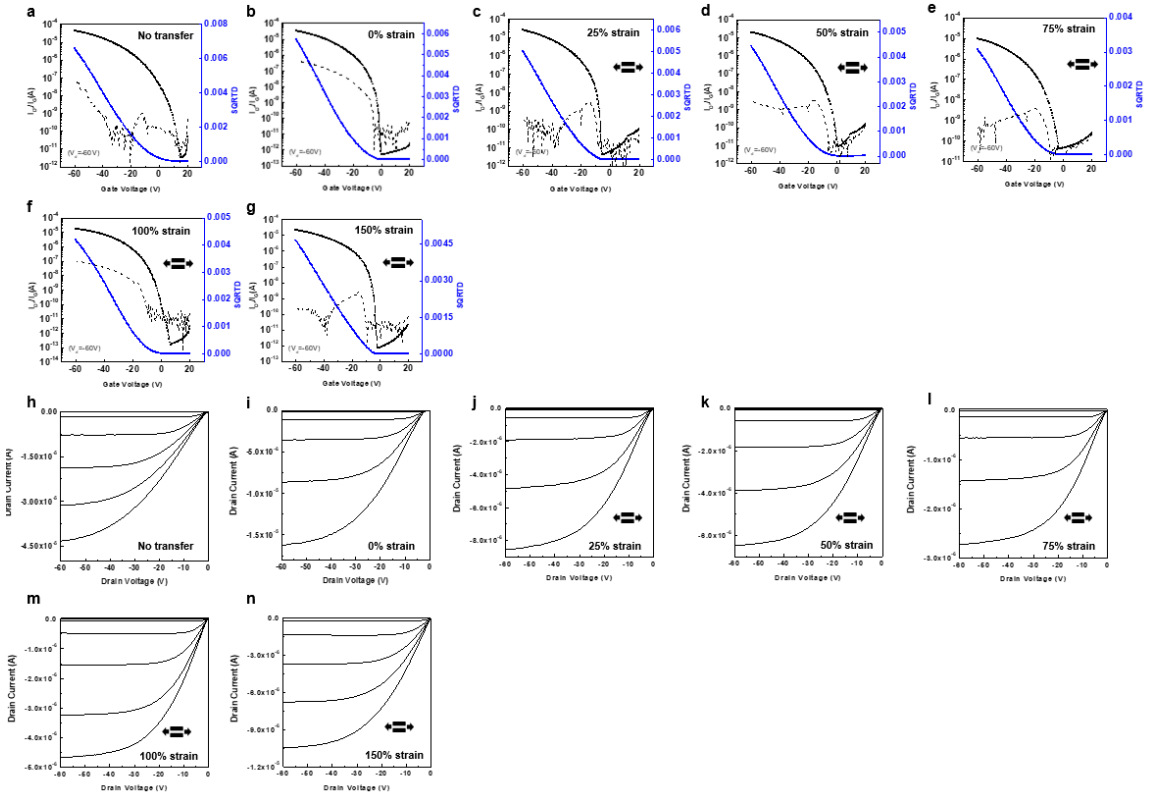

Figure F.7 *Representative transfer curves (a-g) and output curves (h-n) for 1:8.5 PDPPTVT/BR blend systems upon stretching in perpendicular to charge transfer direction at different degrees of strain without annealing. (a,h) no transfer (b,i) 0% strain after transfer (c,j) 25% strain after transfer (d,k) 50% strain after transfer (e,l) 75% strain after transfer (f,m) 100% strain after transfer (g,n) 150% strain after transfer.*

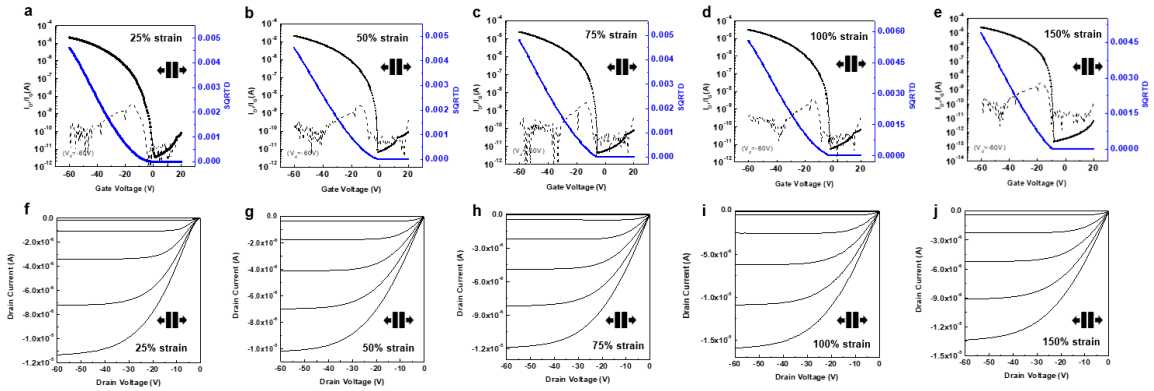

Figure F.8 *Representative transfer curves (a-e) and output curves (f-j) for 1:8.5 PDPPTVT/BR blend systems upon stretching in parallel to charge transfer direction at different degrees of strain without annealing. (a,f) 25% strain after transfer (b,g) 50% strain after transfer (c,h) 75% strain after transfer (d,i) 100% strain after transfer (e,j) 150% strain after transfer.*

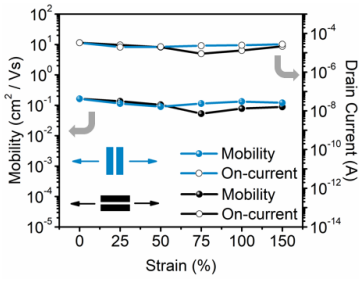

Figure F.9 *Charge carrier mobility and drain current of 1:8.5 PDPPTVT/BR blend system upon stretching in parallel and in perpendicular to charge transfer direction at different degrees of strain without annealing.*

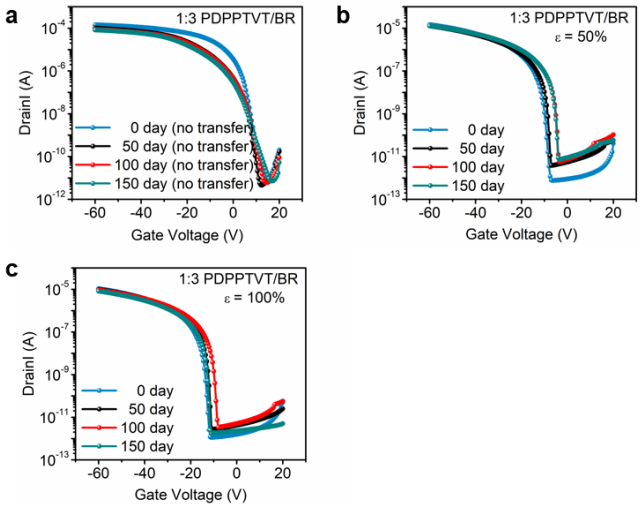

Figure F.10 *Representative transfer curves for 1:3 PDPPTVT/BR blend system at different days. (a) No strain (b) under 50% strain (c) under 100% strain.*

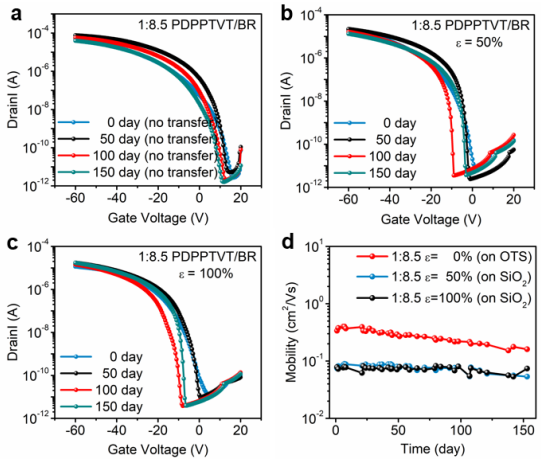

Figure F.11 *Representative transfer curves and charge mobility for 1:8.5 PDPPTVT/BR blend system at different days. (a) No strain (b) under 50% strain (c) under 100% strain (d) change of charge mobility over 150 days.*

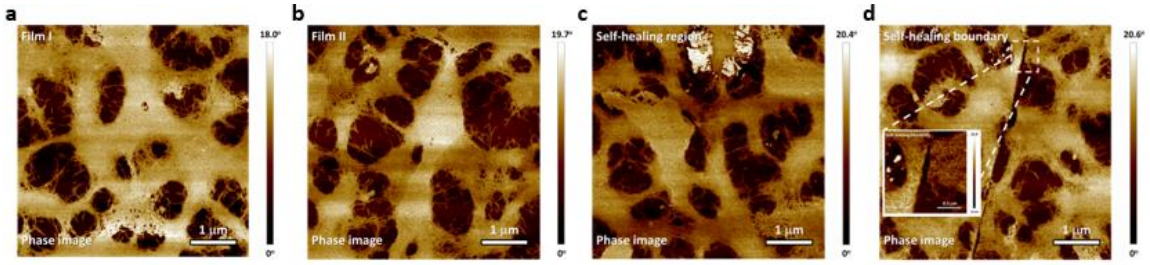

Figure F.12 *AFM phase images for 2:3 PDPPTVT/BR blend system. (a) film I (b) film II (c) within self-healing region (d) self-healing boundary.*

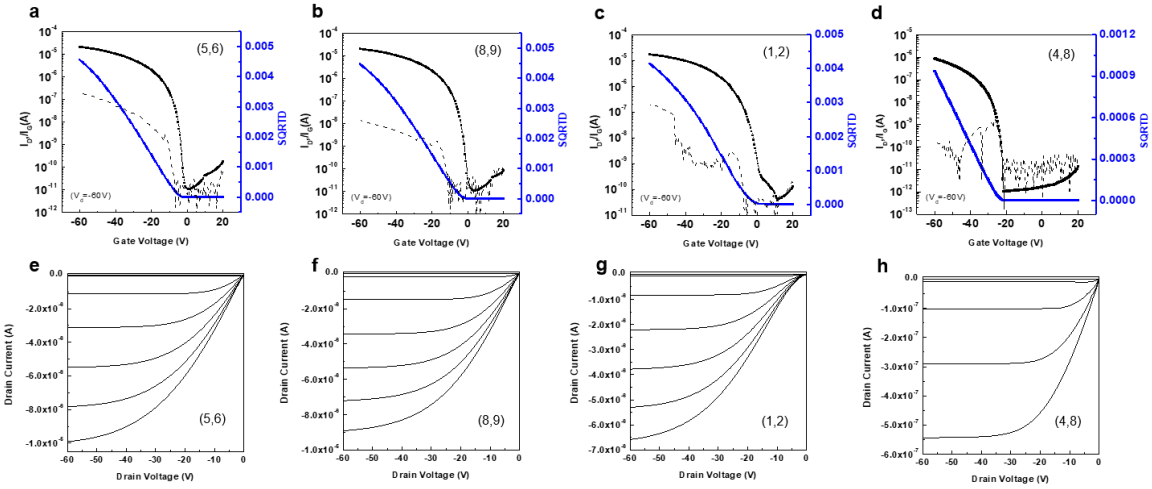

Figure F.13 *Representative transfer curves (a-d) and output curves (e-h) for 2:3 PDPPTVT/BR blend systems after self-healing. (5,6) film I (8,9) film II (1,2) self-healing region (4,8) across self-healing region.*

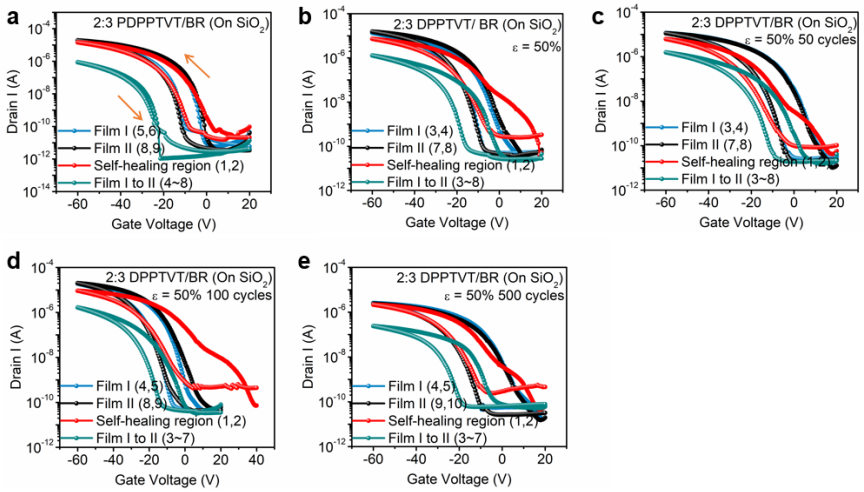

Figure F.14 *Representative transfer curves for self-healed 2:3 PDPPTVT/BR blend system at different degrees of strain for various cycles. (a) No strain (b) under 50% strain (c) under 50% strain for 50 cycles (d) under 50% strain for 100 cycles (e) under 50% strain for 500 cycles.*

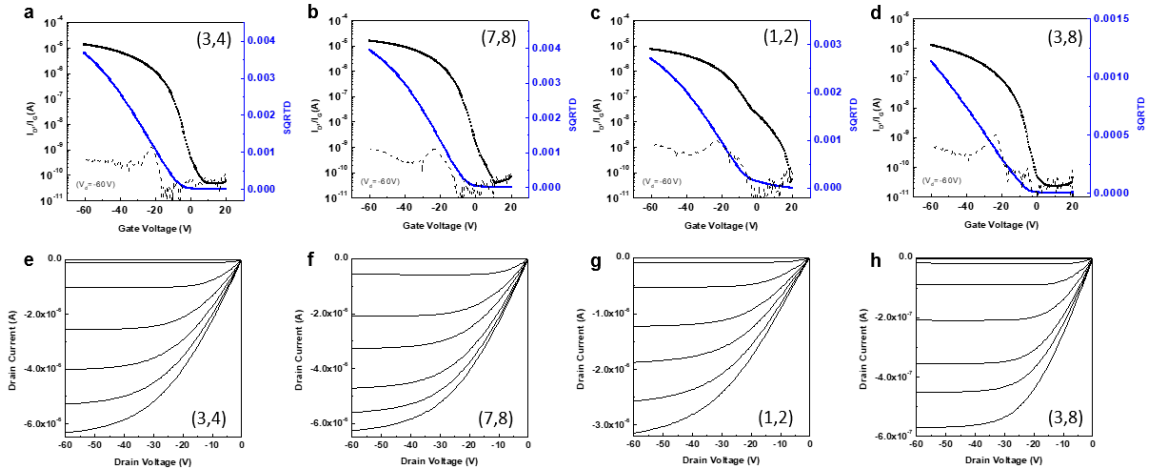

Figure F.15 *Representative transfer curves (a-d) and output curves (e-h) for self-healed 2:3 PDPPTVT/BR blend films upon 50% strain. (3,4) film I (7,8) film II (1,2) self-healing region (3,8) across self-healing region.*

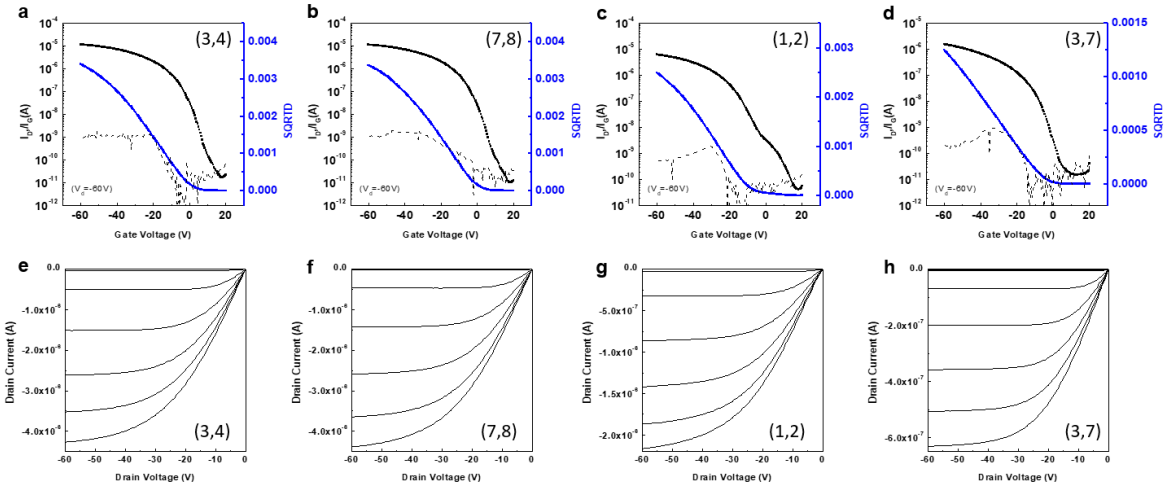

Figure F.16 *Representative transfer curves (a-d) and output curves (e-h) for self-healed 2:3 PDPPTVT/BR blend films upon 50% strain for 50 cycles. (3,4) film I (7,8) film II (1,2) self-healing region (3,7) across self-healing region.*

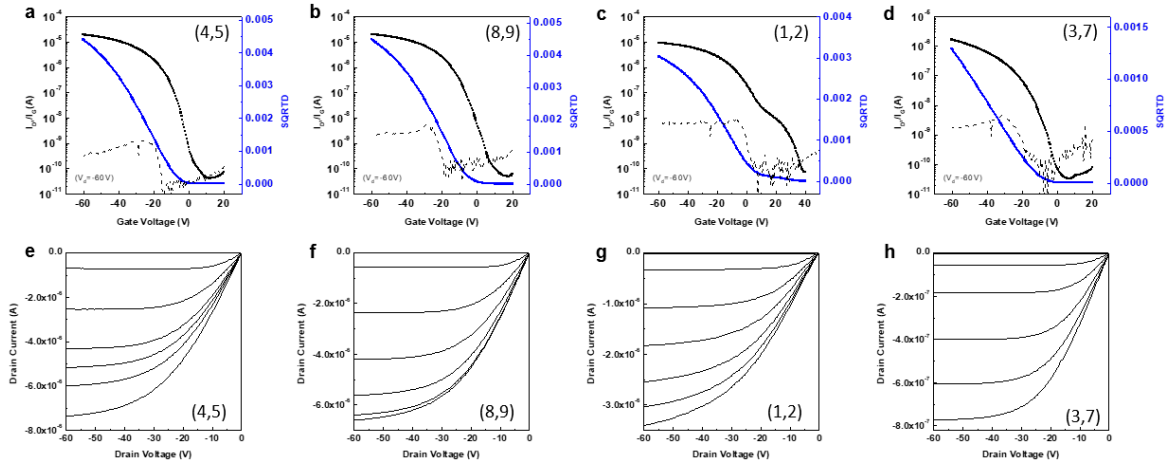

Figure F.17 *Representative transfer curves (a-d) and output curves (e-h) for self-healed 2:3 PDPPTVT/BR blend films upon 50% strain for 100 cycles. (4,5) film I (8,9) film II (1,2) self-healing region (3,7) across self-healing region.*

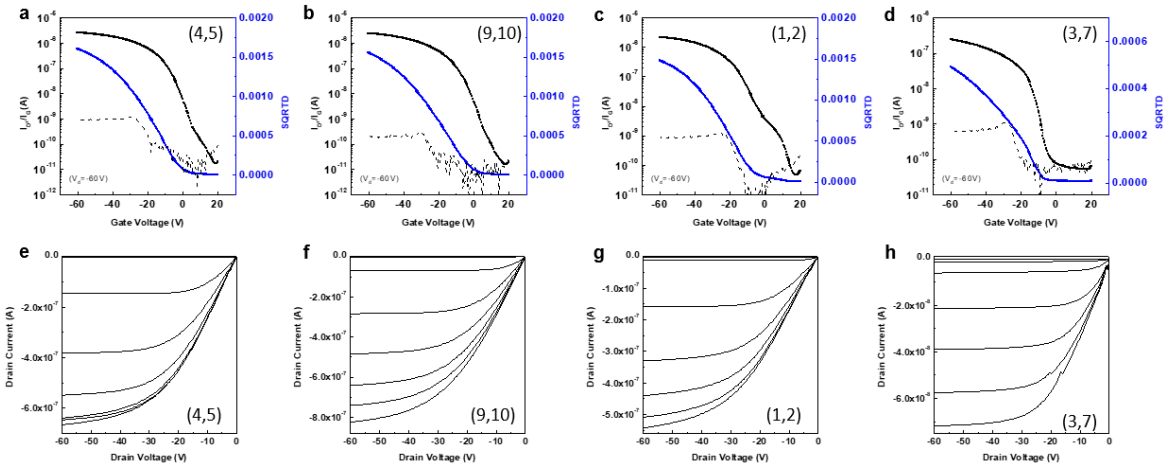

Figure F.18 *Representative transfer curves (a-d) and output curves (e-h) for self-healed 2:3 PDPPTVT/BR blend film upon 50% strain for 500 cycles. (4,5) film I (9,10) film II (1,2) self-healing region (3,7) across self-healing region.*

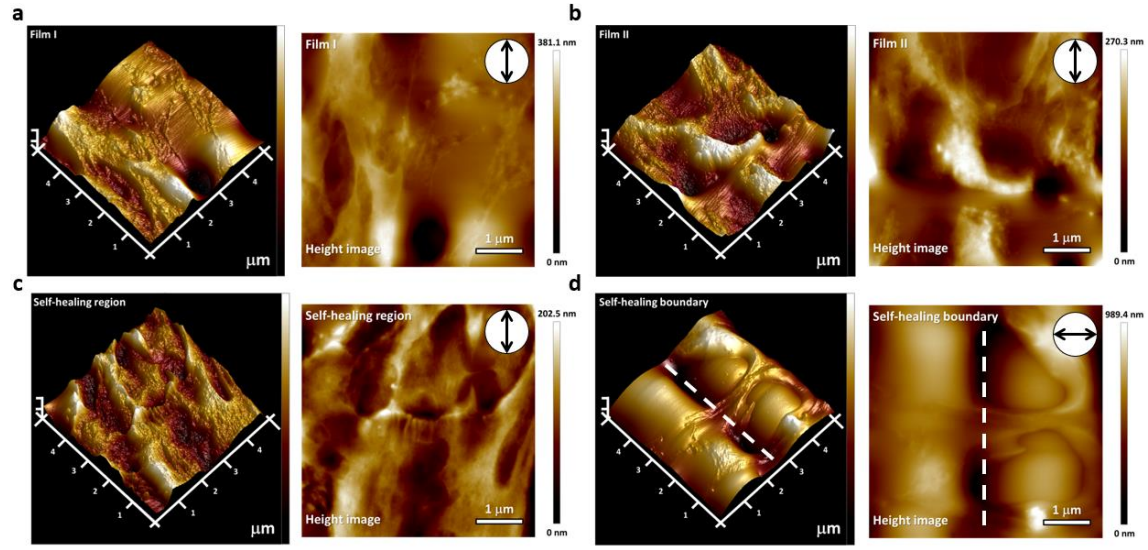

Figure F.19 *AFM 3D images and height images for 2:3 DPPTVT/BR blend systems under 50% strain. (a) film I (b) film II (c) within self-healing region (d) self-healing boundary. The cursor represents for the strain direction. The dotted line represents for the contact position.*

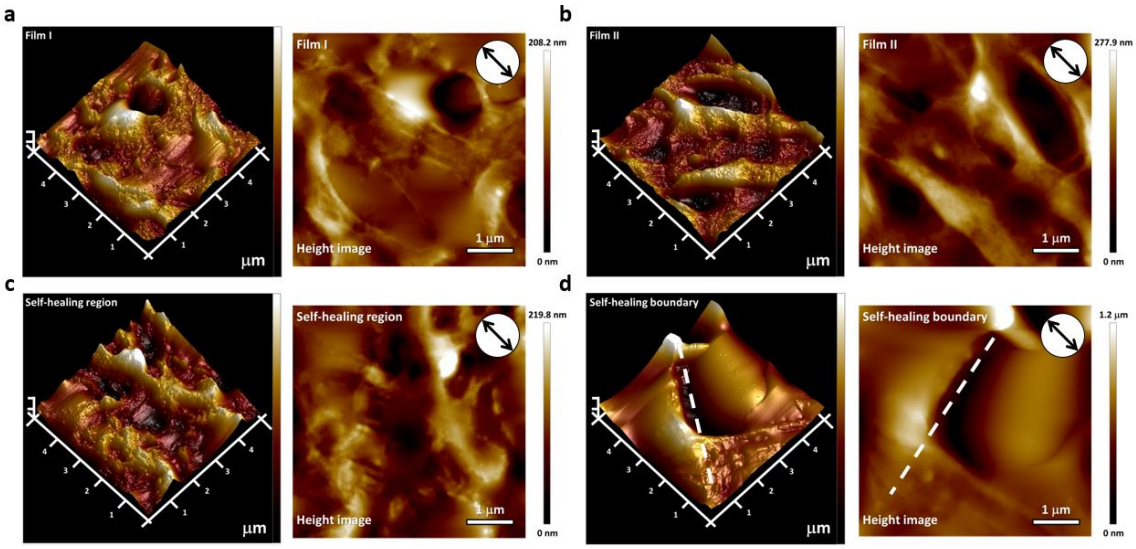

Figure F.20 *AFM 3D images and height images for 2:3 DPPTVT/BR blend systems under 50% strain after 50 cycles. (a) film I (b) film II (c) within self-healing region (d) self-healing boundary.*

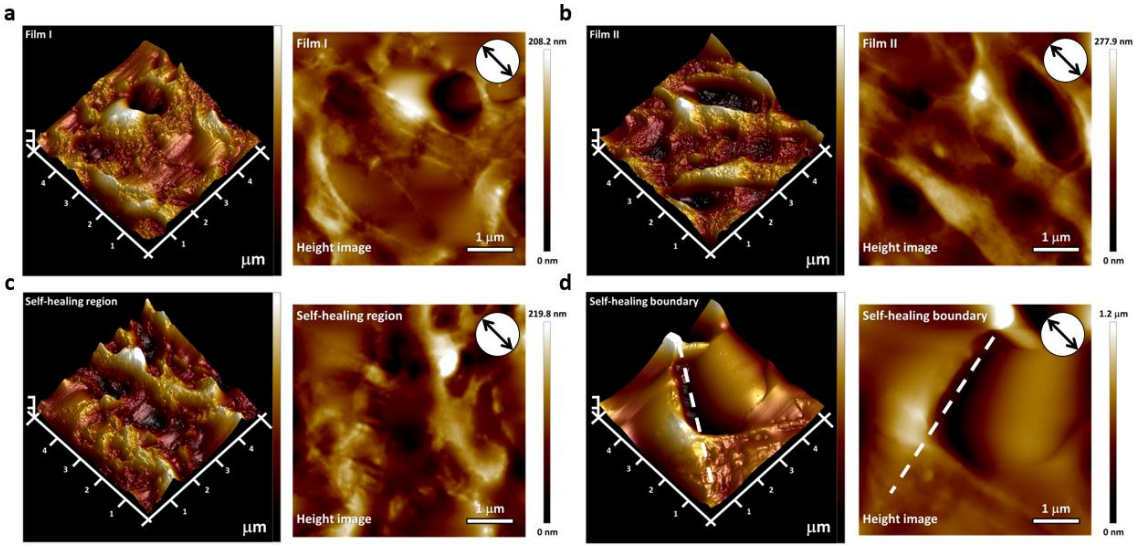

Figure F.21 *AFM 3D images and height images for 2:3 DPPTVT/BR blend systems under 50% strain after 50 cycles. (a) film I (b) film II (c) within self-healing region (d) self-healing boundary.*

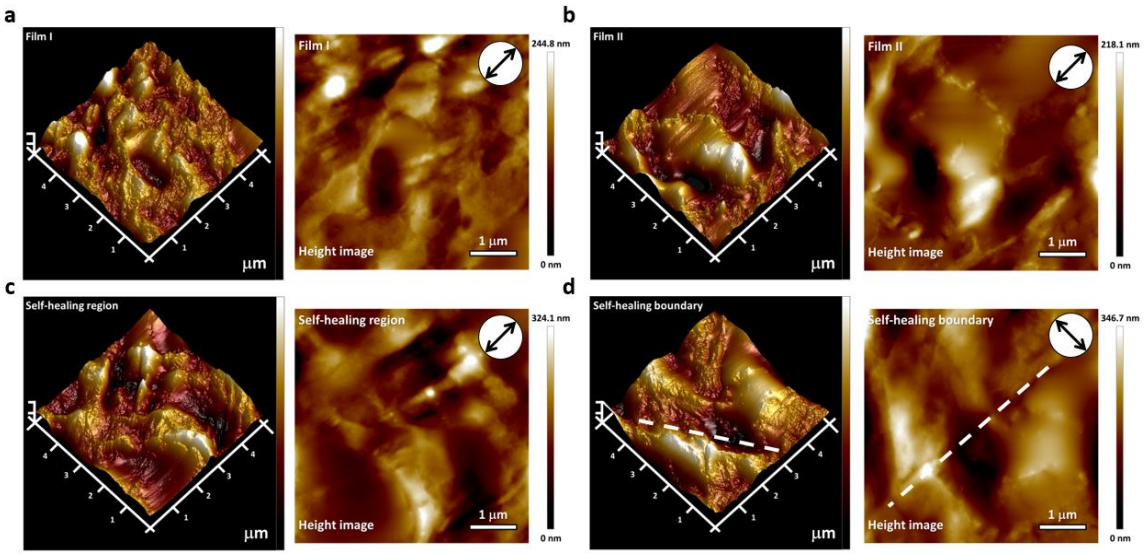

Figure F.22 *AFM 3D images and height images for 2:3 DPPTVT /BR blend systems under 50% strain after 100 cycles. (a) film I (b) film II (c) within self-healing region (d) self-healing boundary.*

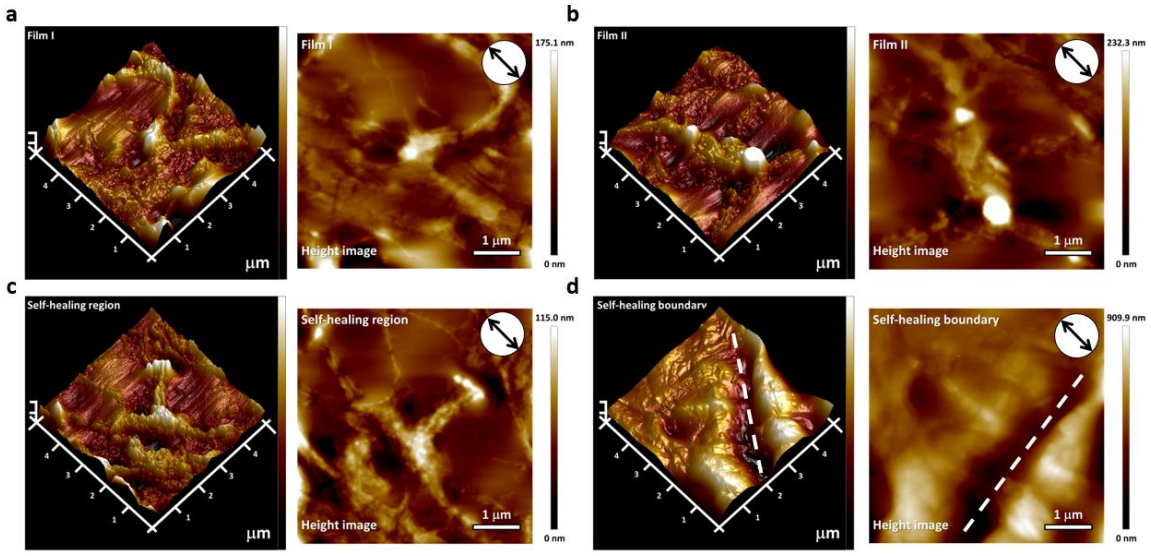

Figure F.23 *AFM 3D images and height images for 2:3 P3HT/BR blend system under 50% strain after 500 cycles. (a) film I (b) film II (c) within self-healing region (d) self-healing boundary.*

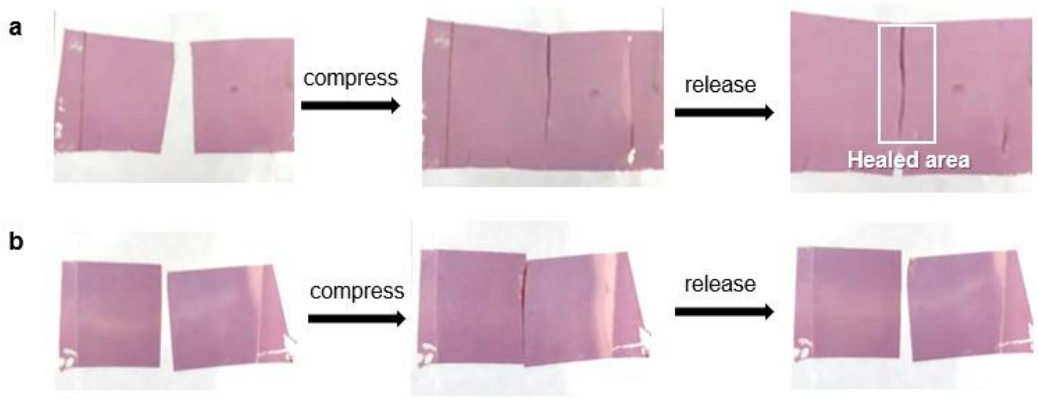

Figure F.24 *Optical images of film compression and release. (a) 2:3 P3HT/BR (b) neat P3HT.*

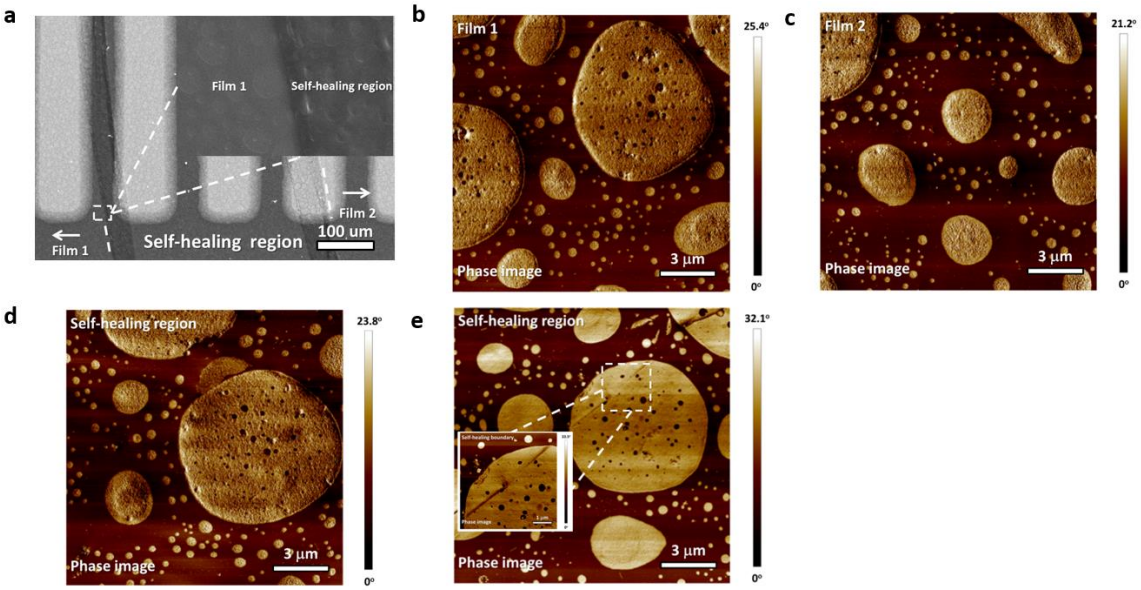

Figure F.25 *SEM and AFM phase image for 2:3 P3HT/BR blend systems. (a) SEM image showing three regions of self-healed device. AFM phase images of (b) film I (c) film II (d) within self-healing region (e) self-healing boundary.*

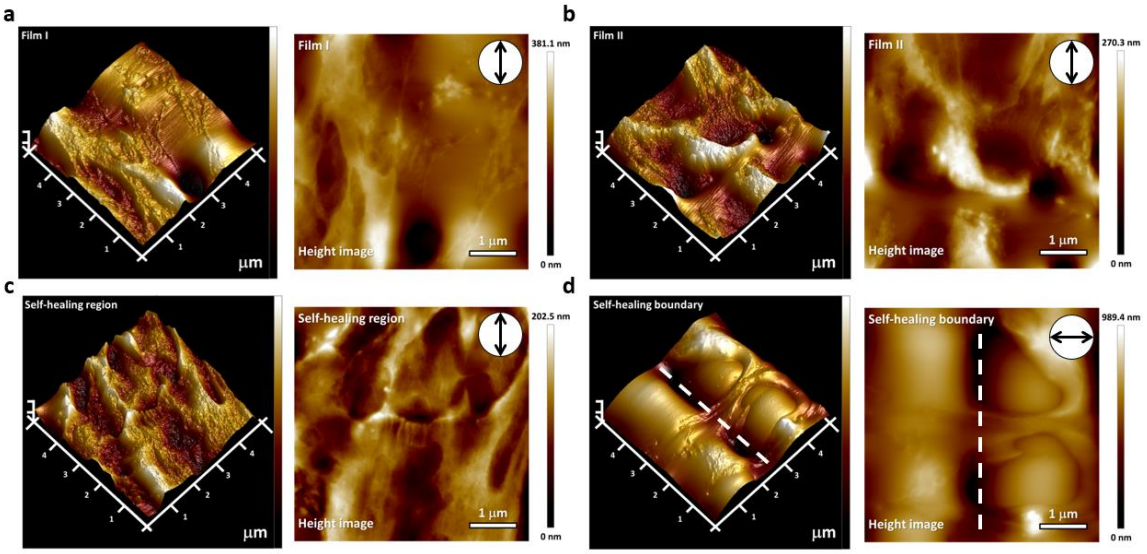

Figure F.26 *AFM 3D images and height images for 2:3 P3HT/BR blend systems under 50% strain. (a) film I (b) film II (c) within self-healing region (d) self-healing boundary.*

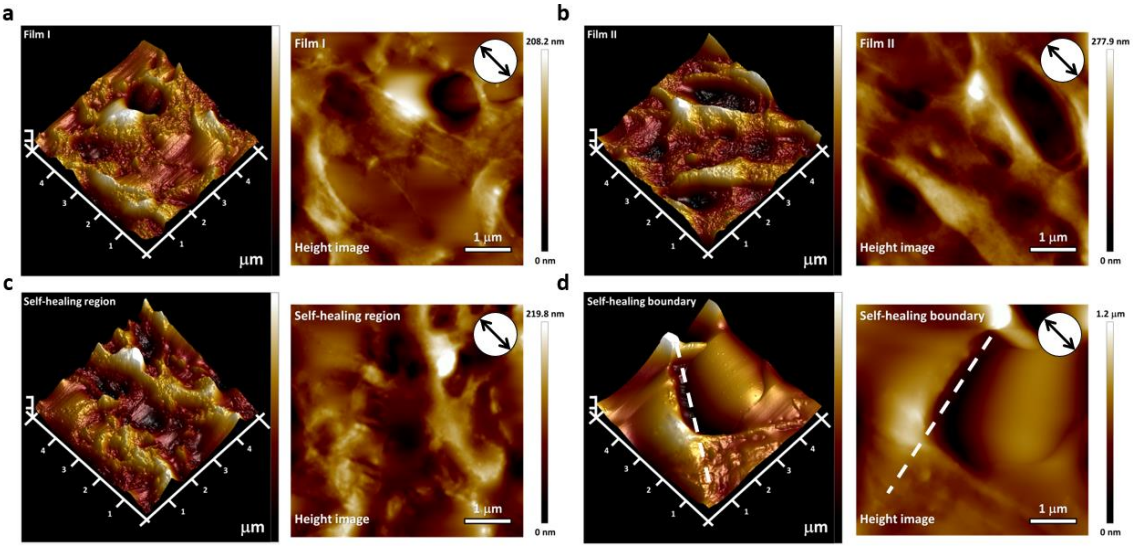

Figure F.27 *AFM 3D images and height images for 2:3 P3HT/BR blend system under 50% strain after 50 cycles. (a) film I (b) film II (c) within self-healing region (d) self-healing boundary.*

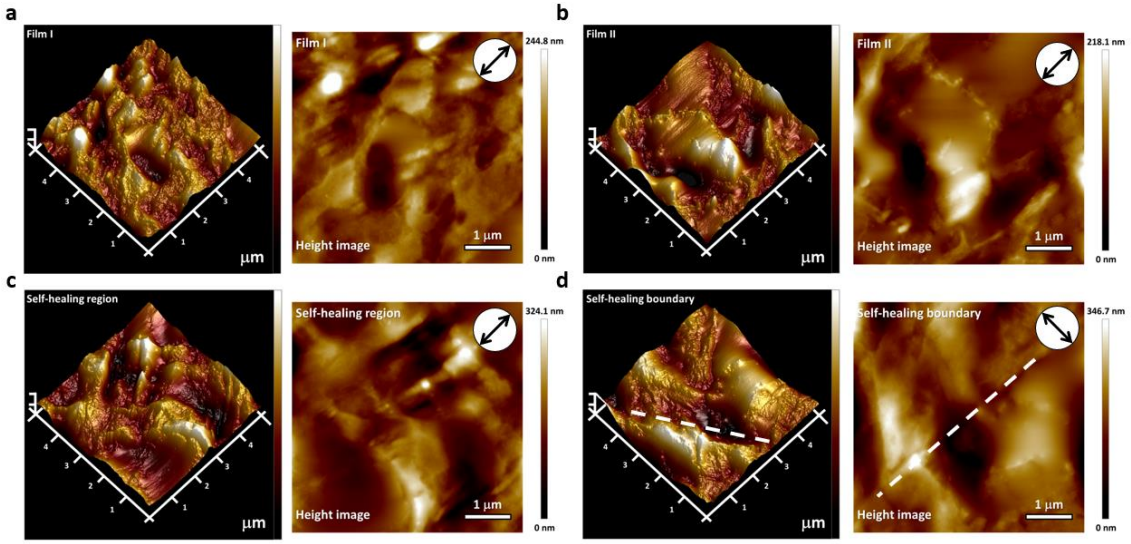

Figure F.28 *AFM 3D and height images for 2:3 P3HT/BR blend system under 50% strain after 100 cycles. (a) film I (b) film II (c) within self-healing region (d) self-healing boundary.*

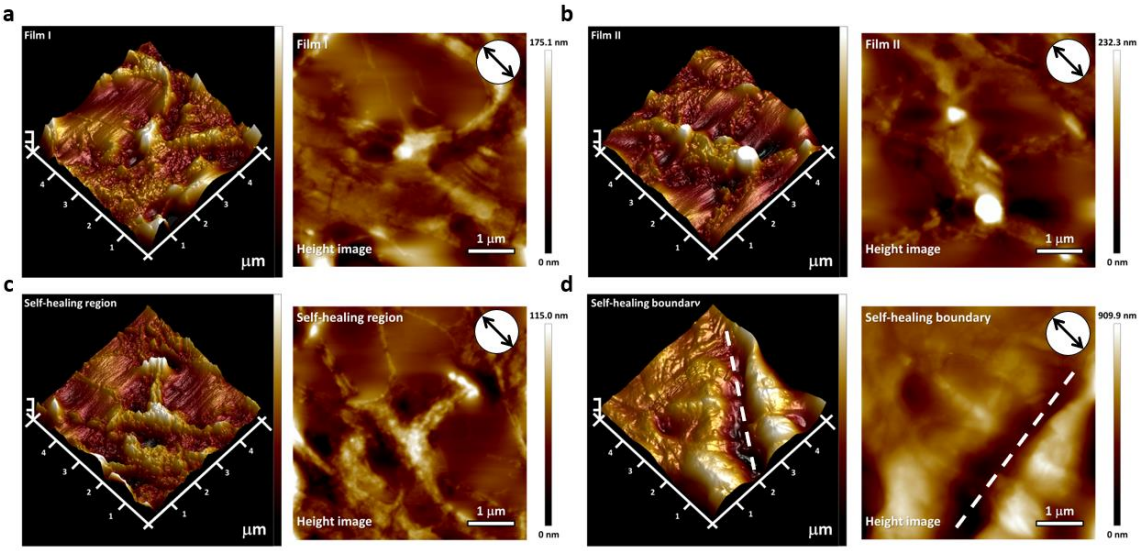

Figure F.29 *AFM 3D and height images for 2:3 P3HT/BR blend system under 50% strain for 500 cycles. (a) film I (b) film II (c) within self-healing region (d) self-healing boundary.*

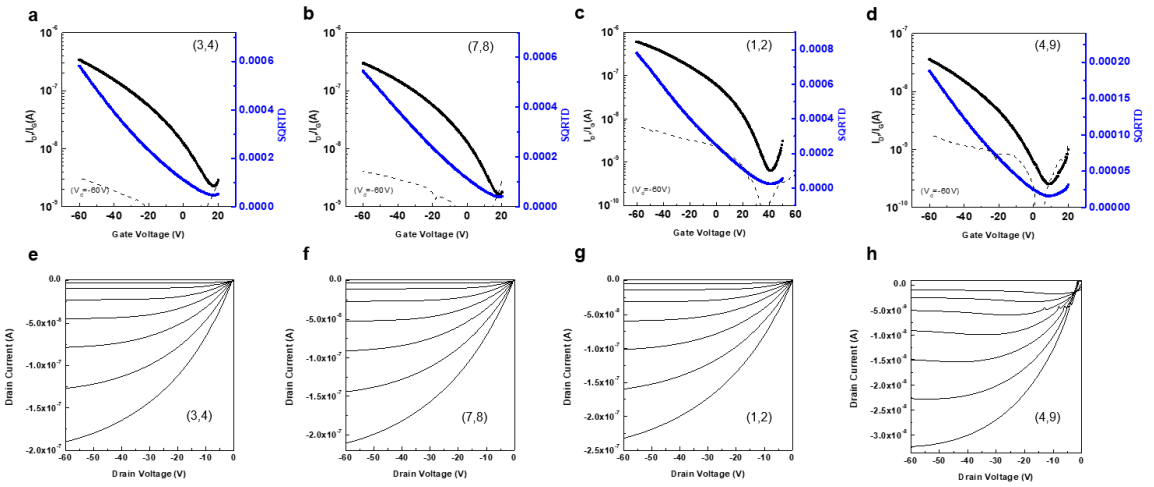

Figure F.30 *Representative transfer curves (a-d) and output curves (e-h) for 2:3 P3HT/BR blend systems after self-healing. (3,4) film I (7,8) film II (1,2) self-healing region (4,9) across self-healing region.*

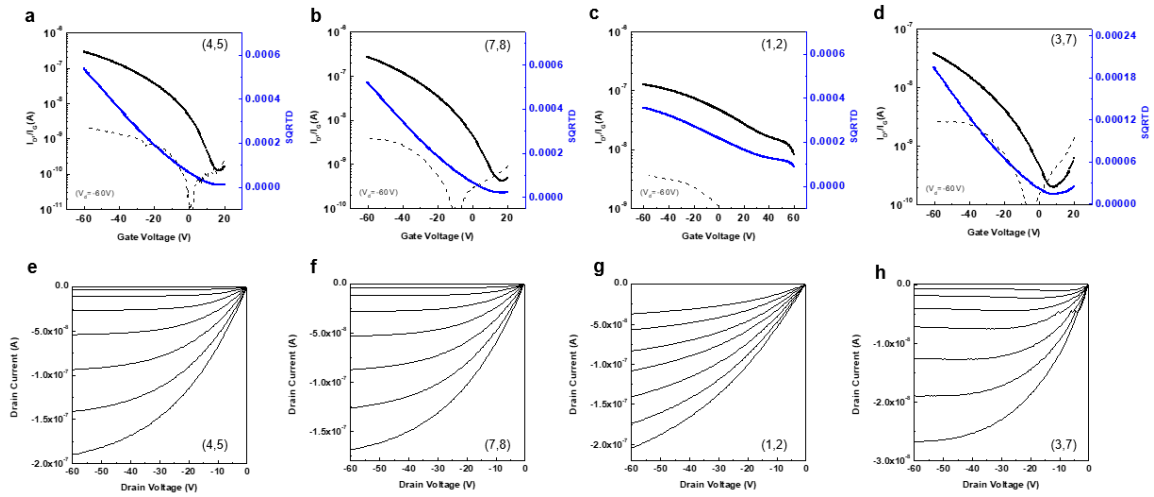

Figure F.31 *Representative transfer curves (a-d) and output curves (e-h) for 2:3 P3HT/BR blend systems being strained at 50% after self-healing. (4,5) film I (7,8) film II (1,2) self-healing region (3,7) across self-healing region.*

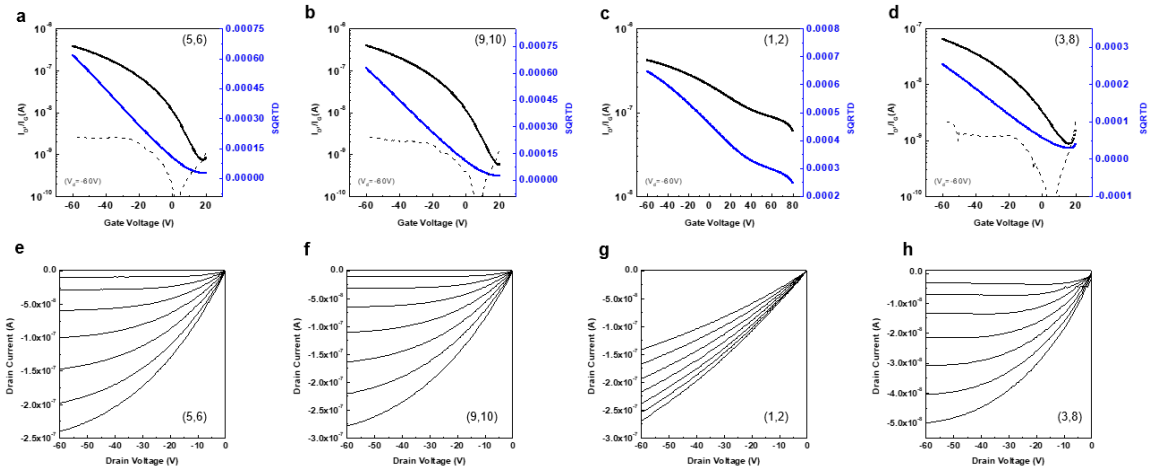

Figure F.32 *Representative transfer curves (a-d) and output curves (e-h) for 2:3 P3HT/BR blend systems being strained at 50% for 50 cycles after self-healing. (5,6) film I (9,10) film II (1,2) self-healing region (3,8) across self-healing region.*

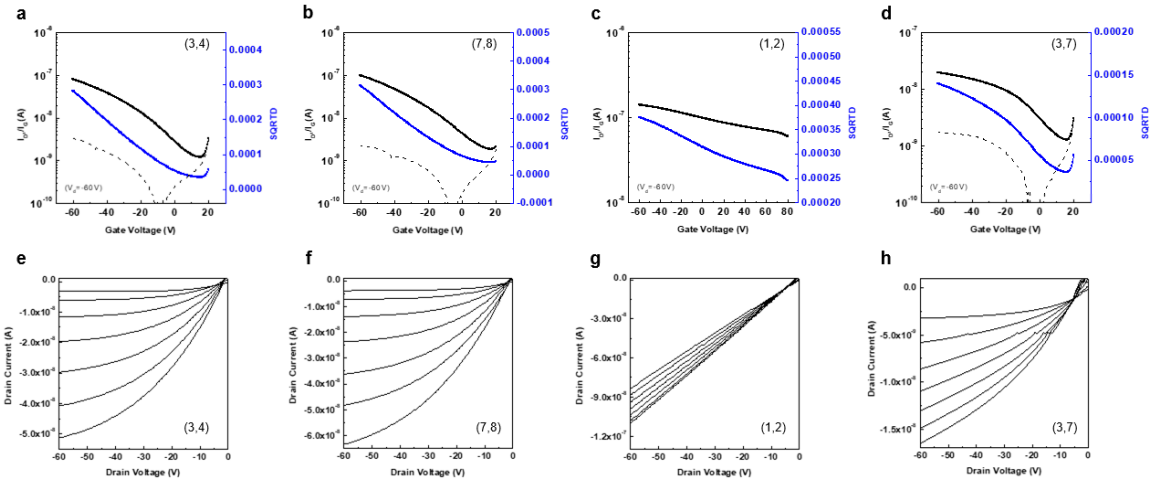

Figure F.33 *Representative transfer curves (a-d) and output curves (e-h) for 2:3 P3HT/BR blend systems being strained at 50% for 100 cycles after self-healing. (3,4) film I (7,8) film II (1,2) self-healing region (3,7) across self-healing region.*

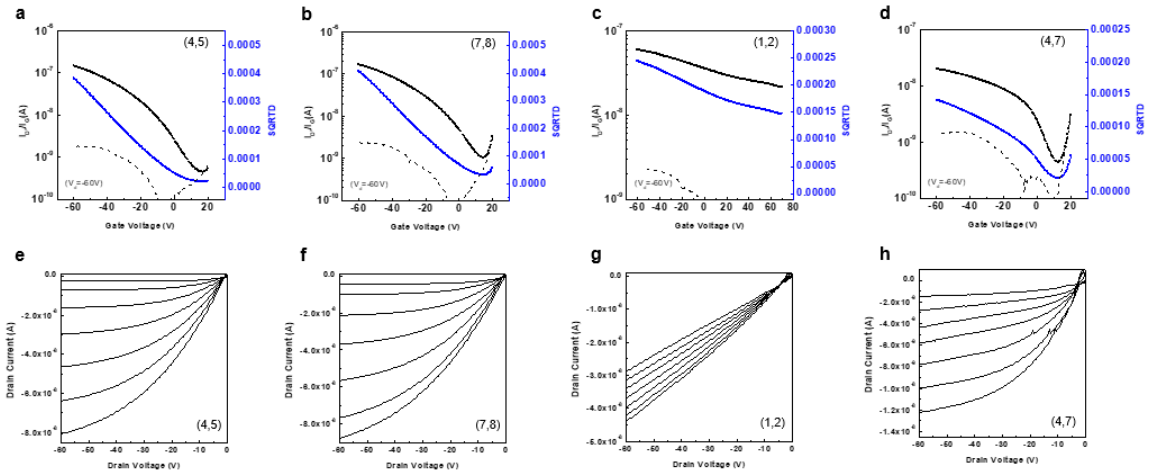

Figure F.34 *Representative transfer curves (a-d) and output curves (e-h) for 2:3 P3HT/BR blend systems being strained at 50% for 500 cycles after self-healing. (4,5) film I (7,8) film II (1,2) self-healing region (4,7) across self-healing region.*

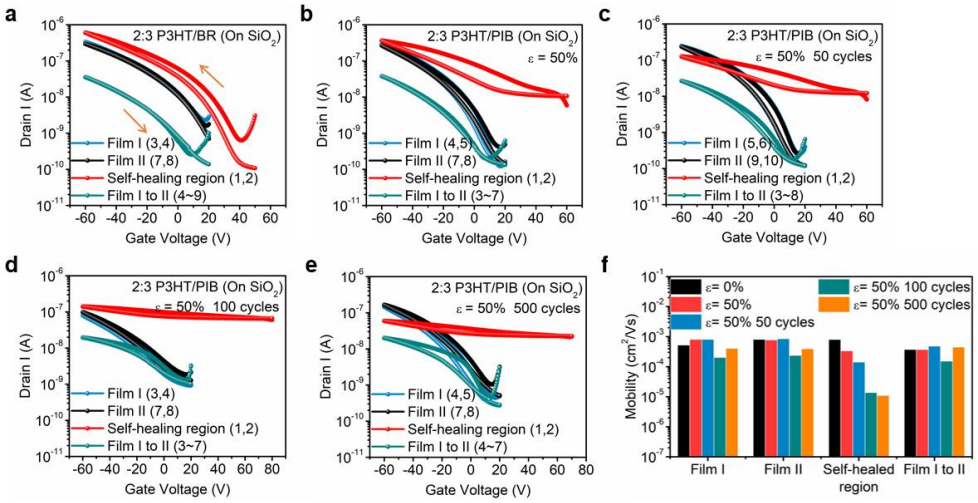

Figure F.35 *Representative transfer curves for self-healed 2:3 P3HT/BR blend systems at different degrees of strain. (a) No strain (b) under 50% strain (c) under 50% strain for 50 cycles (d) under 50% strain for 100 cycles (e) under 50% strain for 500 cycles (f) Summary of charge carrier mobility for self-healed 2:3 P3HT/BR composite film measured at different electrodes before and after strain for various cycles.*

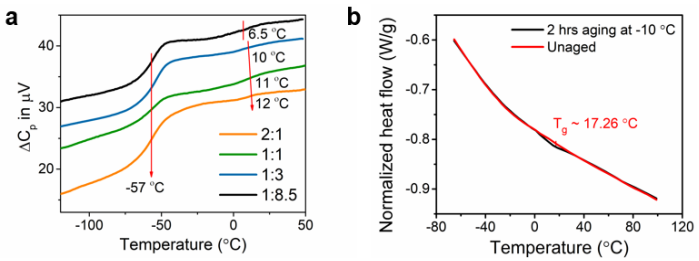

Figure F.36 *Glass transition temperature of different blend ratios of PDPPTVT/BR thin films and PDPPTVT homopolymer detected by AC-chip calorimetry and differential scanning calorimetry (DSC), respectively. (a) cooling curves for four blend ratios of PDPPTVT/BR 50 nm thin films. BR shows a T_g at -57 ℃, and PDPPTVT shows a T_g at around 10 ℃. (b) cooling curve for pure PDPPTVT showing a T_g at around 17.3 ℃.*

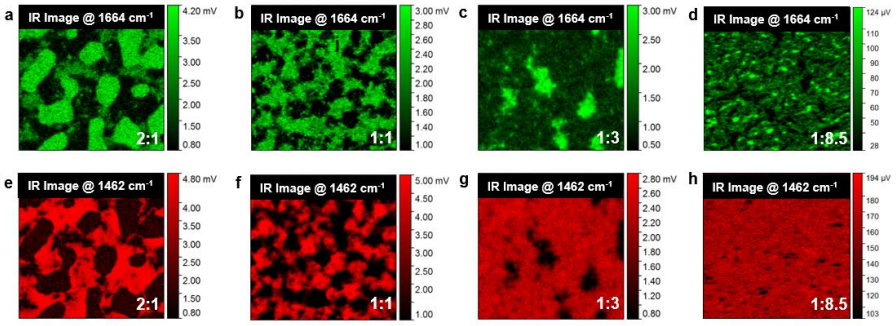

Figure F.37 *AFM-IR images at 1664 cm^{-1} (a-d) and 1462 cm^{-1} (e-h) for different blend ratios of PDPPTVT/BR composite film. Green color represents for PDPPTVT, and red represents for BR.*

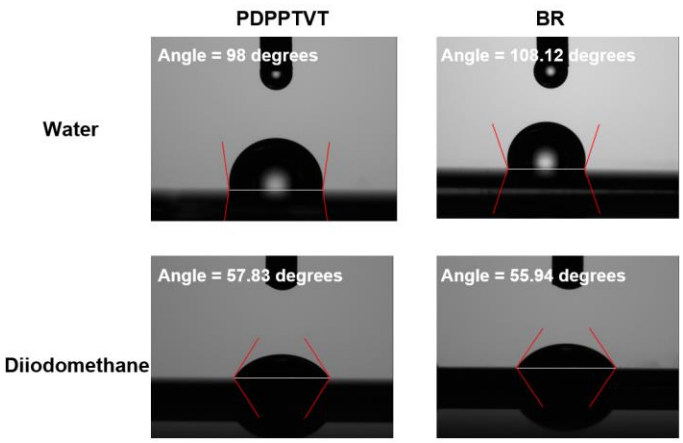

Figure F.38 *Optical images of contact angle test for PDPPTVT and BR.*

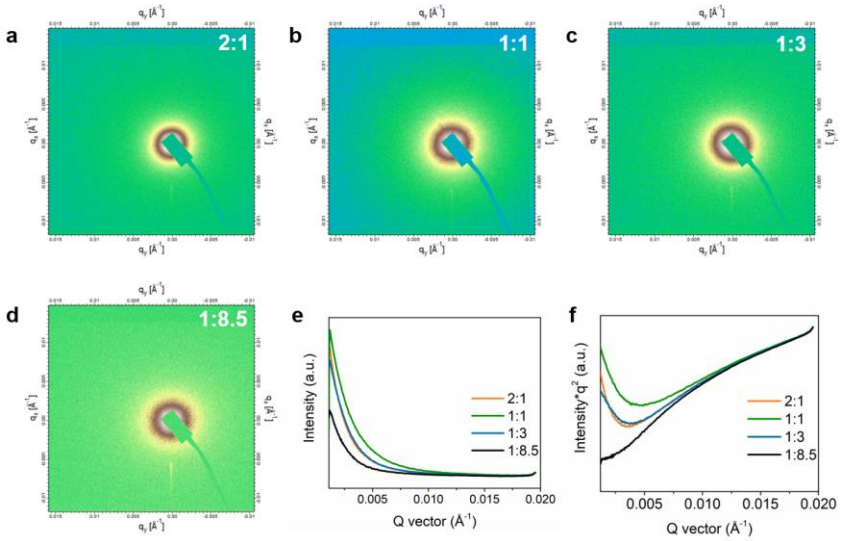

Figure F.39 *RSoXS 2D images (a to d) and 1D profiles of different blend ratios of PDPPTVT/BR (e and f). (a) 2:1 ratio (b) 1:1 ratio (c) 1:3 ratio (d) 1:8.5 ratio. The reduced 1D profile was represented as (e) Intensity versus q vector plots (f) I*q^2 versus q plots. The increasing peak intensity below 0.005 Å^{-1} corresponds to a potential peak at ultra low q region, or a large phase separation size scale between the aggregates of PDPPTVT. The broad peak between 0.005 Å^{-1} and 0.015 Å^{-1} represents for a smaller phase separation size, corresponding to the fiber-fiber distance.*

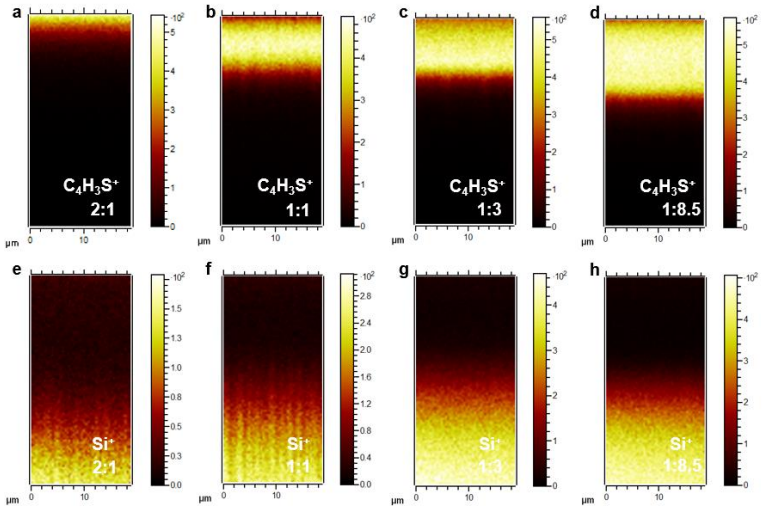

Figure F.40 *TOF-SIMS chemical depth profiling (19 µm lateral field of view × 200 erosion frames) of samples with different blend ratios of PDPPTVT/BR composite films. (a-d) Composition map of m/z 83 (tentatively assigned to $C_4H_3S^+$, which is specific for PDPPTVT). (e-h) Composition map of m/z 28 (assigned to Si^+ from Si wafer substrate).*

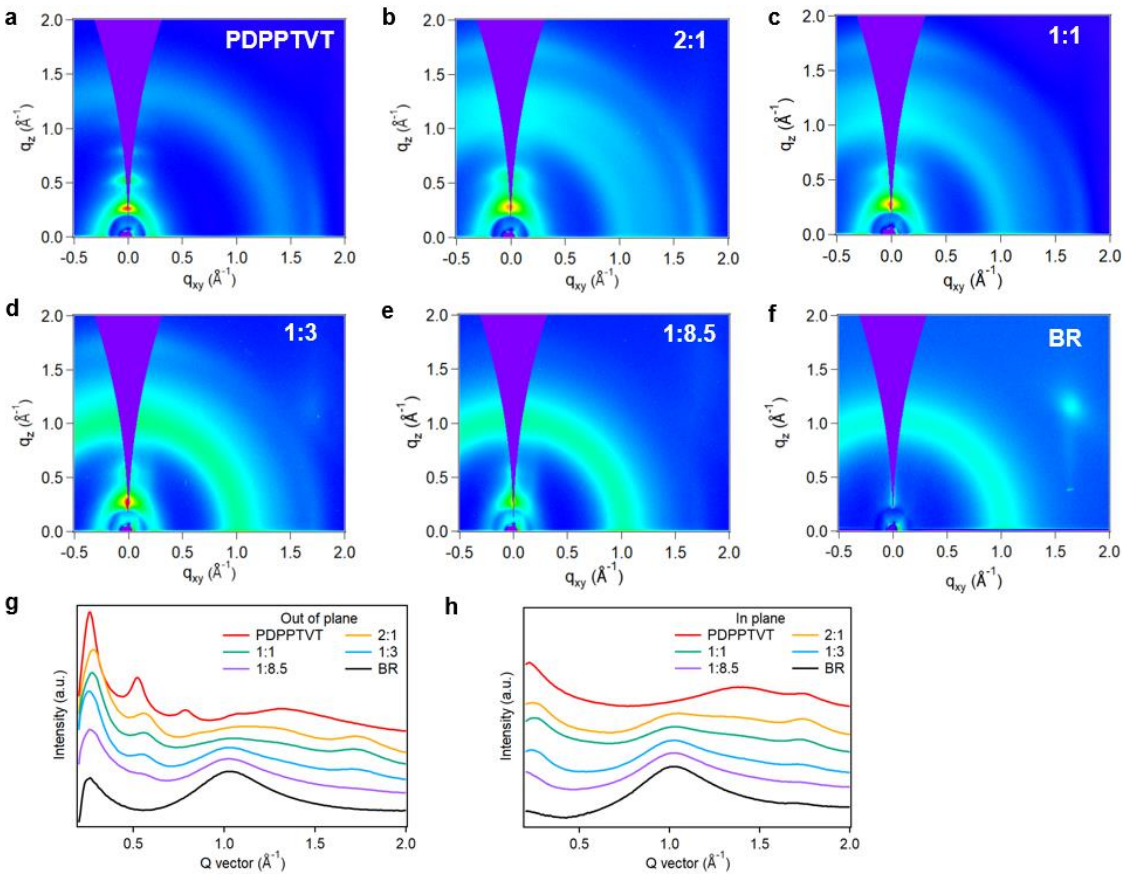

Figure F.41 *2D and 1D GIWAXS profiles for different blend ratios of PDPPTVT-BR systems. 2D scattering patterns for (a) pristine PDPPTVT. (b) 2:1 PDPPTVT-BR. (c) 1:1 PDPPTVT-BR. (d) 1:3 PDPPTVT-BR. (e) 1:8.5 PDPPTVT-BR. (f) pristine BR. 1D reduction along (g) out of plane direction (h) in plane direction.*

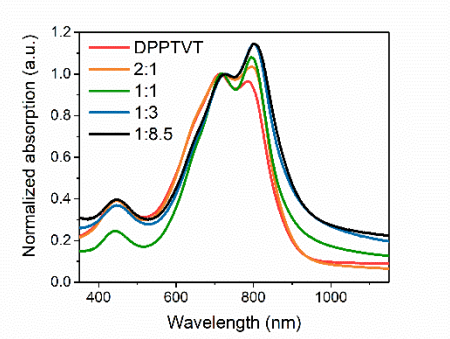

Figure F.42 *UV-vis spectra for different blend ratios of PDPPTVT/BR thin films.*

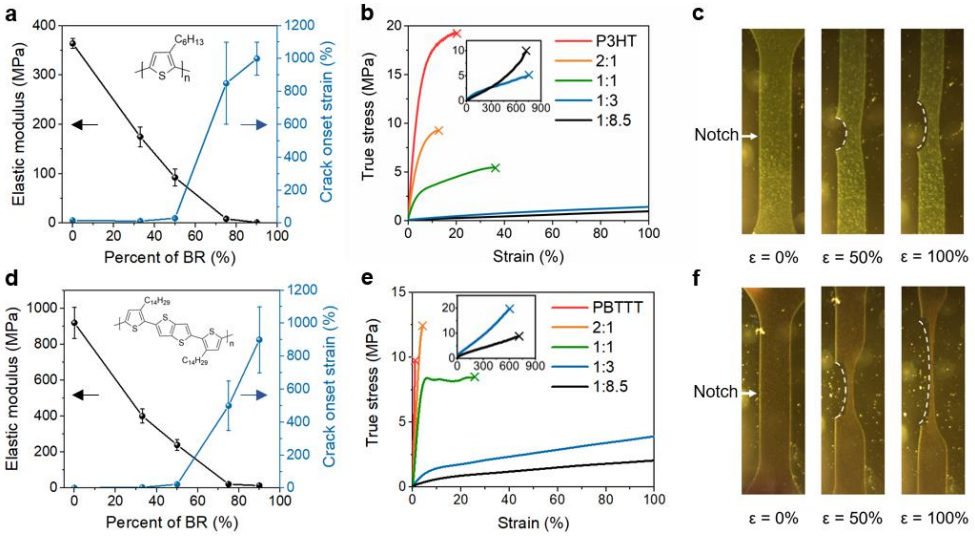

Figure F.43 *Mechanical performance of (a-c) P3HT/BR and (d-f) PBTTT/BR films. Elastic modulus and crack onset strain of the composite film at different percent of BR for (a) P3HT/BR and (d) PBTTT/BR films. Representative stress strain curves for different blend ratios of (b) P3HT/BR and (e) PBTTT/BR films. The inset represents for 1:3 and 1:9 ratio composite film. Notch test of 1:3 ratio of (c) P3HT/BR and (f) PBTTT/BR.*

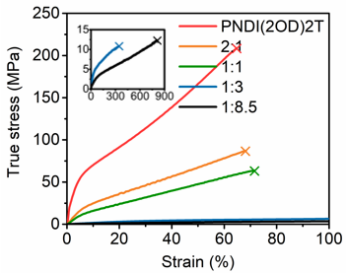

Figure F.44 *Representative stress strain curves for different blend ratios of PNDI(2OD)2T/BR. The inset represents for 1:3 and 1:9 ratio blend film.*

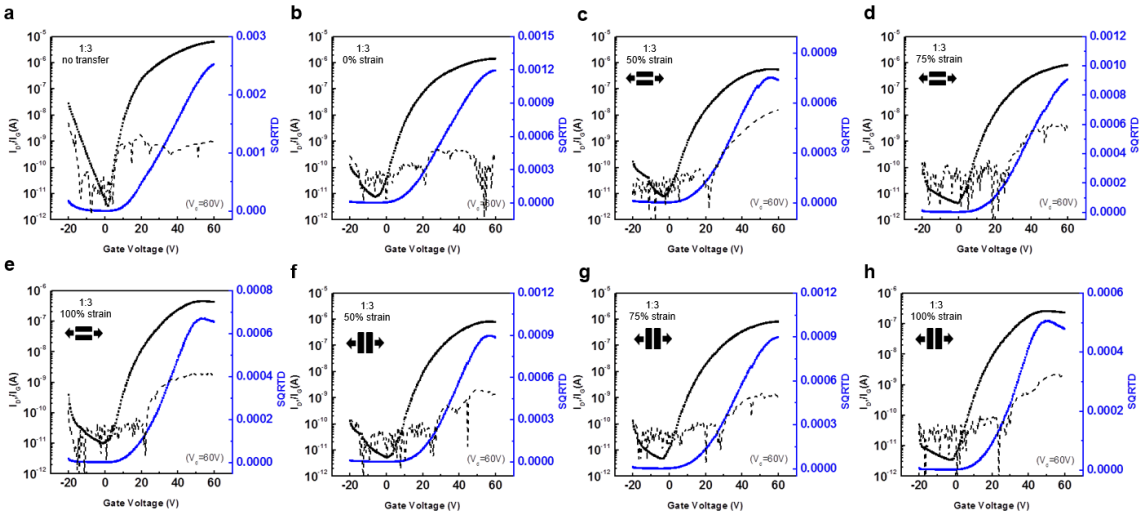

Figure F.45 *Representative transfer curves for 1:3 PNDI(2OD)2T/BR blend systems upon stretching at different degrees of strain without annealing. (a) no transfer (b) 0% strain after transfer (c) 50% strain in parallel to charge transport after transfer (d) 75% strain in parallel to charge transport after transfer (e) 100% strain in parallel to charge transport after transfer (f) 50% strain in perpendicular to charge transport after transfer (g) 75% strain in perpendicular to charge transport after transfer (h) 100% strain in perpendicular to charge transport after transfer.*

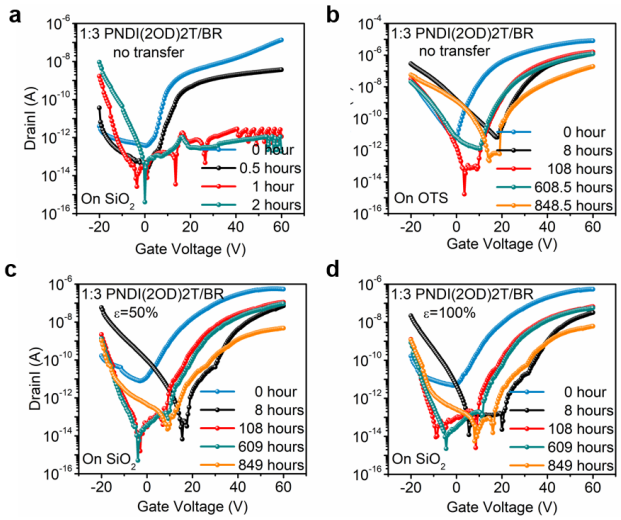

Figure F.46 *Representative transfer curves for 1:3 PNDI(2OD)2T/BR blend systems at different days. (a) No strain on SiO_2 (b) No strain on OTS (c) under 50% strain (d) under 100% strain change of charge mobility over 800 hours.*

Table F.2 *Summary of polymer characteristics.*

Polymer	Mn (kDa)	PDI	Source
Butyl rubber	337	1.29	EXXON Butyl 068
PDPPTVT	41.2	3.4	Gagne's Group
PNDI(2OD)2T	108	2.6	Ossila
P3HT	19.6	2.7	Sigma Aldrich
PBTTT	28.2	2.3	Schroeder's Group

Table F.3 *Summary of mechanical performance for different blend ratios of PDPPTVT/BR.*

Material	**Elastic modulus (MPa)**	**Fracture strain (%)**
PDPPTVT	290.5 ± 11.5	4.1 ± 0.9
2:1 PDPPTVT/BR	53.7 ± 7.2	27.5 ± 2
1:1 PDPPTVT/BR	25.2 ± 3.8	59.5 ± 6.5
1:3 PDPPTVT/BR	5.83 ± 1.02	315 ± 85
1:8.5 PDPPTVT/BR	1.09 ± 0.02	820 ± 40

Table F.4 *Summary of selected past researches on low modulus and highly deformable semiconducting polymer systems.*

Material	Elastic modulus (MPa)	Deformability (%)	Reference
30% PDPPT-TT/SEBS	43.87	200	[19]
P3HT/SEBS	11.7	300	[133]
P3HT-PMA-P3HT (55%P3HT)	6	140	[127]
P3HT-PE (35-65)	240	660	[105]
PDPP-b-PCL (T-75)	196	208	[347]
PDPP-P3 (10% PCDA H bonding)	228	100	[97]
PII2-C8	270	100	[346]
P3HT	252	150	[96]
PII2T-PBA100	41	100	[345]
PIDTBPD	200	40	[210]
20DPPTTECx (crosslinking)	90	150	[134]

Table F.5 *Summary of OFET device performance for different blend ratios of PDPPTVT/BR.*

	W/L	Max mobility ($cm^2 V^{-1} s^{-1}$)	Average Mobility ($cm^2 V^{-1} s^{-1}$)	on/off	Vt_sat (V)
PDPPTVT (as cast)	20	6.48E-01	6.13E-01 ± 0.0354	2.01E+05	8.99
PDPPTVT (annealed)	20	1.07	1.06 ± 0.0904	2.21E+05	7.16
2:1 (as cast)	20	1.67	1.60 ± 0.1718	3.38E+06	6.28
2:1 (annealed)	20	1.66	1.62 ± 0.1822	8.00E+06	3.70
1:1 (as cast)	20	1.51	1.40 ± 0.1719	2.97E+05	7.12
1:1 (annealed)	20	1.40	1.37 ± 0.2148	2.21E+06	5.83
1:3 (as cast)	20	1.17	1.15 ± 0.1175	1.40E+07	6.46
1:3 (annealed)	20	1.08	1.07 ± 0.1260	3.24E+06	5.26
1:8.5 (as cast)	20	6.02E-01	5.93E-01 ± 0.0933	1.49E+07	4.69
1:8.5 (annealed)	20	7.76E-01	7.72E-01 ± 0.0491	3.25E+06	3.27

Table F.6 *Summary of OFET device performance for unannealed 1:3 PDPPTVT/BR blend composites upon stretching in parallel and perpendicular to charge transfer direction at different strain conditions.*

	W/L	Max mobility ($cm^2 V^{-1} s^{-1}$)	Average Mobility ($cm^2 V^{-1} s^{-1}$)	on/off	Vt_sat (V)
No transfer (on OTS)	20	1.17	1.15±0.1175	1.40E+07	6.46
0%	20	1.25E-01	1.24E-01 ± 0.0185	1.57E+07	-2.21
25% (⊥)	20	8.37E-02	8.31E-02 ± 0.0028	1.90E+07	-2.29
50% (⊥)	20	6.37E-02	6.36E-02 ± 0.0039	9.69E+06	-7.92
75% (⊥)	20	9.32E-02	8.49E-02 ± 0.0108	1.10E+07	-6.26
100% (⊥)	20	5.47E-02	5.39E-02 ± 0.0041	4.97E+06	-12.75
150% (⊥)	20	3.66E-02	3.64E-02±0.0020	7.84E+06	-14.09
25% (//)	20	2.65E-01	2.54E-01 ± 0.0363	8.33E+06	-3.13
50% (//)	20	1.38E-01	1.30E-01± 0.0085	2.28E+05	-1.17
75% (//)	20	1.09E-01	1.07E-01 ± 0.0134	6.67E+06	-1.98
100% (//)	20	6.09E-02	6.04E-02±0.0035	8.68E+06	-1.97
150% (//)	20	4.45E-02	4.40E-02±0.0024	1.95E+06	-10.13

Table F.7 *Summary of OFET device performance for unannealed 1:8.5 PDPPTVT/BR blend composites upon stretching in parallel and perpendicular to charge transfer direction at different strain conditions.*

	W/L	Max mobility ($cm^2 V^{-1} s^{-1}$)	Average Mobility ($cm^2 V^{-1} s^{-1}$)	on/off	Vt_sat (V)
No transfer (on OTS)	20	1.95E-01	1.77E-01 ± 0.0134	1.44E+07	-10.08
0%	20	1.75E-01	1.64E-01 ± 0.0124	9.58E+09	-15.38
25% (⊥)	20	1.41E-01	1.36E-01 ± 0.0068	7.42E+06	-16.33
50% (⊥)	20	1.06E-01	1.04E-01 ± 0.0074	7.32E+06	-16.76
75% (⊥)	20	5.45E-02	5.29E-02±0.0045	1.15E+06	-18.63
100% (⊥)	20	8.20E-02	7.83E-02±0.0145	4.22E+07	-14.58
150% (⊥)	20	9.14E-02	8.86E-02±0.0028	1.36E+07	-10.09
25% (//)	20	1.22E-01	1.14E-01±0.0086	7.85E+06	-17.02
50% (//)	20	9.54E-02	9.04E-02±0.0035	5.01E+06	-13.33
75% (//)	20	1.23E-01	1.14E-01±0.0078	5.91E+06	-15.20
100% (//)	20	1.37E-01	1.33E-01±0.0121	3.34E+07	-14.35
150% (//)	20	1.24E-01	1.21E-01±0.0048	4.14E+07	-13.72

Table F.8 *Summary of oxygen and vapor permeability of BR and PDMS.*

Polymer	Oxygen permeability (cc-cm/m^2-day-atm)	Water vapor permeability (cm^3-cm/m^2-day-atm)
Butyl Rubber	1.7530	2473.7
PDMS	5498.0	13952E+01

Table F.9 *Self-healing electrical performance for 2:3 blend of PDPPTVT/BR tested between different electrodes.*

	W/L	Max mobility (cm^2 V^{-1} s^{-1})	Average Mobility (cm^2 V^{-1} s^{-1})	on/off	Vt_sat (V)
Film I (5,6)	20	9.31E-02	9.27E-02	2.30E+06	-3.37
Film II (8,9)	20	8.87E-02	8.84E-02	3.44E+06	-4.24
Self-healing region (1,2)	20	1.07E-01	8.77E-02	4.8E+05	-4.25
Film I to Film II (4,8)	3.33	4.33E-02	4.33E-02	8.2E+05	-24.93

Table F.10 *Self-healing electrical performance for 2:3 blend of PDPPTVT/BR under 50% strain tested between different electrodes.*

	W/L	Max mobility (cm^2 V^{-1} s^{-1})	Average Mobility (cm^2 V^{-1} s^{-1})	on/off	Vt_sat
Film I (3,4)	20	6.34E-02	6.33E-02	2.9E+05	-6.38
Film II (7,8)	20	8.73E-02	8.64E-02	4.3E+05	-5.38
Self-healing region (1,2)	20	3.56E-02	3.46E-02	1.8E+05	-3.55
Film I to Film II (3,8)	4	2.65E-02	2.26E-02	5.7E+04	-6.07

Table F.11 *Self-healing electrical performance for 2:3 blend of PDPPTVT/BR under 50% strain for 50 cycles tested between different electrodes.*

	W/L	Max mobility ($cm^2 V^{-1} s^{-1}$)	Average Mobility ($cm^2 V^{-1} s^{-1}$)	on/off	Vt_sat
Film I (3,4)	20	5.66E-02	5.10E-02	6.7E+05	0.61
Film II (7,8)	20	5.50E-02	4.02E-02	1.1E+06	1.60
Self-healing region (1,2)	20	3.40E-02	3.34E-02	1.5E+05	-8.46
Film I to Film II (3,7)	5	2.30E-02	1.56E-02	1.0E+05	-2.63

Table F.12 *Self-healing electrical performance for 2:3 blend of PDPPTVT/BR under 50% strain for 100 cycles tested between different electrodes.*

	W/L	Max mobility ($cm^2 V^{-1} s^{-1}$)	Average Mobility ($cm^2 V^{-1} s^{-1}$)	on/off	Vt_sat
Film I (4,5)	20	1.08E-01	1.07E-01	5.4E+05	-6.34
Film II (8,9)	20	1.29E-01	1.26E-01	5.0E+05	-5.54
Self-healing region (1,2)	20	4.22E-02	3.99E-02	1.3E+05	6.38
Film I to Film II (3,7)	5	2.98E-02	1.42E-02	5.1E+04	-6.86

Table F.13 *Self-healing electrical performance for 2:3 blend of PDPPTVT/BR under 50% strain for 500 cycles tested between different electrodes.*

	W/L	Max mobility ($cm^2 V^{-1} s^{-1}$)	Average Mobility ($cm^2 V^{-1} s^{-1}$)	on/off	Vt_sat
Film I (4,5)	20	1.69E-02	1.66E-02	1.5E+05	-0.24
Film II (9,10)	20	1.30E-02	1.26E-02	1.6E+05	-0.42
Self-healing region (1,2)	20	1.50E-02	1.49E-02	4.7E+04	-5.14
Film I to Film II (3,7)	5	1.11E-02	1.04E-02	4.7E+03	-7.43

Table F.14 *Self-healing electrical performance for 2:3 blend of P3HT/BR tested between different electrodes.*

	W/L	Max mobility ($cm^2 V^{-1} s^{-1}$)	Average Mobility ($cm^2 V^{-1} s^{-1}$)	on/off	Vt_sat (V)
Film I (3,4)	20	5.41E-04	5.26E-04	4.2E+02	8.49
Film II (7,8)	20	8.12E-04	8.09E-04	4.0E+02	-1.22
Self-healing region (1,2)	20	8.11E-04	8.08E-04	5.6E+03	19.39
Film I to Film II (4,9)	2.85	4.29E-04	3.75E-04	2.6E+02	-4.14

Table F.15 *Self-healing electrical performance for 2:3 blend of P3HT/BR under 50% strain tested between different electrodes.*

	W/L	Max mobility ($cm^2 V^{-1} s^{-1}$)	Average Mobility ($cm^2 V^{-1} s^{-1}$)	on/off	Vt_sat (V)
Film I (4,5)	20	8.39E-04	8.25E-04	2.3E+03	-0.73
Film II (7,8)	20	7.90E-04	7.80E-04	1.9E+03	-1.17
Self-healing region (1,2)	20	2.26E-03	3.36E-04	6.2E+01	48.69
Film I to Film II (3,7)	5	3.80E-04	3.73E-04	2.8E+02	-4.84

Table F.16 *Self-healing electrical performance for 2:3 blend of P3HT/BR under 50% strain for 50 cycles tested between different electrodes.*

P3HT blend with PIB	W/L	Max mobility ($cm^2 V^{-1} s^{-1}$)	Average Mobility ($cm^2 V^{-1} s^{-1}$)	on/off	Vt_sat (V)
Film I (5,6)	20	8.38E-04	8.21E-04	9.4E+02	9.05
Film II (9,10)	20	8.68E-04	8.56E-04	2.7E+02	17.27
Self-healing region (1,2)	20	7.49E-04	1.43E-04	6.9E+00	121.36
Film I to Film II (3,8)	5	6.24E-04	4.84E-04	9.9E+01	14.30

Table F.17 *Self-healing electrical performance for 2:3 blend of P3HT/BR under 50% strain for 100 cycles tested between different electrodes.*

	W/L	Max mobility ($cm^2 V^{-1} s^{-1}$)	Average Mobility ($cm^2 V^{-1} s^{-1}$)	on/off	Vt_sat (V)
Film I (3,4)	20	8.78E-04	2.04E-04	8.7E+01	3.13
Film II (7,8)	20	2.48E-04	2.43E-04	7.8E+01	4.12
Self-healing region (1,2)	20	1.01E-04	1.38E-05	2.3E+00	266.54
Film I to Film II (3,7)	6.66	2.22E-03	1.53E-04	2.0E+01	24.46

Table F.18 *Self-healing electrical performance for 2:3 blend of P3HT/BR under 50% strain for 500 cycles tested between different electrodes.*

	W/L	Max mobility ($cm^2 V^{-1} s^{-1}$)	Average Mobility ($cm^2 V^{-1} s^{-1}$)	on/off	Vt_sat (V)
Film I (4,5)	20	3.85E-04	3.80E-04	5.6E+02	3.97
Film II (7,8)	20	3.91E-04	3.83E-04	8.5E+02	4.70
Self-healing region (1,2)	20	1.46E-05	1.10E-05	2.8E+00	177.40
Film I to Film II (4,7)	5	4.47E-03	4.49E-04	7.1E+01	14.84

Table F.19 *Summary of contact angles and surface energies for all the polymers.*

Material	Contact angle (°)		Surface energy (mN/m)		
	H_2O	CH_2I_2	γ_s	γ_s^d	γ_s^p
Butyl rubber	108.12	55.94	31.84	31.80	0.0415
PDMS	114.62	76.08	19.86	19.86	0.0014
PDPPTVT	98.00	57.83	29.83	29.13	0.6969
PNDI(2OD)2T	103.27	51.90	33.68	33.67	0.0112
P3HT	90.55	50.60	34.19	32.51	1.6795
PBTTT	97.52	52.41	32.92	32.46	0.4601

Table F.20 *Summary of peak positions for UV-Vis spectra.*

	π-π* transition (nm)	0-1 transition (nm)	0-0 transition (nm)
PDPPTVT	443.05	704.82	800.05
2:1	443.54	706.14	805.74
1:1	445.85	709.39	804.83
1:3	446.87	709.65	807.57
1:8.5	447.56	707.52	811.24

Table F.21 *Summary of mechanical performance for different blend ratios of PNDI2HD-T/BR, P3HT/BR and PBTTT/BR.*

Material	Elastic modulus (MPa)	Fracture strain (%)
PNDI(2OD)2T	1146 ± 66.5	69 ± 9
2:1 PNDI(2OD)2T /BR	332 ± 9	64.5 ± 3.5
1:1 PNDI(2OD)2T /BR	219 ± 23	69.5 ± 2.5
1:3 PNDI(2OD)2T /BR	19.06 ± 5.9	355 ± 45
1:8.5 PNDI(2OD)2T /BR	12.46 ± 1.24	790 ± 20
P3HT	364 ± 10	16.5 ± 3.5
2:1 P3HT/BR	175 ± 20	12.7 ± 6
1:1 P3HT/BR	92.5 ± 17.5	30 ± 7
1:3 P3HT/BR	8.8 ± 3.8	850 ± 250
1:8.5 P3HT/BR	1.4 ± 0.9	1000 ± 100
PBTTT	919 ± 85	1.5 ± 0.5
2:1 PBTTT/BR	401 ± 89	4.5 ± 0.5
1:1 PBTTT/BR	240 ± 30	23 ± 3
1:3 PBTTT/BR	22 ± 2	500 ± 150
1:8.5 PBTTT/BR	13.8 ± 1.2	900 ± 200

Table F.22 *Summary of OFET device performance for unannealed 1:3 PNDI(2OD)2T/BR blend systems upon stretching in parallel and perpendicular to charge transfer direction at different strain conditions.*

	W/L	Max mobility ($cm^2 V^{-1} s^{-1}$)	Average Mobility ($cm^2 V^{-1} s^{-1}$)	on/off	Vt_sat (V)
No transfer (on OTS)	20	3.48E-02	3.34E-02 ± 0.0074	1.33E+06	11.83
0%	20	7.66E-03	6.99E-03 ± 0.00147	1.51E+05	11.42
50% (⊥)	20	5.40E-03	4.82E-03 ± 0.0005	1.18E+05	15.73
75% (⊥)	20	5.74E-03	5.25E-03 ± 0.0007	1.50E+05	17.78
100% (⊥)	20	4.92E-03	4.36E-03 ± 0.0002	1.17E+05	18.44
50% (//)	20	6.81E-03	5.95E-03 ± 0.0014	1.35E+05	17.33
75% (//)	20	5.97E-03	5.38E-03 ± 0.0008	1.39E+05	18.06
100% (//)	20	4.00E-03	3.49E-03 ± 0.0001	6.11E+04	20.07

REFERENCES

[1] D.-H. H. Kim, N. Lu, R. Ma, Y.-S. S. Kim, R.-H. H. Kim, S. Wang, J. Wu, S. M. Won, H. Tao, A. Islam, K. J. Yu, T. Il Kim, R. Chowdhury, M. Ying, L. Xu, M. Li, H.-J. J. Chung, H. Keum, M. McCormick, P. Liu, Y.-W. W. Zhang, F. G. Omenetto, Y. Huang, T. Coleman, J. A. Rogers, *Science.* **2011**, *333*, 838 LP.

[2] D. J. Lipomi, Z. Bao, *MRS Bull.* **2017**, *42*, 93.

[3] M. Kaltenbrunner, M. S. White, E. D. Głowacki, T. Sekitani, T. Someya, N. S. Sariciftci, S. Bauer, *Nat. Commun.* **2012**, *3*, 770.

[4] R. Noriega, J. Rivnay, K. Vandewal, F. P. V. Koch, N. Stingelin, P. Smith, M. F. Toney, A. Salleo, *Nat. Mater.* **2013**, *12*, 1038.

[5] J. Mei, Y. Diao, A. L. Appleton, L. Fang, Z. Bao, *J. Am. Chem. Soc.* **2013**, *135*, 6724.

[6] A. F. Paterson, S. Singh, K. J. Fallon, T. Hodsden, Y. Han, B. C. Schroeder, H. Bronstein, M. Heeney, I. McCulloch, T. D. Anthopoulos, *Adv. Mater.* **2018**, *30*, 1801079.

[7] M. S. Vezie, S. Few, I. Meager, G. Pieridou, B. Dörling, R. S. Ashraf, A. R. Goñi, H. Bronstein, I. McCulloch, S. C. Hayes, M. Campoy-Quiles, J. Nelson, *Nat. Mater.* **2016**, *15*, 746.

[8] D. Venkateshvaran, M. Nikolka, A. Sadhanala, V. Lemaur, M. Zelazny, M. Kepa, M. Hurhangee, A. J. Kronemeijer, V. Pecunia, I. Nasrallah, I. Romanov, K. Broch, I. McCulloch, D. Emin, Y. Olivier, J. Cornil, D. Beljonne, H. Sirringhaus, *Nature* **2014**, *515*, 384.

[9] Y. Yamashita, F. Hinkel, T. Marszalek, W. Zajaczkowski, W. Pisula, M. Baumgarten, H. Matsui, K. Müllen, J. Takeya, *Chem. Mater.* **2016**, *28*, 420.

[10] G. Kim, S. J. Kang, G. K. Dutta, Y. K. Han, T. J. Shin, Y. Y. Noh, C. Yang, *J. Am. Chem. Soc.* **2014**, *136*, 9477.

[11] C. Luo, A. K. K. Kyaw, L. A. Perez, S. Patel, M. Wang, B. Grimm, G. C. Bazan, E. J. Kramer, A. J. Heeger, *Nano Lett.* **2014**, *14*, 2764.

[12] L. Meng, Y. Zhang, X. Wan, C. Li, X. Zhang, Y. Wang, X. Ke, Z. Xiao, L. Ding, R. Xia, H. L. Yip, Y. Cao, Y. Chen, *Science.* **2018**, *361*, 1094.

[13] I. Kang, H. J. Yun, D. S. Chung, S. K. Kwon, Y. H. Kim, *J. Am. Chem. Soc.* **2013**, *135*, 14896.

[14] J. T. E. Quinn, J. Zhu, X. Li, J. Wang, Y. Li, *J. Mater. Chem. C* **2017**, *5*, 8654.

[15] C. B. Nielsen, M. Turbiez, I. McCulloch, *Adv. Mater.* **2013**, *25*, 1859.

[16] Z. Qian, Z. Cao, L. Galuska, S. Zhang, J. Xu, X. Gu, *Macromol. Chem. Phys.* **2019**, *220*, 1900062.

[17] S. Savagatrup, A. D. Printz, H. Wu, K. M. Rajan, E. J. Sawyer, A. V. Zaretski, C. J. Bettinger, D. J. Lipomi, *Synth. Met.* **2015**, *203*, 208.

[18] S. Zhang, M. U. Ocheje, S. Luo, D. Ehlenberg, B. Appleby, D. Weller, D. Zhou, S. Rondeau-Gagné, X. Gu, *Macromol. Rapid Commun.* **2018**, *39*, 1800092.

[19] J. Xu, S. Wang, G. J. N. Wang, C. Zhu, S. Luo, L. Jin, X. Gu, S. Chen, V. R. Feig, J. W. F. To, S. Rondeau-Gagné, J. Park, B. C. Schroeder, C. Lu, J. Y. Oh, Y. Wang, Y. H. Kim, H. Yan, R. Sinclair, D. Zhou, G. Xue, B. Murmann, C. Linder, W. Cai, J. B. H. Tok, J. W. Chung, Z. Bao, *Science.* **2017**, *355*, 59.

[20] R. Xie, A. R. Weisen, Y. Lee, M. A. Aplan, A. M. Fenton, A. E. Masucci, F. Kempe, M. Sommer, C. W. Pester, R. H. Colby, E. D. Gomez, *Nat. Commun.* **2020**, *11*, 893.
[21] A. Sharma, X. Pan, J. A. Campbell, M. R. Andersson, D. A. Lewis, *Macromolecules* **2017**, *50*, 3347.
[22] N. Balar, J. J. Rech, R. Henry, L. Ye, H. Ade, W. You, B. T. O'Connor, *Chem. Mater.* **2019**, *31*, 5124.
[23] J. Martín, N. Stingelin, D. Cangialosi, *J. Phys. Chem. Lett.* **2018**, *9*, 990.
[24] N. Van Den Brande, G. Van Assche, B. Van Mele, *Polymer.* **2016**, *83*, 59.
[25] S. Luo, T. Wang, M. U. Ocheje, S. Zhang, J. Xu, Z. Qian, X. Gu, G. Xue, S. Rondeau-Gagné, J. Jiang, W. Hu, E. Zhuravlev, D. Zhou, *Macromolecules* **2020**, *53*, 4480.
[26] D. Zhou, H. Huth, Y. Gao, G. Xue, C. Schick, *Macromolecules* **2008**, *41*, 7662.
[27] A. Sharma, X. Pan, J. M. Bjuggren, D. Gedefaw, X. Xu, R. Kroon, E. Wang, J. A. Campbell, D. A. Lewis, M. R. Andersson, *Chem. Mater.* **2019**, *31*, 6740.
[28] L. W. Martin, A. M. Rappe, *Nat. Rev. Mater.* **2016**, *2*, 1.
[29] A. D. Franklin, *Science.* **2015**, *349*, aab2750.
[30] K. Myny, *Nat. Electron.* **2018**, *1*, 30.
[31] H. Fu, K. Nan, W. Bai, W. Huang, K. Bai, L. Lu, C. Zhou, Y. Liu, F. Liu, J. Wang, *Nat. Mater.* **2018**, *17*, 268.
[32] J. Xu, H. C. Wu, C. Zhu, A. Ehrlich, L. Shaw, M. Nikolka, S. Wang, F. Molina-Lopez, X. Gu, S. Luo, D. Zhou, Y. H. Kim, G. J. N. Wang, K. Gu, V. R. Feig, S. Chen, Y. Kim, T. Katsumata, Y. Q. Zheng, H. Yan, J. W. Chung, J. Lopez, B. Murmann, Z. Bao, *Nat. Mater.* **2019**, *18*, 594.
[33] O. Jin Young, S. Kim, H. K. Baik, U. Jeong, *Adv. Mater.* **2016**, *28*, 4455.
[34] Y. Su, X. Ping, K. J. Yu, J. W. Lee, J. A. Fan, B. Wang, M. Li, R. Li, D. V Harburg, Y. Huang, *Adv. Mater.* **2017**, *29*, 1604989.
[35] S. Wang, J. Y. Oh, J. Xu, H. Tran, Z. Bao, *Acc. Chem. Res.* **2018**, *51*, 1033.
[36] J. A. Rogers, T. Someya, Y. Huang, *Science.* **2010**, *327*, 1603.
[37] S. Il Park, J. H. Ahn, X. Feng, S. Wang, Y. Huang, J. A. Rogers, *Adv. Funct. Mater.* **2008**, *18*, 2673.
[38] C. F. Guo, Q. Liu, G. Wang, Y. Wang, Z. Shi, Z. Suo, C.-W. Chu, Z. Ren, *Proc. Natl. Acad. Sci.* **2015**, *112*, 12332.
[39] D. Akinwande, C. J. Brennan, J. S. Bunch, P. Egberts, J. R. Felts, H. Gao, R. Huang, J.-S. Kim, T. Li, Y. Li, K. M. Liechti, N. Lu, H. S. Park, E. J. Reed, P. Wang, B. I. Yakobson, T. Zhang, Y.-W. Zhang, Y. Zhou, Y. Zhu, *Extrem. Mech. Lett.* **2017**, *13*, 42.
[40] N. Lu, X. Wang, Z. Suo, J. Vlassak, *Appl. Phys. Lett.* **2007**, *91*, 8.
[41] F. Macionczyk, W. Brückner, *J. Appl. Phys.* **1999**, *86*, 4922.
[42] C. M. Stafford, C. Harrison, K. L. Beers, A. Karim, E. J. Amis, M. R. Vanlandingham, H. C. Kim, W. Volksen, R. D. Miller, E. E. Simonyi, *Nat. Mater.* **2004**, *3*, 545.
[43] R. Song, H. Schrickx, N. Balar, S. Siddika, N. Sheikh, B. T. O'Connor, *Macromolecules* **2020**, *53*, 1988.
[44] D. Rodriquez, J. H. Kim, S. E. Root, Z. Fei, P. Boufflet, M. Heeney, T. S. Kim, D.

J. Lipomi, *ACS Appl. Mater. Interfaces* **2017**, *9*, 8855.
[45] S. E. Root, S. Savagatrup, A. D. Printz, D. Rodriquez, D. J. Lipomi, *Chem. Rev.* **2017**, *117*, 6467.
[46] C. A. Tweedie, G. Constantinides, K. E. Lehman, D. J. Brill, G. S. Blackman, K. J. Van Vliet, *Adv. Mater.* **2007**, *19*, 2540.
[47] C. B. Roth, J. R. Dutcher, *J. Electroanal. Chem.* **2005**, *584*, 13.
[48] R. D. Priestley, C. J. Ellison, L. J. Broadbelt, J. M. Torkelson, *Science.* **2005**, *309*, 456.
[49] M. A. Haque, M. T. A. Saif, *Exp. Mech.* **2002**, *42*, 123.
[50] Y. Zhu, H. D. Espinosa, *Proc. Natl. Acad. Sci. U. S. A.* **2005**, *102*, 14503.
[51] H. Huang, F. Spaepen, *Acta Mater.* **2000**, *48*, 3261.
[52] D. S. Gianola, C. Eberl, *JOM* **2009**, *61*, 24.
[53] J.-H. Kim, A. Nizami, Y. Hwangbo, B. Jang, H.-J. Lee, C.-S. Woo, S. Hyun, T.-S. Kim, *Nat. Commun.* **2013**, *4*, 2520.
[54] Y. Liu, Y. C. Chen, S. Hutchens, J. Lawrence, T. Emrick, A. J. Crosby, *Macromolecules* **2015**, *48*, 6534.
[55] H. Hasegawa, T. Ohta, K. Ito, H. Yokoyama, *Polymer.* **2017**, *123*, 179.
[56] J. Huang, M. Juszkiewicz, W. H. De Jeu, E. Cerda, T. Emrick, N. Menon, T. P. Russell, *Science.* **2007**, *317*, 650.
[57] K. Seshan, *Handbook of thin film deposition processes and techniques*, William Andrew, **2001**.
[58] R. K. Bay, S. Shimomura, Y. Liu, M. Ilton, A. J. Crosby, *Macromolecules* **2018**, *51*, 3647.
[59] S. Zhang, Y. Cheng, L. Galuska, A. Roy, M. Lorenz, B. Chen, S. Luo, Y. Li, C. Hung, Z. Qian, P. B. J. St. Onge, G. T. Mason, L. Cowen, D. Zhou, S. I. Nazarenko, R. F. Storey, B. C. Schroeder, S. Rondeau-Gagné, Y. Chiu, X. Gu, *Adv. Funct. Mater.* **2020**, *30*, 2000663.
[60] J. H. Kim, J. Noh, H. Choi, J. Y. Lee, T. S. Kim, *Chem. Mater.* **2017**, *29*, 3954.
[61] S. Zhang, M. U. Ocheje, L. Huang, L. Galuska, Z. Cao, S. Luo, Y. Cheng, D. Ehlenberg, R. B. Goodman, D. Zhou, Y. Liu, Y. Chiu, J. D. Azoulay, S. Rondeau-Gagné, X. Gu, *Adv. Electron. Mater.* **2019**, *5*, 1800899.
[62] S. Kim, J. H. Kim, J. G. Oh, K. L. Jang, B. H. Jeong, B. K. Hong, T. S. Kim, *ACS Appl. Mater. Interfaces* **2016**, *8*, 15391.
[63] T. Yoon, J.-H. Kim, J. H. Choi, D. Y. Jung, I.-J. Park, S.-Y. Choi, N. S. Cho, J.-I. Lee, Y.-D. Kwon, S. Cho, T.-S. Kim, *ACS Nano* **2016**, *10*, 1539.
[64] A. D. Printz, D. J. Lipomi, *Appl. Phys. Rev.* **2016**, *3*, 021302.
[65] J.-H. Kim, K.-L. Jang, K. Ahn, T. Yoon, T.-I. Lee, T.-S. Kim, *Sci. Rep.* **2019**, *9*, 7071.
[66] L. Ma, L. He, Y. Ni, *J. Appl. Phys.* **2020**, *127*.
[67] B. J. Gurmessa, A. B. Croll, *Phys. Rev. Lett.* **2013**, *110*, 1.
[68] M. A. Alkhadra, S. E. Root, K. M. Hilby, D. Rodriquez, F. Sugiyama, D. J. Lipomi, *Chem. Mater.* **2017**, *29*, 10139.
[69] D. Rodriquez, J. G. Kohl, P. Morel, K. Burrows, G. Favaro, S. E. Root, J. Ramírez, M. A. Alkhadra, C. W. Carpenter, Z. Fei, P. Boufflet, M. Heeney, D. J. Lipomi, *ACS Macro Lett.* **2018**, *7*, 1003.

[70] J. L. Keddie, R. A. L. Jones, R. A. Cory, *Europhys. Lett.* **1994**, *27*, 59.
[71] C. B. Roth, *Polymer glasses*, CRC Press, **2016**.
[72] M. Ghasemi, N. Balar, Z. Peng, H. Hu, Y. Qin, T. Kim, J. J. Rech, M. Bidwell, W. Mask, I. McCulloch, W. You, A. Amassian, C. Risko, B. T. O'Connor, H. Ade, *Nat. Mater.* **2021**.
[73] L. Ye, H. Hu, M. Ghasemi, T. Wang, B. A. Collins, J. H. Kim, K. Jiang, J. H. Carpenter, H. Li, Z. Li, T. McAfee, J. Zhao, X. Chen, J. L. Y. Lai, T. Ma, J. L. Bredas, H. Yan, H. Ade, *Nat. Mater.* **2018**, *17*, 253.
[74] G. Zhang, J. Zhao, P. C. Y. Chow, K. Jiang, J. Zhang, Z. Zhu, J. Zhang, F. Huang, H. Yan, *Chem. Rev.* **2018**, *118*, 3447.
[75] X. Gu, L. Shaw, K. Gu, M. F. Toney, Z. Bao, *Nat. Commun.* **2018**, *9*, 534.
[76] Y. Diao, Y. Zhou, T. Kurosawa, L. Shaw, C. Wang, S. Park, Y. Guo, J. A. Reinspach, K. Gu, X. Gu, B. C. K. Tee, C. Pang, H. Yan, D. Zhao, M. F. Toney, S. C. B. Mannsfeld, Z. Bao, *Nat. Commun.* **2015**, *6*, 7955.
[77] Y. Zhao, A. Gumyusenge, J. He, G. Qu, W. W. McNutt, Y. Long, H. Zhang, L. Huang, Y. Diao, J. Mei, *Adv. Funct. Mater.* **2018**, *28*, 1705584.
[78] N. E. Persson, S. Engmann, L. J. Richter, D. M. Delongchamp, *Chem. Mater.* **2019**, *31*, 4133.
[79] K. S. Park, J. J. Kwok, R. Dilmurat, G. Qu, P. Kafle, X. Luo, S.-H. Jung, Y. Olivier, J.-K. Lee, J. Mei, D. Beljonne, Y. Diao, *Sci. Adv.* **2019**, *5*, eaaw7757.
[80] D. Wu, M. Kaplan, H. W. Ro, S. Engmann, D. A. Fischer, D. M. DeLongchamp, L. J. Richter, E. Gann, L. Thomsen, C. R. McNeill, X. Zhang, *Chem. Mater.* **2018**, *30*, 1924.
[81] B. O'Connor, R. J. Kline, B. R. Conrad, L. J. Richter, D. Gundlach, M. F. Toney, D. M. DeLongchamp, *Adv. Funct. Mater.* **2011**, *21*, 3697.
[82] B. T. O'Connor, O. G. Reid, X. Zhang, R. J. Kline, L. J. Richter, D. J. Gundlach, D. M. Delongchamp, M. F. Toney, N. Kopidakis, G. Rumbles, *Adv. Funct. Mater.* **2014**, *24*, 3422.
[83] V. Untilova, J. Hynynen, A. I. Hofmann, D. Scheunemann, Y. Zhang, S. Barlow, M. Kemerink, S. R. Marder, L. Biniek, C. Müller, M. Brinkmann, *Macromolecules* **2020**, *53*, 6314.
[84] S. N. Patel, A. M. Glaudell, K. A. Peterson, E. M. Thomas, K. A. O'Hara, E. Lim, M. L. Chabinyc, *Sci. Adv.* **2017**, *3*, 24.
[85] X. Yan, M. Xiong, J. T. Li, S. Zhang, Z. Ahmad, Y. Lu, Z. Y. Wang, Z. F. Yao, J. Y. Wang, X. Gu, T. Lei, *J. Am. Chem. Soc.* **2019**, *141*, 20215.
[86] C. R. Snyder, D. M. DeLongchamp, *Curr. Opin. Solid State Mater. Sci.* **2018**, *22*, 41.
[87] G. Qu, K. S. Park, P. Kafle, F. Zhang, J. J. Kwok, B. B. Patel, D. M. Smilgies, L. Thomsen, C. R. McNeill, Y. Diao, *Chem. Mater.* **2020**, *32*, 6043.
[88] A. Salleo, R. J. Kline, D. M. DeLongchamp, M. L. Chabinyc, *Adv. Mater.* **2010**, *22*, 3812.
[89] B. Grévin, P. Rannou, R. Payerne, A. Pron, J. P. Travers, *Adv. Mater.* **2003**, *15*, 881.
[90] D. A. Warr, L. M. A. Perdigão, H. Pinfold, J. Blohm, D. Stringer, A. Leventis, H. Bronstein, A. Troisi, G. Costantini, *Sci. Adv.* **2018**, *4*, eaas9543.

[91] S. E. Root, S. Savagatrup, A. D. Printz, D. Rodriquez, D. J. Lipomi, *Chem. Rev.* **2017**, *117*, 6467.
[92] D. J. Lipomi, *Adv. Mater.* **2016**, *28*, 4180.
[93] N. Balar, B. T. O'Connor, *Macromolecules* **2017**, *50*, 8611.
[94] S. E. Root, M. A. Alkhadra, D. Rodriquez, A. D. Printz, D. J. Lipomi, *Chem. Mater.* **2017**, *29*, 2646.
[95] A. D. Printz, A. V. Zaretski, S. Savagatrup, A. S. C. Chiang, D. J. Lipomi, *ACS Appl. Mater. Interfaces* **2015**, *7*, 23257.
[96] B. O'Connor, E. P. Chan, C. Chan, B. R. Conrad, L. J. Richter, R. J. Kline, M. Heeney, I. McCulloch, C. L. Soles, D. M. DeLongchamp, *ACS Nano* **2010**, *4*, 7538.
[97] J. Y. Oh, S. Rondeau-Gagné, Y. C. Chiu, A. Chortos, F. Lissel, G. J. N. Wang, B. C. Schroeder, T. Kurosawa, J. Lopez, T. Katsumata, J. Xu, C. Zhu, X. Gu, W. G. Bae, Y. Kim, L. Jin, J. W. Chung, J. B. H. Tok, Z. Bao, *Nature* **2016**, *539*, 411.
[98] G. J. N. Wang, A. Gasperini, Z. Bao, *Adv. Electron. Mater.* **2018**, *4*, 1700429.
[99] M. U. Ocheje, B. P. Charron, A. Nyayachavadi, S. Rondeau-Gagné, *Flex. Print. Electron.* **2017**, *2*, 043002.
[100] R. Xie, R. H. Colby, E. D. Gomez, *Adv. Electron. Mater.* **2018**, *4*, 1700356.
[101] J. Onorato, V. Pakhnyuk, C. K. Luscombe, *Polym. J.* **2017**, *49*, 41.
[102] T. Kim, J. H. Kim, T. E. Kang, C. Lee, H. Kang, M. Shin, C. Wang, B. Ma, U. Jeong, T. S. Kim, B. J. Kim, *Nat. Commun.* **2015**, *6*, 8547.
[103] J. H. J. S. Kim, J. H. J. S. Kim, W. Lee, H. Yu, H. J. Kim, I. Song, M. Shin, J. H. Oh, U. Jeong, T. S. Kim, B. J. Kim, *Macromolecules* **2015**, *48*, 4339.
[104] H. J. Kim, J. H. Kim, J. H. Ryu, Y. Kim, H. Kang, W. B. Lee, T. S. Kim, B. J. Kim, *ACS Nano* **2014**, *8*, 10461.
[105] C. Müller, S. Goffri, D. W. Breiby, J. W. Andreasen, H. D. Chanzy, R. A. J. Janssen, M. M. Nielsen, C. P. Radano, H. Sirringhaus, P. Smith, N. Stingelin-Stutzmann, *Adv. Funct. Mater.* **2007**, *17*, 2674.
[106] J. Mei, Z. Bao, *Chem. Mater.* **2014**, *26*, 604.
[107] Z. C. Smith, Z. M. Wright, A. M. Arnold, G. Sauvé, R. D. McCullough, S. A. Sydlik, *Adv. Electron. Mater.* **2017**, *3*, 1600316.
[108] M. D. Ediger, J. A. Forrest, *Macromolecules* **2014**, *47*, 471.
[109] C. M. Stafford, B. D. Vogt, C. Harrison, D. Julthongpiput, R. Huang, *Macromolecules* **2006**, *39*, 5095.
[110] J. Y. Chung, J. H. Lee, K. L. Beers, C. M. Stafford, *Nano Lett.* **2011**, *11*, 3361.
[111] J. Y. Chung, A. J. Nolte, C. M. Stafford, *Adv. Mater.* **2011**, *23*, 349.
[112] D. Tank, H. H. Lee, D. Y. Khang, *Macromolecules* **2009**, *42*, 7079.
[113] J. Y. Chung, J. F. Douglas, C. M. Stafford, *J. Chem. Phys.* **2017**, *147*, 154902.
[114] T. F. O'Connor, K. M. Rajan, A. D. Printz, D. J. Lipomi, *J. Mater. Chem. B* **2015**, *3*, 4947.
[115] A. T. Kleinschmidt, S. E. Root, D. J. Lipomi, *J. Mater. Chem. A* **2017**, *5*, 11396.
[116] D. J. Lipomi, H. Chong, M. Vosgueritchian, J. Mei, Z. Bao, *Sol. Energy Mater. Sol. Cells* **2012**, *107*, 355.
[117] E. J. Sawyer, S. Savagatrup, T. F. O'Connor, A. S. Makaram, D. J. Burke, A. V. Zaretski, A. D. Printz, D. J. Lipomi, *Org. Field-Effect Transistors XIII; Org.*

Semicond. Sensors Bioelectron. VII **2014**, *9185*, 91850U.
[118] S. Savagatrup, A. D. Printz, T. F. O'Connor, A. V. Zaretski, D. Rodriquez, E. J. Sawyer, K. M. Rajan, R. I. Acosta, S. E. Root, D. J. Lipomi, *Energy Environ. Sci.* **2015**, *8*, 55.
[119] T. F. O'Connor, A. V. Zaretski, S. Savagatrup, A. D. Printz, C. D. Wilkes, M. I. Diaz, E. J. Sawyer, D. J. Lipomi, *Sol. Energy Mater. Sol. Cells* **2016**, *144*, 438.
[120] D. J. Lipomi, Z. Bao, *Energy Environ. Sci.* **2011**, *4*, 3314.
[121] S. Savagatrup, A. D. Printz, D. Rodriquez, D. J. Lipomi, *Macromolecules* **2014**, *47*, 1981.
[122] A. D. Printz, S. Savagatrup, D. Rodriquez, D. J. Lipomi, *Sol. Energy Mater. Sol. Cells* **2015**, *134*, 64.
[123] B. Roth, S. Savagatrup, N. V. de los Santos, O. Hagemann, J. E. Carlé, M. Helgesen, F. Livi, E. Bundgaard, R. R. Søndergaard, F. C. Krebs, D. J. Lipomi, *Chem. Mater.* **2016**, *28*, 2363.
[124] C. Lu, W. Y. Lee, X. Gu, J. Xu, H. H. Chou, H. Yan, Y. C. Chiu, M. He, J. R. Matthews, W. Niu, J. B. H. Tok, M. F. Toney, W. C. Chen, Z. Bao, *Adv. Electron. Mater.* **2017**, *3*, 1600311.
[125] H. C. Wu, S. J. Benight, A. Chortos, W. Y. Lee, J. Mei, J. W. F. To, C. Lu, M. He, J. B. H. Tok, W. C. Chen, Z. Bao, *Chem. Mater.* **2014**, *26*, 4544.
[126] C. P. Radano, O. A. Scherman, N. Stingelin-Stutzmann, C. Müller, D. W. Breiby, P. Smith, R. A. J. Janssen, E. W. Meijer, *J. Am. Chem. Soc.* **2005**, *127*, 12502.
[127] R. Peng, B. Pang, D. Hu, M. Chen, G. Zhang, X. Wang, H. Lu, K. Cho, L. Qiu, *J. Mater. Chem. C* **2015**, *3*, 3599.
[128] S. Savagatrup, X. Zhao, E. Chan, J. Mei, D. J. Lipomi, *Macromol. Rapid Commun.* **2016**, *37*, 1623.
[129] Y. Zhao, X. Zhao, Y. Zang, C. A. Di, Y. Diao, J. Mei, *Macromolecules* **2015**, *48*, 2048.
[130] B. C. Schroeder, Y. C. Chiu, X. Gu, Y. Zhou, J. Xu, J. Lopez, C. Lu, M. F. Toney, Z. Bao, *Adv. Electron. Mater.* **2016**, *2*, 1600104.
[131] E. Song, B. Kang, H. H. Choi, D. H. Sin, H. Lee, W. H. Lee, K. Cho, *Adv. Electron. Mater.* **2016**, *2*, 1500250.
[132] D. Choi, H. Kim, N. Persson, P. H. Chu, M. Chang, J. H. Kang, S. Graham, E. Reichmanis, *Chem. Mater.* **2016**, *28*, 1196.
[133] M. Shin, J. Y. Oh, K. E. Byun, Y. J. Lee, B. Kim, H. K. Baik, J. J. Park, U. Jeong, *Adv. Mater.* **2015**, *27*, 1255.
[134] G. J. N. Wang, L. Shaw, J. Xu, T. Kurosawa, B. C. Schroeder, J. Y. Oh, S. J. Benight, Z. Bao, *Adv. Funct. Mater.* **2016**, *26*, 7254.
[135] S. D. Oosterhout, V. Savikhin, J. Zhang, Y. Zhang, M. A. Burgers, S. R. Marder, G. C. Bazan, M. F. Toney, *Chem. Mater.* **2017**, *29*, 3062.
[136] J. A. Forrest, K. Dalnoki-Veress, J. R. Stevens, J. R. Dutcher, *Phys. Rev. Lett.* **1996**, *77*, 2002.
[137] J. A. Forrest, K. Dalnoki-Veress, J. R. Dutcher, *Phys. Rev. E - Stat. Physics, Plasmas, Fluids, Relat. Interdiscip. Top.* **1997**, *56*, 5705.
[138] L. Si, M. V. Massa, K. Dalnoki-Veress, H. R. Brown, R. A. L. Jones, *Phys. Rev. Lett.* **2005**, *94*, 1.

[139] J. D. McGraw, K. Dalnoki-Veress, *Phys. Rev. E - Stat. Nonlinear, Soft Matter Phys.* **2010**, *82*, 1.
[140] J. H. Lin, A. C. M. Yang, *Macromolecules* **2001**, *34*, 3698.
[141] J. S. Moon, C. J. Takacs, Y. Sun, A. J. Heeger, *Nano Lett.* **2011**, *11*, 1036.
[142] R. Xie, Y. Lee, M. P. Aplan, N. J. Caggiano, C. Müller, R. H. Colby, E. D. Gomez, *Macromolecules* **2017**, *50*, 5146.
[143] J.-H. Lee, J. Y. Chung, C. M. Stafford, *ACS Macro Lett.* **2012**, *1*, 122.
[144] E. M. Arruda, M. C. Boyce, R. Jayachandran, *Mech. Mater.* **1995**, *19*, 193.
[145] C. Bauwens-Crowet, J. C. Bauwens, G. Homès, *J. Polym. Sci. Part A-2 Polym. Phys.* **1969**, *7*, 735.
[146] A. D. Mulliken, M. C. Boyce, *Int. J. Solids Struct.* **2006**, *43*, 1331.
[147] W. G. Knauss, I. J. Emri, *Comput. Struct.* **1981**, *13*, 123.
[148] J. S. Bergström, M. C. Boyce, *J. Mech. Phys. Solids* **1998**, *46*, 931.
[149] S. S. Sarva, A. J. Hsieh, *Polymer.* **2009**, *50*, 3007.
[150] B. K. Kuila, A. K. Nandi, *Macromolecules* **2004**, *37*, 8577.
[151] S. Hugger, R. Thomann, T. Heinzel, T. Thurn-Albrecht, *Colloid Polym. Sci.* **2004**, *282*, 932.
[152] J. Yi, M. C. Boyce, G. F. Lee, E. Balizer, *Polymer.* **2006**, *47*, 319.
[153] J. M. Torres, C. M. Stafford, B. D. Vogt, *ACS Nano* **2009**, *3*, 2677.
[154] J. M. Torres, C. M. Stafford, B. D. Vogt, *Polymer.* **2010**, *51*, 4211.
[155] T. R. Böhme, J. J. De Pablo, *J. Chem. Phys.* **2002**, *116*, 9939.
[156] B. McCulloch, V. Ho, M. Hoarfrost, C. Stanley, C. Do, W. T. Heller, R. A. Segalman, *Macromolecules* **2013**, *46*, 1899.
[157] C. Du, Y. Ji, J. Xue, T. Hou, J. Tang, S. T. Lee, Y. Li, *Sci. Rep.* **2015**, *5*, 16854.
[158] J. M. Torres, C. Wang, E. B. Coughlin, J. P. Bishop, R. A. Register, R. A. Riggleman, C. M. Stafford, B. D. Vogt, *Macromolecules* **2011**, *44*, 9040.
[159] M. U. Ocheje, B. P. Charron, Y. H. Cheng, C. H. Chuang, A. Soldera, Y. C. Chiu, S. Rondeau-Gagné, *Macromolecules* **2018**, *51*, 1336.
[160] C. Müller, *Chem. Mater.* **2015**, *27*, 2740.
[161] P. Papadopoulos, G. Floudas, C. Chi, G. Wegner, *J. Chem. Phys.* **2004**, *120*, 2368.
[162] S. A. Chen, J. M. Ni, *Macromolecules* **1992**, *25*, 6081.
[163] C. Bruner, F. Novoa, S. Dupont, R. Dauskardt, *ACS Appl. Mater. Interfaces* **2014**, *6*, 21474.
[164] M. Campoy-Quiles, M. I. Alonso, D. D. C. Bradley, L. J. Richter, *Adv. Funct. Mater.* **2014**, *24*, 2116.
[165] A. F. Ismail, M. Padaki, N. Hilal, T. Matsuura, W. J. Lau, *Desalination* **2015**, *356*, 140.
[166] B.-H. Jeong, E. M. V. Hoek, Y. Yan, A. Subramani, X. Huang, G. Hurwitz, A. K. Ghosh, A. Jawor, *J. Memb. Sci.* **2007**, *294*, 1.
[167] N. Y. Yip, A. Tiraferri, W. A. Phillip, J. D. Schiffman, M. Elimelech, *Environ. Sci. Technol.* **2010**, *44*, 3812.
[168] S. Wang, J. Xu, W. Wang, G. J. N. Wang, R. Rastak, F. Molina-Lopez, J. W. Chung, S. Niu, V. R. Feig, J. Lopez, T. Lei, S. K. Kwon, Y. Kim, A. M. Foudeh, A. Ehrlich, A. Gasperini, Y. Yun, B. Murmann, J. B. H. Tok, Z. Bao, *Nature* **2018**, *555*, 83.

[169] J. Y. Oh, Z. Bao, *Adv. Sci.* **2019**, *6*, 1900186.
[170] P. Z. Hanakata, B. A. Pazmiño Betancourt, J. F. Douglas, F. W. Starr, *J. Chem. Phys.* **2015**, *142*, 234907.
[171] Z. Yang, Y. Fujii, F. K. Lee, C. H. Lam, O. K. C. Tsui, *Science.* **2010**, *328*, 1676.
[172] T. P. Russell, Y. Chai, *Macromolecules* **2017**, *50*, 4597.
[173] R. K. Bay, A. J. Crosby, *ACS Macro Lett.* **2019**, *8*, 1080.
[174] X. G. Galuska A. Luke , Eric S. Muckley, Zhiqiang Cao, Dakota F. Ehlenberg, Zhiyuan Qian, Song Zhang, Simon Rondeau-Gagné, Minh D. Phan, John F. Ankner, Ilia N. Ivanov, *Nat. Commun.* **2021**.
[175] J. Murray, D. Hull, *J. Mater. Sci.* **1971**, *6*, 1277.
[176] K. L. DeVries, R. J. Nuismer, *ACS Symp. Ser.* **1985**, *17*, 277.
[177] J. Hyon, O. Lawal, O. Fried, R. Thevamaran, S. Yazdi, M. Zhou, D. Veysset, S. E. Kooi, Y. Jiao, M. S. Hsiao, J. Streit, R. A. Vaia, E. L. Thomas, *Mater. Today* **2018**, *21*, 817.
[178] Q. Ma, H. Fujimoto, P. Flinn, V. Jain, F. Adibi-rizi, F. Moghadam, R. H. Dauskardt, *Mater. Res. Soc. Symp. Proc.* **1995**, *391*, 91.
[179] C. Bruner, R. Dauskardt, *Macromolecules* **2014**, *47*, 1117.
[180] S. R. Dupont, M. Oliver, F. C. Krebs, R. H. Dauskardt, *Sol. Energy Mater. Sol. Cells* **2012**, *97*, 171.
[181] A. B. Martinez, J. Gamez-Perez, M. Sanchez-Soto, J. I. Velasco, O. O. Santana, M. Ll Maspoch, *Eng. Fail. Anal.* **2009**, *16*, 2604.
[182] P. Prentice, *Polymer.* **1983**, *24*, 344.
[183] L. M. Nicholson, K. S. Whitley, T. S. Gates, J. A. Hinkley, *J. Mater. Sci.* **2000**, *35*, 6111.
[184] B. Vorselaars, A. V. Lyulin, M. A. J. Michels, *Macromolecules* **2009**, *42*, 5829.
[185] R. N. Haward, *Polymer.* **1994**, *35*, 3858.
[186] A. Turon, C. G. Dávila, P. P. Camanho, J. Costa, *Eng. Fract. Mech.* **2007**, *74*, 1665.
[187] S. Zhang, A. Alesadi, M. Selivanova, Z. Cao, Z. Qian, S. Luo, L. Galuska, C. Teh, M. U. Ocheje, G. T. Mason, P. B. J. St. Onge, D. Zhou, S. Rondeau-Gagné, W. Xia, X. Gu, S. Rondeau-Gagné, W. Xia, X. Gu, *Adv. Funct. Mater.* **2020**, *30*, 2002221.
[188] E. Cerda, K. Ravi-Chandar, L. Mahadevan, *Nature* **2002**, *419*, 579.
[189] L. Si, M. V. Massa, K. Dalnoki-Veress, H. R. Brown, R. A. L. Jones, *Phys. Rev. Lett.* **2005**, *94*, 127801.
[190] J. Rottler, S. Barsky, M. O. Robbins, *Phys. Rev. Lett.* **2002**, *89*, 148304.
[191] G. P. Marshall, L. E. Culver, J. G. Williams, *Int. J. Fract.* **1973**, *9*, 295.
[192] R. S. Rivlin, A. G. Thomas, *J. Polym. Sci.* **1953**, *10*, 291.
[193] J. A. Beley, J. D. Landes, In *Proceedings of the 1971 National Symposium on Fracture Mechanics, Part II, ASTM STP*, **1972**, pp. 1–20.
[194] J. P. Berry, *J. Polym. Sci.* **1961**, *50*, 313.
[195] R. P. Kusy, M. J. Katz, *Polymer.* **1978**, *19*, 1345.
[196] M. Sambasivam, A. Klein, L. H. Sperling, *J. Appl. Polym. Sci.* **1995**, *58*, 357.
[197] D. Adolf, M. Tirrell, S. Prager, *J. Polym. Sci. Part A-2, Polym. Phys.* **1985**, *23*, 413.

[198] C. Y. Hui, E. J. Kramer, *Polym. Eng. Sci.* **1995**, *35*, 419.
[199] R. P. Kusy, D. T. Turner, *Microstruct Sci* **1977**, *5*, 477.
[200] J. D. Ferry, *Viscoelastic properties of polymers*, John Wiley & Sons, Ltd, New York, **1980**.
[201] T. G. Fox, P. J. Flory, *J. Appl. Phys.* **1950**, *21*, 581.
[202] V. Tvergaard, J. W. Hutchinson, *J. Mech. Phys. Solids* **1992**, *40*, 1377.
[203] J. Y. Sun, X. Zhao, W. R. K. Illeperuma, O. Chaudhuri, K. H. Oh, D. J. Mooney, J. J. Vlassak, Z. Suo, *Nature* **2012**, *489*, 133.
[204] N. A. García, J. L. Barrat, *Macromolecules* **2018**, *51*, 9850.
[205] H. Sirringhaus, *Adv. Mater.* **2014**, *26*, 1319.
[206] C. Wang, H. Dong, W. Hu, Y. Liu, D. Zhu, *Chem. Rev.* **2012**, *112*, 2208.
[207] V. Podzorov, *MRS Bull.* **2013**, *38*, 15.
[208] H. Dong, X. Fu, J. Liu, Z. Wang, W. Hu, *Adv. Mater.* **2013**, *25*, 6158.
[209] L. Lu, T. Zheng, Q. Wu, A. M. Schneider, D. Zhao, L. Yu, *Chem. Rev.* **2015**, *115*, 12666.
[210] Y. Li, W. K. Tatum, J. W. Onorato, S. D. Barajas, Y. Y. Yang, C. K. Luscombe, *Polym. Chem.* **2017**, *8*, 5185.
[211] G. Li, R. Zhu, Y. Yang, *Nat. Photonics* **2012**, *6*, 153.
[212] R. A. J. Janssen, J. Nelson, *Adv. Mater.* **2013**, *25*, 1847.
[213] A. J. Heeger, *Adv. Mater.* **2014**, *26*, 10.
[214] B. Russ, A. Glaudell, J. J. Urban, M. L. Chabinyc, R. A. Segalman, *Nat. Rev. Mater.* **2016**, *1*, 16050.
[215] K. Müllen, W. Pisula, *J. Am. Chem. Soc.* **2015**, *137*, 9503.
[216] V. Coropceanu, J. Cornil, D. A. da Silva Filho, Y. Olivier, R. Silbey, J.-L. Brédas, *Chem. Rev.* **2007**, *107*, 926.
[217] C. Huang, X. Liao, K. Gao, L. Zuo, F. Lin, X. Shi, C. Z. Li, H. Liu, X. Li, F. Liu, Y. Chen, H. Chen, A. K. Y. Jen, *Chem. Mater.* **2018**, *30*, 5429.
[218] S. Zhang, Y. Qin, J. Zhu, J. Hou, *Adv. Mater.* **2018**, *30*, 1800868.
[219] J. Zhang, B. Kan, A. J. Pearson, A. J. Parnell, J. F. K. Cooper, X. K. Liu, P. J. Conaghan, T. R. Hopper, Y. Wu, X. Wan, F. Gao, N. C. Greenham, A. A. Bakulin, Y. Chen, R. H. Friend, *J. Mater. Chem. A* **2018**, *6*, 18225.
[220] A. Chortos, J. Liu, Z. Bao, *Nat. Mater.* **2016**, *15*, 937.
[221] T. Someya, Z. Bao, G. G. Malliaras, *Nature* **2016**, *540*, 379.
[222] M. Chang, D. Choi, G. Wang, N. Kleinhenz, N. Persson, B. Park, E. Reichmanis, *ACS Appl. Mater. Interfaces* **2015**, *7*, 14095.
[223] S. Holliday, J. E. Donaghey, I. McCulloch, *Chem. Mater.* **2014**, *26*, 647.
[224] Z. Yi, X. Sun, Y. Zhao, Y. Guo, X. Chen, J. Qin, G. Yu, Y. Liu, *Chem. Mater.* **2012**, *24*, 4350.
[225] H. S. Kim, E. Song, S. B. Lee, I. N. Kang, K. Cho, D. H. Hwang, *Org. Electron. physics, Mater. Appl.* **2018**, *56*, 129.
[226] B. C. Schroeder, T. Kurosawa, T. Fu, Y. C. Chiu, J. Mun, G. J. N. Wang, X. Gu, L. Shaw, J. W. E. Kneller, T. Kreouzis, M. F. Toney, Z. Bao, *Adv. Funct. Mater.* **2017**, *27*, 1701973.
[227] G. J. N. Wang, F. Molina-Lopez, H. Zhang, J. Xu, H. C. Wu, J. Lopez, L. Shaw, J. Mun, Q. Zhang, S. Wang, A. Ehrlich, Z. Bao, *Macromolecules* **2018**, *51*, 4976.

[228] M. U. Ocheje, B. P. Charron, Y. H. Cheng, C. H. Chuang, A. Soldera, Y. C. Chiu, S. Rondeau-Gagné, *Macromolecules* **2018**, *51*, 1336.
[229] F. S. Kim, X. Guo, M. D. Watson, S. A. Jenekhe, *Adv. Mater.* **2010**, *22*, 478.
[230] X. Zhang, L. J. Richter, D. M. Delongchamp, R. J. Kline, M. R. Hammond, I. McCulloch, M. Heeney, R. S. Ashraf, J. N. Smith, T. D. Anthopoulos, B. Schroeder, Y. H. Geerts, D. A. Fischer, M. F. Toney, *J. Am. Chem. Soc.* **2011**, *133*, 15073.
[231] J. S. Ha, K. H. Kim, D. H. Choi, *J. Am. Chem. Soc.* **2011**, *133*, 10364.
[232] Y. Li, P. Sonar, L. Murphy, W. Hong, *Energy Environ. Sci.* **2013**, *6*, 1684.
[233] J. C. Bijleveld, R. A. M. Verstrijden, M. M. Wienk, R. A. J. Janssen, *J. Mater. Chem.* **2011**, *21*, 9224.
[234] G. Zhang, Y. Fu, Z. Xie, Q. Zhang, *Sol. Energy Mater. Sol. Cells* **2011**, *95*, 1168.
[235] J. W. Jung, F. Liu, T. P. Russell, W. H. Jo, *Energy Environ. Sci.* **2012**, *5*, 6857.
[236] C. Watts, E. Davies, *Trans. Faraday Soc.* **1969**, *66*, 80.
[237] F. P. V. Koch, J. Rivnay, S. Foster, C. Müller, J. M. Downing, E. Buchaca-Domingo, P. Westacott, L. Yu, M. Yuan, M. Baklar, Z. Fei, C. Luscombe, M. A. McLachlan, M. Heeney, G. Rumbles, C. Silva, A. Salleo, J. Nelson, P. Smith, N. Stingelin, *Prog. Polym. Sci.* **2013**, *38*, 1978.
[238] G. Xue, X. Zhao, G. Qu, T. Xu, A. Gumyusenge, Z. Zhang, Y. Zhao, Y. Diao, H. Li, J. Mei, *ACS Appl. Mater. Interfaces* **2017**, *9*, 25426.
[239] J. S. Lee, S. K. Son, S. Song, H. Kim, D. R. Lee, K. Kim, M. J. Ko, D. H. Choi, B. S. Kim, J. H. Cho, *Chem. Mater.* **2012**, *24*, 1316.
[240] X. Liu, B. He, A. Garzón-Ruiz, A. Navarro, T. L. Chen, M. A. Kolaczkowski, S. Feng, L. Zhang, C. A. Anderson, J. Chen, Y. Liu, *Adv. Funct. Mater.* **2018**, *28*, 1801874.
[241] J. Rivnay, S. C. B. Mannsfeld, C. E. Miller, A. Salleo, M. F. Toney, *Chem. Rev.* **2012**, *112*, 5488.
[242] J. L. Baker, L. H. Jimison, S. Mannsfeld, S. Volkman, S. Yin, V. Subramanian, A. Salleo, A. P. Alivisatos, M. F. Toney, *Langmuir* **2010**, *26*, 9146.
[243] T. Sasaki, A. Shimizu, T. H. Mourey, C. T. Thurau, M. D. Ediger, *J. Chem. Phys.* **2003**, *119*, 8730.
[244] X. Xue, G. Chandler, X. Zhang, R. J. Kline, Z. Fei, M. Heeney, P. J. Diemer, O. D. Jurchescu, B. T. O'connor, *ACS Appl. Mater. Interfaces* **2015**, *7*, 26726.
[245] D. J. Lipomi, Z. Bao, *MRS Bull.* **2017**, *42*, 93.
[246] Z. Bao, X. Chen, *Adv. Mater.* **2016**, *28*, 4177.
[247] D. J. Lipomi, B. C. K. Tee, M. Vosgueritchian, Z. Bao, *Adv. Mater.* **2011**, *23*, 1771.
[248] A. Gumyusenge, D. T. Tran, X. Luo, G. M. Pitch, Y. Zhao, K. A. Jenkins, T. J. Dunn, A. L. Ayzner, B. M. Savoie, J. Mei, *Science.* **2018**, *362*, 1131.
[249] D. T. Tran, A. Gumyusenge, X. Luo, M. Roders, Z. Yi, A. L. Ayzner, J. Mei, *ACS Appl. Polym. Mater.* **2020**, *2*, 91.
[250] S.-F. Yang, Z.-T. Liu, Z.-X. Cai, M. J. Dyson, N. Stingelin, W. Chen, H.-J. Ju, G.-X. Zhang, D.-Q. Zhang, *Adv. Sci.* **2017**, *4*, 1700048.
[251] C. M. Stafford, S. Guo, C. Harrison, M. Y. M. Chiang, *Rev. Sci. Instrum.* **2005**, *76*, 062207.

[252] Y. C. Chiang, H. C. Wu, H. F. Wen, C. C. Hung, C. W. Hong, C. C. Kuo, T. Higashihara, W. C. Chen, *Macromolecules* **2019**, *52*, 4393.
[253] S. E. Root, S. Savagatrup, C. J. Pais, G. Arya, D. J. Lipomi, *Macromolecules* **2016**, *49*, 2886.
[254] H. Chen, Y. Guo, G. Yu, Y. Zhao, J. Zhang, D. Gao, H. Liu, Y. Liu, *Adv. Mater.* **2012**, *24*, 4618.
[255] R. Potestio, C. Peter, K. Kremer, *Entropy* **2014**, *16*, 4199.
[256] W. G. Noid, *J. Chem. Phys.* **2013**, *139*, 09B201_1.
[257] W. Xia, N. K. Hansoge, W. S. Xu, F. R. Phelan, S. Keten, J. F. Douglas, *Sci. Adv.* **2019**, *5*.
[258] J. Ilavsky, *J. Appl. Crystallogr.* **2012**, *45*, 324.
[259] A. Chremos, J. F. Douglas, *J. Chem. Phys.* **2018**, *149*, 44904.
[260] S. Plimpton, *J. Comput. Phys.* **1995**, *117*, 1.
[261] M. C. Payne, M. P. Teter, D. C. Allan, T. A. Arias, ad J. D. Joannopoulos, *Rev. Mod. Phys.* **1992**, *64*, 1045.
[262] S.-J. Xie, H.-J. Qian, Z.-Y. Lu, *J. Chem. Phys.* **2015**, *142*, 74902.
[263] J. Dudowicz, K. F. Freed, J. F. Douglas, *J. Chem. Phys.* **2005**, *123*, 111102.
[264] J. Dudowicz, K. F. Freed, J. F. Douglas, *J. Phys. Chem. B* **2005**, *109*, 21285.
[265] J. Dudowicz, K. F. Freed, J. F. Douglas, *J. Phys. Chem. B* **2005**, *109*, 21350.
[266] J. Dudowicz, K. F. Freed, J. F. Douglas, *Adv. Chem. Phys.* **2008**, *137*, 125.
[267] W. Xia, J. Song, D. D. Hsu, S. Keten, *J. Chem. Phys.* **2017**, *146*, 203311.
[268] D. D. Hsu, W. Xia, J. Song, S. Keten, *ACS Macro Lett.* **2016**, *5*, 481.
[269] W. Xia, T. Lan, *Macromolecules* **2019**, *52*, 6547.
[270] W. Xia, J. Song, D. D. Hsu, S. Keten, *Macromolecules* **2016**, *49*, 3810.
[271] J. Fan, H. Emamy, A. Chremos, J. F. Douglas, F. W. Starr, *J. Chem. Phys.* **2020**, *152*, 54904.
[272] F. W. Starr, S. Sastry, J. F. Douglas, S. C. Glotzer, *Phys. Rev. Lett.* **2002**, *89*, 125501.
[273] B. A. P. Betancourt, P. Z. Hanakata, F. W. Starr, J. F. Douglas, *Proc. Natl. Acad. Sci.* **2015**, *112*, 2966.
[274] M. C. Bellissent-Funel, A. Filabozzi, S. H. Chen, *Biophys. J.* **1997**, *72*, 1792.
[275] J. Harada, H. Suzuki, S. Hoshino, *J. Phys. Soc. Japan* **1976**, *41*, 1707.
[276] T. G. Fox, S. Loshaek, *J. Polym. Sci.* **1955**, *15*, 371.
[277] H. A. Schneider, E. A. Di Marzio, *Polymer.* **1992**, *33*, 3453.
[278] H. A. Schneider, *Polymer.* **2005**, *46*, 2230.
[279] J. Schut, D. Bolikal, I. J. Khan, A. Pesnell, A. Rege, R. Rojas, L. Sheihet, N. S. Murthy, J. Kohn, *Polymer.* **2007**, *48*, 6115.
[280] S. A. Chen, J. M. Ni, *Macromolecules* **1992**, *25*, 6081.
[281] A. X. Chen, A. T. Kleinschmidt, K. Choudhary, D. J. Lipomi, *Chem. Mater.* **2020**, *32*, 7582.
[282] O. M. Awartani, B. Zhao, T. Currie, R. J. Kline, M. A. Zikry, B. T. O'Connor, *Macromolecules* **2016**, *49*, 327.
[283] H. Chen, C. Su, G. Shi, X. Li, X. Zhang, G. Liu, D. Wang, *Macromolecules* **2018**, *51*, 8306.
[284] T. Yasuda, L. Han, T. Tsutsui, *J. Photopolym. Sci. Technol.* **2009**, *22*, 713.

[285] H. Heil, T. Finnberg, N. Von Malm, R. Schmechel, H. Von Seggern, *J. Appl. Phys.* **2003**, *93*, 1636.
[286] L. Lin, A. S. Argon, *J. Mater. Sci.* **1994**, *29*, 294.
[287] M. F. Butler, A. M. Donald, A. J. Ryan, *Polymer.* **1997**, *38*, 5521.
[288] M. F. Butler, A. M. Donald, W. Bras, G. R. Mant, G. E. Derbyshire, A. J. Ryan, *Macromolecules* **1995**, *28*, 6383.
[289] M. F. Butler, A. M. Donald, A. J. Ryan, *Polymer.* **1998**, *39*, 781.
[290] M. F. Butler, A. M. Donald, A. J. Ryan, *Polymer.* **1998**, *39*, 39.
[291] C. R. López-Barrón, Y. Zeng, J. J. Schaefer, A. P. R. Eberle, T. P. Lodge, F. S. Bates, *Macromolecules* **2017**, *50*, 3627.
[292] R. Ramachandran, G. Beaucage, A. S. Kulkarni, D. McFaddin, J. Merrick-Mack, V. Galiatsatos, *Macromolecules* **2008**, *41*, 9802.
[293] E. Mena-Osteritz, *Adv. Mater.* **2002**, *14*, 609.
[294] B. Kuei, E. D. Gomez, *Soft Matter* **2017**, *13*, 49.
[295] Z. Cao, Z. Li, S. Zhang, L. Galuska, T. Li, C. Do, W. Xia, K. Hong, X. Gu, *Macromolecules* **2020**, *53*, 11142.
[296] N. R. Tummala, C. Risko, C. Bruner, R. H. Dauskardt, J. L. Brédas, *J. Polym. Sci. Part B Polym. Phys.* **2015**, *53*, 934.
[297] J. Qin, S. T. Milner, *Macromolecules* **2014**, *47*, 6077.
[298] S. A. Mollinger, B. A. Krajina, R. Noriega, A. Salleo, A. J. Spakowitz, *ACS Macro Lett.* **2015**, *4*, 708.
[299] A. Lustiger, R. L. Markham, *Polymer.* **1983**, *24*, 1647.
[300] Y. Men, J. Rieger, G. Strobl, *Phys. Rev. Lett.* **2003**, *91*, 095502.
[301] F. C. Spano, C. Silva, *Annu. Rev. Phys. Chem.* **2014**, *65*, 477.
[302] R. Remy, S. Wei, L. M. Campos, M. E. Mackay, *ACS Macro Lett.* **2015**, *4*, 1051.
[303] D. M. Delongchamp, R. J. Kline, D. A. Fischer, L. J. Richter, M. F. Toney, *Adv. Mater.* **2011**, *23*, 319.
[304] L. J. Richter, D. M. Delongchamp, A. Amassian, *Chem. Rev.* **2017**, *117*, 6332.
[305] T. E. Gartner, A. Jayaraman, *Macromolecules* **2019**, *52*, 755.
[306] S. E. Root, N. E. Jackson, S. Savagatrup, G. Arya, D. J. Lipomi, *Energy Environ. Sci.* **2017**, *10*, 558.
[307] W. S. Xu, J. F. Douglas, W. Xia, X. Xu, *Macromolecules* **2020**, *53*, 6828.
[308] C. Wu, R. Wu, W. Xia, L. ho Tam, *J. Polym. Sci. Part B Polym. Phys.* **2019**, *57*, 1779.
[309] Z. Li, W. Xia, *Extrem. Mech. Lett.* **2020**, *40*, 100942.
[310] M. S. Lavine, N. Waheed, G. C. Rutledge, *Polymer.* **2003**, *44*, 1771.
[311] M. Zhernenkov, N. Canestrari, O. Chubar, E. DiMasi, In *Advances in Computational Methods for X-Ray Optics III*, International Society for Optics and Photonics, **2014**, p. 92090G.
[312] R. J. Pandolfi, D. B. Allan, E. Arenholz, L. Barroso-Luque, S. I. Campbell, T. A. Caswell, A. Blair, F. De Carlo, S. Fackler, A. P. Fournier, *J. Synchrotron Radiat.* **2018**, *25*, 1261.
[313] G. N. Toepperwein, R. A. Riggleman, J. J. de Pablo, *Macromolecules* **2012**, *45*, 543.
[314] G. N. Toepperwein, K. S. Schweizer, R. A. Riggleman, J. J. De Pablo,

Macromolecules **2012**, *45*, 8467.
[315] H. G. H. Van Melick, L. E. Govaert, H. E. H. Meijer, *Polymer.* **2003**, *44*, 2493.
[316] K. Chen, K. S. Schweizer, *Macromolecules* **2011**, *44*, 3988.
[317] W. Zou, S. Moghadam, R. S. Hoy, R. G. Larson, *Macromolecules* **2019**, *52*, 9248.
[318] R. N. Haward, *Macromolecules* **1993**, *26*, 5860.
[319] B. A. G. Schrauwen, R. P. M. Janssen, L. E. Govaert, H. E. H. Meijer, *Macromolecules* **2004**, *37*, 6069.
[320] M. Encinar, A. Martínez-Gómez, R. G. Rubio, E. Pérez, A. Bello, M. G. Prolongo, *J. Phys. Chem. B* **2012**, *116*, 9846.
[321] U. Koldemir, S. R. Puniredd, M. Wagner, S. Tongay, T. D. McCarley, G. D. Kamenov, K. Müllen, W. Pisula, J. R. Reynolds, *Macromolecules* **2015**, *48*, 6369.
[322] M. U. Ocheje, M. Selivanova, S. Zhang, T. H. Van Nguyen, B. P. Charron, C. H. Chuang, Y. H. Cheng, B. Billet, S. Noori, Y. C. Chiu, X. Gu, S. Rondeau-Gagné, *Polym. Chem.* **2018**, *9*, 5531.
[323] Y. Zheng, G. N. Wang, J. Kang, M. Nikolka, H. Wu, H. Tran, S. Zhang, H. Yan, H. Chen, P. Y. Yuen, J. Mun, R. H. Dauskardt, I. McCulloch, J. B. -H. Tok, X. Gu, Z. Bao, *Adv. Funct. Mater.* **2019**, *29*, 1905340.
[324] F. C. Spano, *Acc. Chem. Res.* **2010**, *43*, 429.
[325] J. Balko, R. H. Lohwasser, M. Sommer, M. Thelakkat, T. Thurn-Albrecht, *Macromolecules* **2013**, *46*, 9642.
[326] J. S. Kim, J. H. Kim, W. Lee, H. Yu, H. J. Kim, I. Song, M. Shin, J. H. Oh, U. Jeong, T. S. Kim, B. J. Kim, *Macromolecules* **2015**, *48*, 4339.
[327] M. M. Nahid, E. Gann, L. Thomsen, C. R. McNeill, *Eur. Polym. J.* **2016**, *81*, 532.
[328] B. Watts, S. Swaraj, D. Nordlund, J. Lüning, H. Ade, *J. Chem. Phys.* **2011**, *134*, 024702.
[329] Y. Ito, A. A. Virkar, S. Mannsfeld, H. O. Joon, M. Toney, J. Locklin, Z. Bao, *J. Am. Chem. Soc.* **2009**, *131*, 9396.
[330] J. Mun, G. J. N. Wang, J. Y. Oh, T. Katsumata, F. L. Lee, J. Kang, H. C. Wu, F. Lissel, S. Rondeau-Gagné, J. B. H. Tok, Z. Bao, *Adv. Funct. Mater.* **2018**, *28*, 1804222.
[331] Y. Zhao, J. Liu, X. Li, Y. Lu, S. Q. Wang, *Macromolecules* **2017**, *50*, 2024.
[332] J. W. Mok, Z. Hu, C. Sun, I. Barth, R. Munoz, J. Jackson, T. Terlier, K. G. Yager, R. Verduzco, *Chem. Mater.* **2018**, *30*, 8314.
[333] G.-J. J. N. Wang, Y. Zheng, S. Zhang, J. Kang, H.-C. C. Wu, A. Gasperini, H. Zhang, X. Gu, Z. Bao, *Chem. Mater.* **2019**, *31*, 6465.
[334] B. McCulloch, V. Ho, M. Hoarfrost, C. Stanley, C. Do, W. T. Heller, R. A. Segalman, *Macromolecules* **2013**, *46*, 1899.
[335] J. Hynynen, E. Järsvall, R. Kroon, Y. Zhang, S. Barlow, S. R. Marder, M. Kemerink, A. Lund, C. Müller, *ACS Macro Lett.* **2019**, *8*, 70.
[336] H. Joodaki, M. B. Panzer, *Proc. Inst. Mech. Eng. Part H J. Eng. Med.* **2018**, *232*, 323.
[337] H. J. Kim, A. Thukral, S. Sharma, C. Yu, *Adv. Mater. Technol.* **2018**, *3*, 1800043.
[338] D. C. Kim, H. J. Shim, W. Lee, J. H. Koo, D. Kim, *Adv. Mater.* **2020**, *32*, 1902743.
[339] S. Goffri, C. Müller, N. Stingelin-Stutzmann, D. W. Breiby, C. P. Radano, J. W.

Andreasen, R. Thompson, R. A. J. Janssen, M. M. Nielsen, P. Smith, H. Sirringhaus, *Nat. Mater.* **2006**, *5*, 950.
[340] T. Sun, J. I. Scott, M. Wang, R. J. Kline, G. C. Bazan, B. T. O'Connor, *Adv. Electron. Mater.* **2017**, *3*, 1600388.
[341] W. Yang, V. R. Sherman, B. Gludovatz, E. Schaible, P. Stewart, R. O. Ritchie, M. A. Meyers, *Nat. Commun.* **2015**, *6*, 6649.
[342] J. Kang, J. B. H. Tok, Z. Bao, *Nat. Electron.* **2019**, *2*, 144.
[343] J. Y. Oh, D. Son, T. Katsumata, Y. Lee, Y. Kim, J. Lopez, H.-C. Wu, J. Kang, J. Park, X. Gu, J. Mun, N. G.-J. Wang, Y. Yin, W. Cai, Y. Yun, J. B. H. Tok, Z. Bao, *Sci. Adv.* **2019**, *5*, eaav3097.
[344] P. C. Hiemenz, T. P. Lodge, *Polymer chemistry*, CRC press, **2007**.
[345] H. F. Wen, H. C. Wu, J. Aimi, C. C. Hung, Y. C. Chiang, C. C. Kuo, W. C. Chen, *Macromolecules* **2017**, *50*, 4982.
[346] H. C. Wu, C. C. Hung, C. W. Hong, H. S. Sun, J. T. Wang, G. Yamashita, T. Higashihara, W. C. Chen, *Macromolecules* **2016**, *49*, 8540.
[347] F. Sugiyama, A. T. Kleinschmidt, L. V. Kayser, M. A. Alkhadra, J. M. H. Wan, A. S. C. Chiang, D. Rodriquez, S. E. Root, S. Savagatrup, D. J. Lipomi, *Macromolecules* **2018**, *51*, 5944.
[348] Y. W. Soon, S. Shoaee, R. S. Ashraf, H. Bronstein, B. C. Schroeder, W. Zhang, Z. Fei, M. Heeney, I. McCulloch, J. R. Durrant, *Adv. Funct. Mater.* **2014**, *24*, 1474.
[349] M. L. Chabinyc, F. Endicott, B. D. Vogt, D. M. DeLongchamp, E. K. Lin, Y. Wu, P. Liu, B. S. Ong, *Appl. Phys. Lett.* **2006**, *88*, 113514.
[350] P. Mittal, B. Kumar, Y. S. Negi, B. K. Kaushik, R. K. Singh, *Microelectronics J.* **2012**, *43*, 985.
[351] C. Zou, N. Yanahashi, Y. Wu, J. Wang, C. Zhang, G. Xiong, H. Yang, L. Jiang, T. Ikeda, *Adv. Funct. Mater.* **2019**, *29*, 1804838.
[352] K. L. Gu, Y. Zhou, W. A. Morrison, K. Park, S. Park, Z. Bao, *ACS Nano* **2018**, *12*, 1473.
[353] S. Choi, S. I. Han, D. Jung, H. J. Hwang, C. Lim, S. Bae, O. K. Park, C. M. Tschabrunn, M. Lee, S. Y. Bae, J. W. Yu, J. H. Ryu, S. W. Lee, K. Park, P. M. Kang, W. B. Lee, R. Nezafat, T. Hyeon, D. H. Kim, *Nat. Nanotechnol.* **2018**, *13*, 1048.
[354] I. McCulloch, M. Heeney, C. Bailey, K. Genevicius, I. MacDonald, M. Shkunov, D. Sparrowe, S. Tierney, R. Wagner, W. Zhang, M. L. Chabinyc, R. J. Kline, M. D. McGehee, M. F. Toney, *Nat. Mater.* **2006**, *5*, 328.
[355] H. Yan, Z. Chen, Y. Zheng, C. Newman, J. R. Quinn, F. Dötz, M. Kastler, A. Facchetti, *Nature* **2009**, *457*, 679.
[356] S. Choi, S. I. Han, D. Kim, T. Hyeon, D. H. Kim, *Chem. Soc. Rev.* **2019**, *48*, 1566.
[357] A. J. Howarth, Y. Liu, P. Li, Z. Li, T. C. Wang, J. T. Hupp, O. K. Farha, *Nat. Rev. Mater.* **2016**, *1*, 15018.
[358] P. Z. Moghadam, S. M. J. Rogge, A. Li, C.-M. Chow, J. Wieme, N. Moharrami, M. Aragones-Anglada, G. Conduit, D. A. Gomez-Gualdron, V. Van Speybroeck, D. Fairen-Jimenez, *Matter* **2019**, *1*, 219.
[359] T. Iizuka, K. Honjo, T. Uemura, *Chem. Commun.* **2019**, *55*, 691.
[360] N. C. Burtch, J. Heinen, T. D. Bennett, D. Dubbeldam, M. D. Allendorf, *Adv.*

Mater. **2018**, *30*, 1704124.
[361] I. M. Hönicke, I. Senkovska, V. Bon, I. A. Baburin, N. Bönisch, S. Raschke, J. D. Evans, S. Kaskel, *Angew. Chemie Int. Ed.* **2018**, *57*, 13780.
[362] K. Cao, S. Feng, Y. Han, L. Gao, T. Hue Ly, Z. Xu, Y. Lu, *Nat. Commun.* **2020**, *11*, 284.
[363] P. Zhang, L. Ma, F. Fan, Z. Zeng, C. Peng, P. E. Loya, Z. Liu, Y. Gong, J. Zhang, X. Zhang, P. M. Ajayan, T. Zhu, J. Lou, *Nat. Commun.* **2014**, *5*, 3782.
[364] C. Lee, X. Wei, J. W. Kysar, J. Hone, *Science.* **2008**, *321*, 385.
[365] R. C. Cooper, C. Lee, C. A. Marianetti, X. Wei, J. Hone, J. W. Kysar, *Phys. Rev. B* **2013**, *87*, 035423.
[366] S. S. Zalesskiy, V. P. Ananikov, *Organometallics* **2012**, *31*, 2302.
[367] H. Yu, K. H. Park, I. Song, M. J. Kim, Y. H. Kim, J. H. Oh, *J. Mater. Chem. C* **2015**, *3*, 11697.
[368] A. Yassin, P. Jimenez, B. Lestriez, P. Moreau, P. Leriche, J. Roncali, P. Blanchard, H. Terrisse, D. Guyomard, J. Gaubicher, *Chem. Mater.* **2015**, *27*, 4057.
[369] H. Li, J. Mei, A. L. Ayzner, M. F. Toney, J. B. H. Tok, Z. Bao, *Org. Electron. physics, Mater. Appl.* **2012**, *13*, 2450.
[370] J. H. Kim, A. Gadisa, C. Schaefer, H. Yao, B. R. Gautam, N. Balar, M. Ghasemi, I. Constantinou, F. So, B. T. O'Connor, K. Gundogdu, J. Hou, H. Ade, *J. Mater. Chem. A* **2017**, *5*, 13176.
[371] S. Y. Son, J. H. Kim, E. Song, K. Choi, J. Lee, K. Cho, T. S. Kim, T. Park, *Macromolecules* **2018**, *51*, 2572.
[372] E. L. Melenbrink, K. M. Hilby, M. A. Alkhadra, S. Samal, D. J. Lipomi, B. C. Thompson, *ACS Appl. Mater. Interfaces* **2018**, *10*, 32426.
[373] W. Kim, J. Choi, J. H. Kim, T. Kim, C. Lee, S. Lee, M. Kim, B. J. Kim, T. S. Kim, *Chem. Mater.* **2018**, *30*, 2102.
[374] R. Di Pietro, T. Erdmann, J. H. Carpenter, N. Wang, R. R. Shivhare, P. Formanek, C. Heintze, B. Voit, D. Neher, H. Ade, A. Kiriy, *Chem. Mater.* **2017**, *29*, 10220.
[375] A. R. Han, G. K. Dutta, J. Lee, H. R. Lee, S. M. Lee, H. Ahn, T. J. Shin, J. H. Oh, C. Yang, *Adv. Funct. Mater.* **2015**, *25*, 247.
[376] Y. Li, P. Sonar, S. P. Singh, M. S. Soh, M. Van Meurs, J. Tan, *J. Am. Chem. Soc.* **2011**, *133*, 2198.
[377] S. Chen, B. Sun, W. Hong, H. Aziz, Y. Meng, Y. Li, *J. Mater. Chem. C* **2014**, *2*, 2183.
[378] B. Sun, W. Hong, H. Aziz, N. M. Abukhdeir, Y. Li, *J. Mater. Chem. C* **2013**, *1*, 4423.
[379] Z. Chen, M. J. Lee, R. Shahid Ashraf, Y. Gu, S. Albert-Seifried, M. Meedom Nielsen, B. Schroeder, T. D. Anthopoulos, M. Heeney, I. McCulloch, H. Sirringhaus, *Adv. Mater.* **2012**, *24*, 647.
[380] Y. Li, S. P. Singh, P. Sonar, *Adv. Mater.* **2010**, *22*, 4862.
[381] J. Li, Y. Zhao, H. S. Tan, Y. Guo, C. A. Di, G. Yu, Y. Liu, M. Lin, S. H. Lim, Y. Zhou, H. Su, B. S. Ong, *Sci. Rep.* **2012**, *2*, 754.
[382] M. Shahid, R. S. Ashraf, Z. Huang, A. J. Kronemeijer, T. McCarthy-Ward, I. McCulloch, J. R. Durrant, H. Sirringhaus, M. Heeney, *J. Mater. Chem.* **2012**, *22*, 12817.

[383] T. Hirano, H. Hanamura, M. Inoue, S. Ueda, M. Watanabe, M. Tanabiki, K. Mikami, *Polymer*. **2019**, *177*, 282.
[384] J. H. Kim, A. Gadisa, C. Schaefer, H. Yao, B. R. Gautam, N. Balar, M. Ghasemi, I. Constantinou, F. So, B. T. O'Connor, K. Gundogdu, J. Hou, H. Ade, *J. Mater. Chem. A* **2017**, *5*, 13176.